

Investigation of the Coevolution between
Supermassive Blackholes and Galaxies at
Redshift 3 through Subaru Near-Infrared
Observations

Yuriko Saito

Doctor of Philosophy

Department of Astronomical Science
School of Physical Sciences
SOKENDAI (The Graduate University for
Advanced Studies)

Doctoral Thesis

Investigation of the Coevolution between
Supermassive Blackholes and Galaxies at
Redshift 3 through Subaru Near-Infrared
Observations

Department of Astronomical Science
School of Physical Sciences
The Graduate University for Advanced Studies

20110952

Yuriko Saito

Supervisor : Masatoshi Imanishi

6/30/2016

Contents

1	Introduction	4
1.1	Active Galactic Nucleus	4
1.2	Geometric Structure of AGNs : Unified Model for AGN	5
1.3	Coevolution between Galaxies and Supermassive Blackholes	6
1.4	Purpose of Our Study	9
1.5	Previous Studies	9
1.5.1	M_{BH} estimate	9
1.5.2	M_{spheroid} estimate	13
2	Sample Selection	18
3	Spectroscopic Observations and Data Reduction	21
3.1	Near-infrared observation and noise sources	21
3.2	UKIRT/UIST	23
3.2.1	Background subtraction	23
3.2.2	Flat fielding	25
3.2.3	Correction of cosmic ray and bad pixels	25
3.2.4	Extraction of target signals	26
3.2.5	Wavelength calibration	27
3.2.6	Transmission calibration	28
3.2.7	Flux calibration	28
3.2.8	Error estimate	28
3.3	WHT/LIRIS	29
3.4	Subaru/IRCS	30
3.5	IRTF/Spex	30
3.5.1	Making calibration frames	31
3.5.2	From background subtraction to wavelength calibration	31
3.5.3	Transmission and flux calibration	34
4	Spectral Analysis	44
5	Results of Spectroscopic Observation	51
5.1	M_{BH} and $L_{\text{bol}}/L_{\text{Edd}}$ Estimation	51
5.2	M_{BH} and $L_{\text{bol}}/L_{\text{Edd}}$ distributions	52

6	Findings from Spectroscopic Observations	56
6.1	Comparison of M_{BH} estimated from $\text{H}\beta$ $\lambda 4861$ and $\text{CIV } \lambda 1549$	56
6.2	Growth Time of SMBHs	57
7	Imaging Observation and Data Reduction	60
7.1	Near-infrared imaging observation and noise sources	60
7.2	Our Observation	61
7.3	Data reduction	62
8	Imaging Analysis and Result	65
8.1	PSF fitting	65
8.2	QSO fitting	66
8.2.1	QSO fitting method	66
8.3	M_{spheroid} Estimation	71
8.4	Detection Check	74
8.5	Fitting Accuracy	77
9	$M_{\text{BH}}/M_{\text{spheroid}}$ ratio at $z \sim 3$	79
9.1	Comparison with studies at higher redshift	82
9.2	Selection bias for our result	83
9.3	Relation between $M_{\text{BH}}/M_{\text{spheroid}}$ ratio and AGN luminosity	86
10	Summary	88
	AppendixA	96
	AppendixB	102
	B.1 Error caused by sky variation	102
	B.2 Test of our PSF fitting method	106
	AppendixC	111
	C.1 J0146J	111
	C.2 J0146K	114
	C.3 J0725J	117
	C.4 J0725K	120
	C.5 J0847K	123
	C.6 J1116J	126
	C.7 J1116K	129
	C.8 J1337J	132
	C.9 J1337K	135
	C.10 J1407J	138

C.11	J1407K	141
C.12	J1510J	144
C.13	J1510K	147
C.14	J1551J	150
C.15	J1551K	153
C.16	J2130J	156
C.17	J2130K	159
AppendixD		162
D.1	J0146J	163
D.2	J0146K	165
D.3	J0725J	167
D.4	J0725K	169
D.5	J0847K	171
D.6	J1116J	173
D.7	J1337J	175
D.8	J1337K	177
D.9	J1407J	179
D.10	J1407K	181
D.11	J1510J	183
D.12	J1510K	185
D.13	J1551J	187

Abstract

In the Universe, there are various types of galaxies, and those galaxies have a supermassive black hole (SMBH) at the center of their spheroidal component (elliptical galaxy itself or bulge component). Moreover, the tight correlation between spheroidal stellar mass (M_{spheroid}) and SMBH mass (M_{BH}) was found by previous studies for local galaxies ($M_{\text{BH}}/M_{\text{spheroid}} \sim 0.0015$), suggesting co-evolution between galaxies and SMBHs. To reveal galaxy and SMBH formation mechanisms, one of the keys is exploring the redshift evolution of $M_{\text{BH}}/M_{\text{spheroid}}$ ratio, however it is still not well understood observationally. On the other hand, there are some theoretical studies explaining observed relation between M_{BH} and M_{spheroid} . In each study, physical mechanism behind the relation of M_{BH} and M_{spheroid} is different, therefore different redshift evolutions of $M_{\text{BH}}/M_{\text{spheroid}}$ ratio are predicted. The difference among models is getting larger at higher redshift. In this study, we derive M_{BH} and M_{spheroid} for high- z galaxies independently, and observationally estimate accurate $M_{\text{BH}}/M_{\text{spheroid}}$ ratios. The result also might be able to give a constraint on physical mechanisms behind the relation of M_{BH} and M_{spheroid} predicted by theoretical studies. Although the difference between models becomes larger at higher redshift, an observation of high- z galaxy is getting more difficult due to surface brightness dimming (proportional to $(1+z)^4$). Active Galactic Nucleus (AGN) is an actively mass accreting SMBH, and its M_{BH} can be estimated by single spectroscopic observation without spatially resolving. We chose $z \sim 3$ QSOs (luminous AGNs) as our targets.

M_{BH} is derived from the combination of $\text{H}\beta(4861\text{\AA})$ emission line width and AGN continuum luminosity at rest-frame 5100\AA obtained by near-infrared spectroscopic observations. $\text{CIV}(1549\text{\AA})$ and $\text{MgII}(2800\text{\AA})$ emission lines were often used to estimate M_{BH} for high- z QSOs, however, these emission lines are possibly affected by non-gravitational motion such as AGN outflow, and also not well calibrated by the observations of local galaxies. $\text{H}\beta$ emission line has much less uncertainty by possible non-gravitational motion and is well calibrated by the observations for local galaxies, therefore $\text{H}\beta$ can be the best indicator of M_{BH} . We carried out near-infrared spectroscopic observations for 37 QSOs at $z \sim 3$ by using Subaru telescope and other 4 m-class telescopes, and succeeded in determining M_{BH} for 28 out of 37 QSOs (Saito et al. 2016 PASJ 68 1).

To estimate M_{spheroid} , we adopt multi-band ($J(1.2\mu\text{m})$, $K'(2.2\mu\text{m})$) near-infrared imaging method with Adaptive Optics (AO). From the multi-band galaxy images, we can estimate galaxy color. Since there is a relation between color and mass-to-light (M/L) ratio, we can derive M_{spheroid} accurately by multiplying by spheroidal stellar luminosity (L_{spheroid}). The studies of QSO host galaxies necessitate to subtract AGN contamination with sufficient accuracy, that

requires high-spatial resolution imaging observation using AO. Usually, $0''.4-0''.5$ of seeing size is obtained at K' -band, without AO. Since $1''$ is corresponding to $\sim 8\text{kpc}$ at $z \sim 3$, at least $< 2\text{kpc} \sim 0''.25$ of spatial resolution is required to discuss a few kpc size of galaxy, which is impossible with normal (without AO) observation. Only by using AO, $0''.1-0''.2$ of spatial resolution can be routinely obtained. Moreover, most of previous studies assume M/L ratio from single-band imaging observation for simplicity. However uncertainty of M/L ratio is large due to the assumption, making the interpretation about the redshift evolution of $M_{\text{BH}}/M_{\text{spheroid}}$ difficult. Although multi-band imaging observation method requires a lot of telescope time, we adopt this method for accurate M/L estimation. We carried out near-infrared imaging observations using Subaru telescope/IRCS+AO188 for 9 QSOs whose M_{BH} values have been already estimated from our spectroscopic observations.

For QSOs, it is very difficult to estimate host galaxy mass with high accuracy because AGN glare is much brighter in surface brightness than diffuse host galaxy stellar emission. To resolve this problem, we established our original analysis method. To decompose an AGN component and a galaxy component with two dimensional (2D) fitting, AGN component is fitted with Gaussian (core component which is corrected by AO) + Moffat (seeing-sized extended component which is uncorrected by AO), and galaxy component is fitted with Sersic profile. Since Moffat and Sersic are both spatially extended, it is difficult to clearly separate these magnitudes. In our method, we firstly fit a PSF reference star in the same field of view, and estimate its strelh ratio. By using the relation between strelh ratio and distance from the AO reference star, the strelh ratio at the position of QSO can be estimated. We put a constraint on Moffat magnitude from Gaussian magnitude and the strelh ratio, and carried out fitting, to estimate host galaxy magnitude accurately.

With the above method, we derived M_{BH} for 28 $z \sim 3$ QSOs, and also derived M_{spheroid} for 9 out of 28 QSOs. As a result of our $M_{\text{BH}}/M_{\text{spheroid}}$ estimate for 9 QSOs from their M_{BH} and M_{spheroid} values, we found that $M_{\text{BH}}/M_{\text{spheroid}}$ at $z \sim 3$ is larger ($M_{\text{BH}}/M_{\text{spheroid}}(\text{median}) \sim 0.046$) than the local relation ($M_{\text{BH}}/M_{\text{spheroid}} \sim 0.0015$). With comparing theoretical models, our result seems like not supporting the no-evolution model, rather suggesting steeper evolution than the model assuming that AGN outflow plays major role in $M_{\text{BH}}/M_{\text{spheroid}}$ ratio evolution.

We succeeded in determining more accurate $M_{\text{BH}}/M_{\text{spheroid}}$ ratios for high redshift QSOs than previous studies, by adopting $H\beta$ method for M_{BH} estimate, and our original analysis method for M_{spheroid} estimate. Moreover, we quadrupled the sample number of high redshift QSOs with derived $M_{\text{BH}}/M_{\text{spheroid}}$ ratios. This study brings a remarkable improvement in the study about redshift evolution of the $M_{\text{BH}}/M_{\text{spheroid}}$ ratio.

1 Introduction

1.1 Active Galactic Nucleus

There are various galaxies in the Universe, and some of them are releasing enormous energy with close to more than 10 billion times as much as the Sun from their central region. We call them Active Galactic Nucleus, AGN. An AGN has a supermassive blackhole (SMBH) with mass of more than $10^6 \sim 10^{10}M_{\odot}$ at the center (M_{\odot} is solar mass). It is thought that blackholes can radiate such a large amount of energy because gas near the blackhole releases gravity energy when it falls onto a SMBH. AGNs are classified by historic backgrounds and differences of their apparent properties.

(1) quasars (QSOs)

Although a quasar (QSO) was originally found as a very bright radio source, it is named "Quasi-stellar Radio Sources (quaser in short)" because it optically looks like a star. A quasar radiates enormous energy which is comparable to hundred to thousand times the amount of energy Milky Way-type galaxy radiates. AGNs with luminosity more than $10^{12}L_{\odot}$ are classified as quasars. Strong emission lines are radiated from quasars and their intensity at optical or radio varies on a timescale of hours through days, months to years. Moreover, quasars are categorized into two types according to their radio intensity. Quasars with strong radio emission are called QSS(quasi-stellar radio source) or radio-loud quasar. On the other hand, quasars with non-strong radio emission are named QSO(quasi-stellar object) or radio-quiet quasar, accounting for 90% of quasars.

(2) Seyfert galaxies

Seyfert galaxies are AGN having spiral galaxies as their hosts, compact and blue nuclear emission, and broad emission line spectra at optical. Seyfert galaxies are classified into Type-I or II. The spectra of Type-I Seyfert galaxies show broad emission lines, whose line widths are as large as several 1000 to 10^4 km/s. While, the spectra of Type-II Seyfert galaxies only display narrow emission lines with ~ 500 km/s wide. Luminosity is typically 2–3 dex fainter than quasars.

(3) Radio galaxies

Radio galaxies are more luminous in radio wavelength than normal star-forming galaxies, and their shapes are mostly elliptical. They are categorized into two types in the same way as Seyfert galaxies ; A broad-line radio galaxy (BLRG) has a similar spectrum to a Type-I Serfert galaxy, and the spectrum of narrow-line radio galaxy (NLRG) shows only narrow emission lines like a Type-II Seyfert galaxy.

(4) Blazars

Blazars look like stars in the optical, similar to quasars, however, their spectra show very luminous continuum with very weak (often undetectable) emission lines and violent time variation. Blazars are thought to be AGNs whose relativistic jets from the center of engines are pointing toward us.

1.2 Geometric Structure of AGNs : Unified Model for AGN

Although there are several types of AGNs, it is the same for all AGNs that there is a supermassive blackhole at the center, and nearby gas accretes onto a SMBH, releasing their gravitational energy as enormous radiative energy. Note that where the energy is radiated from is an accretion disk, not a blackhole. What is the difference between Type-I and II? Why do they show different optical spectra? It used to be considered that Type-I had both broad line region which radiates broad emission lines, and narrow line region where narrow emission lines are radiated, while Type-II had only the narrow line region.

Antonucci & Miller (1985) carried out optical spectro-polarimetry for a prototypical nearby Type-II Seyfert galaxy, NGC1068, and they found that there exist broad emission lines in the polarized component. It can be explained as follows ; Type-II Seyfert galaxies also have the broad line region, however it is hidden by something and could not be observed. Based on the observational result, the unified model for AGN is suggested (Figure 1).

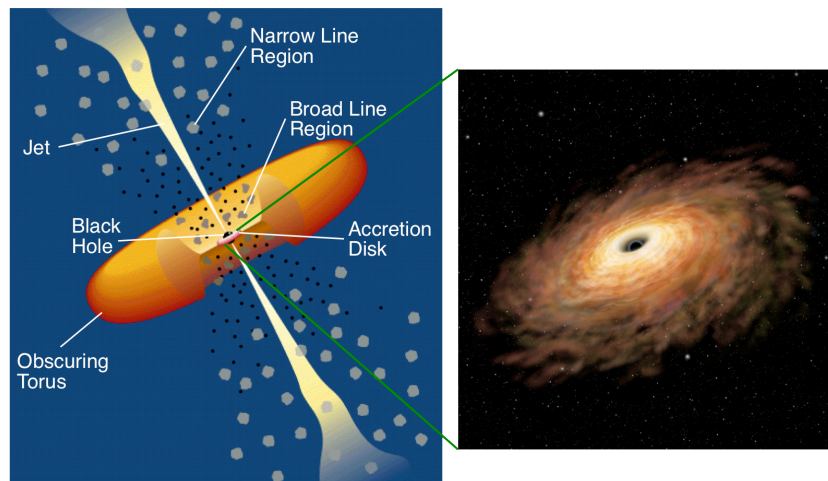


Figure 1 Left : Geometric structure of an AGN. Right : Image of gas accretion onto a SMBH. Credit : (left) C.M. Urry and P. Padovani, (right) NAOJ

There is a supermassive blackhole (SMBH, $10^{-4} \sim 10^{-5}$ pc) and an accretion disk ($\ll 0.1$ pc) at the center. Around them, there exists the broad line region (BLR, < 0.1 pc), which radiates

broad emission lines. Gas distributed at the broad line region is dominated by the gravity of the central SMBH, and photo-ionized by strong UV radiation from the accretion disk. Dust-torus (0.1~dozens pc) is located surrounding SMBH, accretion disk, and BLR. At a higher scale height along the dust-torus, there is narrow line region (NLR, $10 \sim 10^3$ pc), where the narrow emission lines come from. Gas density in BLR is high ($n_e \sim 10^{11} \text{ cm}^{-3}$). When gas density is higher than critical density, flux of forbidden line such as [O III] cannot increase due to collisional de-excitation. While, gas density in NLR is low ($n_e \sim 10^3 \text{ cm}^{-3}$) and volume of NLR is larger than BLR. Therefore forbidden line is predominantly radiated from NLR. Permitted lines such as $H\beta$ are emitted from both BLR and NLR.

According to this model, both broad and narrow line regions can be observed with face-on or along the dust-torus axis, and as a result broad line spectra can be obtained. These AGNs are classified into Type-I AGNs. Type-I Seyfert Galaxies, quasars, and BLRGs are included. On the other hand, when dust-torus is viewed from an edge-on direction, BLR is hidden by the dust-torus and only NLR can be observed. We call these AGNs as Type-II AGNs. Type-II Seyfert galaxies and NLRGs are classified into this type. Therefore, difference between Type-I and II can be explained by a viewing angle, meaning that they are intrinsically the same. This model is widely believed because X-ray observations support this model (Smith & Done 1996; Bassani et al. 1999), and there have been no observational results that could reject the model. We, however, note that there are some studies advocating existence of "pure Seyfert-II galaxies" that intrinsically lack the BLR (e.g., Tran (2001), Tran (2003)).

1.3 Coevolution between Galaxies and Supermassive Blackholes

The tight correlations between the properties of galaxy spheroidal stellar components (e.g., mass M_{spheroid} , velocity dispersion, and luminosity L_{spheroid}) and the SMBH mass (M_{BH}) in the local universe (Kormendy & Richstone (1995); Marconi & Hunt (2003); McConnell & Ma (2013); see also Kormendy & Ho (2013) for a review) indicate that the formation/growth of galaxies and central SMBHs are closely related (so-called coevolution, Figure 2).

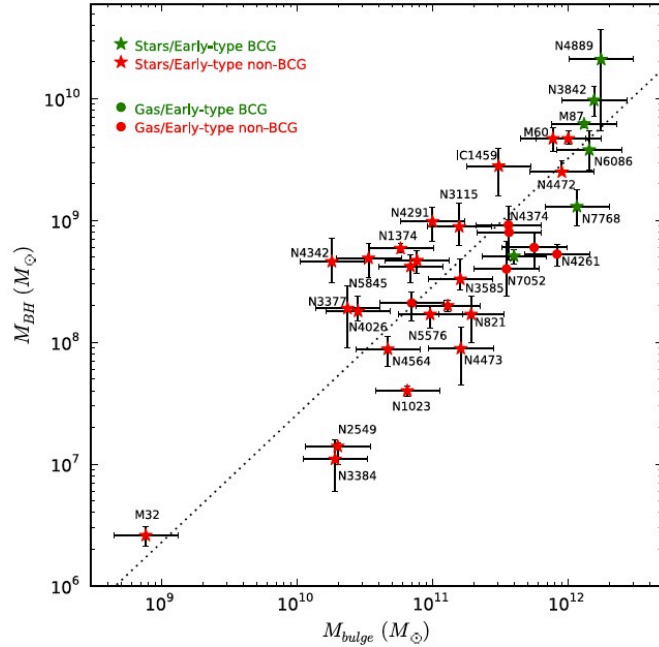


Figure 2 The correlation between bulge mass and SMBH mass (McConnell & Ma (2013)).

Recent multi-wavelength deep surveys have revealed similar downsizing evolution among galaxies, active galactic nuclei (AGNs), and SMBHs in AGNs (Cowie et al. (1996); Kodama et al. (2004); Ueda et al. (2003); Vestergaard et al. (2008)), where more luminous, massive galaxies, more luminous AGNs, and more massive active SMBHs in AGNs show their number density peaks at higher redshift. This implies that the histories of cosmic star formation and the mass accretion of SMBHs may be synchronized (Franceschini et al. (1999); Silverman et al. (2008); Zheng et al. (2009)). It is important to observationally better constrain how SMBHs and galaxies have coevolved from the early to the current universe.

Depending on various galaxy- and SMBH-growth mechanisms, different redshift (z) evolutions of the $M_{\text{BH}}/M_{\text{spheroid}}$ ratio ($\equiv R_{\text{BH/spheroid}}$) can be predicted.

(1) Wyithe & Loeb (2003) considered that SMBHs grow through hierarchal merging, and a QSO radiating with its Eddington luminosity*¹ might have powerful wind that can sweep away surrounding gas if the outflow generates as much energy as the binding energy, and regulate BH growth (Silk & Rees (1998)). They assume that some fraction of energy radiated from QSO is returned to the galaxy, and can unbind the gas when it provides as much energy as the binding energy, resulting in regulating accretion on to SMBH ($M_{\text{BH}} \propto (1+z)^{5/2}$). While, supernovae energy output also can unbind gas, and halt star formation in the galaxy ($M_* \propto (1+z)$). The assumptions above predict redshift evolution of $M_{\text{BH}}/M_{\text{spheroid}} \propto (1+z)^{3/2}$.

*¹ The maximum luminosity a body (such as a star) can achieve when there is balance between the force of radiation acting outward and the gravitational force acting inward.

(2) Robertson et al. (2006) simulate major merging of gas-rich galaxies that have properties suitable to calculate $M_{\text{BH}} - \sigma$ relation at each redshift ($z = 0, 2, 3$ and 6). Each progenitor galaxy does not contain bulges to avoid assumption of the existence of the $M_{\text{BH}} - \sigma$ relation at higher redshift, but allow to produce an $M_{\text{BH}} - \sigma$ relation self-consistently through the merger process. In the simulation, SMBH can grow based on Bondi-Hoyle-Lyttleton accretion (Bondi & Hoyle (1944)), and 5% of radiation energy from SMBH is returned to the galaxy as a feedback. After calculating M_{BH} and σ of completely merged galaxy, and comparing with the result at each redshift, they find that $M_{\text{BH}} - \sigma$ relation is weakly evolving with redshift due to steeper potential well of galaxy at high redshift. Namely, no redshift evolution of $M_{\text{BH}}/M_{\text{spheroid}}$ ratio is predicted ($M_{\text{BH}}/M_{\text{spheroid}} \propto (1+z)^0$).

(3) Kauffman & Haehnelt (2000) introduce the effect of the transformation of disk stars to bulge stars during major mergers, as a key mechanism. In their semi-analytical simulation, SMBH can grow by gas accretion during major or major+minor mergers, depending on total gas mass, m_{cold} ($\Delta M_{\text{BH}} \propto m_{\text{cold}}$). While, bulge can grow by starburst triggered by merger, also depending on m_{cold} ($\Delta M_{\text{starburst}} \propto m_{\text{cold}}$). In addition, galaxy disk is disrupted during major merging and eventually disk stars are added to bulge. This is also considered as a process of bulge growth. Since bulge growth by the second growing process is enhanced in the late stage, relative to SMBH growth, the $M_{\text{BH}}/M_{\text{spheroid}}$ ratio is larger at higher redshift (e.g., $M_{\text{BH}}/M_{\text{spheroid}} \propto (1+z)^{0.5}$, if SMBH accretion is caused by both major and minor mergers Croton (2006)). By additionally taking into account more efficient SMBH growth at higher redshift (Mo et al. (1998)), the $M_{\text{BH}}/M_{\text{spheroid}}$ ratio gets larger at higher redshift ($M_{\text{BH}}/M_{\text{spheroid}} \propto (1+z)^{1.1}$). Both expected evolutions are smaller than model (1).

The redshift evolutions predicted by above theories are summarized in Figure 3. As seen in Figure 3, the difference among models is larger at higher redshift. Therefore, observational investigation of the $M_{\text{BH}}/M_{\text{spheroid}}$ ratio at high redshift is essential to put constraints on the coevolution models and/or the allowable parameter ranges of the key processes.

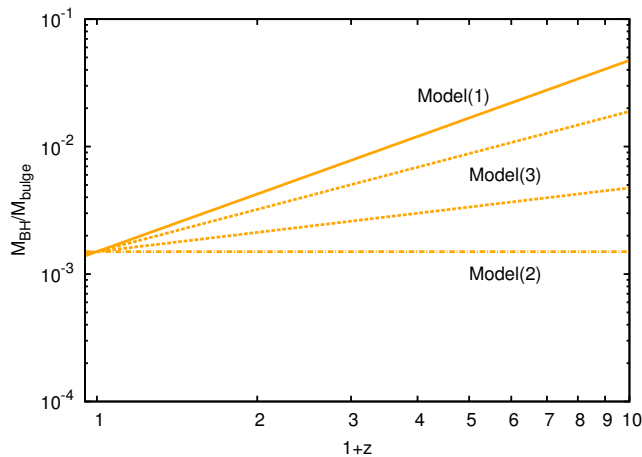


Figure 3 The redshift evolutions of the $M_{\text{BH}}/M_{\text{spheroid}}$ ratio suggested by different theoretical studies (orange lines). The two evolutions in the middle are both corresponding to model (3); upper one is $\propto (1+z)^{1.1}$ and lower one is $\propto (1+z)^{0.5}$.

1.4 Purpose of Our Study

Many previous studies tried to constrain $M_{\text{BH}}/M_{\text{spheroid}}$ ratio at high redshift, however those results contained various uncertainties and bias that make it difficult to discuss redshift evolution of $M_{\text{BH}}/M_{\text{spheroid}}$ ratio (see section 1.5). Therefore, our purpose of this study is to observationally constrain the $M_{\text{BH}}/M_{\text{spheroid}}$ ratio at higher redshift with less uncertainties. We chose a QSO as our target, which is highly luminous object due to gas accretion onto the central SMBH. Since surface brightness of galaxy is getting fainter in proportion to $(1+z)^4$, an observation of QSO host galaxy is very difficult at $z > 4$. Therefore, we observe QSOs at $z \sim 3$ and estimate their M_{BH} and M_{spheroid} with high accuracy. Also, our result may be able to give strong constraints on the theoretical models of $M_{\text{BH}}/M_{\text{spheroid}}$ evolution, because most of previous studies are targeting mainly $z < 2$ (e.g., Jahnke et al. 2009; Merloni et al. 2010), while our sample is $z > 3$, where the difference among the models is getting larger and easier to distinguish.

1.5 Previous Studies

1.5.1 M_{BH} estimate

In the local universe, the M_{BH} is estimated via spatially resolved spectroscopy of normal star-forming galaxies (e.g., Kuo et al. (2011); van den Bosch & de Zeeuw (2010); Genzel et al. (2010); Walsh et al. (2010); Bender et al. (2005); Cappellari et al. (2002); Miyoshi et al.

(1995), see also Kormendy & Ho (2013); Kormendy & Richstone (1995); Genzel et al. (1994) for reviews) by observing Keplerian motion of stars or gas at the center of a galaxy. Figure 4 left is the observational result of stellar kinematics, showing clear rotation motion, and the Figure 4 right shows water maser kinematics, which is consistent with expected Keplerian motion (colored line). Therefore, M_{BH} can be estimated by Kepler's laws. However, it is impossible to apply the same method to distant normal galaxies, due to the lack of spatial resolution.

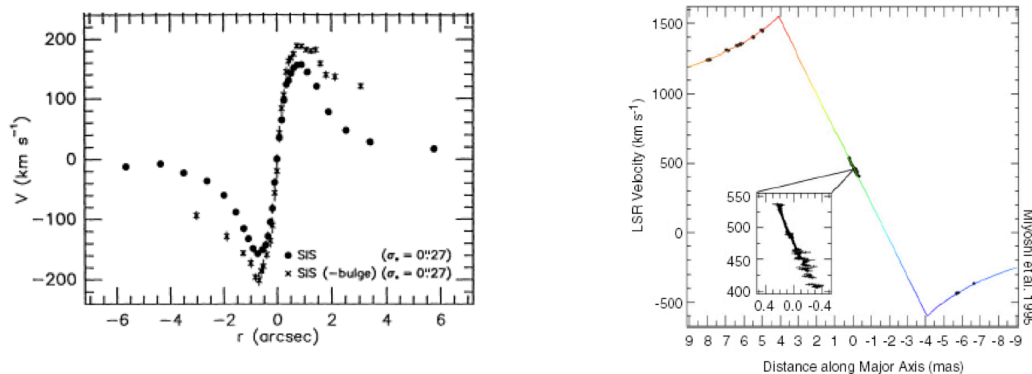


Figure 4 Examples of the observations of stars or gas kinematics. Left : stellar kinematics. Clear rotation motion is observed (Kormendy & Richstone (1995)). Right : Water maser kinematics (Miyoshi et al. (1995)). The colored line corresponds to expected Keplerian motion, which well reproduces the observational data.

To study M_{BH} at high redshift, QSOs (highly luminous AGNs) are useful objects, because various strong emission lines from photo-ionized gas clouds, whose dynamics are dominated by the gravitational potential of the central SMBHs, can be detected and be a good indicator of M_{BH} . For AGNs at the local universe, "reverberation mapping" method is used for M_{BH} estimation (Figure 5).

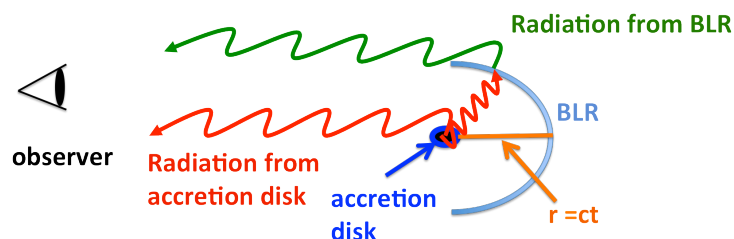


Figure 5 The reverberation mapping method. The distance ($r = t/c$) between accretion disk and broad line region can be estimated from time lag (t) of intensities between continuum and broad emission lines.

UV to optical continuum radiation from accretion disk which is located close to the central SMBH, is known to show time variation. Gas distributed in the BLR is photoionized by the strong UV radiation from accretion disk, and radiates various emission lines. Individual emission lines are thought to distribute in relatively thin spherical shell regions. Therefore, it is expected that intensity of emission lines is also changed in time with time variability of continuum luminosity. Due to the distance (r) between the accretion disk and gas at the BLR, there is a time lag ($t = r/c$, where c is the light speed) between time variation of continuum and emission lines. By measuring the time lag from observation over multiple periods, the distance (r) between accretion disk and the BLR can be estimated (Figure 6). Additionally, we can estimate rotation velocity (v) of gas located in the BLR and dominated by gravity of the central SMBH, from emission line width. Assuming virial theorem, $mv^2/2 = GMm/2r$, $M_{\text{BH}}(\propto rv^2)$ can be derived from observed distance r and rotation velocity v .

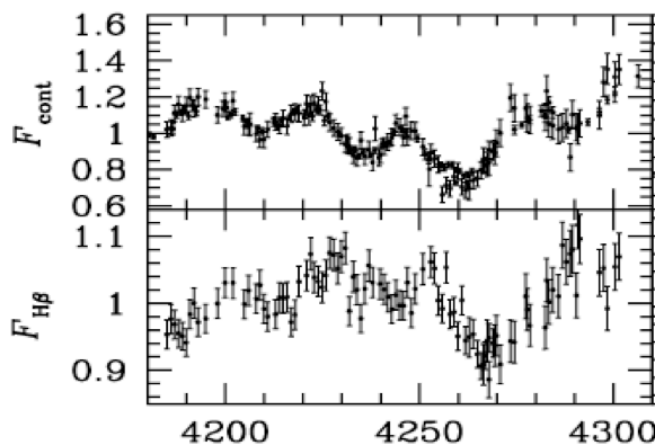


Figure 6 Example of observational results of reverberation mapping method (Denney et al. (2010)). The abscissa is time [Julian days], and the ordinate is flux. Top panel is continuum flux from accretion disk, and bottom panel is $H\beta$ emission line flux radiated from the BLR. Peak position is different between continuum and emission line.

Although this method can derive M_{BH} with high accuracy, it is difficult to be used for a statistical study because it requires many times of observations for each target. Additionally, for high luminosity AGNs at high redshift, the inner diameter of the broad line region becomes larger (see below), and time lag of intensity time variation between continuum and emission line is getting larger due to the effect by cosmological time dilation, requiring decades of time span for monitoring observation. According to the result of reverberation mapping, the relation between the distance from accretion disk to broad line region (r), and optical continuum luminosity of AGN (L_{AGN}) is found (e.g., Denney et al. 2010, Figure 7). Namely, the radius of the broad line region increases with increasing central AGN luminosity in the relation of $r \propto L_{\text{AGN}}^{0.5}$.

This relation is theoretically expected, because the flux of AGN’s ionizing radiation decreases with r^{-2} , and the radius of broad line region is expected to be defined by a fixed ionizing photon flux. Using the relation between r and L_{AGN} , M_{BH} can be estimated from single epoch spectroscopy, based on the combination of emission line widths and nearby AGN continuum luminosity (McLure & Jarvis (2002); Vestergaard (2002); Shemmer et al. (2004); Wu et al. (2004); Vestergaard & Peterson (2006); Netzer et al. (2007); Wang et al. (2009); Trakhtenbrot & Netzer (2012)). This method requires only single spectroscopic observation, and therefore is commonly used for M_{BH} estimate for distant AGNs.

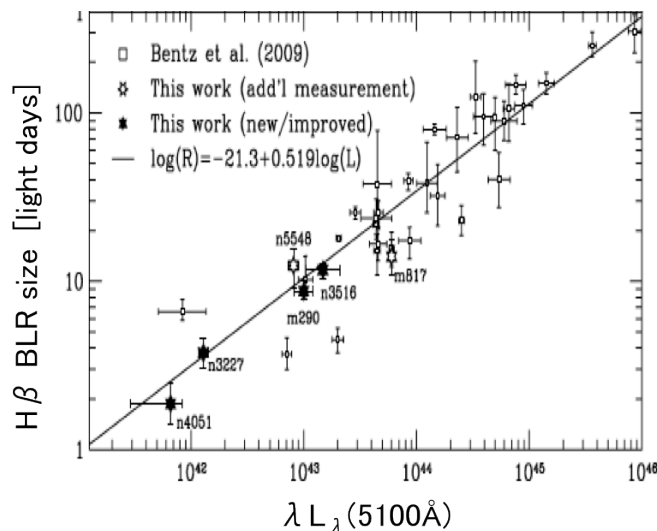


Figure 7 The relation between broad line region size r , and AGN continuum luminosity L_{AGN} , found by reverberation mapping observations for nearby AGNs (Denney et al. (2010)). The abscissa is continuum luminosity at 5100\AA , and the ordinate is broad line region size r derived using $\text{H}\beta$ emission line reverberation mapping. The solid line represents $r \propto L_{\text{AGN}}^{0.5}$ relation.

To estimate M_{BH} of distant QSOs at $z > 2$, the C IV $\lambda 1549$ emission line is commonly used, because it is redshifted into the optical wavelength range, facilitating observation. However, it often shows a large blueshift and an asymmetric profile with respect to low ionization lines (e.g., Gaskell (1982); Tytler & Fan (1992); Richards et al. (2002); Shen et al. (2008), Shen et al. (2011)). Therefore, it is not obvious whether or not the C IV linewidths precisely reflect the gravitational potential well of the SMBH. In fact, M_{BH} estimations based on C IV may have large uncertainty, due to the scatter observed in the C IV-derived SMBH mass distribution, compared to the Mg II $\lambda 2800$ - (more smooth symmetric line profile) and better-calibrated $\text{H}\beta$ $\lambda 4861$ -based SMBH mass estimate (e.g., Baskin & Laor (2005); Netzer et al. (2007); Sulentic et al. (2007); Shen et al. (2008); Marziani & Sulentic (2012)). On the other hand, $\text{H}\beta$ emission

shows a smooth line profile, dominated by the gravitational potential of the SMBH, and is best calibrated to estimate M_{BH} in the local universe, based on the reverberation mapping method (e.g., Peterson & Wandel (1999); Kaspi et al. (2000); Peterson et al. (2004); Bentz et al. (2007), Bentz et al. (2009)). In this study, the $\text{H}\beta$ emission line width and nearby continuum luminosity at 5100 \AA (L_{5100}) were used to estimate M_{BH} of distant QSOs in the most reliable manner. To cover the redshifted $\text{H}\beta$ emission line within the infrared K -band ($2.2 \mu\text{m}$), the longest high-sensitivity atmospheric window for ground-based observations, the redshift range of target QSOs was limited to $z < 3.5$.

1.5.2 M_{spheroid} estimate

To estimate M_{spheroid} of QSO host galaxy, most of previous studies assumed M/L ratio from single band imaging observation, and determined M_{spheroid} by multiplying spheroidal luminosity estimated from imaging data by an assumed M/L ratio (e.g., Decarli et al. 2010). However, since the M/L ratio is largely different depending on galaxy properties, the assumption of a fixed M/L ratio causes large uncertainty on M_{spheroid} estimation. That confuses interpretations of observational result, and prevents to obtain observational understanding about $M_{\text{BH}}/M_{\text{spheroid}}$ ratio evolution. To reduce uncertainty of M_{spheroid} attributed by the assumption of a fixed M/L ratio, we employ the correlation between galaxy color and the M/L ratio. In Figure 8, we show the correlation from Bell & De Jong (2001) for example. By obtaining galaxy color from multi-band observations, we can determine M/L ratio accurately, that enables us to derive M_{spheroid} with less uncertainty. We carried out imaging observations for $z \sim 3$ QSOs in J - ($1.25\mu\text{m}$) and K' -band ($2.2\mu\text{m}$) to estimate galaxy color, which correspond to U - ($0.36\mu\text{m}$) and V -band ($0.55\mu\text{m}$) in the rest frame, respectively (around 4000\AA break).

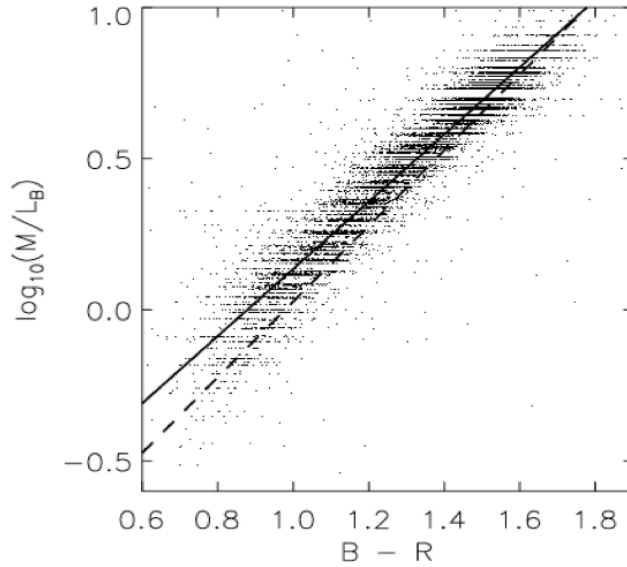


Figure 8 The relation between galaxy color and M/L ratio (Bell & De Jong (2001)). The abscissa is B-R color in the rest frame, and the ordinate is M/L ratio.

For M_{spheroid} estimation of QSO host galaxy, it is required to subtract AGN bright glare with high accuracy, and extract faint, spatially-extended host galaxy stellar light. To obtain imaging data with the highest spatial resolution that can be achieved, we employ Subaru telescope and Adaptive Optics (AO) system. AO system corrects for the influence of fluctuation of Earth atmosphere to be able to obtain high spatial resolution image (Figure 9). Typical galaxy size is several kpc, and at least < 2 kpc of resolution is required to study host galaxy. At $z \sim 3$, $1''.0$ corresponds to 8 kpc, and $2 \text{ kpc} \sim 0''.25$ of resolution is required. However, natural seeing size (without AO system) is typically $> 0''.4 - 0''.5$ at K -band, meaning that it is impossible to achieve required seeing size by normal non-AO observation using ground-based telescopes. Only by using AO system, we can achieve required seeing size of $0''.1 - 0''.2$ at K -band.

Moreover, for highly accurate M/L and thereby M_{spheroid} estimate, observing a longer wavelength range than 4000\AA in the rest frame is crucial. As the instruments on the Hubble Space Telescope is not chilled, K -band sensitivity is poor. Observation with 8–10 m ground-based telescope with AO system is advantageous in terms of K -band sensitivity and seeing size that can be achieved. Additionally, laser guide AO system on Subaru telescope provides the most stable laser stellar image, comparing to other rival telescopes. We chose QSOs having at least one PSF reference star in the same FOV. Although AO correction performance varies depending on distance from AO guide star, we can correct time variable PSF shape by launching laser guide star at the half way between target QSO and PSF reference star. With this method, we can accurately subtract AGN radiation contamination and correctly estimate underlying faint spheroidal host galaxy radiation, that enables us to derive spheroidal stellar luminosity L_{spheroid}

with high accuracy.

We note that, even with AO, there remains light that AO cannot correct (Figure 10). We call it seeing halo. This component is spatially extended and we could misestimate spheroidal stellar luminosity because of this, therefore this component should be considered carefully in our fitting procedure (see Section 8).

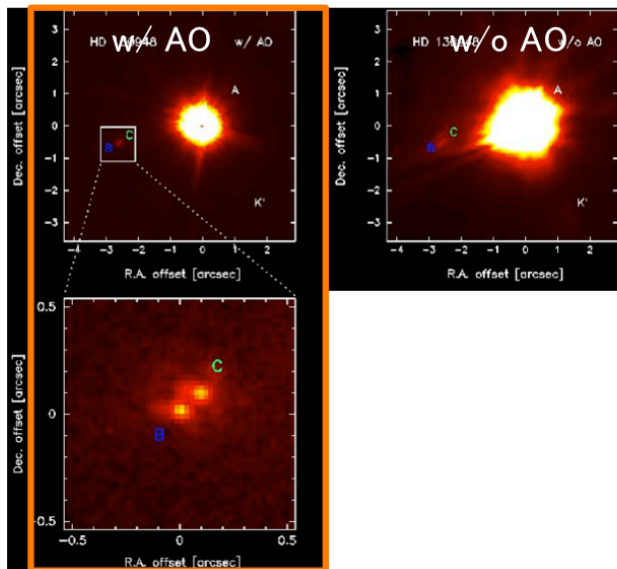


Figure 9 Example images with and without AO (credit : Subaru Telescope). Left : with AO system. Right : without AO system. Star B and C are clearly resolved in the left figures thanks to AO correction.

Previous studies of the $M_{\text{BH}}/M_{\text{spheroidal}}$ ratio at high redshift using QSOs were performed mainly at $z < 2$ (e.g., Häring & Rix (2004); Jahnke et al. (2004b); Schramm et al. (2008); Jahnke et al. (2009); Decarli et al. (2010); Merloni et al. (2010); Bennert et al. (2011); Cisternas et al. (2011); Schramm & Silverman (2013); Matsuoka et al. (2014)). The results from previous studies are summarized in Figure 11. In order to better distinguish among various coevolution scenarios, data at higher redshift are preferable.

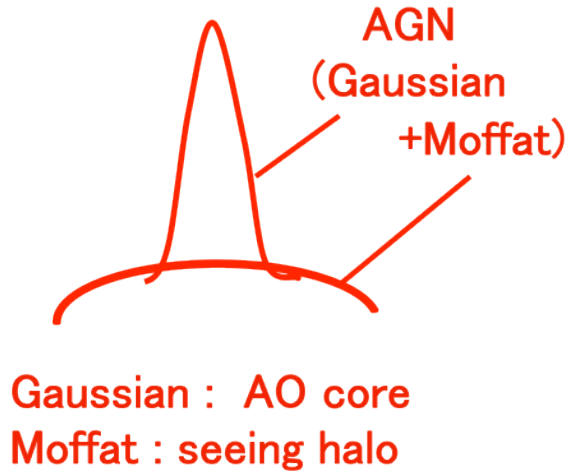


Figure 10 Radiation profile image of PSF (corresponds to AGN radiation profile). Even with AO system, there remains the light AO cannot correct (seeing halo), which is spatially extended. This component should be considered carefully in our fitting procedure for L_{spheroid} estimate.

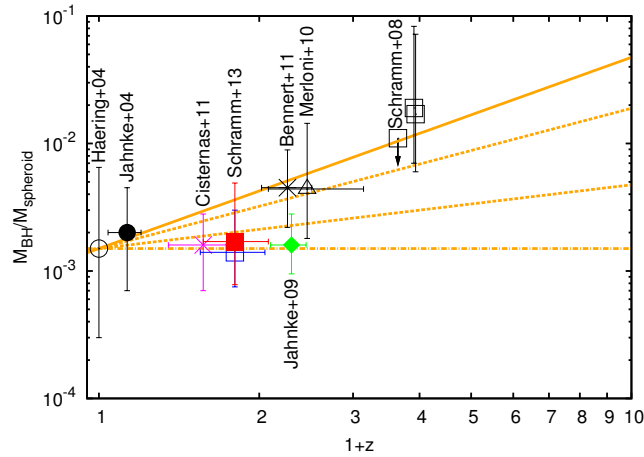


Figure 11 Results of $M_{\text{BH}}/M_{\text{spheroid}}$ estimates by previous studies.

However, detection of the QSO host galaxy to measure the M_{spheroid} becomes more difficult at higher redshift, because the surface brightness of the host galaxy stellar emission becomes faint in proportion to $(1+z)^4$. Thus, the optimal redshift range must be determined by taking into account the practical observational limitations. Detection of the QSOs' host galaxy stellar emission at $z \sim 3.5$ was technically feasible using the latest powerful 8–10 m ground-based observation facilities (e.g., Falomo et al. (2005); Peng et al. (2006); Schramm et al. (2008); McLeod & Bechtold (2009); Targett et al. (2011)). For these reasons, QSOs at $z < 3.5$ were

targeted to constrain their SMBH and galaxy stellar mass ratio, and to observationally better constrain the coevolution of SMBHs and galaxies in the early universe.

Although Schramm & Silverman (2013) estimated M_{spheroid} using M/L ratio derived from multi-band images taken by HST, redshift range of their target is $0.5 < z < 1.2$. Among earlier studies estimating M_{spheroid} at $z \sim 3$, only Schramm et al. (2008) measured colors for accurate M/L ratio, and derived M_{spheroid} using VLT. However, the observation was carried out without AO. Moreover, their targets were extremely luminous AGNs ($M_B < -28$) with high M_{BH} , which possibly cause a bias toward larger $M_{\text{BH}}/M_{\text{spheroid}}$ ratios (Lauer et al. (2007), see also section 5.2, and 9.2).

In this paper, we report the results of our near-infrared spectroscopic and imaging observations of $z < 3.5$ QSOs for their $M_{\text{BH}}/M_{\text{spheroid}}$ ratio estimate. This paper consists of mainly two parts; spectroscopic observation for M_{BH} estimate, and imaging observation for M_{spheroid} estimate. We describe the sample selection in Section 2 and the spectroscopic observations and data reduction in Section 3. The spectral analysis and the method used for the M_{BH} estimate are described in detail in Section 4 and 5, along with the main results. Section 6 provides a discussion of our main findings from spectroscopic observations. We describe the imaging observation in Section 7. In section 8, the detail of our original imaging data analysis method is explained, and its result is provided. Finally, we report our result of $M_{\text{BH}}/M_{\text{spheroid}}$ ratio estimate for $z \sim 3$ QSOs and discuss in Section 9. Throughout this paper, we adopt the Vega magnitude system for all infrared data and the standard Λ CDM cosmology, with $H_0 = 70 \text{ km s}^{-1} \text{ Mpc}^{-1}$, $\Omega_M = 0.3$, and $\Omega_\Lambda = 0.7$.

2 Sample Selection

All of our samples are drawn from the QSOs catalogue in the seventh data release of the Sloan Digital Sky Survey (SDSS DR7; Abazajian et al. (2009)). We first selected QSOs with redshift=3.11–3.50 in SDSS DR7, so that the H β emission line and 5100 Å continuum could be observed within the infrared *K*-band. Next, we set limitations on the optical *r'*-band (0.62 μ m) magnitude, $18.5 < r'(SDSS) < 19$. The faint limit was set to obtain sufficient quality spectra for our discussion within a reasonable amount of exposure time. Assuming that observed luminosity cannot exceed the Eddington luminosity limit of $L_{\text{Edd}} = 3.2 \times 10^4 (M/M_{\odot}) L_{\odot}$, the minimum required M_{BH} is higher for brighter QSOs. The bright limit was set, because observing only the brightest end of the QSOs could strongly bias the data to intrinsically large M_{BH} systems, resulting in a biased view of the $M_{\text{BH}}/M_{\text{spheroid}}$ ratio at high redshift (Lauer et al. (2007)). Radio-loud QSOs were almost excluded because they often show jet-induced extended narrow emission line regions. Since H β line consists of broad and narrow components, and H β narrow line component is derived from the narrow [OIII] emission line, the existence of extended narrow line region could induce considerable uncertainty on accurate H β broad line width measurement particularly if the narrow emission line component is different in shape between H β and [OIII]. We roughly estimate radio-loudness of our targets from the ratio of their rest-frame luminosities at 5 GHz to those at 2500 Å ($L(5 \text{ GHz})/L(2500 \text{ Å})$; Stocke et al. (1992)). The $L(2500 \text{ Å})$ and $L(5 \text{ GHz})$ are derived from the *z'*-band(0.91 μ m) magnitude from the SDSS and the 20 cm flux from Faint Images of the Radio Sky at Twenty-Centimeters (FIRST) survey (Becker et al. (1994)), respectively. Since the wavelength of *z'*-band and 20 cm correspond to 2500 Å and 5 GHz, respectively, in the rest frame of $z \sim 3$ QSOs, we do not take into account the K correction.

Additionally, to study the coevolution of SMBH and galaxies at high redshift, adaptive optics (AO) imaging data are used to derive the host galaxy's spheroidal stellar mass, using the Subaru 8.2 m telescope atop Mauna Kea, Hawaii (latitude $\sim +20^\circ$). For AO observation, an AO guide star with $R(0.64 \mu\text{m}) < 18$ mag within 60" from the target is required. In addition, to observe each object for longer than 4 hours at a higher elevation than 50° from Mauna Kea, with good AO performance and high spatial resolution, we selected QSOs with declination $-5^\circ < \text{Dec} < +45^\circ$. Finally, to subtract the central bright AGN glare with high accuracy, we chose targets that had at least one nearby PSF reference star with a magnitude similar to that of the target QSOs.

Here we summarize the selection criteria explained above.

- $3.11 < z < 3.50$
- QSO magnitude $18.5 < r' < 19$ mag
- $-5^\circ < \text{Dec} < +45^\circ$
- QSOs having AO guide star with magnitude of $R < 18$ within $60''$
- The distance between PSF reference star and target QSO $< 52''$
- The magnitude difference between PSF reference star and target QSO < 1 mag
- Radio-quiet QSOs

Approximately 120 $z \sim 3.5$ QSOs met all of the requirements. Figures 12 and 13 show the distributions of redshift, luminosity, M_{BH} estimated from C IV, and Eddington ratio for our sample. Our sample is a little biased to luminous sample due to our limitation on magnitude. We will discuss the effect of this luminosity bias on our result later (see Section 5.2, and 9.2).

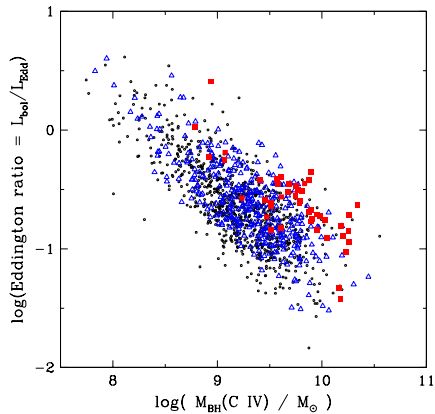


Figure 12 The distribution of our sample and whole SDSS QSOs. The abscissa is M_{BH} estimated by C IV emission line, and the ordinate is Eddington ratio. Black dots are SDSS DR7 QSOs, blue triangles are QSOs with $3.11 < z < 3.50$, and red squares are our sample.

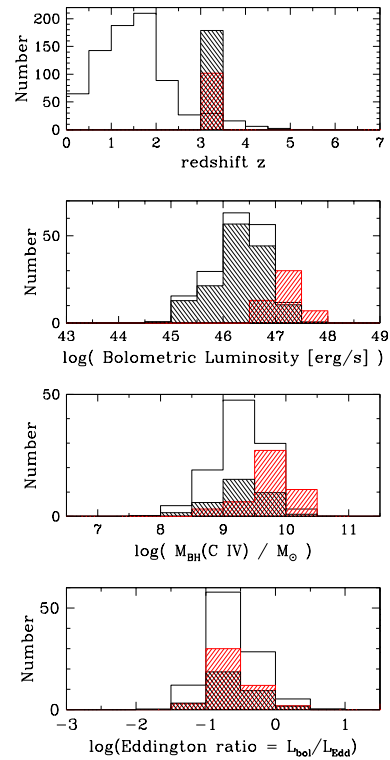


Figure 13 The distributions of redshift, luminosity, M_{BH} estimated by C IV emission line, and Eddington ratio from top to bottom. Open histogram is whole SDSS DR7 QSOs, black shaded histogram is QSOs with $3.11 < z < 3.50$, and red shaded histogram is our sample. Open and black shaded histograms are scaled. Due to our limitation on target magnitude, our sample is little bit brighter.

We randomly chose 37 out of 120 QSOs and observed. Most of our target QSOs (35 out of 37) used in this paper have $L(5 \text{ GHz})/L(2500 \text{ \AA}) < 10$, except for 2 QSOs (J0847+3831 and J1337+3152) which are classified as radio loud QSOs.

3 Spectroscopic Observations and Data Reduction

3.1 Near-infrared observation and noise sources

Unlike the optical which can be observed in all wavelength range from the ground, there are some infrared wavelength ranges whose radiation cannot reach to the ground due to Earth's atmospheric absorption. Therefore, filters for near-infrared observations are made to coincide with the Earth atmospheric windows (Figure 14).

In the near-infrared observation, background radiation from such as the Earth atmosphere, and telescope is large compared to the optical. Therefore, near-infrared observation is more difficult, and also sensitivity is worse due to Poisson noise of background radiation, than optical observation. Figure 15 shows background emission spectrum in the optical to near-infrared. As seen in Figure 15, OH "airglow" dominates the background at the $\lambda < 2.3\mu m$, while at $\lambda > 2.3\mu m$, thermal emission from the Earth's atmosphere and telescope are responsible for the background. Note that the background at $\lambda > 2.3\mu m$ increases precipitously.

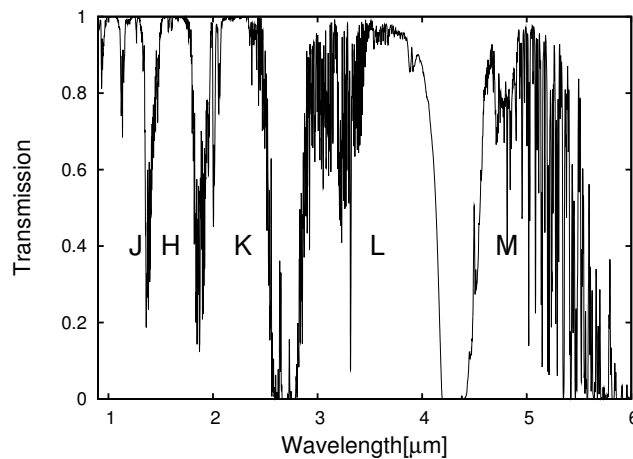


Figure 14 Atmospheric transmission at 0.9–6 μm . The abscissa is wavelength, and the ordinate is transmission.

One of the characteristics of near-infrared detector is non-destructive readout ; NDR, which can read-out multiple times without destructing signal information, during exposure. NDR can reduce read-out noise (noise of n times NDR is $1/\sqrt{n}$). However, the effect of reducing read-out noise by NDR is limited where background noise is dominant, while overhead increases

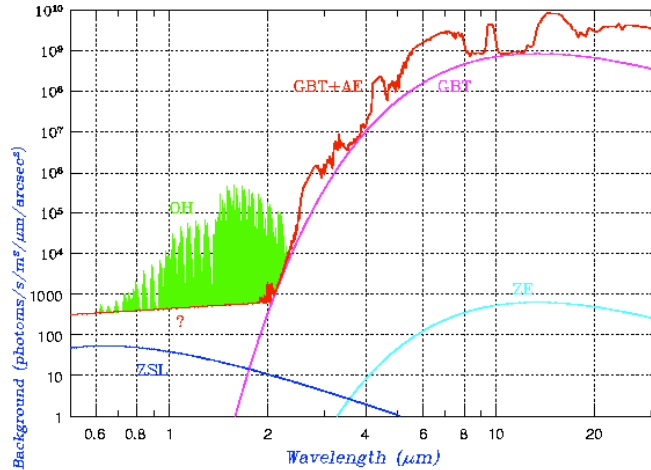


Figure 15 Spectrum of background emission from optical through near-infrared wavelengths. The abscissa is wavelength, and the ordinate is intensity of background emission. OH : OH-airglow, AE : thermal radiation from the atmosphere, GBT : thermal noise from telescope, ZSL : scattered light from the Sun due to dust in zodiacal plane, and ZE : thermal emission from such dust. The plot is from the "Astronomy Lecture Notebook" by Prof. Iwamuro at Kyoto University (<http://www.kusastro.kyoto-u.ac.jp/~iwamuro/LECTURE/OBS/>).

with increasing NDR number. Therefore we set moderate number of NDR for our near-infrared observations. Moreover, due to strong background emission in near-infrared, exposure time for each read-out has to be short to avoid saturation. In order to allow long-integration, we employ COADD method. COADD takes many images with short integration times without moving the telescope, and adds them on the memory to create a long-integration frame without saturation. The number of COADD was set so that Earth's atmospheric conditions do not differ significantly between that telescope position and another telescope nod position.

For our sample, the near-infrared K -band ($2.2 \mu\text{m}$) spectra were obtained using the NASA Infrared Telescope Facility (IRTF 3 m), the United Kingdom Infrared Telescope (UKIRT 3.6 m), the William Herschel Telescope (WHT 4.2 m), and the Subaru Telescope (8.2 m, Iye et al. (2004)). Among the 120 QSOs that met all our selection criteria, 37 QSOs were observed (Table 1). Bright targets were observed primarily with the SpeX instrument (Rayner et al. (2003)) on the IRTF, the UIST (Ramsay et al. (2004)) on the UKIRT, and the LIRIS (Manchado et al. (1998)) on the WHT. Fainter QSOs were observed with the IRCS instrument (Kobayashi et al. (2000)) assisted with the Adaptive Optics system AO188 (Hayano et al. (2010)) on the Subaru. With the exception of the Subaru IRCS, these instruments enabled us to obtain H - ($1.6 \mu\text{m}$) and K -band ($2.2 \mu\text{m}$) spectra simultaneously. For all targets, $H\beta$ $\lambda 4861$ and $[\text{O III}] \lambda\lambda 4959$, 5007 emission lines were observed within the K -band. H -band spectra were used when available to better determine the continuum flux level at the shorter part of these emission lines. We also obtained spectroscopic data of standard star (spectral type is A, G, or

F) for each target (Table 1) for telluric correction and flux calibration. To estimate the telluric correction, we divided the quasar spectra with standard star spectra, and then multiplied simple blackbody spectra with the temperature corresponding to the spectral type of the standard star derived from Allen’s astrophysical quantities (Tokunaga (2000)).

Raw data includes noise sources that should be corrected, such as radiation from Earth’s atmosphere, non-uniformity of optics throughput at different position and array sensitivities, and dark current. To extract these noise sources from raw data to obtain scientific data, we followed steps below.

- Background subtraction
- Flat fielding
- Correction of cosmic ray, and bad pixels
- Extraction of target signals
- Wavelength calibration
- Transmission calibration
- Flux calibration
- Error estimate

The details of each step is explained with example images below. Although data reduction procedure is almost the same regardless of instruments, we describe the detail of data reduction with respect to each instrument, because employed analysis software and parameters are different.

3.2 UKIRT/UIST

UKIRT/UIST spectra of five targets (Table 1) were obtained through the $0''.6 \times 120''.0$ slit with an $H + K$ grism. The achieved spectral resolution is $R \sim 1000$. The spectra were taken at A and B positions along the slit. Each exposure time was 240 s, and 1 coadd was adopted at each position for all targets.

Data were reduced using standard IRAF tasks, which is written by NOAO (National Optical Astronomy Observatories).

3.2.1 Background subtraction

Figure 16 is the raw spectroscopic image of HD63160 (standard star for SDSS J0749+4332) obtained by UKIRT/UIST. Wavelength is getting longer from left to right in the image. Where the signal is fainter (slightly right side from the middle) is corresponding to the wavelength range whose radiation is absorbed by Earth atmosphere. Thus, the left side of where signal is faint, corresponds to H -band, and the other side corresponds to K -band, respectively.

To subtract background signals other than target object such as infrared radiation from Earth atmosphere, telescope, and observational instruments, frames taken with an A (or B) beam were subtracted from frames subsequently taken with a B (or A) beam (Figure 16). By this subtraction, radiation from Earth atmosphere (Sky emission), dark current, and background radiations from telescope and observational instrument can be removed, and the target signal can be clearly seen (Figure 17). The resulting subtracted frames were split into two data set for spectral error estimate later, and added. We carried out the same procedure for the target raw data, and finally obtained 4 images (2 for standard star, and other 2 for target data) in total.

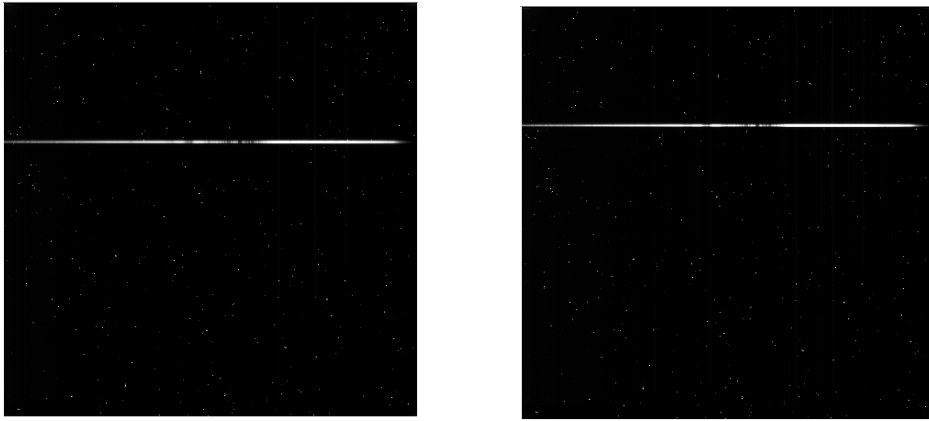


Figure 16 The raw data of HD63160 obtained by UKIRT/UIST. Left : the data taken at A position. Right : the data taken at B position. Signal position is shifted vertically.

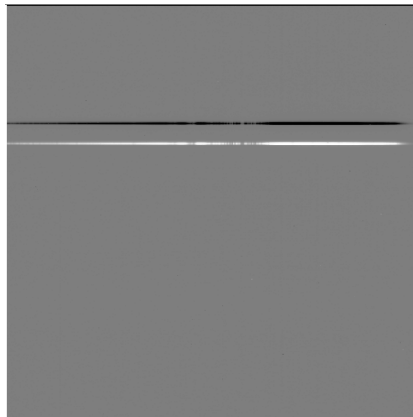


Figure 17 The result of A-B subtraction for HD63160. Target signal is clearly seen by background radiation subtraction.

3.2.2 Flat fielding

Standard stars and targets are observed at the almost same slit position (A, B) in each frame, however, it is possible to slightly shift due to telescope pointing and tracking error. Consequently, signal can be affected by the non-uniformity of slit width throughput of the instrument optics, and array sensitivity. To obtain information about the non-uniformity, we observe uniform light source, so-called "flat frame". Usually, several flat frames are obtained, and make median-combined flat frame.

By dividing the image obtained in Section 3.2.1 by the flat frame, effect of the non-uniformity can be corrected (Figure 18).

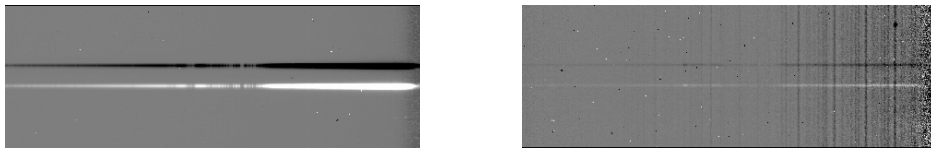


Figure 18 Images after flat fielding. Left : standard star HD63160. Right : target J0749.

3.2.3 Correction of cosmic ray and bad pixels

Sometime pixels do not reflect correct signal value when impacted by cosmic rays, or the pixel itself is dead or something wrong. Those pixels can be corrected by using the IRAF task *cosmicrays*. If there still remain un-corrected pixels, then we use the IRAF task *fixpix* for their correction (Figure 19).

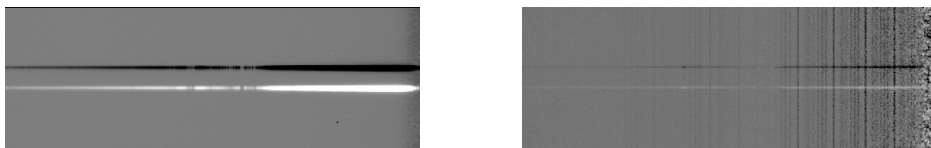


Figure 19 The images after cosmic rays and bad pixel correction. Left : standard star HD63160. Right : target J0749. Bad pixels seen in the Figure 18 are eliminated.

3.2.4 Extraction of target signals

Finally, we extract target signals by using the IRAF task *apall*, to obtain an 1D spectrum. We here explain the flow of signal extraction with HD63160 data. Figure 20 is the 2D spectrum obtained in section 3.2.3. We first slice the 2D spectrum at the position indicated as red box in the image to determine signal profile at the position (Figure 21).

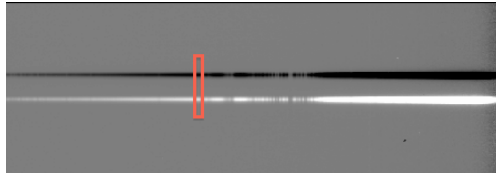


Figure 20 2D spectrum of HD63160 obtained in Section 3.2.3. The spectrum is cut at the position of red box in the image to determine signal profile.

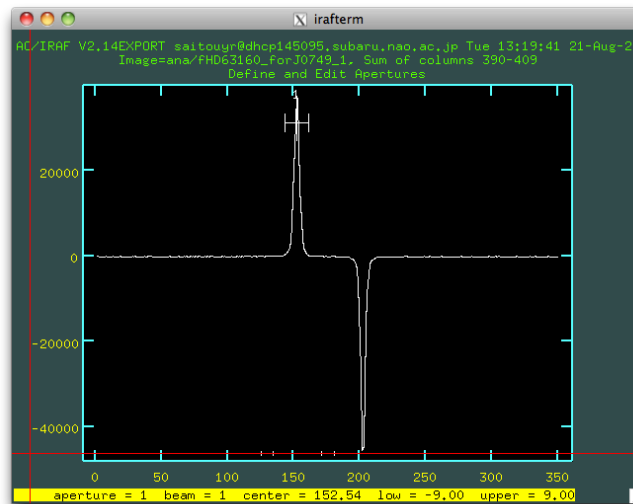


Figure 21 Signal profile at the position of red box in Figure 20. The abscissa is pixel number (spatial direction), and the ordinate is signal intensity.

Next, we fine-tune peak position of the signal, width, and sky level, and then trace target signal in wavelength direction with the assumption that signal profile is not changed. Since the *apall* task can trace only positive signals, we first trace signals at A position, multiply the image by -1, and then trace signals at B position. Both traced signals are summed, and finally 1D spectrum can be obtained (Figure 22).

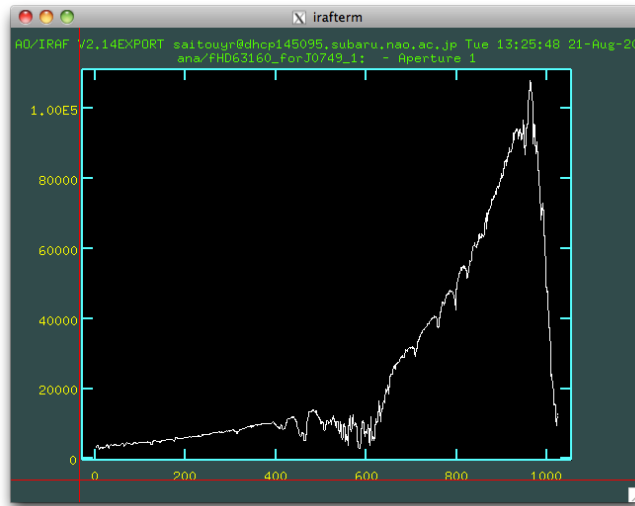


Figure 22 1D spectrum of HD63160. The abscissa is pixel number (wavelength direction), and the ordinate is signal intensity.

We carried out the same procedure for the rest of data to obtain each 1D spectrum.

3.2.5 Wavelength calibration

Here, we convert pixel number in the abscissa of obtained 1D spectra, to wavelength. There are two methods for wavelength calibration; (1) use of rare-gas emission line spectrum such as Argon or Xenon, or (2) calibration by Earth's atmospheric absorption. We adopt method (1), with Argon emission line spectrum. Figure 23 is 2D spectrum obtained by observing Argon lamp. With the same procedure, we extract signals using the *apall* task by tracing the same position as standard star signals (Figure 24).

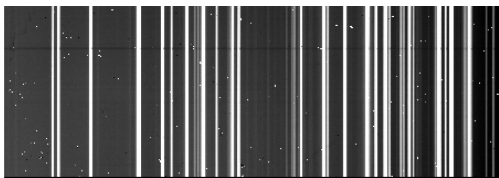


Figure 23 The raw data of Argon lamp observation. The horizontal direction is wavelength direction.

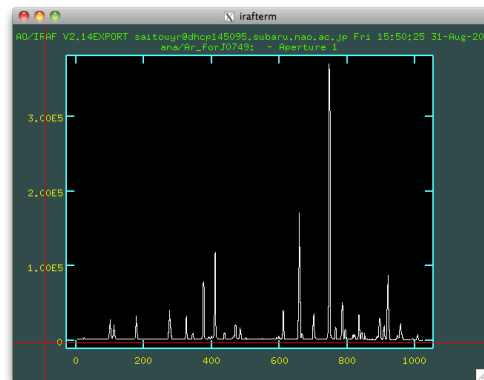


Figure 24 1D spectrum of Argon data. The abscissa is pixel number (wavelength direction), and the ordinate is signal intensity.

Since the wavelength of rare-gas emission line is well known, pixel number and corresponding wavelength of each emission line is identified by using the IRAF task *identify*, which enables us to obtain conversion equation from pixel to wavelength. Using the conversion equation, wavelength calibration is carried out with the IRAF task *disocor*. We observed standard star and target at the almost same slit position. Since target signals are not bright enough to trace the profile with sufficient accuracy, we employed the standard star signal positions to trace Argon lamp signal, and applied the same conversion equation between slit position and wavelength to the target.

3.2.6 Transmission calibration

The obtained target signal so far is the product of actual target signal and transmission determined from the Earth atmosphere, telescope, instrument optics, and detector. The transmission has wavelength dependence and it is the same between target and standard star. Spectrum of standard star can be considered as blackbody spectrum at the temperature corresponding to the spectral type, multiplied by transmission. Thus, we can obtain target spectrum without effect of transmission, by data processing of (target spectrum/standard star spectrum) \times (blackbody spectrum corresponding to the spectral type of standard star). Standard stars we observed are all main-sequence stars, whose spectral types are already known, and the temperatures are provided in Allen's Astrophysical Quantities.

3.2.7 Flux calibration

The last step of data analysis is flux calibration, determining target magnitude by comparing standard star whose magnitude is known. For example, the magnitude of standard star HD63160 is 9.09 mag at *H*-band (1.509-1.799 μm), and by comparing total signal values between standard star and target in *H*-band, target magnitude can be determined. Note that the difference of exposure time should be taken into account. According to Allen's Astrophysical Quantities, flux at *H* = 0 mag is $F_\lambda = 1.15 \times 10^{-9} [\text{Wm}^{-2}\mu\text{m}^{-1}]$, *K* = 0 mag is $F_\lambda = 4.14 \times 10^{-10} [\text{Wm}^{-2}\mu\text{m}^{-1}]$ and by combining estimated target magnitude, target flux can be obtained.

3.2.8 Error estimate

Spectral error can be estimated from dispersion of multiple data which are observed with the same parameter for the same target. Therefore, we split data observed with the same parameter for the same target, into several data set, and estimate dispersion among those data set. The scatter of larger number of data set better reflects the actual spectral error, however, S/N of each data set is getting worse with shortening exposure time. Hence, we split target data into two data set, and carried out data reduction following the steps explained above, and

obtained two spectra for each target. Then we calculated the average and the standard deviation (corresponding to spectral error) at each wavelength.

The data points of a spectrum are corresponding to actual pixel number of the detector. While, the spectral resolution of this observation is $R \sim 1000$, corresponding to four pixels. Therefore, four pixel binning is carried out. Error was re-calculated from square root of (the sum of squares of error at each pixel)/4(binned pixel number), since error is independent among each pixel.

3.3 WHT/LIRIS

WHT/LIRIS spectra of five targets (Table 1) were taken with the $0''.75 \times 252''.0$ slit and the $H + K$ grism. The spectral resolution was $R \sim 945$. The exposure time and coadd at each slit position (A or B) were 300 s and 1 coadd, respectively. Data reduction was carried out in the same manner as for UKIRT/UIST. Figure 25 is an example image of raw data of standard star (HD15004) obtained by WHT/LIRIS.

After executing *cosmicrays* task for bad pixel correction, *qzap* (developed by Dickinson, <http://titan.physx.u-szeged.hu/opt/iraf/extern/stsdas/pkg/analysis/dither/qzap.cl>) software that works on the IRAF was used to correct remained bad pixels. Since the spectral resolution of $R \sim 945$ corresponds to four pixels, four pixel binning was carried out.

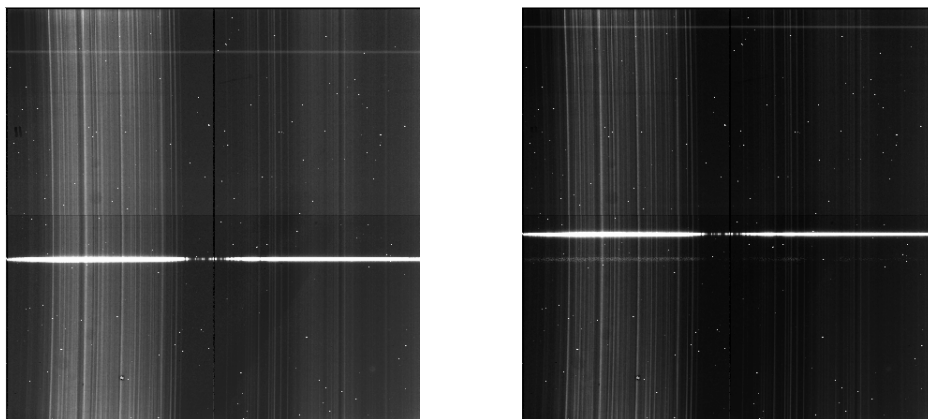


Figure 25 Example images of raw data of standard star (HD15004) obtained by WHT/LIRIS. Left : the data taken at A position. Right : the data taken at B position. Signal position is shifted vertically.

3.4 Subaru/IRCS

Subaru/IRCS spectra of seven targets (Table 1) were obtained using the $0''.45 \times 18''.0$ slit in the 52-mas mode. We used the K -grism that covers the $1.93\text{--}2.48 \mu\text{m}$ range. The spectral resolution was $R \sim 400$. The exposure time and coadd at each slit position (A and B) were 600 s and 1, respectively. We used IRAF for data reduction similar to that used for UKIRT/UIST and WHT/LIRIS data. Example raw data of standard star (HR8041) taken by Subaru/IRCS are shown in Figure 26. Spatial direction is different from other instruments. Since target signal was clearly seen in one data set (A–B data), we split data into three data set for error estimation. The spectral resolution for this data is $R \sim 400$, corresponding to eight pixels. According to Nyquist-Shannon sampling theorem, twice the resolution has meaningful information, therefore four pixel binning was carried out to make spectral resolution similar to other instruments.

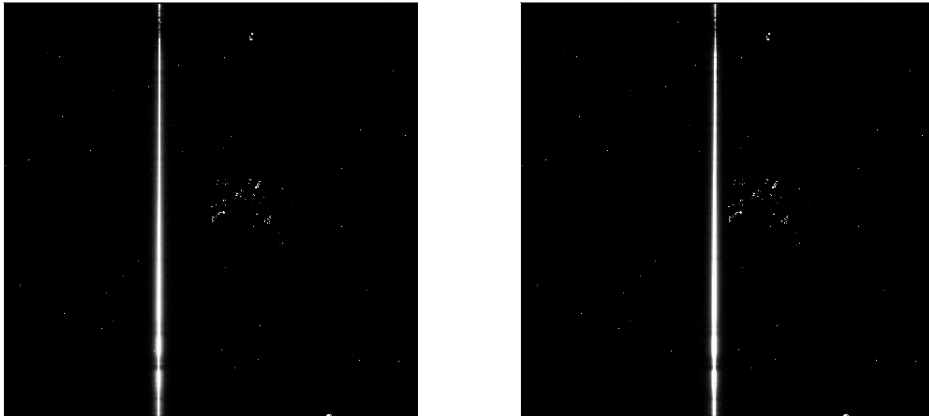


Figure 26 Example raw data of HR8041 obtained by Subaru/IRCS. Left : the data taken at A position. Right : the data taken at B position. Signal position is shifted in the horizontal direction.

3.5 IRTF/SpeX

IRTF/SpeX spectra of 20 targets (Table 1) were obtained in the $0.8\text{--}2.5 \mu\text{m}$ cross-dispersed mode with a $1''.6 \times 15''.0$ slit. This mode provided spectral resolution with $R \sim 375$. Although the R was relatively low compared to other observations, we choose this mode to minimize slit loss by tracking/guiding error and for obtaining better S/N ratios. Spectra were taken at two different positions (A and B) along the slit. Each exposure time ranged from 60–300 s, depending on the magnitude of the targets and the weather conditions. Also, one to two coadds were used at each slit position.

The reduction was carried out using the Spectral Extraction Package for SpeX (Spextool; Cushing et al. (2004)) that works on IDL. The Spextool goes through almost all data reduction processes, including spectral flat fielding, sky emission subtraction, bad pixel correction, extraction of one-dimensional (1D) spectra, and wavelength calibration (using Argon lines). We first created A–B data and then median-combined multiple A–B data sets to increase the S/N ratios. After extraction of a 1D spectrum, the data at the A and B slit positions were summed using the IDL task *xcombspec*. Then the *xtellcor-basic* task in IDL was used for telluric correction and flux calibration. Finally, different order spectra were merged into a single spectrum corresponding to the *H*- and *K*-bands (1.41–2.42 μm). We did not use other wavelength range (0.9–1.41 μm , 2.42–2.5 μm) for this study.

3.5.1 Making calibration frames

Calibration frames for flat fielding and wavelength calibration were created first. Calibration frames were taken by macro for Spex, and flat data and Argon lamp data were sequentially-numbered. By specifying file number and executing, flat frame and conversion equation for wavelength calibration were automatically created. Both flat data and Argon lamp data were median-combined from multiple data.

3.5.2 From background subtraction to wavelength calibration

Figure 27 is an example image of raw data of standard star (HD140775) obtained by IRTF/SpeX. In cross-dispersed mode observation, target signal is dispersed by grating, and additionally prism disperses orders (cross-disperser). Therefore, spectrum is expanded in 2D. The order is 3 to 8 from top to bottom in the Figure 27, order 3 and order 4 are corresponding to *K*-band (1.88–2.42 μm), and *H*-band (1.41–1.81 μm) respectively.

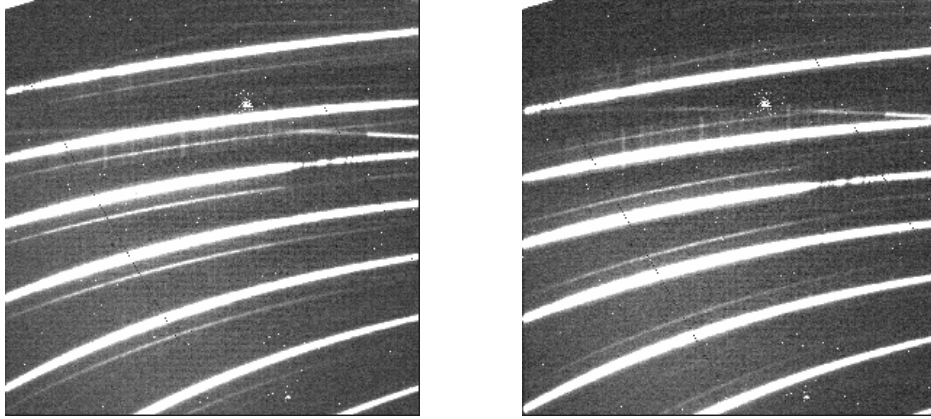


Figure 27 Example images of raw data of standard star (HD140775) obtained by IRTF/SpeX. Left : data taken at A position. Right : data taken at B position. The spectrum is expanded in 2D by the use of cross-dispersed mode.

Here we show background subtraction to wavelength calibration steps with example images of standard star, HD140775. Figure 28 is the actual operation panel of spextool. By specifying the data number of HD140775 observed at position A and B, and the file name of calibration frame, A-B subtraction to flat fielding steps are automatically carried out (Figure 29).

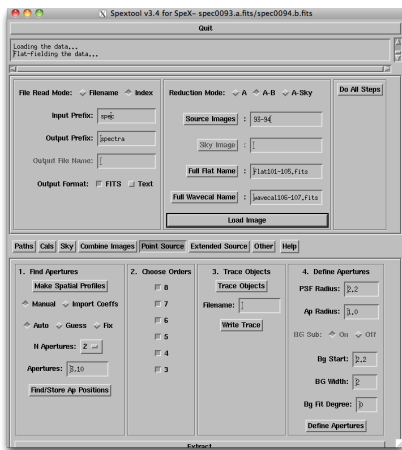


Figure 28 Operation panel of spextool.

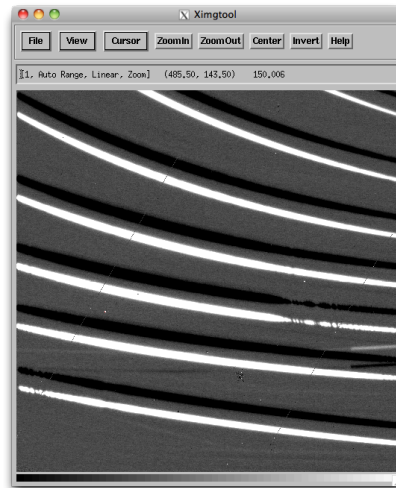


Figure 29 Image of HD140775 after background subtraction and flat fielding. The image is flipped from Figure 27 (upside down).

Next, target signal is extracted. Figure 30 shows average signal profile at each order, which is median signal profile at each position along the wavelength direction. The data at low signal pixel is not included. The blue line represents the peak position of signal profile.

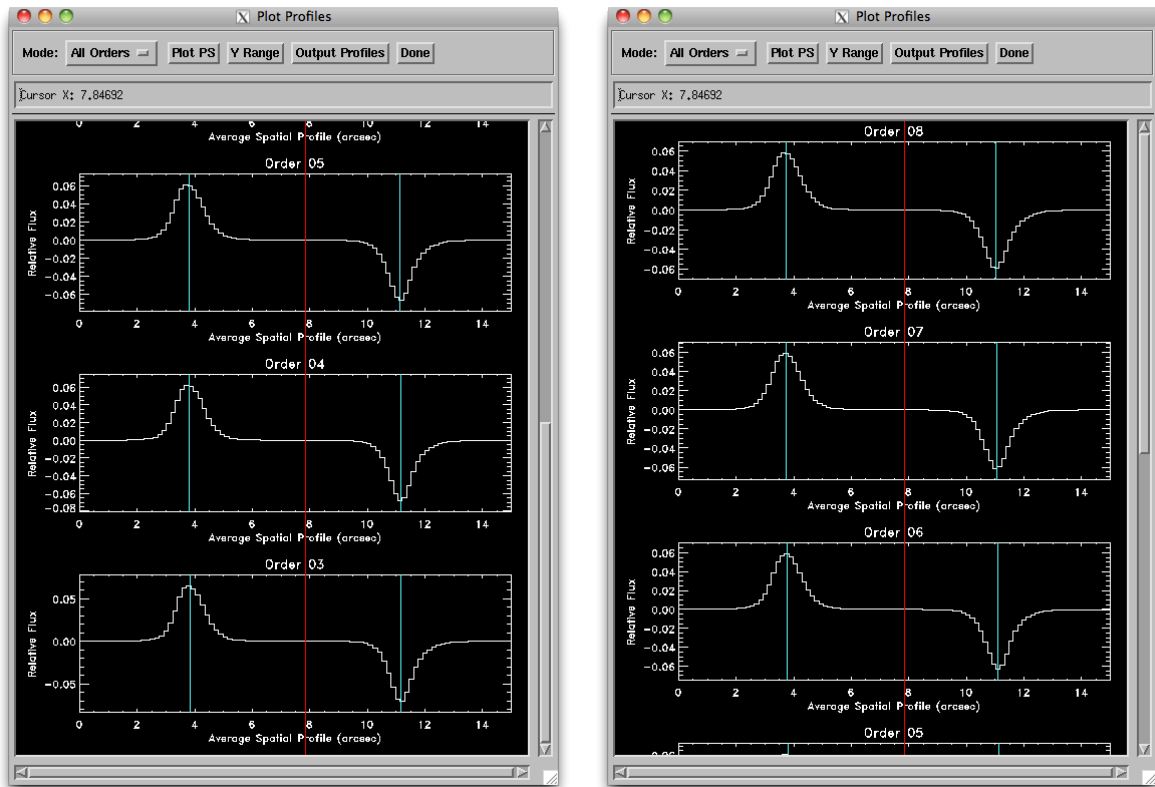


Figure 30 Average signal profile at each order. The abscissa is spatial direction, and the ordinate is flux. Left : Order 3–5 from bottom to top. Right : Order 6–8 from bottom to top.

With the profile, 1D spectra are extracted (Figure 31).

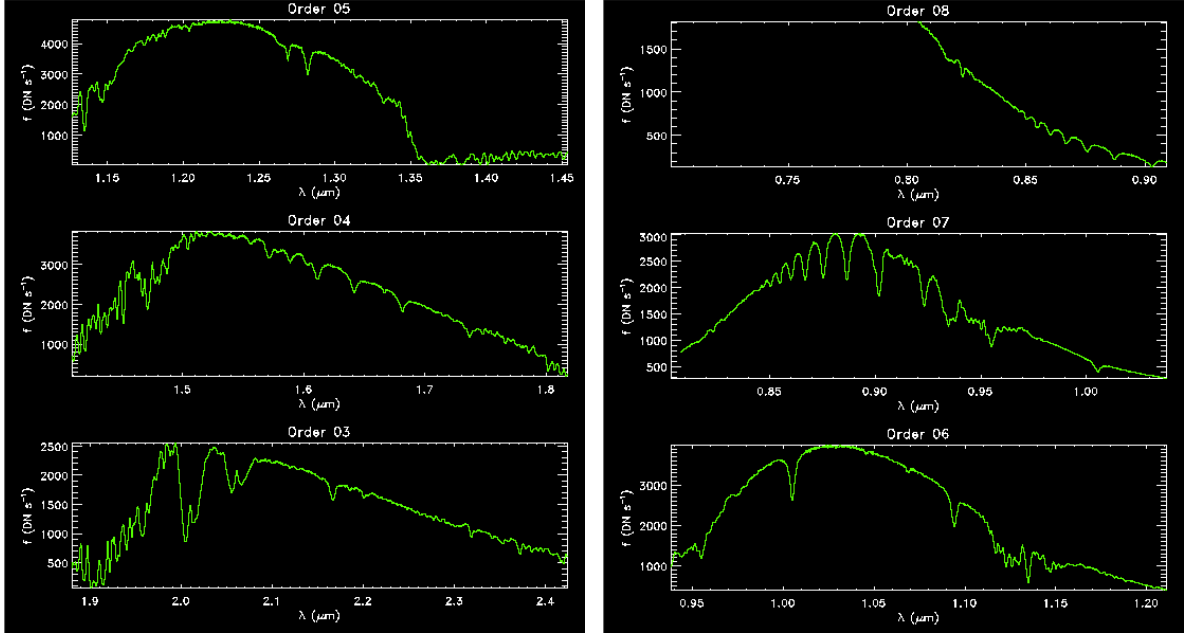


Figure 31 The results of signal extraction of HD140775. The abscissa is wavelength, and the ordinate is flux. Left : Order 3–5 from bottom to top. Right : Order 6–8 from bottom to top.

The same data reduction was carried out for other data, and reduced data were combined to obtain 1D spectra. For target data, target signal was not enough in one data set (A-B), therefore all raw data were summed first, and then the same data reduction was carried out.

3.5.3 Transmission and flux calibration

For transmission and flux calibration, the IDL *xtellcor_basic* program was used. First, shift between standard star spectrum and target spectrum along the wavelength direction was measured from Earth’s atmosphere absorption features. If there is offset of absorption feature between the both spectra in wavelength direction, spectra are shifted to be consistent. By giving effective temperature and V -band magnitude of standard star, transmission and flux calibration were automatically carried out.

The spectral resolution for this data is $R \sim 375$, corresponding to 16 pixels. Following Nyquist-Shannon sampling theorem, eight pixel binning was carried out.

The details of the spectroscopic observations are summarized in Table 1. Redshift and r' -band magnitude are from SDSS catalog. Final spectra are shown in Figures 32 and 33. We also obtained imaging data for all targets and standard stars just before or after spectroscopic observations by using the same instruments used for the spectroscopic observations, and measured photometric magnitudes of the targets. The magnitudes derived from our slit spectra that were

calibrated by spectroscopic standard star (possibly affected by slit loss) and those from imaging data generally agreed within 0.4 mag (Table 2 and Figure 34). We adopted the photometric magnitude from the imaging data for flux calibration.

Table 1 Observation log.

(1) Object ID (SDSS J)	(2) z	(3) r' mag	(4) Instrument	(5) Date	(6) Exposure time[sec]	(7) Standard star	(8) Spectral type
014619.97-004628.7	3.17	18.86	IRTF/SpeX	2009 Jan 19, 21	1800+1600	HD13936	A0
031845.17-001845.3	3.22	18.80	WHT/LIRIS	2009 Jan 10	7200	HD15004	A0
072554.52+392243.4	3.25	19.10	Subaru/IRCS	2013 Mar 11	2400	SAO42621	G2
074628.71+301419.0	3.11	18.43	IRTF/SpeX	2009 Jan 19	2120	HD56386	A0
074939.01+433217.6	3.14	18.56	UKIRT/UIST	2009 Jan 20	1920	HD63160	A0
075515.93+154216.6	3.30	19.63	WHT/LIRIS	2009 Jan 10	10500	HD87737	A0
075841.66+174558.0	3.17	18.98	WHT/LIRIS	2010 Mar 3	7200	HR2692	G9
082645.88+071647.0	3.13	18.28	IRTF/SpeX	2009 Jan 20, 21	920+3120	HD65241	A0
083700.82+350550.2	3.31	18.38	UKIRT/UIST	2009 Jan 20	2880	HD71906	A0
084715.16+383110.0	3.18	18.42	UKIRT/UIST	2009 Jan 20	2880	HD63160	A0
094202.04+042244.5	3.28	17.18	IRTF/SpeX	2009 Jan 19	2120	HR3906	A0
095406.40+290208.0	3.24	18.57	IRTF/SpeX	2013 Mar 21	5200	HD91163	G2
095735.37+353520.6	3.27	18.13	IRTF/SpeX	2013 Mar 20	4800	HD77930	F6
100610.55+370513.8	3.20	17.83	IRTF/SpeX	2009 Jan 19	4920	HD88960	A0
103456.31+035859.4	3.36	17.86	IRTF/SpeX	2009 Jan 20	3400	HR3906	A0
111137.72+073305.9	3.46	18.68	WHT/LIRIS	2010 Mar 3	7200	HR4079	F6
111656.89+080829.4	3.23	18.22	IRTF/SpeX	2009 Jan 21	2800	HD97585	A0
113002.35+115438.3	3.39	18.41	UKIRT/UIST	2009 Jan 20	3840	HD101060	A0
114412.77+315800.8	3.23	18.56	UKIRT/UIST	2009 Jan 20	7440	HD98989	A0
123815.03+443026.2	3.25	18.17	IRTF/SpeX	2013 Mar 22	6000	HD111859	F2
133724.69+315254.5	3.18	18.53	IRTF/SpeX	2013 Mar 21	4080	HD121149	G0
133757.87+021820.9	3.33	18.13	IRTF/SpeX	2009 Jan 21, Apr 2	3000+6480	HD124224	A0
140745.50+403702.2	3.20	18.47	IRTF/SpeX	2013 Mar 20	4800	HD134169	G1
142755.85-002951.1	3.36	18.23	IRTF/SpeX	2011 Feb 19	2640	HD116960	A0
150238.38+030228.2	3.35	18.53	IRTF/SpeX	2013 Mar 22	6000	HD34495	F6
150726.32+440649.2	3.12	17.85	IRTF/SpeX	2009 Jan 20	800	HD127304	A0
151044.66+321712.9	3.48	19.83	Subaru/IRCS	2013 Apr 18	2400	HIP81272	F5
155036.80+053749.9	3.15	17.99	IRTF/SpeX	2013 Mar 20	5760	HD145436	F6
155137.22+321307.5	3.18	20.15	Subaru/IRCS	2013 Apr 17	2400	HIP87556	F2
155823.22+353252.2	3.20	19.90	Subaru/IRCS	2013 Apr 19	2400	HIP81272	F5
162508.09+265052.2	3.44	18.92	WHT/LIRIS	2010 Mar 3	6000	HR5728	G2
165523.09+184708.4	3.32	17.81	IRTF/SpeX	2013 Mar 21	4560	HD145228	F0
211936.77+104623.9	3.24	19.19	Subaru/IRCS	2012 Oct 14	3600	HR8041	G1
213023.61+122252.2	3.26	18.04	IRTF/SpeX	2008 Aug 28	4800	HD208108	A0
213455.08+001056.8	3.24	18.77	Subaru/IRCS	2012 Oct 14	3600	HR8041	G1
231858.56-005049.6	3.20	19.56	Subaru/IRCS	2012 Oct 14	3600	HR8041	G1
234150.01+144906.0	3.18	18.44	IRTF/SpeX	2008 Aug 29	8000	BD+14 4774	A0

Notes. Column (1): Object name. Column (2): Sloan Digital Sky Survey (SDSS) redshift. Column (3): SDSS r' -band magnitude (PSF magnitude). Column (4): Used telescope and instrument. Column (5): Observation date in UT. Column (6): Net on source exposure time. Column (7): Standard star used for flux calibration and telluric correction. Column (8): Spectral type of the standard star.

Table 2 K -band magnitude.

(1)	(2)	(3)	(4)	(5)
Object ID (SDSS J)	Spectroscopic K mag	Imaging K mag	UKIDSS K mag	2MASS K mag
014619.97–004628.7	16.21	16.69	16.59	–
031845.17–001845.3	16.57	16.38	16.47	–
072554.52+392243.4	17.00	16.95	–	–
074939.01+433217.6	16.24	16.07	–	15.66
075515.93+154216.6	16.53	16.68	–	–
075841.66+174558.0	15.56	16.08	–	–
083700.82+350550.2	16.03	16.06	–	–
084715.16+383110.0	16.07	15.99	–	–
094202.04+042244.5	13.71	14.58	14.58	14.62
095735.37+353520.6	16.31	16.14	–	–
100610.55+370513.8	14.45	15.15	–	15.27
111656.89+080829.4	15.62	15.63	15.56	15.39
113002.35+115438.3	16.19	16.29	16.18	15.98
133724.69+315254.5	16.08	16.15	16.04	–
133757.87+021820.9	15.15	15.74	15.72	>15.17
140745.50+403702.2	14.59	14.48	–	14.63
142755.85–002951.1	14.65	15.49	15.39	15.27
150238.38+030228.2	16.21	16.54	16.15	–
151044.66+321712.9	17.38	17.34	–	–
155036.80+053749.9	15.51	15.76	15.84	>15.59
155137.22+321307.5	18.29	–*	–	–
155823.22+353252.2	17.43	–*	–	–
165523.09+184708.4	15.38	15.43	–	–
211936.77+104623.9	16.88	16.84	–	–
213023.61+122252.2	15.06	–*	–	15.29
213455.08+001056.8	16.72	16.97	16.69	–
231858.56–005049.6	16.85	17.09	16.95	–
234150.01+144906.0	16.15	15.87	15.92	–

Notes. Column (1): Object name. Column (2): Spectroscopic magnitude based on our data. Column (3): Imaging magnitude based on our data (Total magnitude). Column (4): UKIDSS magnitude (aperture magnitude). Column (5): 2MASS magnitude (PSF magnitude). Only sources whose SMBH masses (M_{BH}) were estimated are listed. Imaging magnitudes were used for flux calibration.

* Imaging data quality is not good enough to obtain reliable photometric magnitude.

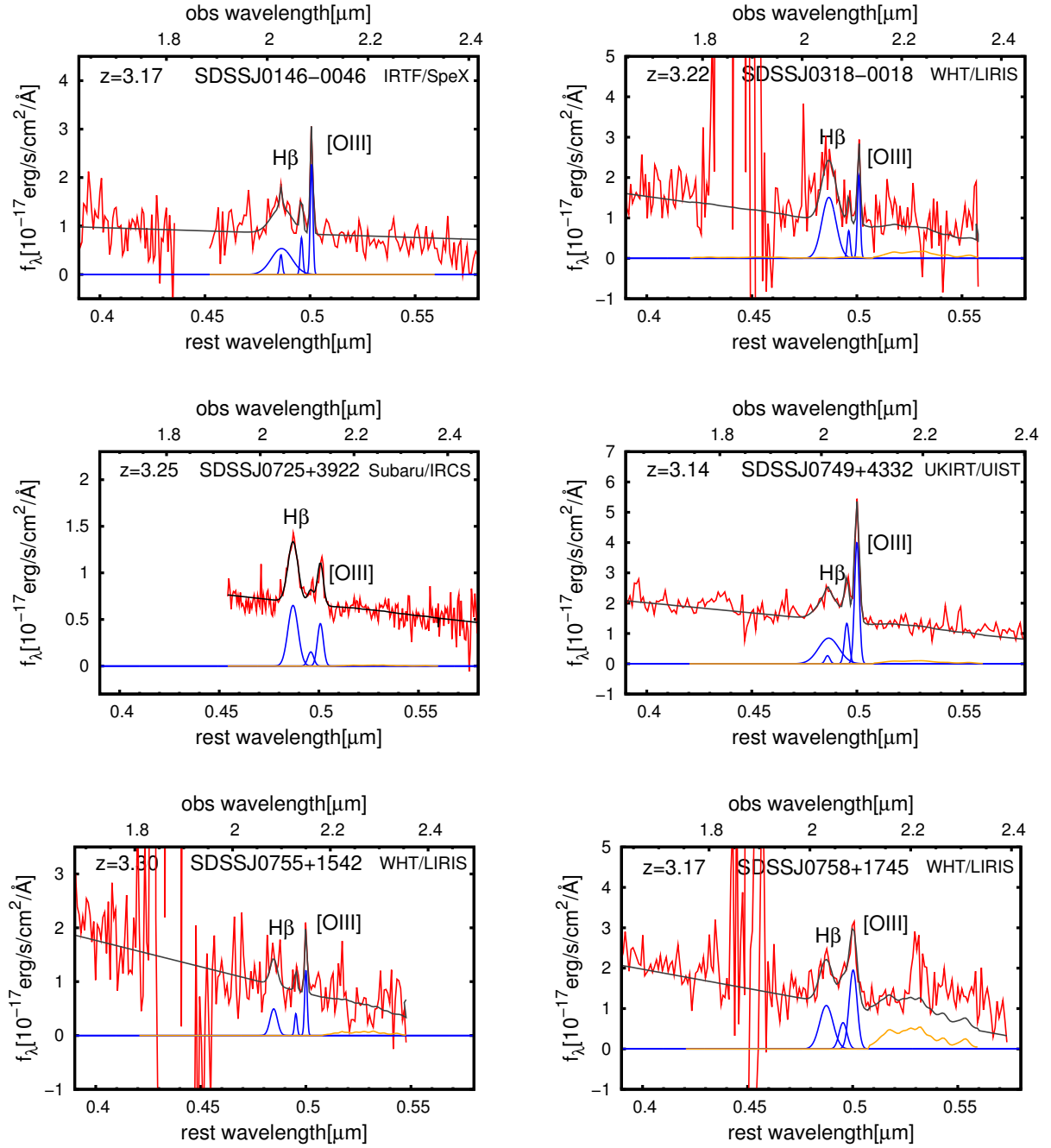


Figure 32 All spectra of 28 $z \sim 3$ QSOs with fitted $H\beta$ and the [O III] emission lines in our sample. The abscissa is the rest-frame (bottom) and the observed (top) wavelength in [μ m]. The ordinate is the flux in [10^{-17} erg/s/cm²/ \AA]. The best-fit model (black line) in each panel is composed of a continuum component, Fe II emission (orange line), and $H\beta$ and [O III] emission lines (blue lines).

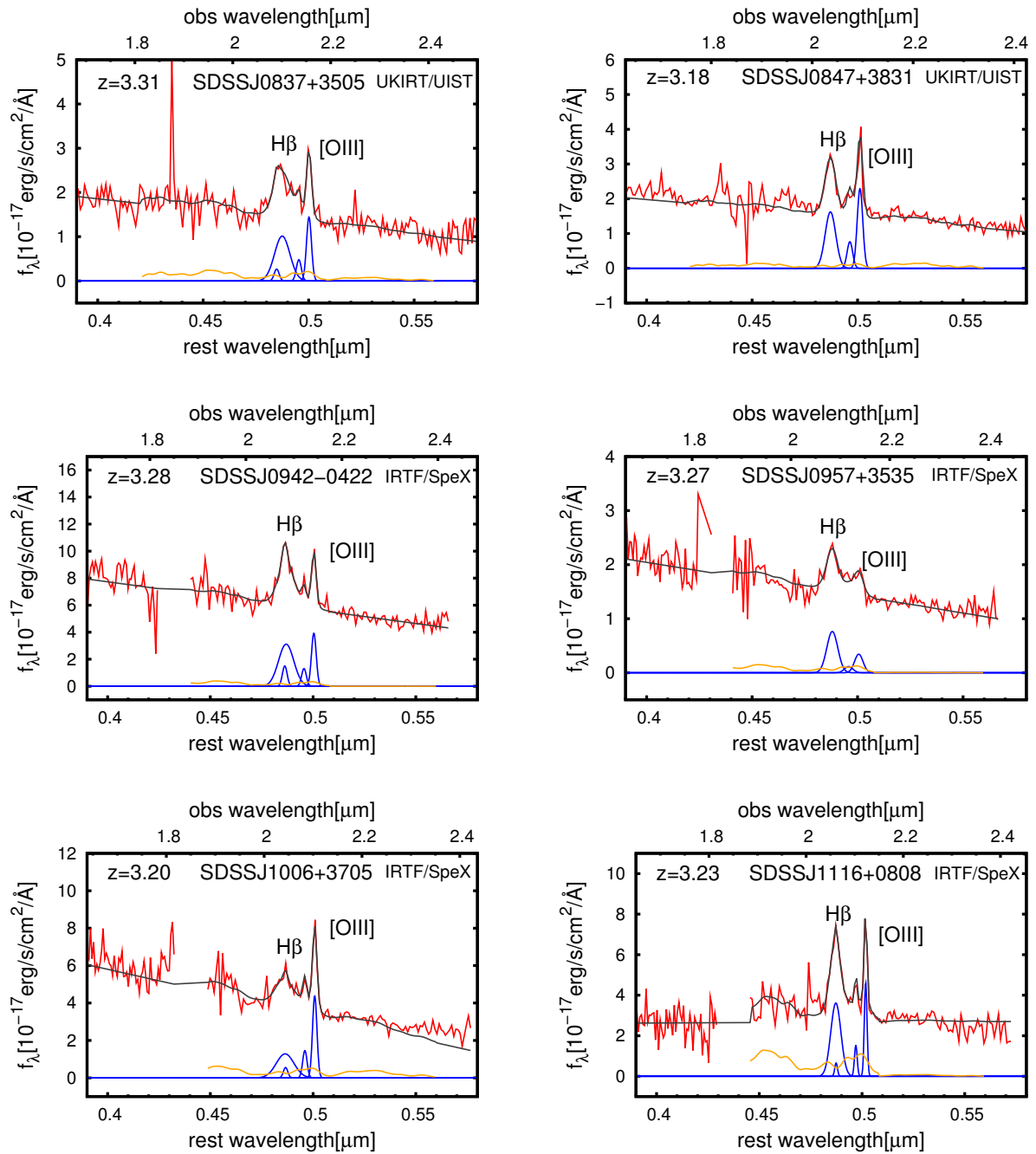


Figure 32 continued

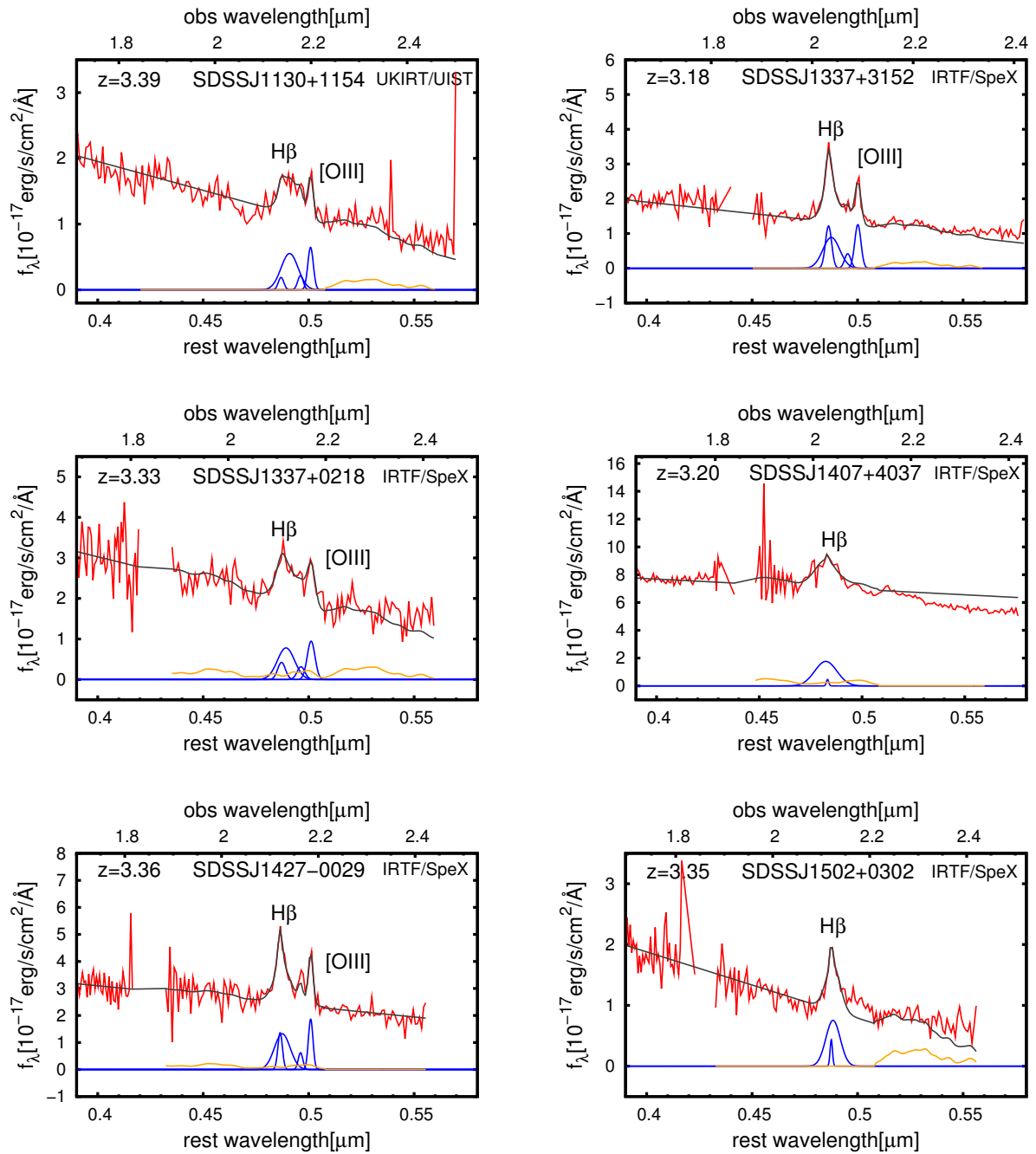


Figure 32 continued

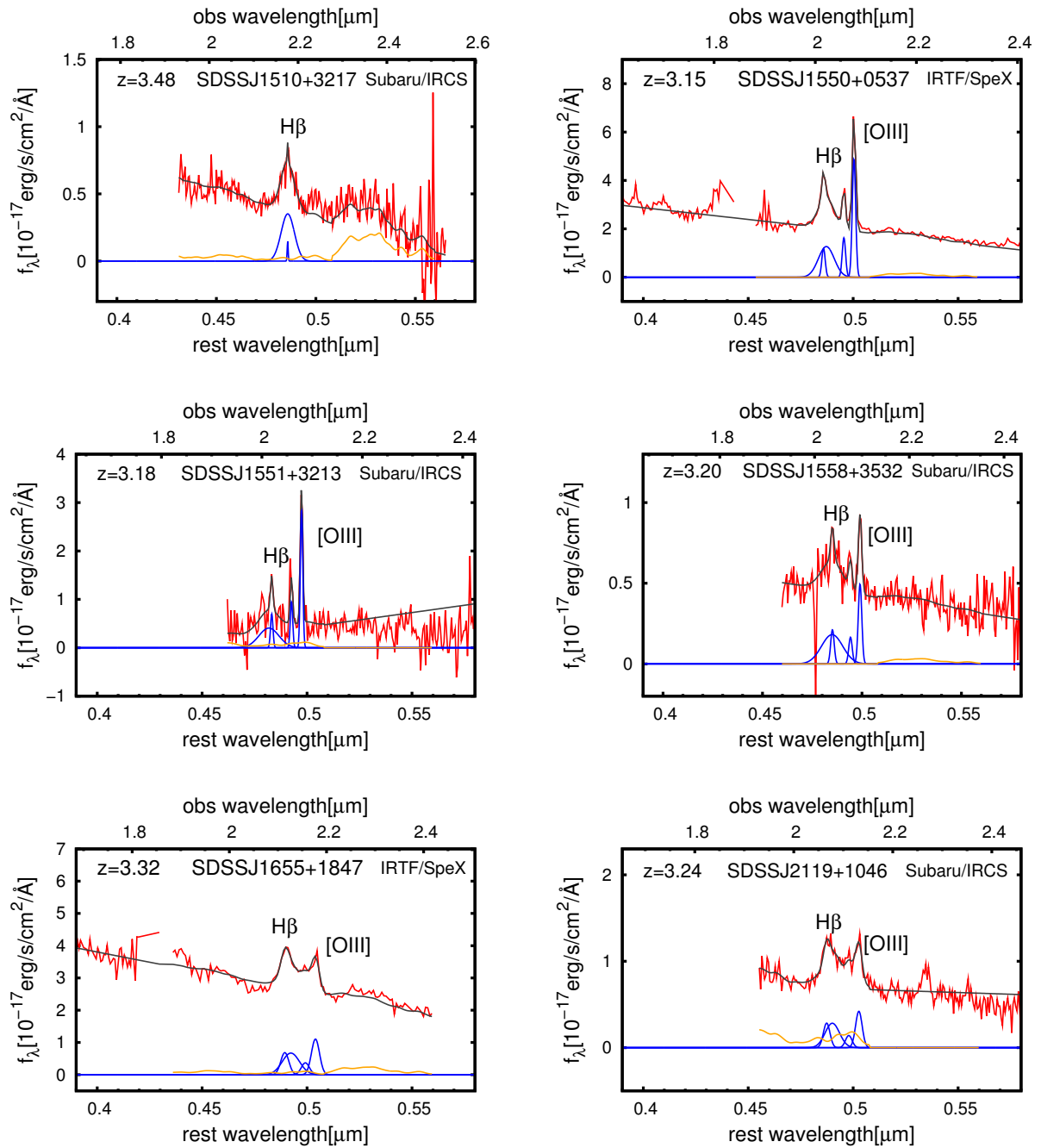


Figure 32 continued

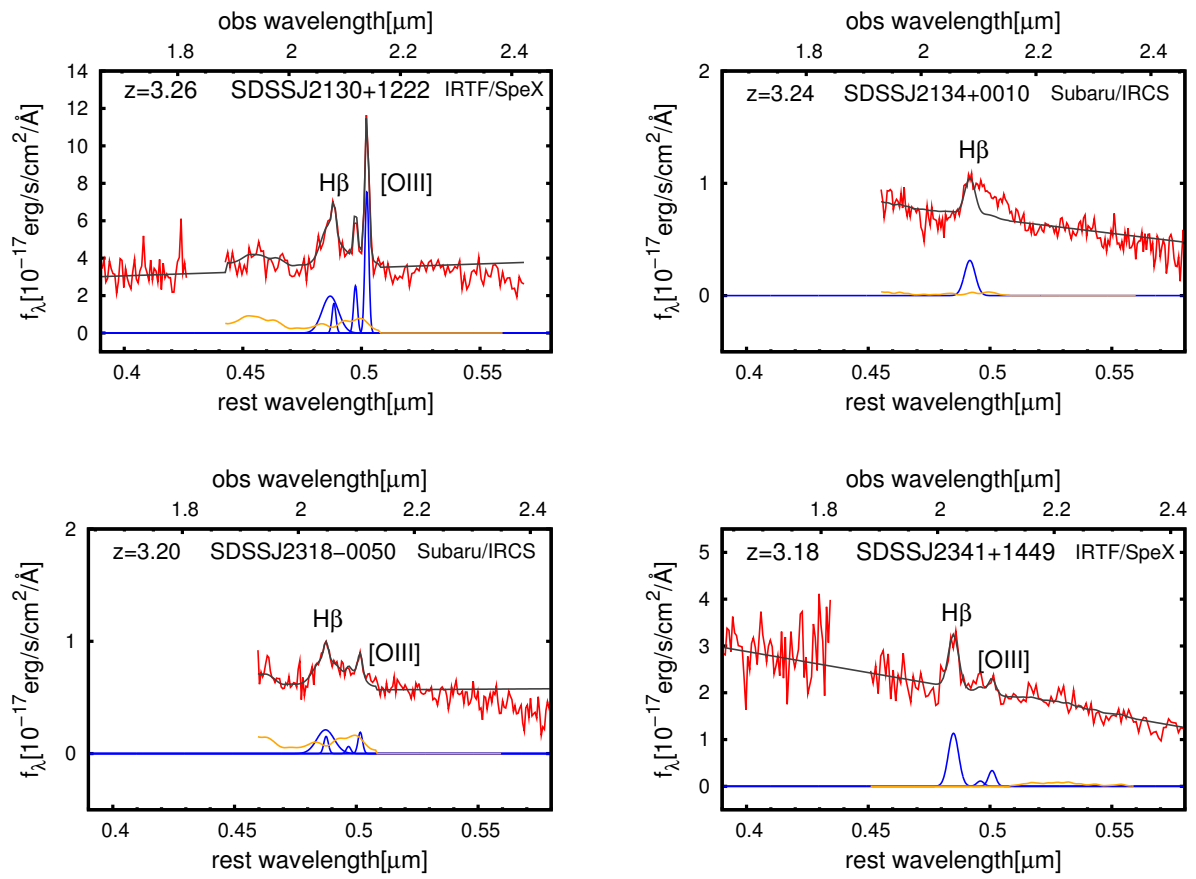


Figure 32 continued

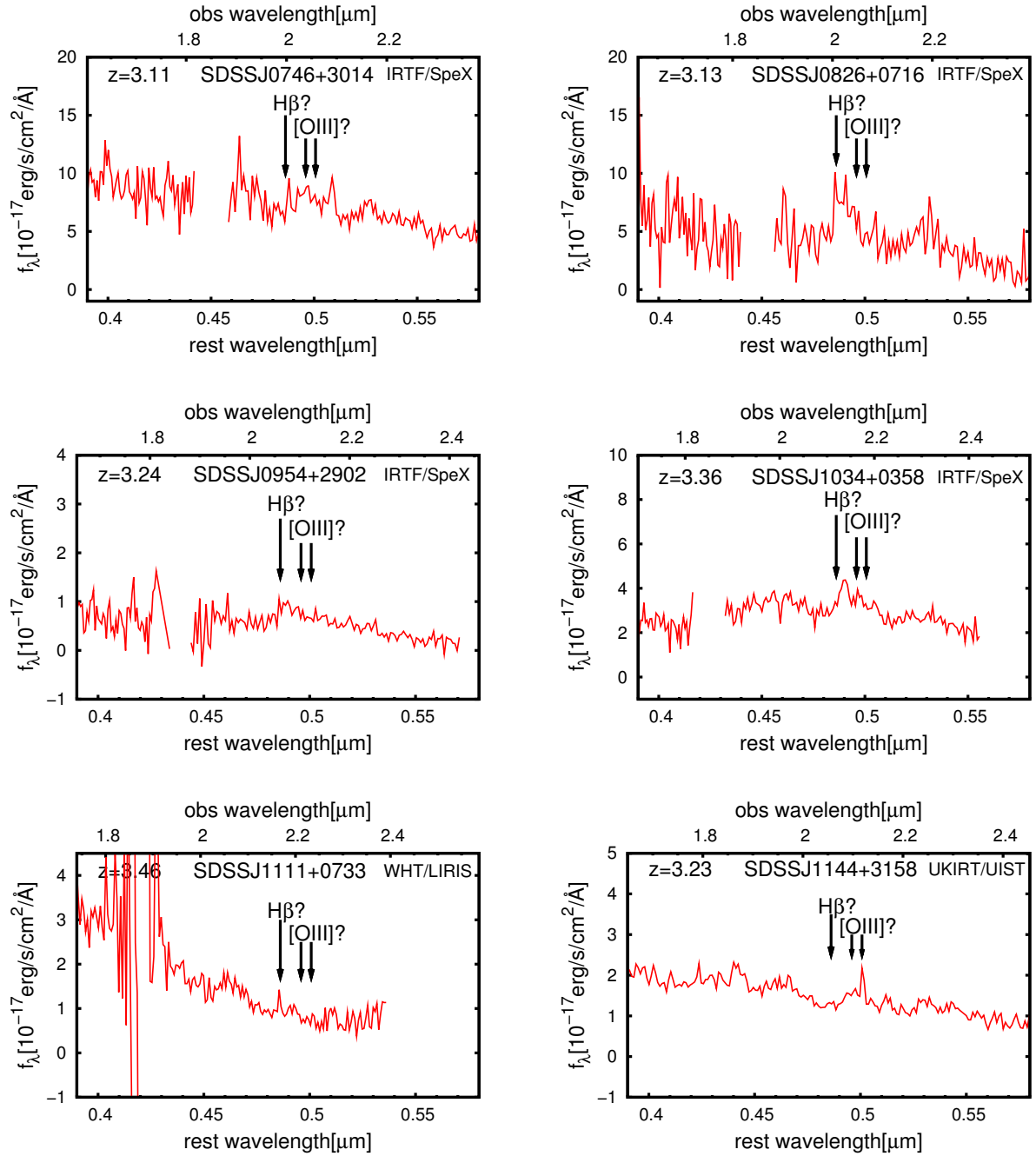


Figure 33 Spectra without clearly detected emission lines. The abscissa is the rest frame (bottom) and the observed (top) wavelength in $[\mu\text{m}]$. The ordinate is the flux in $[10^{-17}\text{erg/s/cm}^2/\text{\AA}]$. $\text{H}\beta$ and $[\text{O III}]$ emission lines should be positioned as indicated by the downward arrows in each panel.

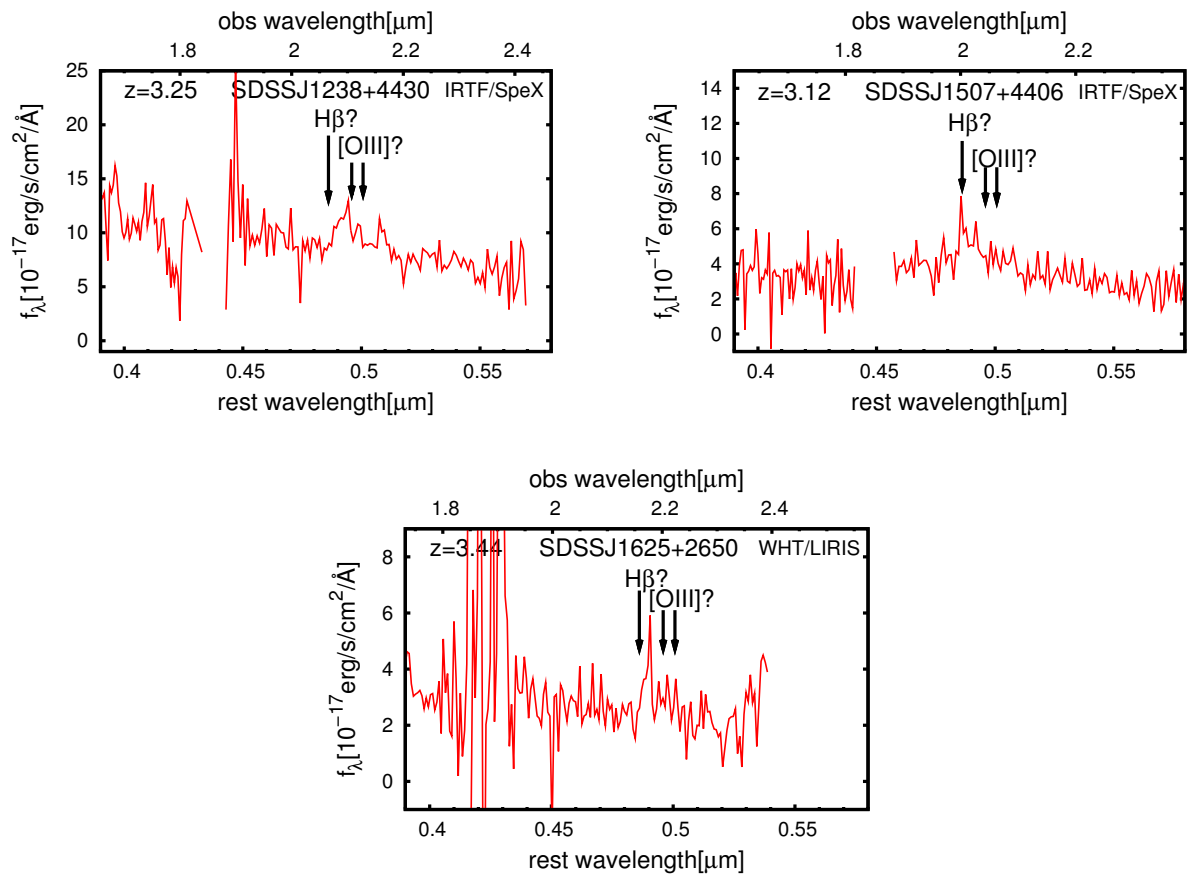


Figure 33 continued

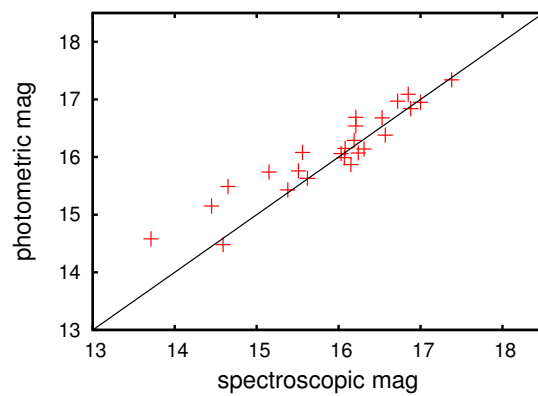


Figure 34 Comparison of K -band magnitudes derived from spectroscopic data (abscissa) and imaging data (ordinate). The dashed line represents a 1:1 correspondence.

4 Spectral Analysis

To estimate M_{BH} , we fitted the observed spectra with a model combining the linear continuum, the underlying very broad Fe II emission line complex ($\lambda_{\text{rest}}=4500\text{--}5600 \text{ \AA}$), the broad and narrow H β $\lambda_{\text{rest}}4861$ emission lines, and two narrow [O III] $\lambda_{\text{rest}}4959, 5007$ emission lines (as the forbidden [O III] emission line originates primarily from the narrow line regions). The fitting of the spectra of the $z \sim 3$ QSOs was performed individually using QDP (Tennant 1991)^{*2} and IDL. The following is our spectral fitting procedure.

1. Continuum fitting
2. [O III] and H β emission lines fitting
3. Fe II template fitting and subtraction
4. Re-fitting of continuum, [O III], and H β emission lines

First, a tentative linear continuum ($y = ax + b$) was determined using several data points that were not strongly affected by H β , [O III], and Fe II emission lines (Figure 35). For the IRTF, UKIRT, WHT targets, data points at $\lambda_{\text{rest}}=4000\text{--}4050 \text{ \AA}$ or $4150\text{--}4200 \text{ \AA}$, and $5080\text{--}5120 \text{ \AA}$ were used. For the Subaru targets, because the H -band spectral data were not available, data from $\lambda_{\text{rest}}=4700\text{--}4750 \text{ \AA}$, $5080\text{--}5120 \text{ \AA}$, and $5470\text{--}5500 \text{ \AA}$ were adopted. Several data points in the wavelength range considered for continuum determination were significantly affected by the Earth's atmospheric absorption (Figure 36), depending on the redshifts of individual QSOs, and were considerably noisy. Thus, these noisy data points were excluded from the continuum determination.

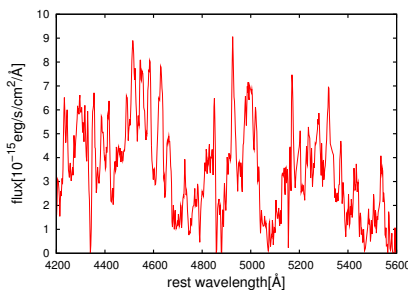


Figure 35 Fe II emission template from Tsuzuki et al. (2006). The abscissa is wavelength, and the ordinate is flux of Fe II emission.

^{*2} The detailed information is available at <http://heasarc.gsfc.nasa.gov/ftools/others/qdp/node3.html>.

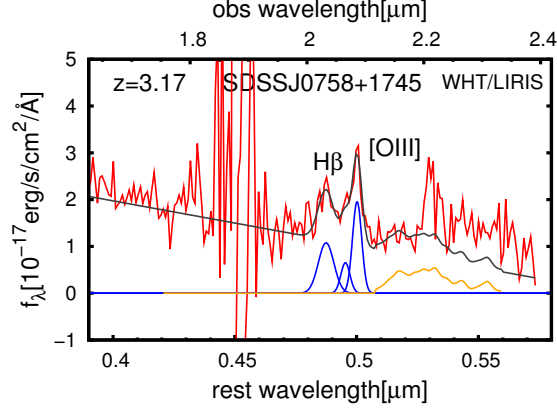


Figure 36 Top : An example of spectra. Bottom : Earth atmospheric absorption in near-infrared wavelength range. The abscissa is wavelength, and the ordinate is intensity. Left : 1.5–2.0 μm . Right : 2.0–2.5 μm . Noisy region at $\sim 1.9 \mu\text{m}$ at the observed wavelength in the top figure is affected by Earth atmospheric absorption.

Next, we fitted the [O III] $\lambda\lambda_{\text{rest}}4959, 5007$ doublet emission lines with two narrow Gaussian components. The line width and the redshift of the two components were set to be the same. The relative 5007 \AA -to-4959 \AA strength was fixed at 3.0 (Dimitrijević et al. (2007)). Then the $H\beta$ emission line was fit with two Gaussian (broad and narrow) components. Although some previous studies adopt more complex model (Shemmer et al. (2004); Netzer & Trakhtenbrot (2007); Schulze & Wisotzki (2010)), we use only one broad Gaussian and one narrow Gaussian models for $H\beta$ line fitting, because of limited spectral resolution and S/N of our data. For the narrow $H\beta$ emission component, the same line width as the [O III] line was adopted. Another Gaussian component with a larger linewidth, corresponding to the broad components of the $H\beta$ emission line, was added. All parameters of this broad component were set as free parameters. We allowed the velocity shift of the peak wavelength between the narrow $H\beta$ and [O III] lines to be up to 200 km s^{-1} , following Netzer et al. (2007). Figure 37 is an example image of [O III] and $H\beta$ emission line fitting.

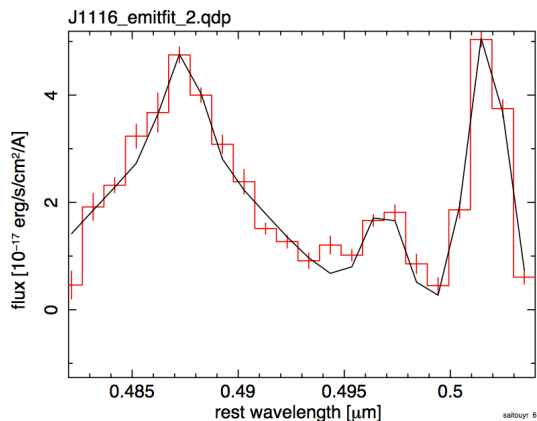


Figure 37 Example image of [O III] and H β emission line fitting for J1116, fitted with four components (two narrow Gaussians for [O III] and broad and narrow Gaussians for H β).

Then Fe II emission line fitting was carried out using the template derived from the nearby well-studied QSO, I Zw 1, by Tsuzuki et al. (2006) (Figure 35). We note that our aim is not to try to accurately fit the Fe II emission features, but to obtain a reliable estimate of the H β line width and nearby continuum flux, unaffected by the contamination from the Fe II emission lines. The template was convolved with a Gaussian that had the same line width as the broad H β emission line, as determined above, because the Fe II emission-line complex originates predominantly from the broad line regions (Figure 38). The fitting wavelength ranges for the Fe II features were $\lambda_{\text{rest}}=4500\text{--}4650 \text{ \AA}$ and $5100\text{--}5600 \text{ \AA}$. Because not all QSOs have exactly the same Fe II emission line profile as the template used (Fe II spectrum extracted from I Zw 1), we divided the Fe II template into two, $\lambda_{\text{rest}} < 5080 \text{ \AA}$ and $\lambda_{\text{rest}} > 5080 \text{ \AA}$ (the Fe II feature shows a minimum value at $\lambda_{\text{rest}}=5080 \text{ \AA}$ in the template), and varied their relative strengths to better fit the spectral features actually observed near the Fe II emission in our QSOs spectra. The scaled template was subtracted from the observed spectra.

Finally, the Fe II subtracted spectrum was refit using the approach described above. This time, the peak wavelength shift between the narrow H β and [O III] was allowed to be up to 450 km s^{-1} . We determined the final fitting parameters for a linear continuum, H β , and the [O III] emission lines. The contribution of the instrumental resolution was removed from the fitted line width to obtain the actual H β emission line width.

For the objects that [O III] lines were not detected, we employed spectral resolution as a minimum narrow line width. Some QSOs were fit with only a broad Gaussian component for the H β emission line, because the χ^2 values became larger when both broad and narrow Gaussian components were added. For J2134+0011, the H β line and [O III] lines were not clearly deblended (Figure 32). Therefore, only wavelengths shorter than 4861 \AA were used to fit the broad H β emission line. For some sources, continuum fits at the longest wavelength is

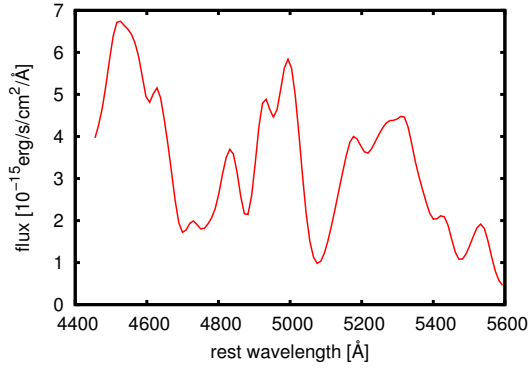


Figure 38 Example image of broadened Fe II template convolved with Gaussian, whose width is the same as J1116 broad H β component.

problematic, because our continuum fitting ranges do not cover longer wavelength part. Also, longer wavelength part of Fe II emission is not well fitted for some sources. However these problematic fits do not affect L_{5100} value significantly.

We succeeded in fitting the H β emission lines for 28 out of 37 observed objects (Figure 32).

Based on the above best Gaussian fit, line flux and luminosity can be estimated. The definition of Gaussian in QDP used for line fitting, is

$$ae^{-\frac{(x-\mu)^2}{2\sigma^2}} \quad (4.1)$$

where a is intensity of Gaussian, μ is peak wavelength, and σ is width. Since emission line flux is corresponding to area of gaussian,

$$f_{\text{line}} = \sqrt{2\pi}a\sigma. \quad (4.2)$$

Moreover, line luminosity can be derived by

$$L_{\text{line}} = 4\pi d_L^2 f_{\text{line}}, \quad (4.3)$$

where d_L is luminosity distance that corresponds to distance from the target to us.

Tables 3 and 4 show the flux and luminosity of H β and [O III] emission lines, respectively. In Table 5, the redshift values estimated from H β and [O III] lines are compared to that from the SDSS; they show good agreement.

Table 3 5100Å continuum flux densities and H β flux and luminosity.

(1) Object ID (SDSS J)	(2) 5100Å continuum flux [10 ⁻¹⁷ erg/s/cm ² /Å]	Flux [10 ⁻¹⁵ erg/s/cm ²]		Luminosity [10 ⁴⁴ erg/s]	
		(3) H β broad	(4) H β narrow	(5) H β broad	(6) H β narrow
014619.97–004628.7	0.860 ± 0.047	0.661 ± 0.097	0.065 ± 0.025	0.584 ± 0.086	0.057 ± 0.022
031845.17–001845.3	0.727 ± 0.121	1.270 ± 0.144	–	1.164 ± 0.132	–
072554.52+392243.4	0.631 ± 0.014	0.415 ± 0.016	–	0.386 ± 0.015	–
074939.01+433217.6	1.278 ± 0.064	1.033 ± 0.116	0.075 ± 0.045	0.891 ± 0.100	0.065 ± 0.039
075515.93+154216.6	0.690 ± 0.151	0.216 ± 0.085	–	0.210 ± 0.083	–
075841.66+174558.0	0.932 ± 0.087	0.857 ± 0.012	–	0.757 ± 0.107	–
083700.82+350550.2	1.268 ± 0.093	0.922 ± 0.148	0.078 ± 0.070	0.903 ± 0.145	0.077 ± 0.069
084715.16+383110.0	1.405 ± 0.061	1.017 ± 0.059	–	0.905 ± 0.053	–
094202.04+042244.5	5.473 ± 0.110	2.900 ± 0.179	0.435 ± 0.064	2.779 ± 0.171	0.417 ± 0.061
095735.37+353520.6	1.354 ± 0.034	0.497 ± 0.029	–	0.473 ± 0.028	–
100610.55+370513.8	3.223 ± 0.043	1.383 ± 0.144	0.148 ± 0.048	1.250 ± 0.130	0.134 ± 0.043
111656.89+080829.4	2.692 ± 0.119	2.235 ± 0.174	0.109 ± 0.053	2.064 ± 0.160	0.101 ± 0.049
113002.35+115438.3	0.981 ± 0.065	0.559 ± 0.059	0.062 ± 0.028	0.580 ± 0.061	0.064 ± 0.029
133724.69+315254.5	1.163 ± 0.025	0.887 ± 0.056	0.448 ± 0.030	0.789 ± 0.050	0.399 ± 0.027
133757.87+021820.9	1.601 ± 0.079	0.790 ± 0.114	0.194 ± 0.066	0.785 ± 0.113	0.193 ± 0.066
140745.50+403702.2	7.128 ± 0.031	2.378 ± 0.050	–	2.148 ± 0.045	–
142755.85–002951.1	2.274 ± 0.082	1.240 ± 0.018	0.370 ± 0.057	1.259 ± 0.181	0.376 ± 0.058
150238.38+030228.2	0.665 ± 0.030	0.644 ± 0.031	–	0.649 ± 0.031	–
151044.66+321712.9	0.265 ± 0.016	0.295 ± 0.028	–	0.325 ± 0.031	–
155036.80+053749.9	1.793 ± 0.032	1.203 ± 0.046	0.242 ± 0.015	1.046 ± 0.040	0.210 ± 0.013
155137.22+321307.5	0.506 ± 0.035	0.487 ± 0.105	0.102 ± 0.024	0.434 ± 0.093	0.090 ± 0.021
155823.22+353252.2	0.413 ± 0.019	0.243 ± 0.116	0.047 ± 0.014	0.219 ± 0.105	0.042 ± 0.013
165523.09+184708.4	2.388 ± 0.039	0.691 ± 0.047	0.331 ± 0.031	0.682 ± 0.046	0.326 ± 0.031
211936.77+104623.9	0.684 ± 0.015	0.229 ± 0.059	0.115 ± 0.050	0.213 ± 0.055	0.107 ± 0.046
213023.61+122252.2	3.620 ± 0.117	1.692 ± 0.139	0.321 ± 0.040	1.597 ± 0.131	0.303 ± 0.038
213455.08+001056.8	0.664 ± 0.015	0.169 ± 0.017	–	0.157 ± 0.016	–
231858.56–005049.6	0.567 ± 0.015	0.189 ± 0.028	0.040 ± 0.018	0.171 ± 0.025	0.036 ± 0.016
234150.01+144906.0	1.891 ± 0.046	0.604 ± 0.072	–	0.537 ± 0.064	–

Notes. Column (1): Object name. Column (2): Continuum flux at $\lambda_{\text{rest}} = 5100\text{\AA}$ (3): Flux of broad H β emission line. Column (4): Flux of narrow H β emission line. Column (5): Luminosity of broad H β emission line. Column (6): Luminosity of narrow H β emission line. The values were calculated from fitting results. "–" means that H β line was fitted with only broad Gaussian because χ^2 got larger when narrow components were added, or [O III] lines were not clearly detected.

Table 4 [O III] flux and luminosity.

(1)	Flux [10^{-15} erg/s/cm 2]		Luminosity [10^{44} erg/s]	
	(2)	(3)	(4)	(5)
Object ID (SDSS J)	[O III] λ 5007	[O III] λ 4959	[O III] λ 5007	[O III] λ 4959
014619.97–004628.7	0.361 ± 0.016	0.120 ± 0.005	0.318 ± 0.014	0.106 ± 0.005
031845.17–001845.3	0.351 ± 0.084	0.117 ± 0.028	0.322 ± 0.078	0.107 ± 0.026
072554.52+392243.4	0.170 ± 0.016	0.057 ± 0.005	0.158 ± 0.015	0.053 ± 0.005
074939.01+433217.6	1.127 ± 0.040	0.376 ± 0.013	0.973 ± 0.035	0.324 ± 0.012
075515.93+154216.6	0.185 ± 0.161	0.062 ± 0.054	0.180 ± 0.156	0.060 ± 0.052
075841.66+174558.0	0.922 ± 0.098	0.307 ± 0.033	0.814 ± 0.087	0.271 ± 0.029
083700.82+350550.2	0.422 ± 0.094	0.141 ± 0.031	0.413 ± 0.092	0.138 ± 0.031
084715.16+383110.0	0.755 ± 0.031	0.252 ± 0.010	0.672 ± 0.027	0.224 ± 0.009
094202.04+042244.5	1.137 ± 0.063	0.379 ± 0.021	1.090 ± 0.060	0.363 ± 0.020
095735.37+353520.6	0.173 ± 0.030	0.058 ± 0.010	0.165 ± 0.028	0.055 ± 0.009
100610.55+370513.8	1.171 ± 0.046	0.390 ± 0.015	1.058 ± 0.041	0.353 ± 0.014
111656.89+080829.4	0.765 ± 0.058	0.255 ± 0.019	0.707 ± 0.053	0.236 ± 0.018
113002.35+115438.3	0.212 ± 0.038	0.071 ± 0.013	0.219 ± 0.039	0.073 ± 0.013
133724.69+315254.5	0.462 ± 0.022	0.154 ± 0.007	0.411 ± 0.020	0.137 ± 0.007
133757.87+021820.9	0.436 ± 0.061	0.145 ± 0.020	0.433 ± 0.061	0.014 ± 0.020
140745.50+403702.2	–	–	–	–
142755.85–002951.1	0.507 ± 0.050	0.169 ± 0.017	0.514 ± 0.050	0.171 ± 0.017
150238.38+030228.2	–	–	–	–
151044.66+321712.9	–	–	–	–
155036.80+053749.9	0.993 ± 0.017	0.331 ± 0.006	0.864 ± 0.015	0.288 ± 0.005
155137.22+321307.5	0.416 ± 0.027	0.139 ± 0.009	0.370 ± 0.024	0.123 ± 0.008
155823.22+353252.2	0.110 ± 0.017	0.037 ± 0.006	0.099 ± 0.015	0.033 ± 0.005
165523.09+184708.4	0.534 ± 0.028	0.178 ± 0.009	0.527 ± 0.027	0.176 ± 0.009
211936.77+104623.9	0.159 ± 0.024	0.053 ± 0.008	0.148 ± 0.022	0.049 ± 0.007
213023.61+122252.2	1.535 ± 0.051	0.512 ± 0.017	1.449 ± 0.048	0.483 ± 0.016
213455.08+001056.8	–	–	–	–
231858.56–005049.6	0.049 ± 0.018	0.016 ± 0.006	0.044 ± 0.016	0.015 ± 0.005
234150.01+144906.0	0.013 ± 0.005	0.004 ± 0.002	0.111 ± 0.046	0.037 ± 0.015

Notes. Column (1): Object name. Column (2): Flux of [O III] λ_{rest} 5007 emission line. Column (3): Flux of [O III] λ_{rest} 4959 emission line. Column (4): Luminosity of [O III] λ 5007 emission line. Column (5): Luminosity of [O III] λ_{rest} 4959 emission line. The values were calculated from fitting results. “–” means that [O III] lines were clearly not detected.

Table 5 Redshift comparison.

(1)	(2)	(3)	(4)
Object ID (SDSS J)	H β	[O III] $\lambda_{\text{rest}}5007$	SDSS
014619.97–004628.7	3.173	3.170	3.173
031845.17–001845.3	3.225	3.222	3.224
072554.52+392243.4	3.258	3.251	3.249
074939.01+433217.6	3.144	3.134	3.141
075515.93+154216.6	3.288	3.294	3.298
075841.66+174558.0	3.182	3.166	3.170
083700.82+350550.2	3.322	3.305	3.311
084715.16+383110.0	3.189	3.184	3.180
094202.04+042244.5	3.287	3.277	3.276
095735.37+353520.6	3.287	3.269	3.276
100610.55+370513.8	3.203	3.201	3.201
111656.89+080829.4	3.240	3.239	3.234
113002.35+115438.3	3.434	3.392	3.394
133724.69+315254.5	3.192	3.175	3.208
133757.87+021820.9	3.358	3.334	3.333
140745.50+403702.2	3.168	–	3.200
142755.85–002951.1	3.373	3.362	3.365
150238.38+030228.2	3.370	–	3.358
151044.66+321712.9	3.478	–	3.474
155036.80+053749.9	3.159	3.147	3.153
155137.22+321307.5	3.143	3.152	3.184
155823.22+353252.2	3.191	3.186	3.198
165523.09+184708.4	3.375	3.349	3.323
211936.77+104623.9	3.274	3.257	3.248
213023.61+122252.2	3.267	3.274	3.272
213455.08+001056.8	3.289	–	3.289
231858.56–005049.6	3.211	3.208	3.209
234150.01+144906.0	3.170	3.181	3.184

Notes. Column (1): Object name. Column (2): Redshift measured by broad H β emission line. Column (3): Redshift measured by [O III] $\lambda_{\text{rest}}5007$ emission line. Column (4): SDSS redshift. "–" means [O III] lines were not clearly detected.

5 Results of Spectroscopic Observation

5.1 M_{BH} and $L_{\text{bol}}/L_{\text{Edd}}$ Estimation

The SMBH mass (M_{BH}) of the 28 QSOs (with successful $\text{H}\beta$ fit) were estimated from the following formula (Vestergaard & Peterson (2006)):

$$\log_{10}(M_{\text{BH}}/M_{\odot}) = \log_{10} \left\{ \left[\frac{\text{FWHM}(\text{H}\beta)}{1000 \text{ km s}^{-1}} \right]^2 \left[\frac{\lambda L_{\lambda}(5100 \text{ \AA})}{10^{44} \text{ erg s}^{-1}} \right]^{0.5} \right\} + (6.91 \pm 0.02), \quad (5.1)$$

and are summarized in Table 6.

We employed a resampling approach to obtain realistic uncertainties of L_{5100} , the full-width at half maximum (FWHM) of the $\text{H}\beta$ broad emission line, and M_{BH} (e.g., Schulze & Wisotzki (2010), Assef et al. (2011), Shen & Liu (2012)). Namely, we artificially added Gaussian random noise that is scaled by the observed S/N, and refit them. We attempted this procedure for 100 simulated spectra for each target. The L_{5100} , FWHM, and M_{BH} error were estimated from the resulting scatter of the derived L_{5100} , FWHM, and M_{BH} values from 100 spectra.

For comparison, we also calculated M_{BH} using the different formula proposed by McLure & Jarvis (2002).

$$\log_{10}(M_{\text{BH}}/M_{\odot}) = \log_{10} \left\{ \left[\frac{\text{FWHM}(\text{H}\beta)}{\text{km s}^{-1}} \right]^2 \left[\frac{\lambda L_{\lambda}(5100 \text{ \AA})}{10^{44} \text{ erg s}^{-1}} \right]^{0.61} \right\} + 0.68. \quad (5.2)$$

The difference of M_{BH} related to choice of estimator is typically (median) 0.03 dex (range of $-0.36 \sim +0.03$ dex). Table 6 and Figure 39 show a comparison of the M_{BH} values derived from both methods, which mutually agree within statistical error.

The AGN bolometric luminosity L_{bol} was calculated from the observed L_{5100} luminosity, using a bolometric correction, $f_L(L_{\text{bol}} = f_L \lambda L_{5100})$. For Type 1 unobscured luminous AGNs, f_L was estimated to be 5–13 (e.g., Elvis et al. (1994); Kaspi et al. (2000); Netzer (2003); Marconi et al. (2004); Richards et al. (2006)). We adopt a constant ratio of $f_L = 7$, following Netzer et al. (2007). The AGN bolometric luminosity, relative to the Eddington luminosity for a given M_{BH} ($L_{\text{Edd}} = 3.2 \times 10^4 (M_{\text{BH}}/M_{\odot}) L_{\odot}$), the so-called Eddington ratio ($L_{\text{bol}}/L_{\text{Edd}}$), is often used to estimate the activity of SMBHs (i.e., the SMBH-mass normalized accretion rate). In the case of $f_L = 7$, the Eddington ratio is given by

$$L_{\text{bol}}/L_{\text{Edd}} = \frac{7\lambda L_{5100}}{1.5 \times 10^{38} (M_{\text{BH}}/M_{\odot})}. \quad (5.3)$$

The estimated $L_{\text{bol}}/L_{\text{Edd}}$ of 28 QSOs are summarized in Table 6.

5.2 M_{BH} and $L_{\text{bol}}/L_{\text{Edd}}$ distributions

The upper panels of Figure 40(a) and 40(b) show the distribution of M_{BH} and the Eddington ratio ($L_{\text{bol}}/L_{\text{Edd}}$) for our sample, respectively. Netzer et al. (2007) and Shemmer et al. (2004) performed near-infrared spectroscopy of QSOs at $z = 2-4$, and measured the SMBH masses in 15 and 29 sources, respectively, based on the $\text{H}\beta$ method, of which 14 QSOs in total (8 sources in Netzer’s sample, and 6 sources in Shemmer’s sample) were at $z > 3$. Our near-infrared spectroscopy tripled the number of $z > 3$ QSOs, with $\text{H}\beta$ -based reliably estimated M_{BH} information.

The M_{BH} and $L_{\text{bol}}/L_{\text{Edd}}$ distributions of these 14 QSOs at $z > 3$ studied by Netzer et al. (2007) and Shemmer et al. (2004) are shown in the lower panels of Figure 40(a) and 40(b), respectively, for comparison. The M_{BH} and $L_{\text{bol}}/L_{\text{Edd}}$ of the comparison sample are re-calculated using Eq.(5.1) and (5.3) with $\text{FWHM}(\text{H}\beta)$ and L_{5100} drawn from the literature (Table 2 in Netzer et al. (2007), and Table 2 in Shemmer et al. (2004)). The difference of M_{BH} due to choice of estimator (Eq.(5.1) in this paper and Eq.(1) in Netzer et al. (2007), or Eq.(1) in Shemmer et al. (2004)) is typically 0.25 dex (range of 0.19–0.30 dex) for Netzer’s sample and 0.15 dex (range of 0.06–0.23 dex) for Shemmer’s sample. The comparison sample has slightly fainter luminosity than our sample (median value of $L_{\text{bol}} = 7.88 \times 10^{46}$ erg s $^{-1}$ for Netzer’s sample and $L_{\text{bol}} = 1.61 \times 10^{47}$ erg s $^{-1}$ for our sample), and M_{BH} of the comparison sample is smaller (range of $10^{8.59}$ – $10^{9.59} M_{\odot}$) than our sample (range of $10^{8.81}$ – $10^{10.13} M_{\odot}$) as shown in Figure 40(a). On the other hand, the Eddington ratios of our sample are systematically smaller than those of the comparison sample, as shown in Figure 40(b). We performed Kolmogorov-Smirnov test to check if those distributions are statistically the same or not. P-values were calculated to be $P(M_{\text{BH}}) = 0.005$ for the M_{BH} distributions, and $P(L_{\text{bol}}/L_{\text{Edd}}) = 0.045$ for the $L_{\text{bol}}/L_{\text{Edd}}$ distributions, respectively. The result of K-S test shows that two samples (our sample and the reference sample) are drawn from different parent distributions for both M_{BH} mass distributions and $L_{\text{bol}}/L_{\text{Edd}}$ distributions (K-S probability of being drawn from the same population < 0.05).

There are two possible reasons to produce the high AGN luminosity, as observed for our QSO sample: (1) the QSO has a modest SMBH mass and a large Eddington ratio, or (2) the QSO has a large SMBH mass and a normal Eddington ratio. If we pick up only the second sample (i.e., QSOs at the higher end of the M_{BH} distribution), $M_{\text{BH}}/M_{\text{spheroid}}$ ratios could be systematically larger than the typical values (e.g., Lauer et al. (2007); Schulze & Wisotzki (2011), Schulze & Wisotzki (2014)), possibly providing systematically biased results regarding the redshift evolution of the $M_{\text{BH}}/M_{\text{spheroid}}$ ratios. M_{BH} of our sample and the comparison sample agree within a factor of a few. As shown in Table 6 and Figure 40, it is unlikely that majority of our sample have the M_{BH} much larger than the break (cut-off) of the SMBH mass

function at $z = 3.2$ ($\sim 10^{9.7} M_{\odot}$; Kelly & Shen (2013)). The cut-off mass of $\log M_{\text{BH}} = 9.7$ was estimated by eye using the mass function at $z = 3.2$ in Figure 4 by Kelly & Shen (2013), although it might be risky to believe the mass function estimated by C IV-based M_{BH} at face values. We compared the $\text{H}\beta$ -based and C IV-based M_{BH} (Figure 41, left) and found that C IV-based M_{BH} is not always biased toward large M_{BH} . Therefore, we consider that our QSO sample corresponds to the case (1) and that the Lauer-bias is not affecting our sample so severely for a study of redshift evolution of $M_{\text{BH}}/M_{\text{spheroid}}$. This suggests that we can use our QSO sample to discuss the redshift evolution of the $M_{\text{BH}}/M_{\text{spheroid}}$ ratios, without obvious strong bias, using the combination of the near-infrared spectroscopy of the M_{BH} estimate (before this Section) and near-infrared, multi-band, high-spatial-resolution AO imaging observations to estimate M_{spheroid} (from Section 7). If the local scaling relations hold all the way to $z > 3$, the expected M_{spheroid} for our observed QSOs with $M_{\text{BH}} = 6.5 \times 10^8 - 1.4 \times 10^{10} M_{\odot}$, are $4.3 \times 10^{11} - 9.0 \times 10^{12} M_{\odot}$, which are detectable with 8 – 10 m telescopes.

Table 6 Observed and derived properties related to SMBHs.

(1)	(2)	(3)	(4)	(5)	(6)	(7)
Object ID (SDSS J)	FWHM(H β)[10 ³ km/s]	$\lambda L_{\lambda}(5100\text{\AA})[10^{46} \text{ erg/s}]$	$\log M_{\text{BH}}[M_{\odot}]$	$\log L_{\text{bol}}/L_{\text{Edd}}$	$t_{\text{grow}}/t_{\text{universe}}$	$\log M_{\text{BH}}[M_{\odot}] \text{ McL}$
014619.97-004628.7	6.92 ± 1.30	1.61 ± 0.09	9.68 ± 0.17	-0.804	1.76	9.69 ± 0.17
031845.17-001845.3	4.79 ± 0.48	1.43 ± 0.24	9.34 ± 0.09	-0.516	0.87	9.34 ± 0.09
072554.52+392243.4	4.32 ± 0.41	1.27 ± 0.03	9.23 ± 0.08	-0.457	0.76	9.23 ± 0.08
074939.01+433217.6	7.14 ± 0.53	2.33 ± 0.12	9.80 ± 0.06	-0.764	1.63	9.82 ± 0.06
075515.93+154216.6	2.70 ± 0.80	1.47 ± 0.32	8.81 ± 0.28	0.026	0.23	8.81 ± 0.28
075841.66+174558.0	4.64 ± 1.03	1.75 ± 0.16	9.34 ± 0.20	-0.428	0.70	9.35 ± 0.20
083700.82+350550.2	5.18 ± 0.53	2.73 ± 0.20	9.55 ± 0.09	-0.445	0.80	9.59 ± 0.09
084715.16+383110.0	4.29 ± 0.46	2.67 ± 0.12	9.38 ± 0.09	-0.284	0.51	9.41 ± 0.09
094202.04+042244.5	5.34 ± 0.22	11.45 ± 0.23	9.89 ± 0.03	-0.162	0.44	10.00 ± 0.03
095735.37+353520.6	6.07 ± 0.71	2.80 ± 0.07	9.69 ± 0.11	-0.574	1.08	9.73 ± 0.11
100610.55+370513.8	5.94 ± 0.40	6.23 ± 0.08	9.85 ± 0.06	-0.387	0.71	9.93 ± 0.06
111656.89+080829.4	3.34 ± 0.22	5.36 ± 0.24	9.32 ± 0.05	0.078	0.22	9.39 ± 0.05
113002.35+115438.3	6.05 ± 0.42	2.28 ± 0.15	9.65 ± 0.06	-0.623	1.26	9.67 ± 0.06
133724.69+315254.5	5.73 ± 0.24	2.21 ± 0.05	9.60 ± 0.04	-0.587	1.06	9.62 ± 0.04
133757.87+021820.9	5.18 ± 1.09	3.51 ± 0.17	9.59 ± 0.22	-0.376	0.69	9.63 ± 0.22
140745.50+403702.2	6.72 ± 0.17	13.79 ± 0.06	10.13 ± 0.02	-0.389	0.74	10.24 ± 0.02
142755.85-009251.1	5.49 ± 0.87	5.13 ± 0.19	9.73 ± 0.13	-0.351	0.73	9.80 ± 0.13
150238.38+030228.2	5.28 ± 0.21	1.49 ± 0.07	9.44 ± 0.03	-0.598	1.13	9.45 ± 0.03
151044.66+321712.9	5.04 ± 0.60	0.67 ± 0.04	9.22 ± 0.10	-0.725	1.51	9.19 ± 0.10
155036.80+053749.9	6.11 ± 0.29	3.30 ± 0.06	9.74 ± 0.04	-0.552	1.00	9.78 ± 0.04
155137.22+321307.5	6.70 ± 1.12	0.96 ± 0.07	9.54 ± 0.18	-0.889	2.11	9.52 ± 0.18
155823.22+353252.2	8.49 ± 2.98	0.80 ± 0.04	9.67 ± 0.28	-1.098	3.52	9.65 ± 0.28
165523.09+184708.4	5.93 ± 0.21	5.19 ± 0.08	9.81 ± 0.03	-0.426	0.80	9.88 ± 0.03
211936.77+104623.9	4.72 ± 0.78	1.38 ± 0.03	9.31 ± 0.16	-0.501	0.85	9.31 ± 0.16
213023.61+122252.2	4.39 ± 0.35	7.43 ± 0.24	9.63 ± 0.07	-0.090	0.35	9.71 ± 0.06
213455.08+001056.8	>3.09 ± 0.31*	1.34 ± 0.03	>8.95 ± 0.09	<-0.157	>0.36	>8.95 ± 0.08
231858.56-005049.6	5.21 ± 0.75	1.10 ± 0.03	9.35 ± 0.13	-0.650	1.19	9.35 ± 0.13
234150.01+144906.0	7.49 ± 4.36	3.59 ± 0.09	9.72 ± 0.69	-0.496	0.88	9.77 ± 0.69

Notes. Column (1): Object name. Column (2): Full-width at half maximum (FWHM) of broad H β emission line. Column (3): Continuum luminosity at 5100 Å. Column (4): Decimal logarithm of SMBH mass. Statistical errors were estimated by resampling approach (Section 5.1; Schulze & Wisotzki (2010), Assef et al. (2011), Shen & Liu (2012)). Column (5): Decimal logarithm of Eddington ratio. Column (6): Ratio of SMBH growth time (t_{grow}) and the age of the universe (t_{universe}). t_{grow} is the time scale of SMBH growth, calculated using the measured M_{BH} and the Eddington ratio. t_{universe} is dependent on the redshift of each target. See Section 5.2 for more details. Column (7): Decimal logarithm of SMBH masses derived from the formula in McLure & Jarvis (2002).

* For this object, we cannot measure the [O III] emission linewidth, therefore, the H β narrow component is not subtracted. If the H β narrow component exists, then the H β broad emission linewidth broadens and the estimated M_{BH} becomes larger.

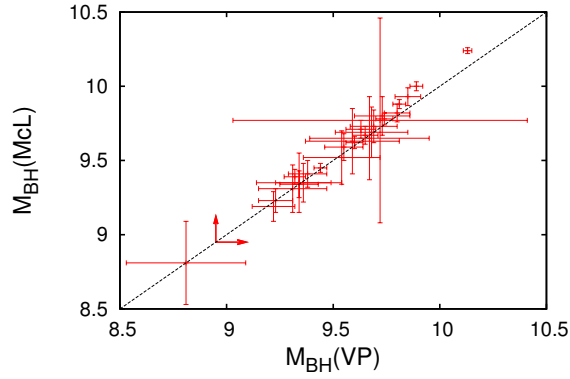


Figure 39 Comparison of M_{BH} derived from a different formula (Table 6). The abscissa and ordinate are the values derived based on Vestergaard & Peterson (2006), and McLure & Jarvis (2002), respectively. Arrows mean lower limits. The dashed line represents a 1:1 correspondence.

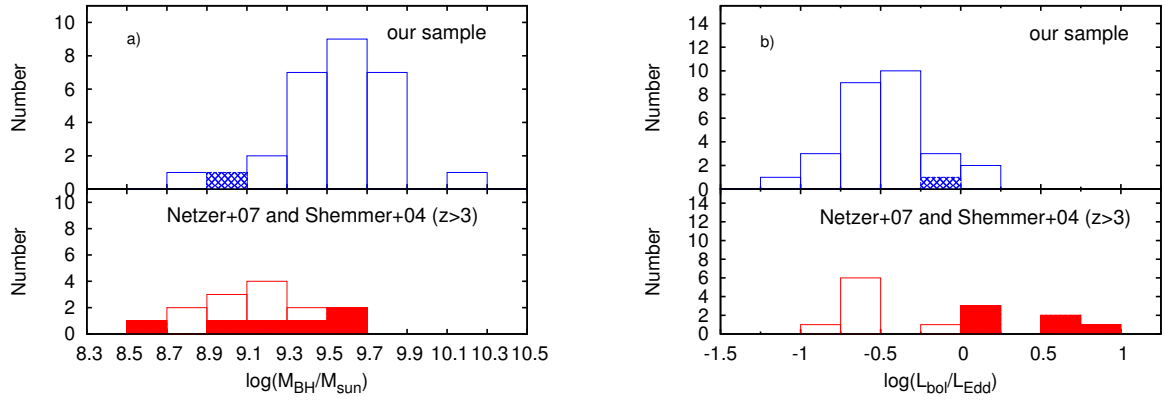


Figure 40 (a) Histogram of M_{BH} estimated in this study (upper panel) and in the literature (Netzer et al. (2007); Shemmer et al. (2004)) for only $3 < z < 4$ sources (lower panel). A lower limit object is shown as a shaded area. (b) Comparison of the $L_{\text{bol}}/L_{\text{Edd}}$ distribution for our sample (upper panel) and Netzer's sample at $z > 3$ (lower panel). An upper limit object is displayed by a shaded area. In the lower panels of both a) and b), open and filled histograms correspond to Netzer's sample and Shemmer's sample, respectively.

6 Findings from Spectroscopic Observations

6.1 Comparison of M_{BH} estimated from $\text{H}\beta$ $\lambda 4861$ and $\text{C IV } \lambda 1549$

The combination of the $\text{C IV } \lambda 1549$ emission line and continuum luminosity at 1450 \AA has often been used to estimate SMBH mass (hereafter, the C IV method) for distant QSOs, because the C IV emission line is redshifted into the optical wavelength range where spectroscopic observations are easier to attain. However, as mentioned in Section 1, the C IV emission line often shows an asymmetric profile. This suggests that, in addition to the motion dominated by the gravitational potential of SMBH, some other non-gravitational component may be contaminated, such as outflow (Vestergaard & Peterson (2006); Marziani & Sulentic (2012)). In fact, several previous studies indicated significant scatter about the comparison of SMBH masses estimated using the $\text{H}\beta$ method and the C IV method (e.g., Netzer et al. (2007); Shen et al. (2008); Ho et al. (2012); Shen & Liu (2012); Trakhtenbrot & Netzer (2012)).

Shen et al. (2011) reported C IV-based BH masses for our QSO sample, using the following formula (Vestergaard & Peterson (2006)):

$$\log_{10}(M_{\text{BH}}/M_{\odot}) = \log_{10} \left\{ \left[\frac{\text{FWHM}(\text{CIV})}{1000 \text{ km s}^{-1}} \right]^2 \left[\frac{\lambda L_{\lambda}(1350 \text{ \AA})}{10^{44} \text{ erg s}^{-1}} \right]^{0.53} \right\} + (6.66 \pm 0.01). \quad (6.1)$$

We adopt their estimates to compare with our M_{BH} using the $\text{H}\beta$ method. The FWHM of the C IV emission line and C IV-based M_{BH} of our targets are shown in Table 7. For two QSOs, C IV data are not available in Shen et al. (2011). The left panel of Figure 41 shows a comparison between SMBH masses obtained by the two methods for our sample. The scatter is large (0.41 dex) and no significant correlation between $\text{H}\beta$ -based and C IV-based M_{BH} is observed. Shen et al. (2008) compared BH masses estimated using different methods for $\sim 60,000$ QSOs at $0.1 \leq z \leq 4.5$, and found that while M_{BH} obtained by the $\text{H}\beta$ - and Mg II-methods are tightly correlated, a comparison between C IV-based and Mg II-based M_{BH} shows large scatter with ~ 0.34 dex (see also Shen et al. (2011)). Given these results, the large scatter shown in the left panel of Figure 41 for our QSO sample is most likely due to the large uncertainty associated with C IV-based M_{BH} . For a reliable M_{BH} estimate for $z \sim 3$ QSOs, the $\text{H}\beta$ -method based on near-infrared spectroscopy is preferred over the C IV-method based on optical spectroscopy.

The right panel of Figure 41 is the same plot as that shown in the left panel of Figure 41;

the marks are distinguished, depending on the Eddington ratio. The samples with high Eddington ratios appear to be distributed slightly to the upper side than those with low Eddington ratios, indicating that the C IV-based M_{BH} was larger than H β -based M_{BH} for sources with high Eddington ratios. Figure 42 shows the relationship between the Eddington ratio and the linewidth ratio (FWHM(C IV)/FWHM(H β)). A weak correlation is seen $\log(\text{FWHM}(\text{C IV})/\text{FWHM}(\text{H}\beta))=(0.32\pm 0.15)\times\log(L_{\text{bol}}/L_{\text{Edd}})+(0.03\pm 0.08)$ for our sample only or $\log(\text{FWHM}(\text{C IV})/\text{FWHM}(\text{H}\beta))=(0.35\pm 0.11)\times\log(L_{\text{bol}}/L_{\text{Edd}})+(0.05\pm 0.06)$ for all plotted samples. This correlation indicates that objects with a higher Eddington ratio have a larger C IV linewidth, compared to H β . QSOs with higher Eddington ratios can have stronger radiation pressure and thereby stronger outflow motion of gas than those with lower Eddington ratios. The C IV line-emitting region is more inside than the H β line-emitting region (Peterson & Wandel (1999)). It may be possible that this outflow-origin motion broadens the C IV line profile, compared to the SMBH's gravitational motion alone, resulting in a larger M_{BH} estimate than the H β -based method.

6.2 Growth Time of SMBHs

From the AGN bolometric luminosity, we can obtain information on the mass accretion rate. When the measured SMBH mass is divided by the accretion rate, the time scale of SMBH growth can be derived (t_{grow}). Following Netzer et al. (2007), we adopt the following formula:

$$t_{\text{grow}} = t_{\text{Edd}} \frac{\eta/(1-\eta)}{f_L \lambda L_{5100}/L_{\text{Edd}}} \ln \left(\frac{M_{\text{BH}}}{M_{\text{seed}}} \right) \frac{1}{f_{\text{active}}}, \quad (6.2)$$

where t_{Edd} is the Eddington time scale ($= 3.8 \times 10^8$ yr), η is the accretion efficiency, M_{seed} is the seed SMBH mass, f_{active} is the duty cycle (the fractional activity time) of the SMBH, and f_L is the bolometric correction (Section 5.1). We assume fiducial values for $\eta = 0.1$, $M_{\text{seed}} = 10^4 M_{\odot}$, $f_{\text{active}} = 1$, and $f_L = 7$, similar to Netzer et al. (2007). We now define t_{universe} , which is the age of the universe at the redshift of each QSO (calculated from our adopted cosmology). The $t_{\text{grow}}/t_{\text{universe}}$ value is summarized in Table 6. Since we have identical choices for f_L , M_{seed} and f_{active} for all samples, the t_{growth} difference is due to M_{BH} and $L_{\text{bol}}/L_{\text{Edd}}$. The comparison of these values in our and other samples is shown in Figure 40. For Netzer's and Shemmer's sample, we calculated $t_{\text{grow}}/t_{\text{universe}}$ value by using Eq.(6.2) by adopting recalculated M_{BH} and Eddington ratio in Section 5.2. (1) If $t_{\text{grow}}/t_{\text{universe}} < 1$, then the measured M_{BH} can be reproduced with the estimated mass accretion rate. On the other hand, (2) if $t_{\text{grow}}/t_{\text{universe}} > 1$, the measured M_{BH} cannot be reproduced with the estimated mass accretion rate, requiring a more active phase in the past at higher redshift than the QSO's redshift. This means that QSOs are not sufficiently active at the QSO redshift. Most of our sample have less than 1 of $t_{\text{grow}}/t_{\text{universe}}$ values. The range of $t_{\text{grow}}/t_{\text{universe}}$ values for our sample is 0.22–3.52, and most of our sample have similar value as Netzer et al. (2007) (0.45–2.27). While, QSOs in Shemmer et

al. (2004) have systematically smaller $t_{\text{grow}}/t_{\text{universe}}$ values (0.05–0.16) than ours, which could be due to their sample being selected only from luminous sources ($\log \lambda L_{\lambda}(5100) \gtrsim 10^{46} \text{ erg s}^{-1}$). Some of objects, with $t_{\text{grow}}/t_{\text{universe}} > 1$, in our and Netzer’s samples should have experienced a rapidly growing phase in the past, while, Shemmer’s sample and most of our sample are in rapidly growing phase at $z \sim 3$.

Table 7 C IV-based SMBH mass in our QSO sample.

(1)	(2)	(3)
Object ID (SDSS J)	FWHM(C IV)[10^3 km/s]	$\log M_{\text{BH}}[M_{\odot}]$
014619.97–004628.7	2.70 ± 0.15	8.91 ± 0.05
031845.17–001845.3	3.96 ± 0.14	9.25 ± 0.03
072554.52+392243.4	3.39 ± 0.18	9.11 ± 0.05
074939.01+433217.6	2.52 ± 0.07	8.92 ± 0.03
075515.93+154216.6	2.87 ± 0.24	8.78 ± 0.07
075841.66+174558.0	3.37 ± 0.11	9.04 ± 0.03
083700.82+350550.2	3.89 ± 0.30	9.36 ± 0.07
084715.16+383110.0	2.25 ± 0.11	8.87 ± 0.04
094202.04+042244.5	3.32 ± 0.10	9.49 ± 0.03
095735.37+353520.6	7.56 ± 0.55	9.96 ± 0.06
100610.55+370513.8	4.23 ± 0.11	9.42 ± 0.02
111656.89+080829.4	2.81 ± 0.20	9.07 ± 0.06
113002.35+115438.3	6.28 ± 1.38	9.76 ± 0.19
133724.69+315254.5	4.03 ± 0.33	9.34 ± 0.07
133757.87+021820.9	7.39 ± 0.41	9.96 ± 0.03
140745.50+403702.2	4.54 ± 1.75	9.41 ± 0.34
142755.85–002951.1	3.04 ± 0.06	9.20 ± 0.02
150238.38+030228.2	6.45 ± 0.70	9.80 ± 0.09
151044.66+321712.9	5.84 ± 0.61	9.44 ± 0.09
155036.80+053749.9	2.76 ± 0.09	9.12 ± 0.03
155137.22+321307.5	–*	–
155823.22+353252.2	2.05 ± 0.08	8.43 ± 0.04
165523.09+184708.4	9.56 ± 0.59	10.32 ± 0.05
211936.77+104623.9	5.63 ± 0.26	9.53 ± 0.04
213023.61+122252.2	2.52 ± 0.10	9.11 ± 0.03
213455.08+001056.8	6.10 ± 0.41	9.66 ± 0.06
231858.56–005049.6	3.21 ± 0.37	8.87 ± 0.10
234150.01+144906.0	–*	–

Notes. Column (1): Object name. Column (2): FWHM of C IV emission line from SDSS (Shen et al. (2011)). Column (3): C IV-based SMBH mass from SDSS (Shen et al. (2011)).

* For these objects, C IV data are not available in Shen et al. (2011).

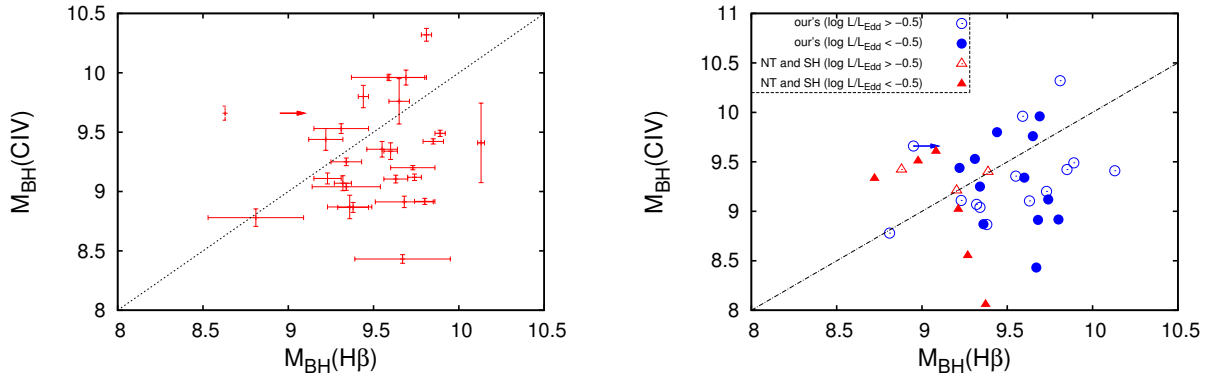


Figure 41 Left: Comparison of the SMBH masses (M_{BH}) estimated from the $\text{H}\beta$ method (abscissa) and the C IV method (ordinate). C IV data are from Shen et al. (2011). Two QSOs are not plotted here due to lack of C IV data. The right arrow means a lower limit. The dashed line represents a 1:1 correspondence. Right: The same plot as the left figure but with the Eddington ratio information added. The open blue circles are targets with high Eddington ratios with $\log(L_{\text{bol}}/L_{\text{Edd}}) > -0.5$. The filled blue circles are those with low Eddington ratios with $\log(L_{\text{bol}}/L_{\text{Edd}}) < -0.5$. The open red triangles correspond to Netzer and Shemmer’s sample which has a high Eddington ratio of $\log(L_{\text{bol}}/L_{\text{Edd}}) > -0.5$. The filled red triangles are those with low Eddington ratios of $\log(L_{\text{bol}}/L_{\text{Edd}}) < -0.5$. For two QSOs in our sample and five QSOs in Netzer and Shemmer’s sample, C IV data are not available in Shen et al. (2011). The right arrow indicates a lower limit. We find that samples with high Eddington ratios appear to be distributed slightly in the upper-left side compared to those with low Eddington ratios which distribute in both the upper-left and lower-right sides.

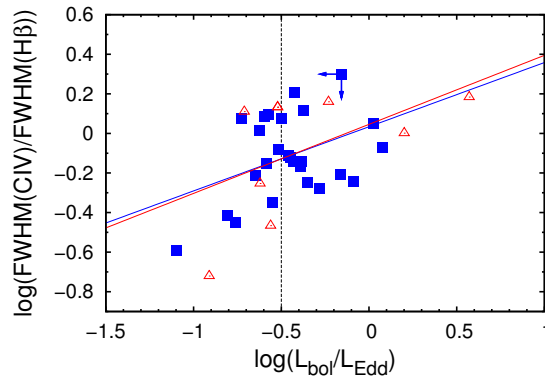


Figure 42 Relationship between Eddington ratio (abscissa) and the $\text{FWHM}(\text{C IV})$ to $\text{FWHM}(\text{H}\beta)$ ratio (ordinate). The filled blue boxes show our sample, and the open red triangles show the sample of Netzer et al. (2007) and Shemmer et al. (2004). Two QSOs in our sample and five QSOs in Netzer and Shemmer’s sample are not plotted here because C IV data are not available in Shen et al. (2011). The blue line represents the best fit for our sample only. The red line shows the best fit for combined samples (ours, Netzer’s, and Shemmer’s). Arrows mean upper limits. The dashed line represents the border between the high and low Eddington ratios in Figure 41.

7 Imaging Observation and Data Reduction

We estimate host galaxy spheroidal masses for our target QSOs by imaging observation.

7.1 Near-infrared imaging observation and noise sources

As mentioned in section 3, the background emission is strong in the near-infrared (Figure 15), compared to the optical wavelength range, and NDR and COADD methods are also employed for detector read-out for imaging observations as well.

The background is usually much brighter than science targets and has time variability. The brightness and gradient in the FOV could change in individual frames taken at different times. In order to remove the time varying background emission from raw imaging data, we take images with slightly shifting target positions in each image. This observation method is called "dithering" (Figure 43). Dithering is also useful to eliminate effects of bad pixels on the detector. Then we compare and adjust the median value of background emission, and subtract them. As a result of these procedures, only signals from science targets can be extracted. After shifting target position and average combining, we obtain final images of the science targets.

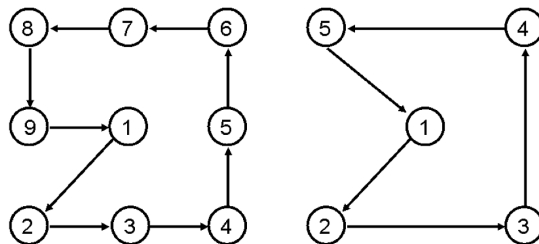


Figure 43 Typical 9 points (left) and 5 points (right) dithering patterns used for IRCS imaging observations.

Raw imaging data include noise sources. For example, pixel count value $RAW(x, y, t)$ of raw data observed at time of t , consists of the following components,

$$RAW(x, y, t) = f(x, y) \{OBJ(x, y, t) + SKY(x, y, t)\} + DARK(x, y) \quad (7.1)$$

where, $OBJ(x, y)$ is signal from object, $DARK(x, y)$ is dark current from detector, $f(x, y, t)$ is a weighting function that represents non-uniformity of sensitivity, and $SKY(x, y, t)$ is background

emission such as thermal emission from Earth’s atmosphere, telescope, and observational instrument. *OBJ* and *SKY* are function of t , that represents time variations of seeing, atmospheric transmissivity, and the background radiation. The time variation of *SKY* in near-infrared is large compared to the optical, while dark and flat are not significantly changed through a night, for IRCS imaging observations.

7.2 Our Observation

The near-infrared imaging observations for the targets whose spectroscopic observations had been done, were carried out using the IRCS instrument with AO188 on Subaru Telescope (8.2 m). To obtain spheroidal stellar mass (M_{spheroid}) of QSO host galaxy, AGN contamination has to be subtracted accurately from original target image, requiring high spatial resolution imaging observation. As mentioned in Section 1, since imaging observation using 8 m ground-based telescopes with Adaptive Optics (AO) is better than non-cryogenic space based instrument in terms of K -band sensitivity, we use Subaru telescope with AO system. By using AO188 on the Subaru telescope, we can usually get $0''.1$ to $0''.2$ of image size at K' -band. That means we can resolve less than 2 kpc at $z \sim 3$ which is a high enough resolution for our study to resolve QSO host galaxy. However, even with AO, there remains a seeing halo, residual of AO correction. Since this component is spatially extended and we could misestimate spheroidal stellar luminosity (L_{spheroid}), the seeing halo component should not be ignored in fitting procedure (see Section 8).

We observed targets at $J(1.25 \mu\text{m})$ - and $K'(2.12 \mu\text{m})$ -band, to determine accurate Mass-to-Light (M/L) ratio (details in Section 8.3). In most of previous studies, M/L was assumed from single band imaging observation for simplicity, however, it was the cause of large uncertainty on M_{spheroid} estimate, because the M/L ratio changes depending on the age of galaxy stellar population. For accurate spheroidal stellar mass estimate, our observation covers K' - and J -band corresponding to around 4000\AA break in the rest frame, which is a good indicator of mean age of galaxy stellar population.

Error budgets for our study are estimated as follows.

1. Accuracy of apparent J - and K' -bands magnitude ~ 0.1 mag (based on our observational data), and that of M/L ratios ~ 0.2 dex (based on the uncertainty of rest-frame U-V color; Bell et al. (2003); Borch et al. (2006)), resulting in the final M_{spheroid} accuracy of ~ 0.26 dex. PSF subtraction error is expected to be smaller than M/L error.

2. The BH mass(M_{BH}) estimated via $H\beta$ widths and L_{5100} has a 0.22 dex scatter around the M_{BH} based on reverberation mapping (Wandel et al. (1999), described as in section 5.3, scatter in their figure 2).

3. In total, we can measure $M_{\text{BH}}/M_{\text{spheroid}}$ with ~ 0.33 dex accuracy for each object. If we use only K' -band data, the error will be ~ 0.6 dex (due to assumption of M/L) which cannot

distinguish various $M_{\text{BH}}/M_{\text{spheroid}}$ evolution models in Figure 3. Therefore, it is very important to obtain both J - and K' -band data.

With the adopted method for M_{BH} and M_{spheroid} estimations, we can directly compare $M_{\text{BH}}/M_{\text{spheroid}}$ at $z \sim 3$ with those from low- z data set (Dunlop et al. (2003); Jahnke et al. (2004a)) in almost the same manner (i.e., determinations of M_{spheroid} using multi-color imaging and M_{BH} using $\text{H}\beta$ emission lines), which minimizes systematic errors.

Our imaging observations were carried out from May 2012 to Sep 2015. Imaging data of nine targets were obtained with J - and K' -band in the IRCS 52-mas mode. The target data were taken with 9 points dithering and the standard star data were taken with 5 points dithering. There are two modes for AO observation; natural guide star (NGS) mode, and laser guide star (LGS) mode. For the NGS mode, there should be a bright nearby star ($R = 16.5$ or brighter) within $30''$ from the target, and the bright star is used for correcting the blurred PSF due to Earth's atmosphere. For the LGS mode, a faint tip-tilt star ($R=18.0$ or brighter) is required within $60''$ from the target. The tip-tilt star is used to correct for the low-order tip-tilt and focus modes, and artificial laser guide star is launched for measuring high-order atmospheric turbulence. We used the NGS mode for 4 objects in J - and K' -band. Others were observed in LGS mode (Table 8). Seeing size with AO was $\sim 0''.20$ at J -band and $\sim 0''.19$ at K' -band. The exposure time were typically 7000 s for J -band, and 6000 s for K' -band, respectively. The details of the observations are summarized in Table 8.

7.3 Data reduction

The following is the steps to extract these noise sources from raw data, which are similar to spectroscopic data reduction.

- Making flat frame
- Flat fielding
- Making sky frame (the background radiation) and subtraction
- Measuring offset
- Combining frames

In K' -band, background radiation is bright enough to obtain a self-flat frame with enough S/N for accurate flat fielding. In J -band, we have to use dome flat because the background radiation is faint in J -band to make self-flat frame, even though dome flat includes non-uniform thermal radiation from screen that might cause reducing accuracy of flat fielding. Therefore, for K' -band data, self-flat frame is created from the data including science target (Figure 44, top right), while for J -band, domeflat frames are taken at the end of observation. After flat fielding (Figure 44, bottom left) and background subtraction, we measure the offset occurred by dithering. Then objects' positions are adjusted by shifting images, and all shifted images

are combined with average (Figure 44, bottom right). The same data reduction procedure is carried out for both target data and standard star data, whose magnitude is already known. The standard star data are used for target magnitude estimate by comparing flux of both target and standard star, in the same way as spectroscopic data. All the reduction steps above are carried out automatically by using the data reduction script for IRCS. We measured FWHM of PSF reference star and QSO, and checked their FWHM distribution (Figure 45). Frames having too large FWHM are excluded in the final combined image.

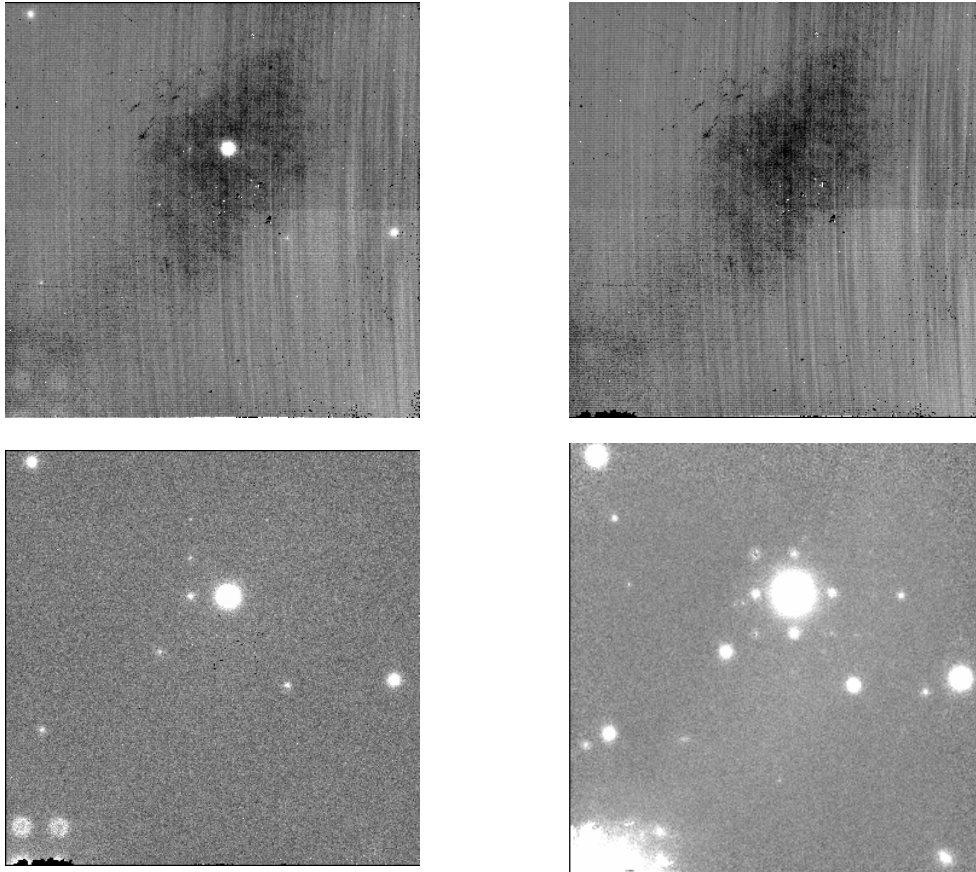


Figure 44 Top left : example of the raw image of J0725 K' -band. Top right : skyflat frame for J0725 K' -band, created by using the target data themselves. Bottom left : example image after flat fielding for J0725 K' -band. Bottom right : average-combined final image of J0725 K' -band.

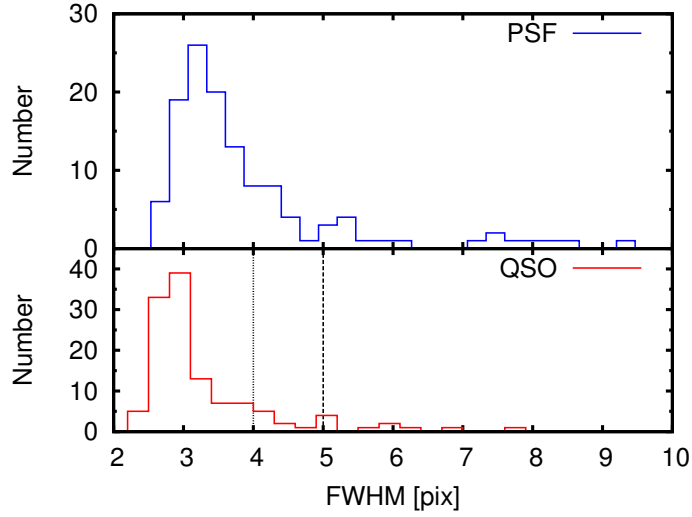


Figure 45 FWHM distribution of J0725 K' -band PSF reference star. For this target, we combined frames with QSO FWHM < 4.0 pix ($= 4.0$ pix $\times 0.052$ "/pix $= 0.21$ " , dotted line in the figure).

Table 8 Imaging Observation Log

(1) Object name	(2) Date (UT)	(3) band	(4) mode	(5) exp time [s]	(6) FWHM limit	(7) FWHM(psf)	(8) mag(AB)
SDSSJ014619.97-004628.7	2015 Sep 19	J	NGS	8280/8640	0.27"	0.22"	18.49
SDSSJ014619.97-004628.7	2013 Jan 14	K'	LGS	4200/5400	0.18"	0.16"	18.32
SDSSJ072554.52+392243.4	2014 Dec 14	J	NGS	6800/12780	0.21"	0.18"	18.70
SDSSJ072554.52+392243.4	2013 Mar 10, 11	K'	NGS	8400/9280	0.21"	0.18"	18.70
SDSSJ084715.16+383110.0	2013 Jan 14, Apr 17	K'	LGS	3280/5760	0.18"	0.16"	17.79
SDSSJ111656.89+080829.4	2015 Jun 9, 10	J	LGS	5520/7020	0.27"	0.22"	17.63
SDSSJ111656.89+080829.4	2013 Apr 18	K'	LGS	5400/5400	0.18"	0.15"	17.50
SDSSJ133757.87+021820.9	2013 May 9	J	NGS	3240/3240	-	0.25"	17.74
SDSSJ133757.87+021820.9	2013 May 9, 2014 Jan 12, Mar 24	K'	NGS	6520/16110	0.23"	0.22"	17.66
SDSSJ140745.50+403702.2	2015 Jun 10	J	LGS	5220/5340	0.21"	0.18"	16.89
SDSSJ140745.50+403702.2	2012 May 21	K'	LGS	6660/7560	0.23"	0.23"	16.53
SDSSJ151044.66+321712.9	2013 Apr 17, 18	J	NGS	6600/10950	0.26"	0.17"	19.26
SDSSJ151044.66+321712.9	2013 Mar 11	K'	NGS	5700/10800	0.22"	0.19"	19.16
SDSSJ155137.22+321307.5	2015 Jun 9, 10	J	LGS	9960/10260	0.23"	0.16"	19.68
SDSSJ155137.22+321307.5	2013 Apr 19	K'	NGS	6600/7020	0.24"	0.18"	19.60
SDSSJ213023.61+122252.2	2015 Jun 9, 10	J	LGS	6660/10260	0.21"	0.20"	17.32
SDSSJ213023.61+122252.2	2012 May 21	K'	LGS	2740/4140	0.18"	0.16"	17.04

Column(1) : Object name. Column (2) : Observation date (UT). Column (3) : Observed band. Column (4) : Observation mode. Column (5) : Exposure time. (Total exposure time of the final combined image)/(Total exposure time). Column (6) : FWHM limit value used for combining frames. Column (7) : FWHM of PSF image. Column (8) : Total magnitude.

8 Imaging Analysis and Result

To estimate the spheroidal mass (M_{spheroid}), we first decompose the AGN and host galaxy to estimate the flux from the host galaxy. After that, we multiply spheroid luminosity by M/L ratio, and then we can finally obtain M_{spheroid} . Decomposition of spheroidal and AGN components is carried out by 2D fitting using GALFIT (Peng et al. (2002)).

8.1 PSF fitting

An AGN bright glare is much brighter in surface brightness than diffuse host galaxy emission, therefore we have to carefully subtract the AGN bright glare. AGN radiation can be assumed as a point source, same as a star, and radiation from a point source is expressed as a point spread function (PSF). In our analysis, we assume that PSF consists of 2 components, Gaussian and Moffat functions. Gaussian corresponds to AO core, which is the light corrected by AO, while Moffat describes a seeing halo, which is the light not corrected by AO. The Gaussian shape should be varied in a FOV because AO correction depends on distance from a guide star and Earth's atmospheric condition. On the other hand, since seeing halo is extended with natural seeing size, Moffat shape does not significantly change in a FOV. Thus, firstly we fit PSF reference star to determine Moffat shape, and then we can use the same Moffat parameter as PSF reference star to the target. Therefore, PSF fitting is one of main sources that affects final M_{spheroid} error.

We used 50×50 ($2.6'' \times 2.6''$) pix size of image around the PSF reference star in the combined image (Figure 44, bottom right). PSF reference star was fitted with three components, Gaussian for AO core, and Moffat for seeing halo, and Sky residual. Gaussian profile is defined as follow,

$$\text{Gaussian} : \Sigma(r) = \Sigma_0 \exp\left(\frac{-r^2}{2\sigma^2}\right), \quad (8.1)$$

where $\text{FWHM} = 2.355\sigma$, while, Moffat profile is defined as

$$\text{Moffat} : \Sigma(r) = \frac{\Sigma_0}{[1 + (r/r_d)^2]^n}, \quad (8.2)$$

where, n is power law index, and

$$r_d = \frac{\text{FWHM}}{2\sqrt{2^{1/n} - 1}}. \quad (8.3)$$

Sky residual was estimated before fitting and the value was fixed. The fitting result is largely affected if sky residual is ignored in the fitting, particularly when it remains. (see Appendix

B). An example of the best fit parameters are summarized in Table 9, and best fit model and residual images are shown in Figure 46.

Table 9 J1510 K' -band image PSF reference star fitting result

	Gaussian		Moffat
position x	720.8479	position x	720.8708
position y	310.9843	position y	310.9938
integral magnitude	20.4772	integral magnitude	19.3613
FWHM[pix]	4.3812	FWHM[pix]	11.0077
axis ratio(b/a)	0.7926	Moffat power law index	1.9343
position angle (PA)	22.9808	axis ratio(b/a)	0.8532
		position angle (PA)	17.1767

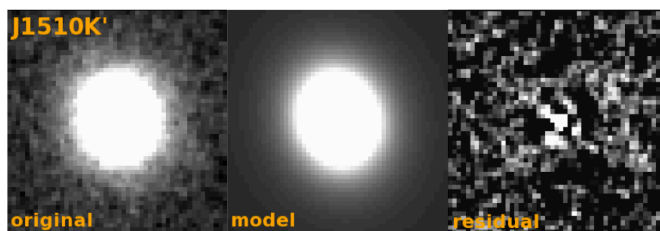


Figure 46 Fitting result. Left : original PSF reference star image. Middle : best fit PSF model image. Right : residual image (original-model).

8.2 QSO fitting

Next, we fit a target image with four components, Gaussian + Moffat + Sersic + Sky.

8.2.1 QSO fitting method

Sersic profile is defined as,

$$\text{Sersic} : \Sigma(r) = \Sigma_e \exp(-\kappa[(r/r_e)^{1/n} - 1]), \quad (8.4)$$

where r_e is the effective radius of the galaxy, Σ_e is the surface brightness at r_e , n is the sersic index, and κ is coupled to n such that half of the total flux is always within r_e . For $n \gtrsim 2$, $\kappa \approx 2n - 0.331$, at low n , $\kappa(n)$ flattens out toward 0.

In the QSO fitting, separating Moffat and Sersic components is very difficult because both are spatially extended. Moreover, when sky component is added as a free parameter, the three components (Moffat, Sersic, and Sky) are degenerated each other and decomposition is getting more difficult. Therefore, we here suggest our original fitting method that gives a constraint

on magnitude difference between Gaussian and Moffat components by using a relation between core-to-halo ratio and distance from a NGS or LGS. In our method, core-to-halo ratio (S) is defined as

$$S = I_g / (f_g + f_m) \quad (8.5)$$

where, I_g is a peak value of Gaussian, f_g and f_m are flux of Gaussian and Moffat components, respectively.

$$I_g \propto f_g / (q_g * \text{fwhm}_g^2) \quad (8.6)$$

where q_g is axis ratio, and fwhm_g is FWHM of Gaussian components, respectively. Therefore,

$$S \propto 1 / (q_g * \text{fwhm}_g^2) (1 + f_m / f_g). \quad (8.7)$$

By using distance r from a NGS or LGS, strehl ratio can also be expressed as follows (Beckers (1993)),

$$S = S_0 \exp(-(r/\theta_0)^{5/3}) \quad (8.8)$$

where, θ_0 is isoplanatic angle and S_0 is core-to-halo ratio at the location of the guide star. Those are changed depending on the sky turbulence condition. When S is large, core-to-halo ratio can be approximated by strehl ratio.

Eq. (8.8) predicts that objects closer to NGS/LGS have larger strehl ratio. When θ_0 is large, PSF shape does not vary significantly in a FOV. On the other hand, when θ_0 is small, degradation of AO correction is severe as a function of the distance from guide star. Our analysis of the globular cluster image actually shows clear difference of strehl ratios within the same FOV depending on the distance from the NGS (see Appendix B.2 Figure 87). This is the reason why we do not simply employ the same PSF shape from the PSF reference star to the target QSO in our fitting method.

Now, the core-to-halo ratio of the PSF reference star is known from the GALFIT fitting result. Given core-to-halo ratio of PSF reference star and Eq. (8.8), target QSO's core-to-halo ratio can be estimated at a certain θ_0 . Then, magnitude difference between Gaussian and Moffat can be estimated by using the estimated QSO's core-to-halo ratio and Eq (8.7), for a parameter set of q_g and fwhm_g . To search for the best parameter set of q_g , fwhm_g , and θ_0 , we change those values within the range of 0.7–1.3 times of initial q_g , 0.6–1.2 times of initial fwhm_g , and $10'' < \theta_0 < 100''$, respectively. This method is described in Figure 47.

Since the fit should be converged to the best fit parameter at plausible parameter set of q_g , fwhm_g and θ_0 , we plot χ^2 map, and take the parameter set of q_g , fwhm_g and θ_0 where χ^2 shows the minimum value, as the best fit parameter.

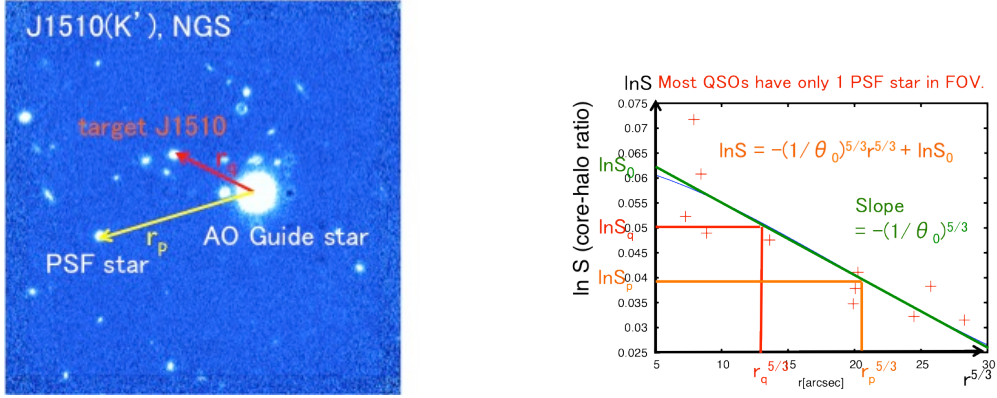


Figure 47 new method

Following is the actual fitting procedures.

1. Estimation of the sky residual.

Since fit does not converge when sky component is free parameter, sky residual value is estimated in advance around QSO, and the value is fixed.

2. Fit QSO with three components (Gaussian + Moffat + Sky)

Gaussian : free parameter

Moffat : position and magnitude are free, other parameters are fixed to the same parameters as PSF reference star fitting result.

Sky : fixed in step 1.

3. Set initial parameters using fitting result at step 2, and then fit QSO with four components (Gaussian + Moffat + Sersic + Sky).

constraint1 : difference between x,y position of Moffat and Sersic from Gaussian are within ± 0.5 pix.

constraint2 : magnitude difference between Gaussian and Moffat are fixed to the value calculated with the above method using the relation of core-to-halo ratio and distance from NGS/LGS.

4. Repeat step 3 with different parameter set of q_g , $fwhm_g$ and θ_0 varied in the range of 0.7–1.3 times of initial q_g , 0.6–1.2 times of initial $fwhm_g$, and $10'' < \theta_0 < 100''$, respectively (when q_g , $fwhm_g$ and θ_0 are changed, magnitude difference in step 3 will also be changed (Eq. 8.5 to 8.8)). Plot χ^2 map (Figure 50) to find minimum.

5. Adopt the fitting result with the parameter set of q_g , $fwhm_g$ and θ_0 where χ^2 shows the minimum value, as the best fit parameter.

As shown in Figure 47, when r_p (the distance between PSF reference star and NGS/LGS) is almost the same as r_q (the distance between QSO and NGS/LGS), our method does not work because the slope in Figure 47 (right) cannot be specified. In such case, we assume the same core-to-halo ratio for target as PSF reference star. For the LGS observations, LGS position is moved with dithering (Figure 48), because LGS is located at the sodium layer in the Earth's mesosphere. We adopt the center of the LGS position distribution as the LGS position in

the combined frame (Figure 49). Therefore, we also assume the same core-to-halo ratio as PSF reference star when the difference between r_p and $r_q (= r_p - r_q)$ is smaller than the LGS position distribution. The size of LGS position distribution and distances from NGS/LGS is summarized in Table 10.

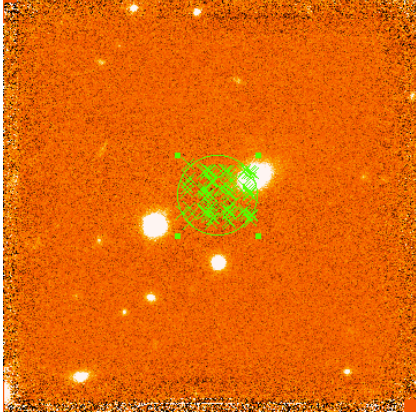


Figure 48 LGS position distribution of J1116 J -band data, due to dithering.

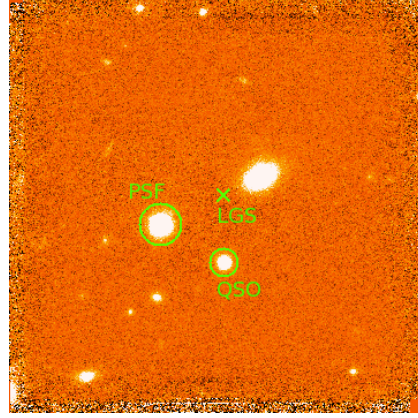


Figure 49 The combined image of J1116 J -band. The center of LGS position distribution in Figure 48 is adopted.

Table 10 distance from NGS/LGS

(1) Object name	(2) band	(3) mode	(4) LGS dist size	(5) r_p	(6) r_q	(7) θ_0
SDSSJ014619.97-004628.7	J	NGS	-	0"	27.80"	80"
SDSSJ014619.97-004628.7	K'	LGS	6.92"	12.38"	15.89"	-
SDSSJ072554.52+392243.4	J	NGS	-	13.77"	11.33"	-
SDSSJ072554.52+392243.4	K'	NGS	-	13.73"	11.34"	-
SDSSJ084715.16+383110.0	K'	LGS	7.62"	5.35"	1.43"	-
SDSSJ111656.89+080829.4	J	LGS	5.95"	10.40"	9.92"	-
SDSSJ111656.89+080829.4	K'	LGS	6.18"	0.38"	11.28"	30"
SDSSJ133757.87+021820.9	J	NGS	-	29.74"	18.38"	30"
SDSSJ133757.87+021820.9	K'	NGS	-	29.72"	18.38"	40"
SDSSJ140745.50+403702.2	J	LGS	5.20"	12.76"	12.55"	-
SDSSJ140745.50+403702.2	K'	LGS	10.92"	12.63"	7.30"	-
SDSSJ151044.66+321712.9	J	NGS	-	24.72"	13.84"	60"
SDSSJ151044.66+321712.9	K'	NGS	-	24.71"	13.84"	30"
SDSSJ155137.22+321307.5	J	LGS	5.84"	6.77"	4.43"	-
SDSSJ155137.22+321307.5	K'	NGS	-	15.45"	20.23"	90"
SDSSJ213023.61+122252.2	J	LGS	6.49"	16.28"	20.01"	-
SDSSJ213023.61+122252.2	K'	LGS	7.97"	21.47"	24.19"	80

Column(1) : Object name. Column (2) : band. Column (3) : observation mode. Column (4) : the size of LGS position distribution for LGS observation. Column (5) : distance between PSF and NGS/LGS. Column (6) : distance between QSO and NGS/LGS. Column (7) : θ_0 value of the best fit result. "-" means that θ_0 could not be specified because the distance from NGS/LGS was almost same and therefore strehl ratio of PSF was applied for QSO.

Figure 50 is an example of χ^2 map obtained as fitting result.

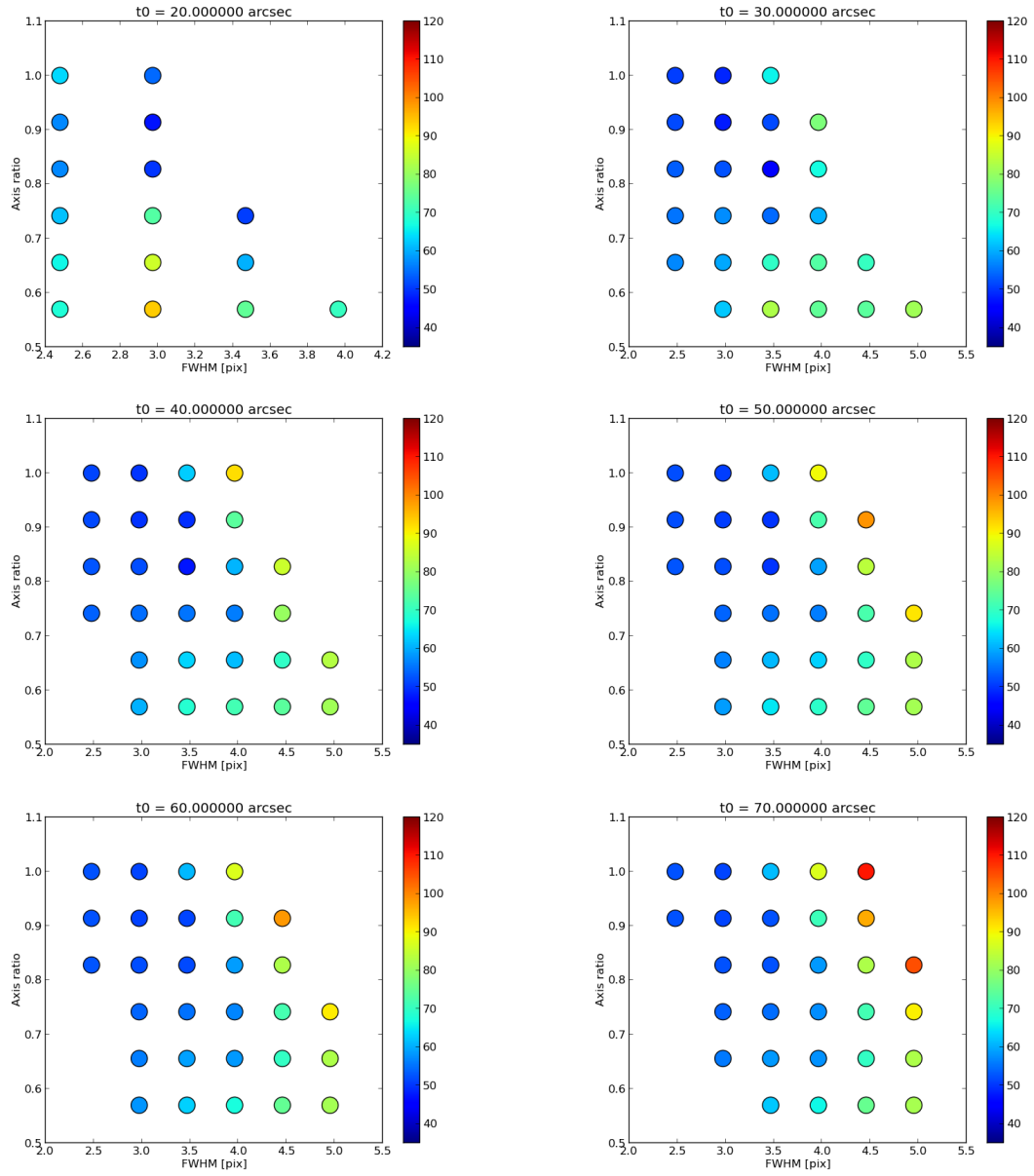


Figure 50 χ^2 map obtained by fitting of J1510 K' -band data. X-axis is FWHM [pix], and Y-axis is axis ratio. The color bar represents χ^2 value (blue=small, red=large). From top left figure to bottom right figure, θ_0 ["] = 20, 30, 40, ..., 90. We adopted fitting result with the parameter set of q_g , $fwhm_g$ and θ_0 where χ^2 shows the minimum value, as the best fit parameter. For this object, $\theta_0=30''$, $fwhm_g=3.47$ pix, and $q_g=0.83$.

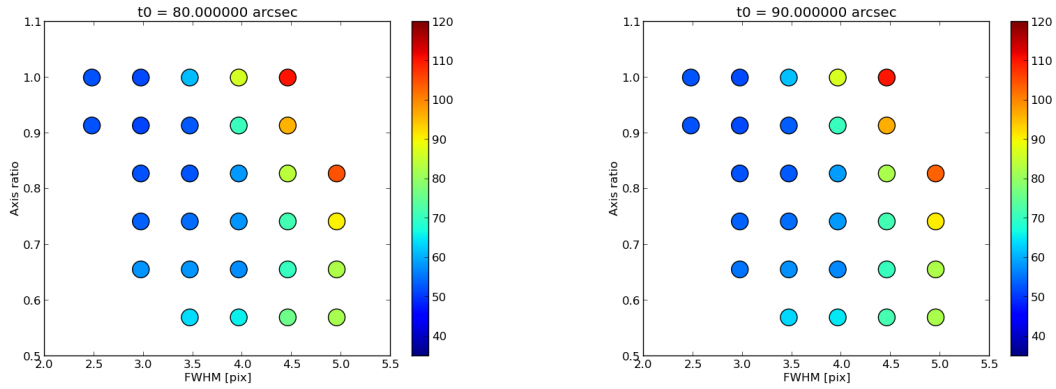


Figure 50 continued.

8.3 M_{spheroid} Estimation

Figure 51 shows example images of QSO fitting results. Images for the all QSOs are shown in Appendix C.

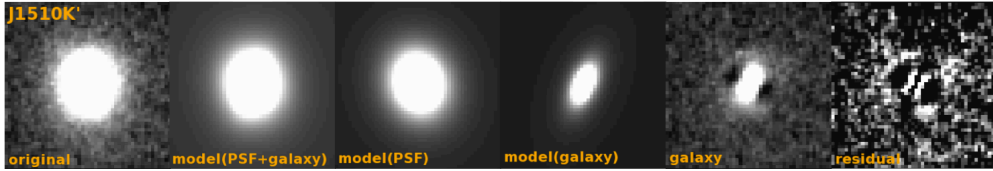


Figure 51 Fitting result image of J1510 K' -band. From left to right, original QSO image, best fit model (PSF+galaxy) image, best fit PSF model image, best fit galaxy model image, galaxy image (original – best fit PSF model image), and residual image (original – model(PSF+galaxy) image).

We obtained the value which is around the optimal value, from the fitting by GALFIT. We here employed Markov Chain Monte Carlo (MCMC) methods to obtain more optimal values and uncertainties of each (Gaussian, Moffat, and Sersic) components. The MCMC method is a general simulation method for sampling from prior distributions and computing posterior quantities of interest. Each sample depends on the previous one, hence the notion of the Markov chain. A Markov chain is a sequence of random variables, $\theta^1, \theta^2, \dots$ for which the random variable θ^I depends on all previous θ s only through its immediate predecessor θ^{I-1} . We can think of a Markov chain applied to sampling as a mechanism that traverses randomly through a target distribution without having any memory of where it has been. Where it moves next is entirely dependent on where it is now. Monte Carlo, as in Monte Carlo integration, is mainly used to approximate an expectation by using the Markov chain samples.

We assumed normal distribution for positions and sky, and uniform distribution for other

parameters as their initial distributions. Also, the value derived from the GALFIT fitting as described in Section 8.2, was adopted as the initial value. Figure 52 is an example probability map of Sersic components as a result of MCMC simulation.

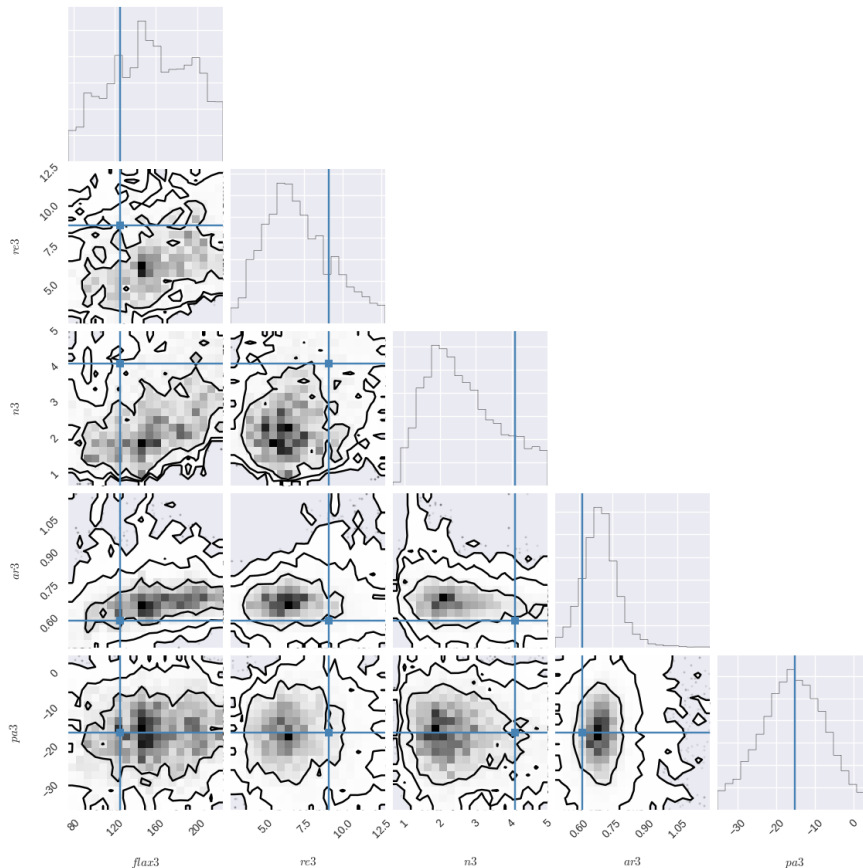


Figure 52 Probability map for Sersic component of J1510 K' -band. Flux3 = flux, ar3 = axis ratio, n3 = Sersic index, re3 = effective radius, and pa3 = position angle of Sersic component. Each line of the contours shows 1σ , 2σ , and 3σ towards the outside. Blue lines correspond to the best fit values by GALFIT, and is also initial value for MCMC.

We adopted Sersic flux obtained as a result of MCMC simulation for the final calculation of M_{spheroid} .

Finally, we here derive M_{spheroid} by multiplying L_{spheroid} by M/L ratio. Firstly, we calculate V -band absolute magnitude $M_{V,AB}$ from apparent K' -band magnitude $m_{K',AB}$ obtained by fitting, as follows

$$M_{V,AB} = m_{K',AB} + 2.5 \log(1 + z) - [5 \log(d_L) - 5] \quad (8.9)$$

where, d_L is luminosity distance. Since K' -band in observed frame is corresponding to V -band in rest frame at $z \sim 3$, we did not consider about k -correction. Therefore,

$$L_V/L_\odot = 10^{-0.4(M_{V,AB} - M_{\odot,V,AB})}, \quad (8.10)$$

where $L_{\odot} = 3.85 \times 10^{33}$ [erg/s] is solar luminosity, and $M_{\odot,V,AB}=4.85$ is V -band solar absolute magnitude (AB).

We employed the relation between M/L versus $(U - V)_{\text{rest}}$ color derived by Akiyama et al. (2008) for $z \sim 3$ LBG, to calculate M/L ratio for our targets.

$$\log(M_*/L_V) = 0.95(U - V)_{\text{rest,Vega}} - 0.50. \quad (8.11)$$

Since they use Salpeter IMF, the above equation is re-scaled for Chabrier IMF. We calculated $(U - V)_{\text{rest}}$ and $(J - K)_{\text{obs}}$ relation appropriate for $z \sim 3.25$ corresponding to the average redshift of our targets. We adopted Bruzual & Charlot (2003) models to produce the $(U - V)_{\text{rest}}$ and $(J - K)_{\text{obs}}$ colors of stellar populations appropriate for $z = 3.25$. We considered various star formation histories; single stellar populations (SSP), constant star formation (CSF), and exponentially decreasing star formation models with timescale of 10 Myr to 1Gyr. The calculation was performed with ages up to 1.5 Gyr, and $Z = Z_{\odot}$ of metallicity was considered. We employed Chabrier (2003) IMF. Figure 53 plots the $(U - V)_{\text{rest,Vega}}$ and $(J - K')_{\text{obs,AB}}$ obtained by our calculation.

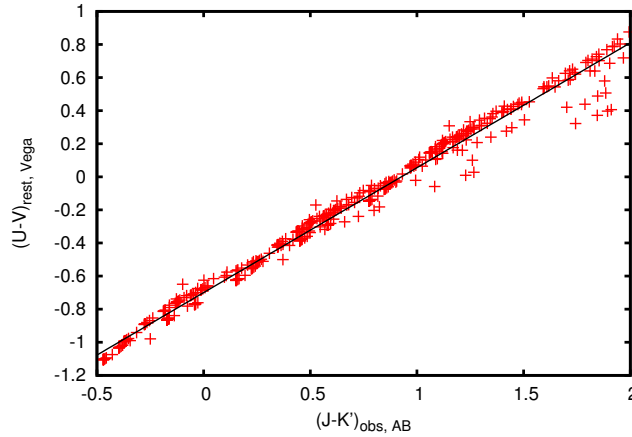


Figure 53 The relation between $(U - V)_{\text{rest}}$ and $(J - K)_{\text{obs}}$ calculated appropriate for our target. Black solid line is the fitting result.

We therefor employ the relationship derived by our calculation, as

$$(U - V)_{\text{rest,Vega}} = 0.755(J - K')_{\text{obs,AB}} - 0.700. \quad (8.12)$$

By combining Eq (8.11) and (8.12), we obtain

$$\log(M_*/L_V) = 0.717(J - K')_{\text{obs,AB}} - 1.165. \quad (8.13)$$

We also adopt the same M/L standard deviation of 0.25 dex, following Akiyama et al. (2008).

With the fitting result and above equations, estimated nuclear and host magnitude in both J - and K' -band is listed in Table 11.

Table 11 Nucleus and host magnitudes

Object name	<i>J</i> -band			<i>K'</i> -band		
	nucleus mag _{AB}	host mag _{AB}	total mag _{AB}	nucleus mag _{AB}	host mag _{AB}	total mag _{AB}
SDSSJ0146	18.78	19.91	18.45	18.56	20.46	18.32
SDSSJ0725	18.64	20.88	18.70	18.82	20.65	18.70
SDSSJ0847	-	-	-	18.02	19.87	17.79
SDSSJ1116	18.17	18.50	17.63	-	-	17.50
SDSSJ1337	18.45	18.52	17.74	17.82	19.44	17.66
SDSSJ1407	17.34	18.15	16.89	16.70	18.42	16.53
SDSSJ1510	19.48	20.38	19.26	19.57	19.97	19.16
SDSSJ1551	20.06	20.32	19.68	-	-	19.55
SDSSJ2130	-	-	17.32	-	-	17.04

8.4 Detection Check

Since so far we have not discussed whether the host galaxy is actually detected or not, we check host galaxy detection in this section. MCMC simulation did not converge for some objects, possibly because their host galaxies were not detected. We here summarize host galaxy detection of our sample. To judge whether QSO host galaxy is detected or not, we first check fitting results of PSF reference star and QSO with Gaussian + Moffat. We consider that if QSO host galaxy is detected, χ^2 of QSO fitting only with Gaussian + Moffat profiles would be larger than PSF fitting. χ^2 values are listed in Table 12. Also, in the radial profile plot, residual (observed data – best fit model) should be different shape of profile between both fitting result, because galaxy components can not be perfectly fitted by 2 (Gaussian+Moffat) components. Figure 54 is an example radial profile. The radial profiles for all targets are shown in Appendix C. Additionally, we consider the result of whether MCMC simulation is converged or not. Our detection check result is summarized in Table 12. Derived properties of each object are summarized in Table 13. For the objects whose hosts were not detected or MCMC simulation did not converge in *K'*-band, lower/upper limit was calculated. For the object that was observed in only *K'*-band, we assumed possible allowable M/L ratio range.

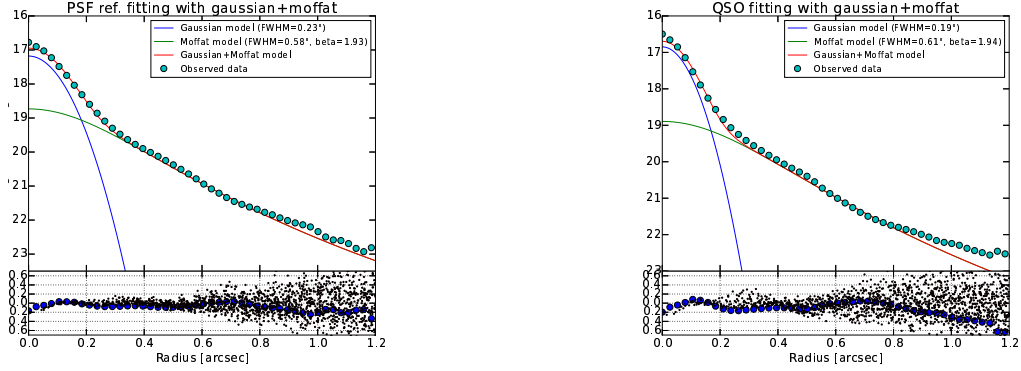


Figure 54 Radial profiles of J1510K. Left : PSF reference star fitting with Gaussian + Moffat. Right : QSO fitting with Gaussian + Moffat. Dots represent observed data, blue line shows Gaussian profile, green line shows Moffat profile, and red line shows Gaussian + Moffat profile. Lower Panels of both plots are residual (observed data – model) profile.

Table 12 Detection Check

(1) Object name	(2) band	(3) mode	(4) exp time [s]	(5) χ^2 PSF	(6) χ^2 QSO	(7) χ^2	(8) radial profile	(9) convergence	(10) detection
SDSSJ014619.97-004628.7	J	NGS	8280	0.0234	0.1022	yes	yes	yes	detected
SDSSJ014619.97-004628.7	K'	LGS	4200	0.0821	0.1457	yes	yes	yes	detected
SDSSJ072554.52+392243.4	J	NGS	6800	0.0909	0.1256	yes	yes	yes	detected
SDSSJ072554.52+392243.4	K'	NGS	8400	0.0391	0.0667	yes	yes	yes	detected
SDSSJ084715.16+383110.0	K'	LGS	3280	0.1093	0.0781	no	?	yes	less convincing
SDSSJ111656.89+080829.4	J	LGS	5520	0.0533	0.0823	yes	no	yes	less convincing
SDSSJ111656.89+080829.4	K'	LGS	5400	0.0724	0.0408	no	no	no	not detected
SDSSJ133757.87+021820.9	J	NGS	3240	0.2722	0.1813	no	no	yes	less convincing
SDSSJ133757.87+021820.9	K'	NGS	6520	0.0468	0.0315	no	?	yes	less convincing
SDSSJ140745.50+403702.2	J	LGS	5220	0.0794	0.0976	yes	no	yes	less convincing
SDSSJ140745.50+403702.2	K'	LGS	6660	0.0136	0.0303	yes	no	yes	less convincing
SDSSJ151044.66+321712.9	J	NGS	6600	0.2915	0.4733	yes	?	yes	less convincing
SDSSJ151044.66+321712.9	K'	NGS	5700	0.0891	0.1336	yes	yes	yes	detected
SDSSJ155137.22+321307.5	J	LGS	9960	0.0256	0.1029	yes	yes	yes	detected
SDSSJ155137.22+321307.5	K'	NGS	6600	0.0137	0.1022	yes	yes	no	less convincing
SDSSJ213023.61+122252.2	J	LGS	6660	0.0341	0.0583	yes	no	no	less convincing
SDSSJ213023.61+122252.2	K'	LGS	2740	0.0441	0.0626	yes	no	no	less convincing

Column(1) : Object name. Column (2) : Band. Column (3) : Observation mode. Column (4) : Exposure time. Column (5) : χ^2 of PSF reference star fitting. Column (6) : χ^2 of QSO fitting. Column (7) : Result of χ^2 check. Column (8) : Result of radial profile check. Column (9) : Result of MCMC simulation convergence. Column (10) : Final result of detection check.

Table 13 Observed and derived properties related to QSO host galaxies, and $M_{\text{BH}}/M_{\text{spheroid}}$ ratio at $z \sim 3$.

(1)	(2)	(3)	(4)	(5)	(6)	(7)	(8)	(9)	(10)	(11)
Object name	z	$\text{mag}(J)$	$\text{mag}(K')$	host M_V	$\log L_V$	$J - K'$	$\log M/L$	$\log M^*$	$\log M_{\text{BH}}$	$\log M_{\text{BH}}/M_*$
SDSSJ0146	3.17	19.91	20.46	-25.16	12.01	-0.548	-1.56	10.45	9.68 ± 0.17	-0.77 ± 0.34
SDSSJ0725	3.25	20.88	20.65	-25.01	11.94	0.227	-1.00	10.94	9.23 ± 0.08	-1.71 ± 0.30
SDSSJ0847	3.18	-	19.87	-25.75	12.24	-	-1.30 - 0.10	10.94 - 12.34	9.38 ± 0.09	$-2.96 - -1.56$
SDSSJ1116	3.23	18.50	>18.09	> -27.56	<12.96	-	-1.32*	<11.64	9.32 ± 0.05	> -2.32
SDSSJ1337	3.33	18.52	19.44	-26.26	12.45	-0.918	-1.82	10.62	9.59 ± 0.22	-1.03 ± 0.36
SDSSJ1407	3.20	18.15	18.42	-27.22	12.83	-0.271	-1.36	11.47	10.13 ± 0.02	-1.34 ± 0.25
SDSSJ1510	3.48	20.38	19.97	-25.81	12.27	0.406	-0.87	11.39	9.22 ± 0.10	-2.17 ± 0.29
SDSSJ1551	3.18	20.32	>21.44	> -24.18	<11.61	-	-1.32*	<10.29	9.54 ± 0.18	> -0.75
SDSSJ2130	3.26	-	>17.45	> -28.22	<13.23	-	-1.32*	<11.90	9.63 ± 0.07	> -2.27

Column(1) : Object name. Column (2) : redshift. Column (3) : J -band magnitude. Column (4) : K' -band magnitude. For the objects that host was not detected, we calculated upper limit by assuming effective radius = 8 (maximum value obtained by fitting for host detected objects). Column (5) : Host galaxy V -band absolute magnitude. Column (6) : V -band luminosity. Column (7) : $J-K'$ magnitude difference. Column (8) : Decimal logarithm of M/L ratio. For the objects that host was not detected, we adopted average value of host detected objects. Column (9) : Decimal logarithm of M_{spheroid} . For the objects that host was not detected, upper limit was calculated. Column (10) : Decimal logarithm of M_{BH} . Column (11) : Decimal logarithm of $M_{\text{BH}}/M_{\text{spheroid}}$ ratio. For the objects that host was not detected, lower limit was calculated.

8.5 Fitting Accuracy

Our final radial profiles (after MCMC, 3 components (Gaussian, Moffat, and Sersic)) are shown in Appendix D. Here we discuss accuracy of our fitting result. The final radial profiles for some host detected objects show brighter PSF profile than Sersic profile at outer region. We consider that even though PSF is brighter than host galaxy, host galaxy can be detected if it is bright enough. Therefore, we concluded that the host galaxy is detected when χ^2 check and all other detection check are ok. Also, some radial profiles show peaky Sersic profile than PSF, at the center of galaxy. This is because PSF convolution is not carried out for Sersic model, and is not considered in our fitting process. If PSF convolution is carried out, Gaussian profile will be shifted upward in the radial profile and Moffat profile will not be significantly changed, because ratio of Gaussian and Moffat is not fixed. Therefore, we consider that total flux of Sersic component is not largely affected.

J0146

For this objects, χ^2 check result says ok, and radial profile of two components (Gaussian and Moffat) shows that it looks like there remains unfitted component in QSO radial profile for both J - and K' -band data. Also, MCMC simulation converged. Although PSF profile is brighter than Sersic profile in the final radial profile, we concluded that the host galaxy is detected according to our detection check result in both J - and K' -band.

J0725

Our χ^2 check result is ok, and radial profiles show remaining unfitted components at outer radii in QSO radial profile for both J - and K' -band data. Also, MCMC simulation converged. Though this object also shows brighter PSF profile than Sersic profile in the final radial profile in the same way as J0146, we concluded that the host galaxy is detected in both J - and K' -band, following our detection check result.

J0847

This QSO is observed only at K' -band. In our χ^2 check, QSO χ^2 is smaller than PSF χ^2 . Also, according to QSO radial profile, it looks like well fitted with two components. Therefore, the detection of the host galaxy is less convincing even though MCMC simulation converged.

J1116

For J -band data, χ^2 check and MCMC convergence result are ok, however, PSF and QSO radial profiles do not show significant difference. Therefore, host detection in J -band is less convincing. While, K' -band data does not satisfy all the detection checks. The host galaxy in K' -band is not detected.

J1337

In both J - and K' -band, χ^2 check and radial profile check are not satisfied, and only MCMC convergence is ok. Therefore, we concluded that the host galaxy detection for this object is less

convincing in both J - and K' -band.

J1407

For this object, χ^2 check and MCMC convergence result are ok in both J - and K' -band data. However, PSF and QSO radial profiles look almost the same in both bands. Therefore, the host detection of this objects is less convincing in both J - and K' -band.

J1510

For J -band, we concluded that the host detection is less convincing because radial profile check does not show any significant difference, even though other checks are ok. For K' -band, all the checks are satisfied. Although the final radial profile shows the peaky Sersic profile at the center, we consider that total flux of Sersic component is not largely affected as mentioned above. Since M_{spheroid} is estimated mainly based on K' -band luminosity, this object is regarded as a host detected object.

J1551

For J -band, all the checks are cleared. However, K' -band detection is less convincing, because MCMC simulation is not converged. Since M_{spheroid} is estimated mainly based on K' -band luminosity, the host galaxy detection of this object is concluded as less convincing.

J2130

This object cleared χ^2 check and radial profile check in both J - and K' -band data. However, MCMC simulation does not converge. Therefore, we consider the host detection is less convincing for this object, in both J - and K' -band data.

9 $M_{\text{BH}}/M_{\text{spheroid}}$ ratio at $z \sim 3$

Figure 55 is our result of $M_{\text{BH}}/M_{\text{spheroid}}$ estimate for 9 QSOs at $z \sim 3$. Purple filled diamonds show the results of host-galaxy-firmly-detected objects. For the objects whose host galaxy were undetected or MCMC simulation did not converge in K' -band, lower limits are shown as purple open circles with arrows. The objects whose hosts were not very convincing in K' -band, are plotted as purple open circles with error bars. The object that was observed in only K' -band (J0847) is plotted with large error bar. In Figure 56, only host-galaxy-firmly-detected objects are plotted. Figure 57 and Figure 58 show $M_{\text{BH}} - M_{\text{spheroid}}$ relation for our $z \sim 3$ QSOs. Our result shows that $M_{\text{BH}}/M_{\text{spheroid}}$ at $z \sim 3$ is more than ~ 10 times larger ($M_{\text{BH}}/M_{\text{spheroid}}(\text{median}) \sim 0.046$) than the well-known local relation ($M_{\text{BH}}/M_{\text{spheroid}} \sim 0.0015$). By comparing with theoretical models, our result seems not to support the no-evolution model, rather it suggests steeper evolution than the model assuming that AGN outflow plays a major role in $M_{\text{BH}}/M_{\text{spheroid}}$ ratio evolution (e.g, Wyithe & Loeb (2003), Silk & Rees (1998), Figure 3). Schramm et al. (2008) carried out multi-band imaging observation for 3 very bright QSOs at $2 < z < 3$, and derived accurate M_{spheroid} . Their result shows a larger $M_{\text{BH}}/M_{\text{spheroid}}$ ratio, which is almost consistent with our result. However, M_{BH} of their sample were estimated by CIV emission line, which has possibly large uncertainty (Section 6). Additionally, their sample consists of extremely luminous QSOs and the M_{BH} are also large, that might be resulting in larger $M_{\text{BH}}/M_{\text{spheroid}}$ ratio due to a sample bias. We selected fainter QSOs to avoid such a bias, and M_{BH} are estimated from $\text{H}\beta$ emission line which is well calibrated method. Therefore, we consider that our sample is less biased, and is a better sample to discuss $M_{\text{BH}}/M_{\text{spheroid}}$ ratio at high redshift. We will summarize similarity and difference of sample between Schramm et al. (2008) and ours, and discuss the selection bias in Section 9.3.

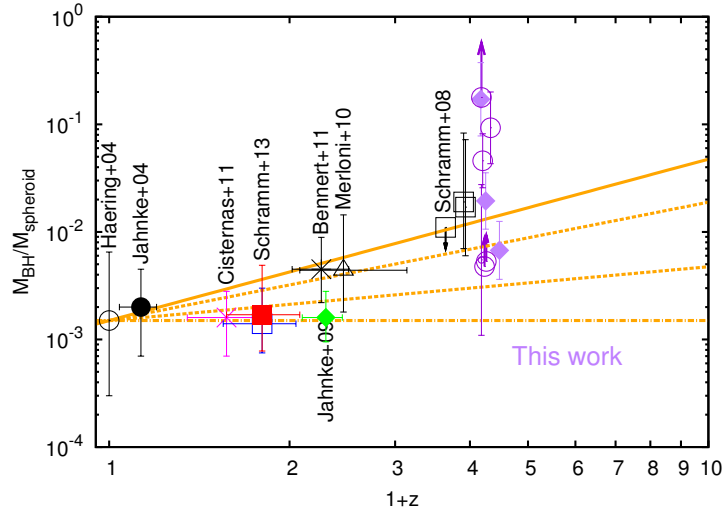


Figure 55 $M_{\text{BH}}/M_{\text{spheroid}}$ ratio for $z \sim 3$ QSOs (purple points). Purple filled diamonds show the results of host-galaxy-firmly-detected objects. For the objects whose host galaxy was undetected or MCMC simulation did not converge in K' -band, lower limit are shown as purple open circles with arrows. The objects whose host was not very convincing in K' -band are plotted as purple open circles with error bars. The object that was observed in only K' -band (J0847) is plotted with large error bar.

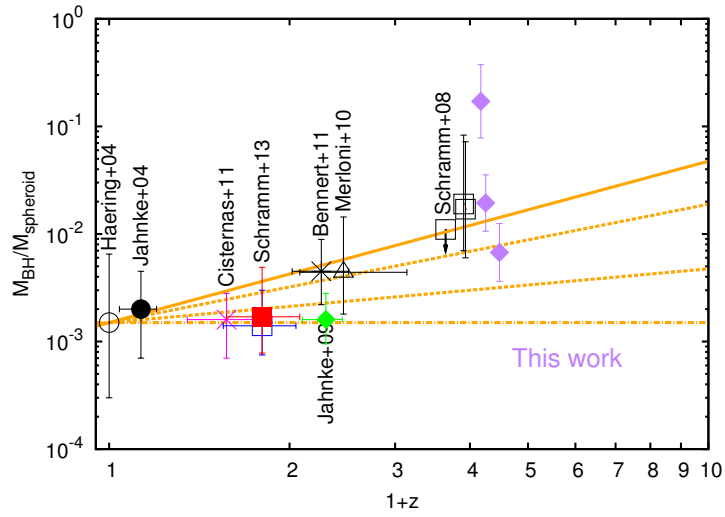


Figure 56 $M_{\text{BH}}/M_{\text{spheroid}}$ ratio for $z \sim 3$ QSOs (purple points) with only host-galaxy-firmly-detected objects.

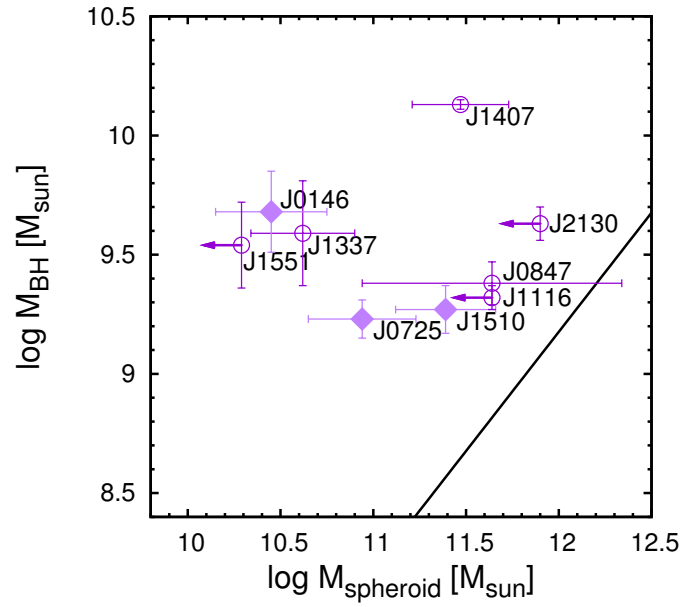


Figure 57 $M_{\text{BH}} - M_{\text{spheroid}}$ relation for our $z \sim 3$ QSOs. Purple filled diamonds show the results of host-galaxy-firmly-detected objects. For the objects whose host galaxy was undetected or MCMC simulation did not converge in K' -band, lower limit are shown as purple open circles with arrows. The objects whose host was not very convincing in K' -band are plotted as purple open circles with error bars. The object that was observed in only K' -band (J0847) is plotted with large error bar. The black solid line shows the local $M_{\text{BH}} - M_{\text{spheroid}}$ relation.

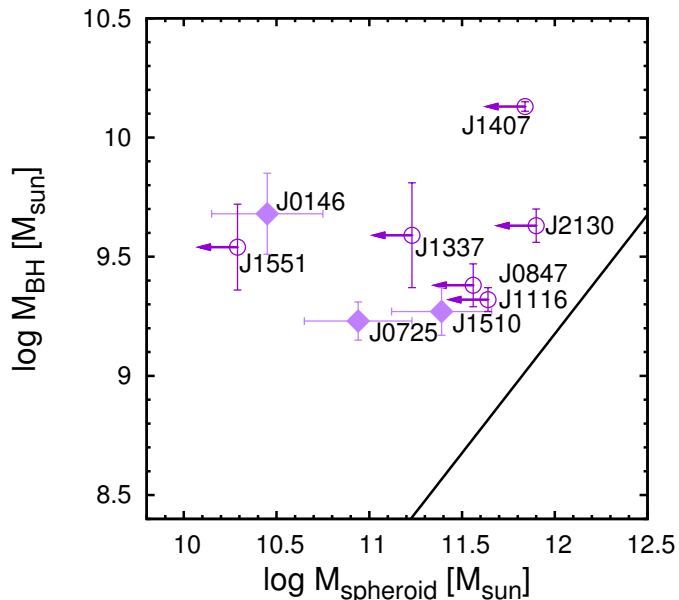


Figure 58 In Figure 57, we simply adopted MCMC result when it converged, regardless of the results of host detection check. In this plot, we assumed non-detection of host galaxies for the all the host-detection-less-convincing objects, and calculated upper limit of M_{spheroid} . All the host-detection-less-convincing objects are plotted with open circles with arrows.

9.1 Comparison with studies at higher redshift

Targett et al. (2012) observed two $z \sim 4$ SDSS QSOs in K' -band with Very Large Telescope (VLT) to obtain their host galaxy properties. Their > 5 hrs integration observation succeeded in detecting $z \sim 4$ QSO host galaxy. They subtracted nuclear light by using scaled PSF observed in the same FOV, and estimated host galaxy luminosity from the PSF subtracted residual light. The host galaxy mass was calculated with assumption of single starburst and extreme cases of star formation epoch ($z_f = 5, 10$). The M_{BH} for the two QSOs were measured from SDSS CIV emission line width. The combination of their host galaxy and black hole mass estimates led $M_{\text{BH}}/M_{\text{spheroid}}=0.024\text{--}0.120$ (re-scaled for Chabrier IMF). Although their host galaxy mass has very large uncertainty due to no-color information and also there might be large uncertainty for M_{BH} due to use of CIV emission line, their result shows higher $M_{\text{BH}}/M_{\text{spheroid}}$ ratios in the similar way to our result.

At even higher redshift, Walter et al. (2004) resolved molecular gas in a QSO host galaxy at $z = 6.42$ with Very Large Array (VLA) observation. They observed CO (3–2) emission and found that molecular gas was clearly extended out to ~ 2.5 kpc and had 65° inclination if the molecular gas concentration formed an inclined disk. With the above values and the assumption

that the molecular gas is gravitationally bound, they derived dynamical mass of $5.5 \times 10^{10} M_{\odot}$. While, its $M_{\text{BH}} = 3 \times 10^9 M_{\odot}$ was derived by Willott et al. (2003) from MgII emission line width. By combining both results, $M_{\text{BH}}/M_{\text{spheroid}}=0.054$ is obtained, which also shows higher $M_{\text{BH}}/M_{\text{spheroid}}$ ratios than the local universe.

Also, Wang et al. (2013) observed CII emission of four $z \sim 6$ QSOs with ALMA, and obtained dynamical mass of 1.3×10^{10} – $1.2 \times 10^{11} M_{\odot}$. Combining with M_{BH} of 1.7×10^8 – $2.8 \times 10^9 M_{\odot}$ roughly estimated from L_{bol} assuming Eddington accretion, they obtained $M_{\text{BH}}/M_{\text{spheroid}}=0.012$ – 0.030 .

9.2 Selection bias for our result

As in Figure 55, many observational studies have found redshift evolution of $M_{\text{BH}}/M_{\text{spheroid}}$ at high redshift. However, there has been discussed that a selection effect alone might be able to account for the apparent $M_{\text{BH}}/M_{\text{spheroid}}$ redshift evolution (e.g., Lauer et al. (2007), Schulze & Wisotzki (2011)). Schulze & Wisotzki (2011) provided comprehensive study of various selection biases that arise due to usage of type I AGN sample to discuss $M_{\text{BH}}/M_{\text{spheroid}}$ redshift evolution;

(1) Luminosity bias

The AGN sample selected based on their luminosity tends to have higher SMBH mass than average, especially if the luminosity limit is high, due to Eddington luminosity (Luminous QSOs need to have a certain level of minimum mass of SMBH to explain their such high luminosity). Also the most massive SMBHs occur more often as rare outliers in galaxies of modest mass than in the rare high-mass galaxies, because galaxy mass function falls rapidly at high-mass end compared to BH mass function. This effect has been also discussed by other studies (e.g., Lauer et al. (2007)). This leads a bias towards higher $M_{\text{BH}}/M_{\text{spheroid}}$ ratio.

(2) Bias from measurement uncertainty

The measurement errors of SMBH mass and spheroidal properties may introduce additional bias with combining selection limit. This uncertain doesn't change a mean $M_{\text{BH}}-M_{\text{spheroid}}$ ratio but leads a large scatter.

(3) AGN evolution bias

The stellar mass function, and the spheroid mass function, are certainly changing with z . Also, AGN population itself strongly evolves, apparent in the evolution of the AGN luminosity function. The AGN distribution function regulates the magnitude of bias, and therefore, redshift evolution of the AGN distribution function will change the expected sample bias with redshift, towards higher $M_{\text{BH}}/M_{\text{spheroid}}$.

(4) Active fraction bias

In the local universe, very high mass SMBHs are commonly quiescent than lower mass SMBH which are often actively mass accreting. Therefore, AGN sample that is in an active phase contains higher fraction of low mass BH. This leads a bias towards lower $M_{\text{BH}}/M_{\text{spheroid}}$ ratio.

The combination of these selection bias can affect the final $M_{\text{BH}}/M_{\text{spheroid}}$ ratio derived by observation. To accurately correct the bias, well-defined probability distribution is required, such as distribution of spheroidal mass, or velocity dispersion, the active fraction as a function of BH mass, active black hole mass function, and Eddington ratio distribution function. Those distributions are well known for the local universe, however, less established for the early universe. Thus there also remains uncertainty on the bias estimation.

With collaboration with A. Schulze (private communication), we obtained expected bias for our sample (Figure 59). The contour represents expected $M_{\text{BH}}/M_{\text{spheroid}}$ distribution with our sample selection bias, and solid line shows the M_{BH} to M_{bulge} relation at the local universe. We plot our M_{BH} and M_{spheroid} value over these contours. We also show the same plot for the sample of Schramm et al. (2008) provided in Schulze & Wisotzki (2011) in Figure 60 as a comparison. The sample of Schramm et al. (2008) is distributed at the center of the contour, therefore their apparent evolution of $M_{\text{BH}}/M_{\text{spheroid}}$ ratio could be explained by bias alone (indicating that the true $M_{\text{BH}} - M_{\text{spheroid}}$ relation could be the same as the local relation). On the other hand, our sample has a significant offset from the center of the contour towards upper-left. Therefore we consider that our result of $M_{\text{BH}}/M_{\text{spheroid}}$ also might contain some bias effect, but the evolution of $M_{\text{BH}}/M_{\text{spheroid}}$ unlikely to be explained only by bias. We consider that our result shows physical evolution of $M_{\text{BH}}/M_{\text{spheroid}}$. Our selection bias should be little smaller than the sample of Schramm et al. (2008) because our sample is less luminous than their sample. We summarize similarity and difference between sample of Schramm et al. (2008) and ours in Table 14. The selection bias of our sample may be smaller, however, even our sample could contain a non-negligible amount of selection bias. Therefore, to ensure our result, fainter and lower Eddington ratio AGN sample might be needed. Subaru HSC QSO survey is expected to find such AGN sample.

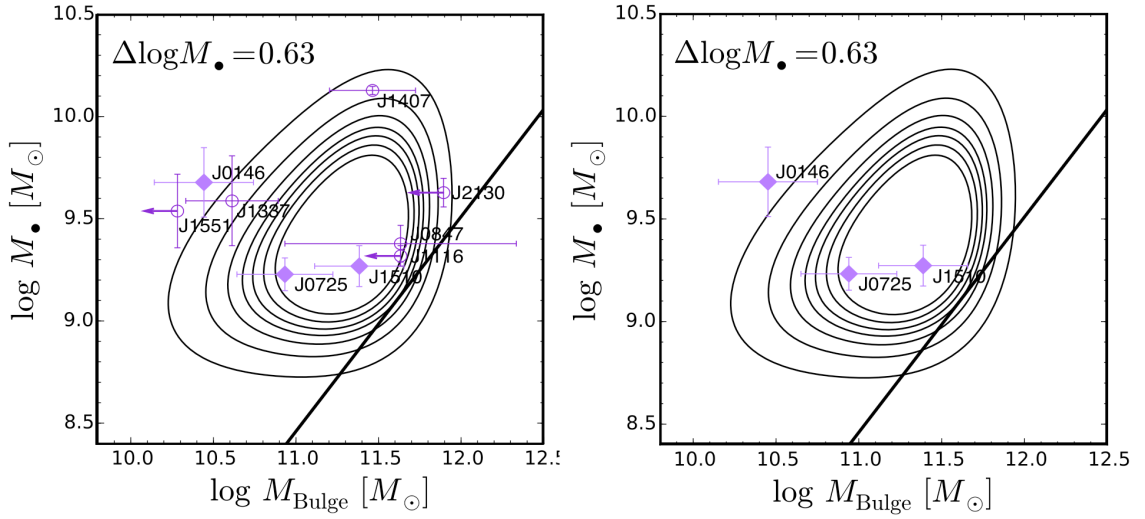


Figure 59 The expected sample selection bias for our sample estimated by A. Schulze. The distribution of objects in the $M_{\text{BH}} - M_{\text{spheroid}}$ plane is given by the bivariate distribution function of spheroid and BH masses, which ideally describes the true underlying relation. In real observations, the probability distribution is inevitably modified. Therefore, they incorporate the modification of the bivariate distribution by using an appropriate selection function which corresponds to selection criteria (such as luminosity limit). Left : The black contour shows the predicted $M_{\text{BH}} - M_{\text{spheroid}}$ probability distribution. Each line shows the $\log(\text{constant probability})$ equals to -3.6 , -3.8 , -4 , -4.2 , -4.5 , -5 , and -6 . The $\log(\text{constant probability})$ becomes smaller, then the probability that the result can be explained solely by bias becomes smaller. (ex., $\log(\text{constant probability})$ changes from -3.8 to -4.0 , probability of the bias is reduced to $1/10$. See Schulze & Wisotzki (2011) for more detail). Black solid line represents the local $M_{\text{BH}} - M_{\text{spheroid}}$ relation. All our sample are plotted. Purple filled diamonds show the results of host-galaxy-firmly-detected objects. For the objects whose host galaxy were undetected or MCMC simulation did not converge in K' -band, lower limit are shown as purple open circles with arrows. The objects whose host were not very convincing in K' -band are plotted as purple open circles with error bars. The object that was observed in only K' -band (J0847) is plotted with large error bar. Right : the same plot as left figure with only host detected objects.

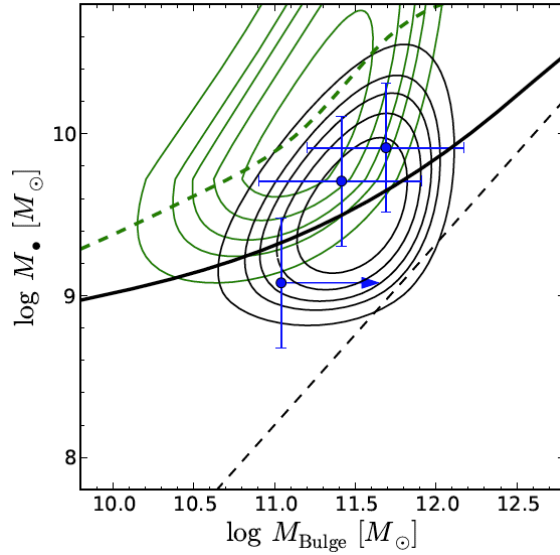


Figure 60 The expected sample selection bias for Schramm et al. (2008). Blue points are result of Schramm et al. (2008). The black contour shows the predicted $M_{\text{BH}} - M_{\text{spheroid}}$ probability distribution. Black dashed line represents the local $M_{\text{BH}} - M_{\text{spheroid}}$ relation. For comparison, the offset green contours show the expected distribution if $M_{\text{BH}}/M_{\text{spheroid}}$ were to evolve as strongly as with $(1+z)^\gamma$, $\gamma = 2$. Green dashed line represents the expected relation for $M_{\text{BH}}/M_{\text{spheroid}}$ evolving model.

Table 14 Comparison between Schramm+08 and our sample

	Schramm et al. (2008)	ours
redshift	~ 2.8	~ 3.3
Imaging observation	VLT without AO	Subaru with AO
Image size	0.5''	0.15''
Color	$H - K$	$J - K$
BH mass estimate	CIV	$\text{H}\beta$
$M_{V,nuclei}(\text{AB})$	$-(27-30)\text{mag}$	$-(26-29)\text{mag}$
$M_{V,host}(\text{AB})$	$-(25-26)\text{mag}$	$-(25-27)\text{mag}$
BH mass	$10^{(9.1-9.9)}$	$10^{(9.2-10.1)}$
Stellar mass	$\sim 10^{11.5}$	$\sim 10^{11.5}$

9.3 Relation between $M_{\text{BH}}/M_{\text{spheroid}}$ ratio and AGN luminosity

Figure 61 is the relation between $M_{\text{BH}}/M_{\text{spheroid}}$ ratio and AGN luminosity for our sample. We found that there is no significant correlation between $M_{\text{BH}}/M_{\text{spheroid}}$ ratio and AGN luminosity for our sample. We consider that our sample is less biased in terms of luminosity. Therefore our

result of $M_{\text{BH}}/M_{\text{spheroid}}$ ratio shows physical evolution, it is not due solely to selection bias.

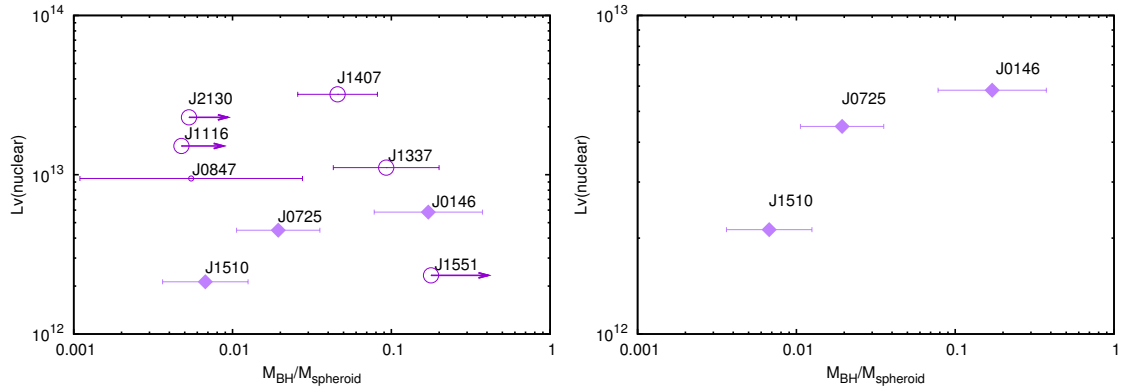


Figure 61 Left : Relation between $M_{\text{BH}}/M_{\text{spheroid}}$ ratio and AGN luminosity. Purple filled diamonds show the results of host-galaxy-firmly-detected objects. For the objects whose host galaxy were undetected or MCMC simulation did not converge in K' -band, lower limits are shown as purple open circles with arrows. The objects whose host were not very convincing in K' -band are plotted as purple open circles with error bars. The object that was observed in only K' -band (J0847) is plotted with large error bar. Right : Same figure as left panel only for host-galaxy-firmly-detected objects.

10 Summary

We present new near-infrared spectroscopic observations of 37 QSOs, and near-infrared AO imaging observations of 9 QSOs at $z \sim 3$, to observationally estimate accurate $M_{\text{BH}}/M_{\text{spheroid}}$ ratios at high redshift.

In our spectroscopic observations, we successfully estimated the SMBH masses of 28 out of 37 observed QSOs, using the well-calibrated $\text{H}\beta$ -method, based on a broad $\text{H}\beta$ emission linewidth and nearby continuum luminosity. A summary of the main findings from spectroscopic observation is given below.

1. A comparison of our work to similar studies of $z = 2\text{--}4$ QSOs by Netzer et al. (2007) and Shemmer et al. (2004) indicated that our sample had slightly larger M_{BH} and smaller Eddington ratios than the comparison sample. Also, it is unlikely that most of our sample have the M_{BH} much larger than the break of the BH mass function at that redshift. Given that all our QSOs have at least one nearby bright star, high-spatial-resolution AO observations to investigate the detailed properties of the host galaxies are possible. Our sample is suited to an investigation of $M_{\text{BH}}/M_{\text{spheroid}}$ evolution at $z \sim 3$, without obvious selection bias.

2. A comparison of the $\text{H}\beta$ -based SMBH mass estimate through near-infrared spectroscopy and previous CIV-based SMBH mass estimates using optical spectroscopy showed large scatter and no significant correlation. As argued in previous studies, the use of CIV for the M_{BH} estimate could introduce large uncertainty. $\text{H}\beta$ -based M_{BH} estimation using near-infrared spectroscopy is desirable for reliable M_{BH} estimates of $z \sim 3$ QSOs.

In our imaging observations, we successfully estimated the QSO host galaxy spheroidal masses of 9 out of 28 QSOs whose SMBH masses were estimated from our spectroscopic observations, using our original imaging analysis method.

3. We established original imaging analysis method for a study of distant QSO host galaxy. In most of previous studies, the same PSF shape as the PSF reference star in the same field of view was used to subtract AGN component for obtaining host galaxy component. However, PSF shape is varied in the field of view, depending on the distance from AO guide star. Therefore, we estimated the PSF shape at the location of QSO, by using the relation between core-to-halo ratio and distance from AO guide star. Also, we adopt multi-band imaging method to obtain color information for estimate of accurate M/L ratio.

4. Combination of our spectroscopic and imaging observation results showed that $M_{\text{BH}}/M_{\text{spheroid}}$ ratios at $z \sim 3$ is more than ~ 10 times larger than local relation. This result is consistent with previous studies using other methods which potentially contain large

uncertainties. Our sample is luminosity limited to avoid selection bias which arises artificial redshift evolution of $M_{\text{BH}}/M_{\text{spheroid}}$ ratios.

5. A comparison of our $M_{\text{BH}}/M_{\text{spheroid}}$ ratios to selection bias estimate by A. Schulze showed significant offset from the center of the contour, which corresponds to expected $M_{\text{BH}}/M_{\text{spheroid}}$ with our selection bias effect. Also, a comparison of AGN luminosity and $M_{\text{BH}}/M_{\text{spheroid}}$ ratios showed no significant correlation. Therefore, although our sample may contain some selection bias, our result about $M_{\text{BH}}/M_{\text{spheroid}}$ is unlikely to be explained solely by the possible bias, and a physical evolution of $M_{\text{BH}}/M_{\text{spheroid}}$ is suggested. To ensure our result, fainter and lower Eddington ratio AGN sample might be needed as less biased sample, and Subaru HSC QSO survey (Matsuoka et al. (2016)) is expected to find such AGN sample.

Acknowledgments

I am deeply grateful to Dr. Masatoshi Imanishi, for his comments, advices, and encouragement throughout the course of my study. I am also grateful to Dr. Saeko Hayashi for the observation time with Subaru Telescope and her concerns, and Dr. Nobunari Kashikawa for his supports and advices to acquire basic knowledge for this study. I would like to express my heartfelt appreciation to Dr. Yosuke Minowa for his great technical help to establish imaging analysis method, and all the discussions, and Dr. Toshihiro Kawaguchi for his detailed discussions, anonymous advices and suggestions, and Dr. Tomoki Morokuma for his comments and supports on data analysis and discussions. Also I would like to thank all the other QSOhost team members (Dr. Takeo Minezaki, Dr. Nagisa Oi, Dr. Tohru Nagao, Dr. Nozomu Kawatatu, and Dr. Kenta Matsuoka) for their help with observations and discussions. I wish to thank Dr. Andreas Schulze for bias estimate for our sample and helpful discussion, Dr. Hiroaki Sameshima for his advice on spectroscopic data analysis, and Dr. Kentaro Aoki for general discussions about QSOs.

I would also like to express my gratitude to my family and all my friends for their support and warm encouragements.

References

- [Abazajian et al. (2009)] Abazajian, K. N., et al. 2009, *ApJS*, 182, 543
- [Akiyama et al. (2008)] Akiyama, M., Minowa, Y., Kobayashi, N., Ohta, K., Ando, M., & Iwata, I. 2008, *ApJ*, 175, 1
- [Assef et al. (2011)] Assef, R. J., et al. 2011, *ApJ*, 742, 93
- [Baskin & Laor (2005)] Baskin, A., & Laor, A. 2005, *MNRAS*, 356, 1029
- [Bassani et al. (1999)] Bassani, L., Dadina, M., Maiolino, R., Salvati, M., Risaliti, G., Della Ceca, R., Matt, G., & Zamorani, G. 1999, *ApJ*, 121, 473
- [Becker et al. (1994)] Becker, R. H., White, R. L., & Helfand, D. J. 1994, *ASPC*, 61, 165
- [Beckers (1993)] Beckers, J. M. 1993, *ARA&A*, 1993, 31, 13
- [Bell & De Jong (2001)] Bell, E. F., & De Jong, R. S. 2001, *ApJ*, 550, 212
- [Bell et al. (2003)] Bell, E. F., McIntosh, D. H., Katz, N., & Weinberg, M. D. 2003, *ApJS*, 149, 289
- [Bender et al. (2005)] Bender, R., et al. 2005, *ApJ*, 631, 280
- [Bennert et al. (2011)] Bennert, V. N., Auger, M. W., Treu, T., Woo, J.-H., & Malkan, M. A. 2011, *ApJ*, 742, 107
- [Bentz et al. (2007)] Bentz, M. C., et al. 2007, *ApJ*, 662, 205
- [Bentz et al. (2009)] Bentz, M. C., et al. 2009, *ApJ*, 705, 199
- [Bondi & Hoyle (1944)] Bondi, H., & Hoyle, F. 1944, *MNRAS*, 104, 273
- [Borch et al. (2006)] Borch, A., et al. 2006, *A&A*, 453, 869
- [Bruzual & Charlot (2003)] Bruzual, A. G., & Charlot, S. 2003, *MNRAS*, 344, 1000
- [Calzetti et al. (2000)] Calzetti, D., Armus, L., Bohlin, R. C., Kinney, A. L., Koornneef, J., & Storchi-Bergmann, T. 2000, *ApJ*, 533, 682
- [Cappellari et al. (2002)] Cappellari, M., Verolme, E. K., van der Marel, R. P., Verdoes Kleijn, G. A., Illingworth, G.D., Franx, M., Carollo, C. M., & de Zeeuw, P. T. 2002, *ApJ*, 578, 787
- [Chabrier (2003)] Chabrier, G. 2003, *PASP*, 115, 763
- [Cisternas et al. (2011)] Cisternas, M., et al. 2011, *ApJ*, 741, L11
- [Cowie et al. (1996)] Cowie, L. L., Songaila, A., Hu, E., & Cohen, J. G. 1996, *AJ*, 112, 839
- [Croton (2006)] Croton, D. J. 2006, *MNRAS*, 369, 1808
- [Cushing et al. (2004)] Cushing, M. C., Vacca, W. D., & Rayner J. T. 2004, *PASP*, 116, 362.
- [Davies (2008)] Davies, R. 2008 arXiv : astro-ph/0703044
- [Decarli et al. (2010)] Decarli, R., Falomo, R., Treves, A., Labit, M., Kotilainen, J. K., & Scarpa, R. 2010, *MNRAS*, 402, 2453
- [Denney et al. (2010)] Denney, K. D., et al. 2010, *ApJ*, 721, 715

- [Dimitrijević et al. (2007)] Dimitrijević, M. S., Popović, L.Č., Kovačević, J., Dačić, M., & Llić, D. 2007, MNRAS, 374, 1181
- [Dunlop et al. (2003)] Dunlop, J. S., McLure, R. J., Kukula, M. J., Baum, S. A., O’Dea, C. P., & Hughes, D. H. 2003, MNRAS, 340, 1095
- [Elvis et al. (1994)] Elvis, M., et al. 1994, ApJ, 95, 1
- [Falomo et al. (2005)] Falomo, R., Kotilainen, J. K., Scarpa, R., & Treves, A. 2005, A&A, 434, 469
- [Falomo et al. (2008)] Falomo, R., Treves, A., Kotilainen, J. K., Scarpa, R., & Uslenghi, M. 2008, ApJ, 673, 694
- [Franceschini et al. (1999)] Franceschini, A., Hasinger, G., Miyaji, T., & Malquori, D. 1999, MNRAS, 310, L5
- [Gaskell (1982)] Gaskell, C. M. 1982, APJ, 263, 79
- [Genzel et al. (1994)] Genzel, R., Hollenbach, D., & Townes, C. H. 1994, Rep. Prog. Phys., 57, 417
- [Genzel et al. (2010)] Genzel, R., Eisenhauer, F., & Gillessen, S. 2010, Rev. Mod. Phys., 82, 3121
- [Häring & Rix (2004)] Häring, N., & Rix, H.-W. 2004, ApJ, 604, L89
- [Hayano et al. (2010)] Hayano, Y., et al. 2010, Proc. SPIE, vol. 7736, 21
- [Ho et al. (2012)] Ho, L. C., Goldoni, P., Dong, X.-B., Greene, J. E., & Ponti, G. 2012, ApJ, 754, 11
- [Iye et al. (2004)] Iye et al. 2004, PASJ, 56, 381
- [Jahnke et al. (2004a)] Jahnke, K., Kuhlbrodt, B., & Wisotzki, L. 2004, MNRAS, 352, 399
- [Jahnke et al. (2004b)] Jahnke, K., et al. 2004, ApJ, 614, 568
- [Jahnke et al. (2009)] Jahnke, K., et al. 2009, ApJ, 706, L215
- [Kaspi et al. (2000)] Kaspi, S., Smith, P. S., Netzer, H., Maoz, D., Jannuzi, B., & Giveon, U. 2000, ApJ, 533, 631
- [Kauffman & Haehnelt (2000)] Kauffmann, G., & Haehnelt, M. 2000, MNRAS, 311, 576
- [Kawaguchi (2003)] Kawaguchi, T. 2003, ApJ, 593, 69
- [Kawaguchi et al. (2004)] Kawaguchi, T., Aoki, K., Ohta, K., & Collin, S. 2004, A&A, 420, L23
- [Kawakatu et al. (2003)] Kawakatu, N., Umemura, M., & Mori, M. 2003, ApJ, 583, 85
- [Kelly & Shen (2013)] Kelly, C. B., & Shen, Y. 2013, ApJ, 764, 45
- [Kobayashi et al. (2000)] Kobayashi, N., et al. 2000, Proc. SPIE, vol. 4008, 1056
- [Kodama et al. (2004)] Kodama, T., et al. 2004, MNRAS, 350, 1005
- [Kormendy & Ho (2013)] Kormendy, J., & Ho, L. C. 2013, ARA&A, 51, 511
- [Kormendy & Richstone (1995)] Kormendy, J., & Richstone, D. O. 1995, ARA&A, 33, 581
- [Kuo et al. (2011)] Kuo, C. Y., et al. 2011, ApJ, 727, 20
- [Lauer et al. (2007)] Lauer, R. T., Tremaine, S., Richstone, D., & Faber, M. S. 2007, ApJ, 670, 249

- [Magorrian et al. (1998)] Magorrian, J., et al. 1998, *ApJ*, 115, 2285
- [Manchado et al. (1998)] Manchado, A., et al. 1998, *Proc. SPIE*, vol. 3354, 448
- [Marconi & Hunt (2003)] Marconi, A., & Hunt, L. K. 2003, *ApJ*, 589, L21
- [Marconi et al. (2004)] Marconi, A., Risaliti, G., Gilli, R., Hunt, L. K., Maiolino, R., & Salvati, M. 2004, *MNRAS*, 351, 169
- [Marziani & Sulentic (2012)] Marziani, P., & Sulentic, J. W. 2012, *NewAR*, 56, 49
- [Matsuoka et al. (2014)] Matsuoka, Y., Strauss, M. A., Price III, T. N., and DiDonato, M. S. 2014, *ApJ*, 780, 162
- [Matsuoka et al. (2016)] Matsuoka, Y., et al. 2016, *ApJ Submitted* (arXiv:1603.02281)
- [McConnell & Ma (2013)] McConnell, N. J., & Ma, C-P. 2013, *ApJ*, 764, 184
- [McLeod & Bechtold (2009)] McLeod, K. K., & Bechtold, J. 2009, *MNRAS*, 704, 415
- [McLure & Dunlop (2004)] McLure, R. J., & Dunlop, J. S. 2004, *MNRAS*, 352, 1390
- [McLure & Jarvis (2002)] McLure, R. J., & Jarvis, M. J. 2002, *MNRAS*, 337, 109
- [Merloni et al. (2010)] Merloni, A., et al. 2010, *ApJ*, 708, 137
- [Miyoshi et al. (1995)] Miyoshi, M., Moran, J., Herrnstein, J., Greenhill, L., Nakai, N., Diamond, P., & Inoue, M. 1995, *Nature*, 373, 127
- [Mo et al. (1998)] Mo, H. J., Mao, S., & White, S. D. M. 1998, *MNRAS*, 295, 319
- [Netzer (2003)] Netzer, H. 2003, *ApJ*, 583, L5
- [Netzer et al. (2007)] Netzer, H., Lira, P., Trakhtenbrot, B., Shemmer, O., & Cury, I. 2007, *ApJ*, 671, 1256
- [Netzer & Trakhtenbrot (2007)] Netzer, H., & Trakhtenbrot, B. 2007, *ApJ*, 654, 763
- [Peng et al. (2002)] Peng, C. Y., Ho, L. C., Impey, C. D., & Rix, H-W. 2002, *ApJ*, 124, 266
- [Peng et al. (2006)] Peng, C. Y., Impey, C. D., Rix, H-W., Kochanek, C. S., Keeton, C. R., Falco, E. E., Lehár, J., & McLeod, B. A. 2006, *ApJ*, 649, 616
- [Peterson et al. (2004)] Peterson, B. M., et al. 2004, *ApJ*, 613, 682
- [Peterson & Wandel (1999)] Peterson, B. M., & Wandel, A. 1999, *ApJ*, 521, L95
- [Ramsay et al. (2004)] Ramsay, H., et al. 2004, *Proc. SPIE*, vol. 5492, 1160
- [Rayner et al. (2003)] Rayner, J. T., et al. 2003, *PASP*, 115, 362.
- [Richards et al. (2002)] Richards, G. T., van den Berk, D. E., Reichard, T. A., Hall, P. B., Schneider, D. P., SubbaRao, M., Thakar, A. R., & York, D. G. 2002, *ApJ*, 124, 1
- [Richards et al. (2006)] Richards, G. T., et al. 2006, *ApJ*, 166, 470
- [Robertson et al. (2006)] Robertson, B., Hernquist, L., Cox, T. J., Matteo, T. D., Hopkins, P. F., Martini, P., & Springel, V. 2006, *ApJ*, 641, 90
- [Schramm et al. (2008)] Schramm, M., Wisotzki, L., & Jahnke, K. 2008, *A&A*, 478, 311
- [Schramm & Silverman (2013)] Schramm, M., & Silverman, J. D. 2013, *ApJ*, 767, 13
- [Schulze & Wisotzki (2010)] Schulze, A., & Wisotzki, L. 2010, *A&A*, 516, A87
- [Schulze & Wisotzki (2011)] Schulze, A., & Wisotzki, L. 2011, *A&A*, 535, A87
- [Schulze & Wisotzki (2014)] Schulze, A., & Wisotzki, L. 2014, *MNRAS*, 438, 3422

- [Shemmer et al. (2004)] Shemmer, O., Netzer, H., Maiolino, R., Oliva, E., Croom, S., Corbett, E., & di Fabrizio, L. 2004, *ApJ*, 614, 547
- [Shen et al. (2008)] Shen, Y., Greene, J. E., Strauss, M. A., Richards, G. T., & Schneider, D. P. 2008, *ApJ*, 680, 169
- [Shen et al. (2011)] Shen, Y., et al. 2011, *ApJS*, 194, 45
- [Shen & Liu (2012)] Shen, Y., & Liu, X. 2012, *ApJ*, 753, 125
- [Silk & Rees (1998)] Silk, J., & Rees, M. J. 1998, *A&A*, 331, L1
- [Silverman et al. (2008)] Silverman, J. D., et al. 2008, *ApJ*, 679, 118
- [Smith & Done (1996)] Smith, D. A., & Done, C. 1996, *MNRAS*, 280, 355
- [Stocke et al. (1992)] Stocke, J. T., Morris, S. L., Weymann, R. J., & Foltz C. B. 1992, *ApJ*, 396, 487
- [Sulentic et al. (2007)] Sulentic, J. W., Bachev, R., Marziani, P., Negrete, C. A., & Dultzin, D. 2007, *ApJ*, 666, 757
- [Targett et al. (2011)] Targett, T. A., Dunlop, J. S., McLure, R. J., Best, P. N., Cirasuolo, M., & Almaini, O. 2011, *MNRAS*, 412, 295
- [Targett et al. (2012)] Targett, T. A., Dunlop, J. S., & McLure, R. J. 2012, *MNRAS*, 420, 3621
- [Tokunaga (2000)] Tokunaga, A. T. 2000, in *Allen's Astrophysical Quantities*, 4th ed, ed. A. N. Cox (New York : AIP Press), 143
- [Trakhtenbrot & Netzer (2012)] Trakhtenbrot, B., & Netzer, H. 2012, *MNRAS*, 427, 3081
- [Tran (2001)] Tran, H. D. 2001, *ApJ*, 554, L19
- [Tran (2003)] Tran, H. D. 2003, *ApJ*, 583, 632
- [Tsuzuki et al. (2006)] Tsuzuki, Y., Kawara, K., Yoshii, Y., Oyabu, S., Tanabe, T., & Matsuoka, Y. 2006, *ApJ*, 650, 57
- [Tytler & Fan (1992)] Tytler, D., & Fan, X.-M. 1992, *ApJS*, 79, 1
- [Ueda et al. (2003)] Ueda, Y., Akiyama, M., Ohta, K., & Miyaji, T. 2003, *ApJ*, 598, 886
- [van den Bosch & de Zeeuw (2010)] van den Bosch, R. C. E., & de Zeeuw, P. T. 2010, *MNRAS*, 401, 1770
- [Vestergaard (2002)] Vestergaard, M. 2002, *ApJ*, 571, 733
- [Vestergaard & Peterson (2006)] Vestergaard, M., & Peterson, B. M. 2006, *ApJ*, 641, 689
- [Vestergaard et al. (2008)] Vestergaard, M., Fan, X., Tremonti, C. A., Osmer, P. S., & Richards, G. T. 2008, *ApJ*, 674, L1
- [Volonteri & Rees (2005)] Volonteri, M., & Rees, M. J. 2005, *ApJ*, 633, 624
- [Walsh et al. (2010)] Walsh, J. L., Barth, A. J., & Sarzi, M. 2010, *ApJ*, 721, 762
- [Walter et al. (2004)] Walter, F., Carilli, C., Bertoldi, F., Menten, K., Cox, P., Lo, K. Y., Fan, X., & Strauss, M. A. 2004, *ApJ*, 615, L17
- [Wandel et al. (1999)] Wandel, A., Peterson, B. M., & Malkan, M. A. 1999, *ApJ*, 526, 579
- [Wang et al. (2009)] Wang, J.-G., et al. 2009, *ApJ*, 707, 1334
- [Wang et al. (2013)] Wang, R., et al. 2013, *ApJ*, 773, 44

[Willott et al. (2003)] Willott, C. J., McLure, R. J., & Jarvis, M. J. 2003, ApJ, 587, L15

[Wu et al. (2004)] Wu, X.-B., Wang, R., Kong, M. Z., Liu, F. K., & Han, J. L. 2004, A&A, 424, 793

[Wyithe & Loeb (2003)] Wyithe, J. S. B., & Loeb, A. 2003, ApJ, 595, 614

[Zheng et al. (2009)] Zheng, X. Z., et al. 2009, ApJ, 707, 1566

Appendix A FWHM distribution

FWHM distribution of each object and time variation of FWHM. These are used when combining observed frames.

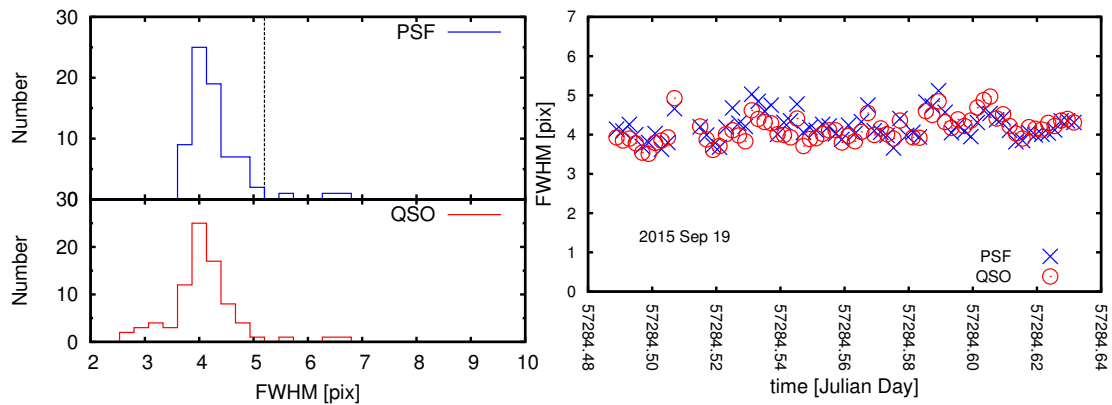


Figure 62 Left : FWHM distribution of J0146 J -band PSF reference star (top panel) and QSO (bottom panel). Dashed line in the figure is the FWHM limit to combine. Right : time variation of FWHM. Blue crosses : PSF, and red circles : QSO.

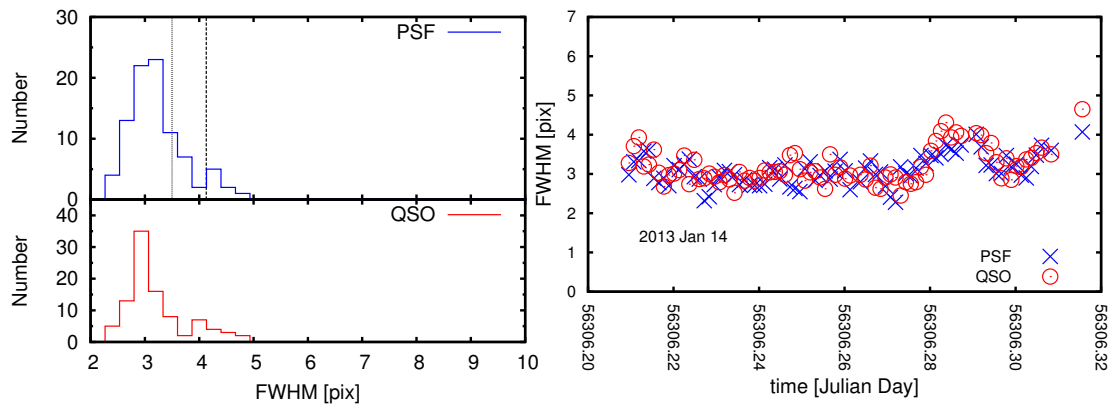


Figure 63 Left : FWHM distribution of J0146 K' -band PSF reference star (top panel) and QSO (bottom panel). Dotted line in the figure is the FWHM limit to combine. Right : time variation of FWHM. Blue crosses : PSF, and red circles : QSO.

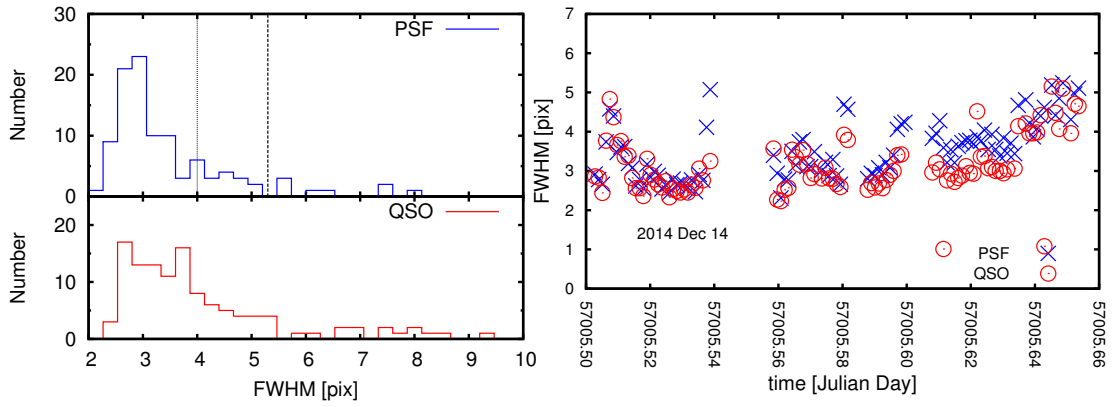


Figure 64 J0725J

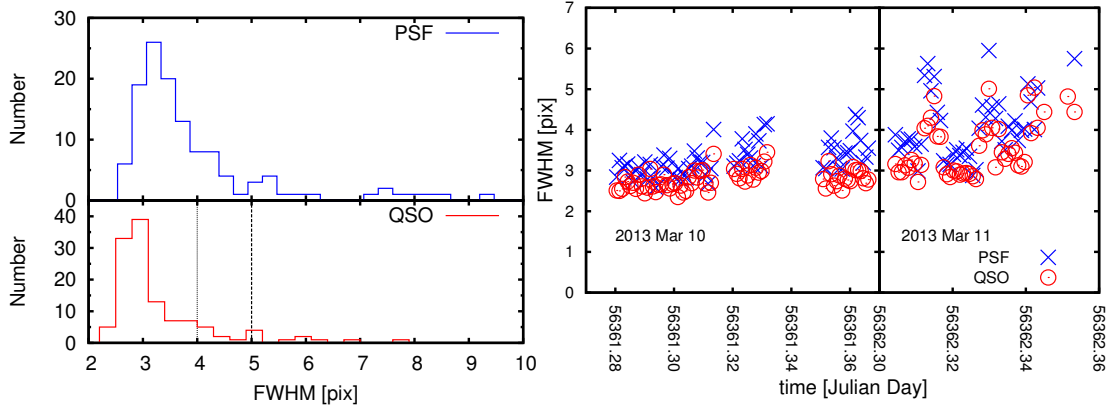


Figure 65 J0725K

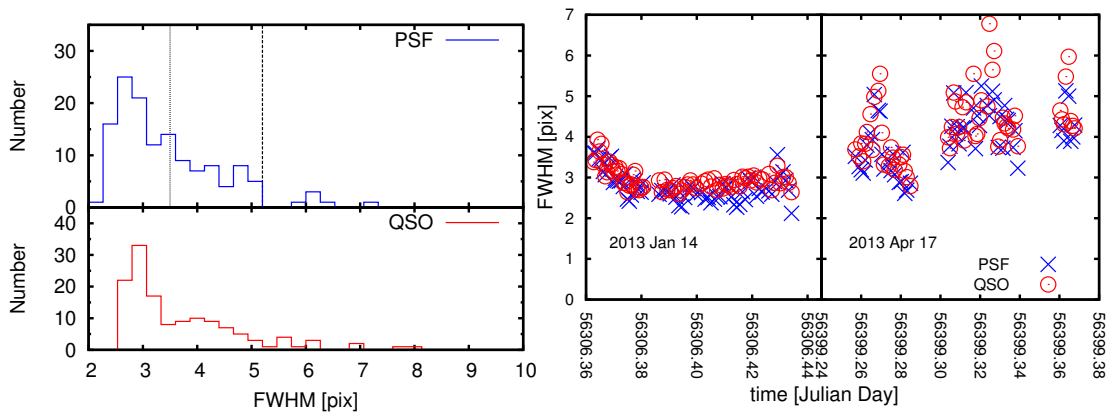


Figure 66 J0847K

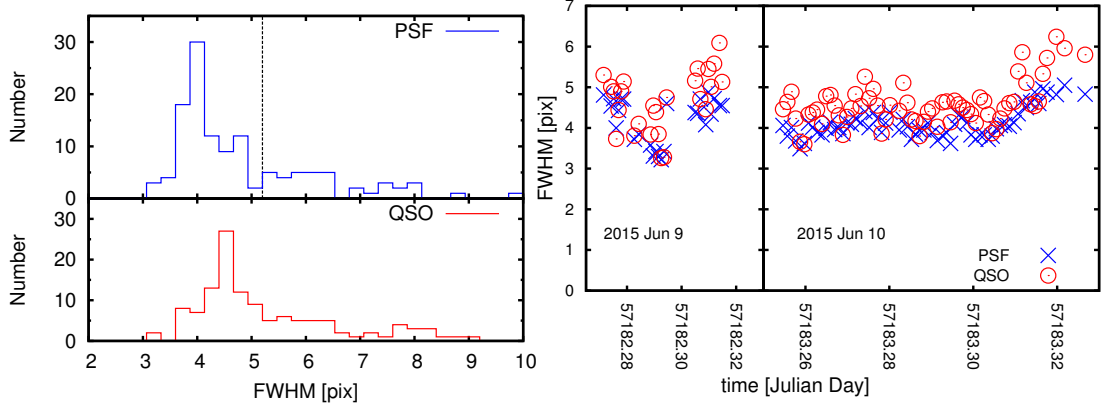


Figure 67 J1116J

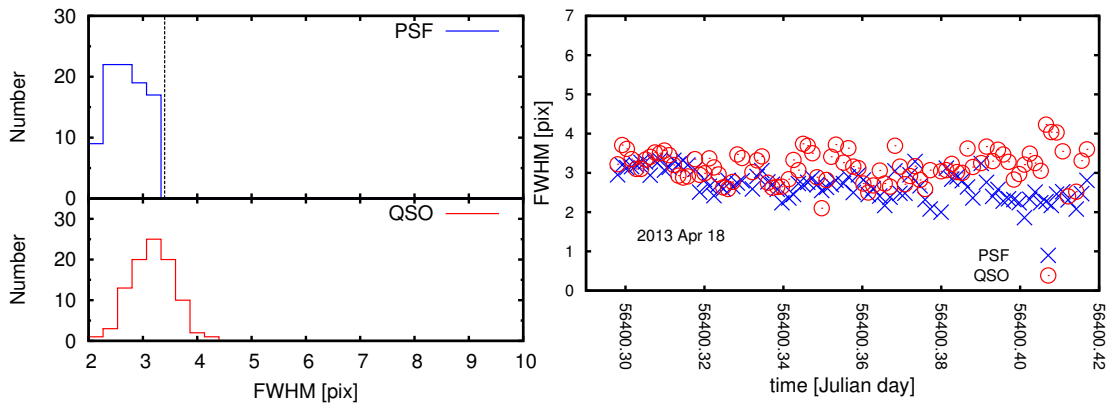


Figure 68 J1116K

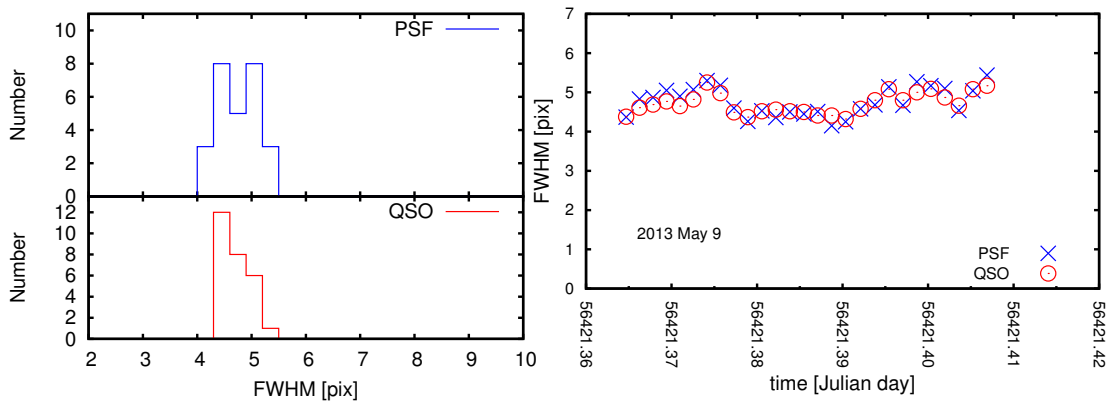


Figure 69 J1337J

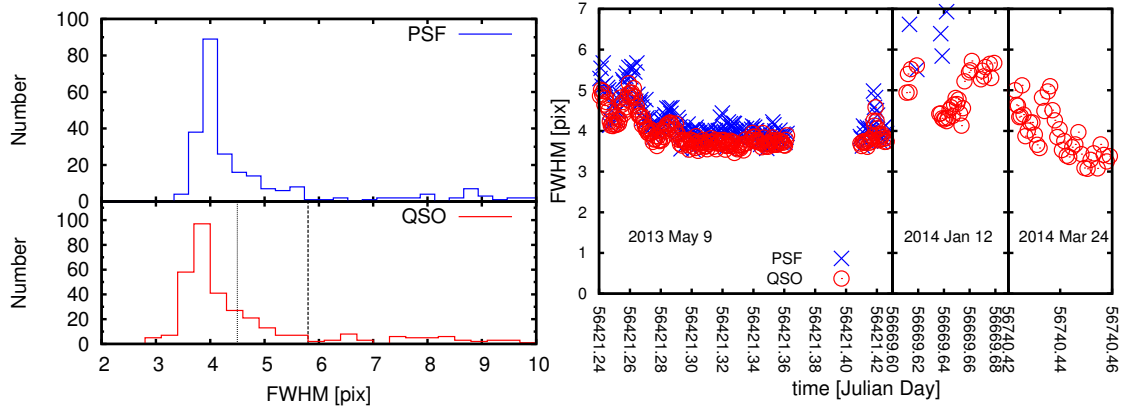


Figure 70 J1337K

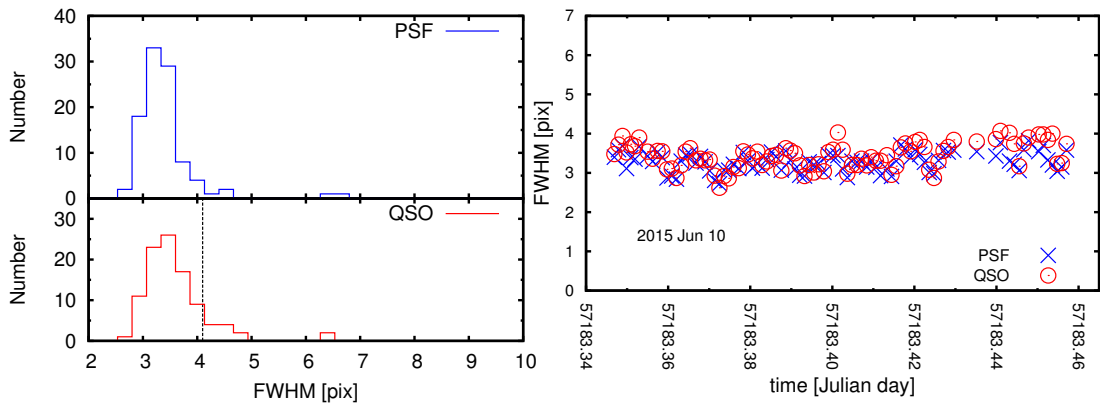


Figure 71 J1407J

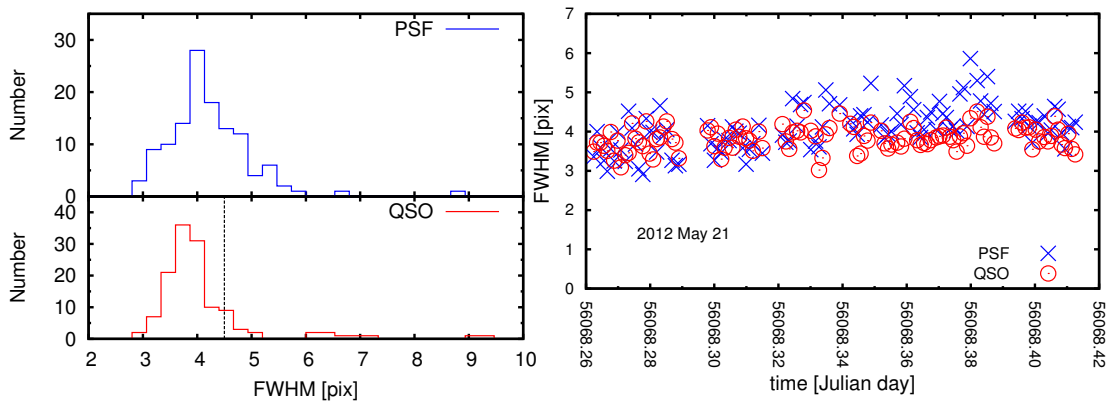


Figure 72 J1407K

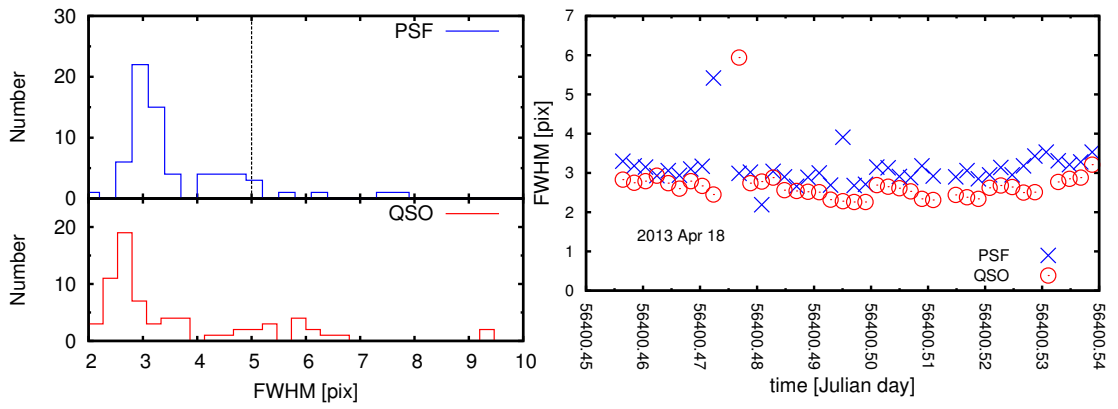


Figure 73 J1510J

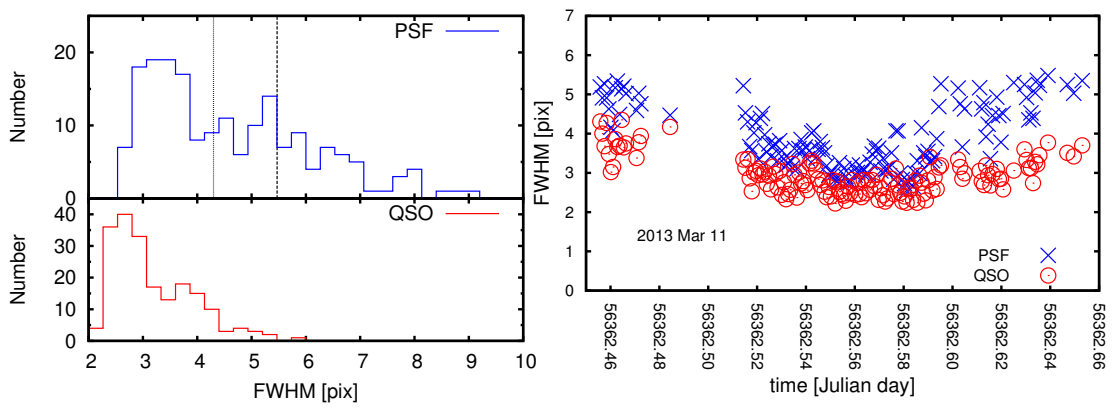


Figure 74 J1510K

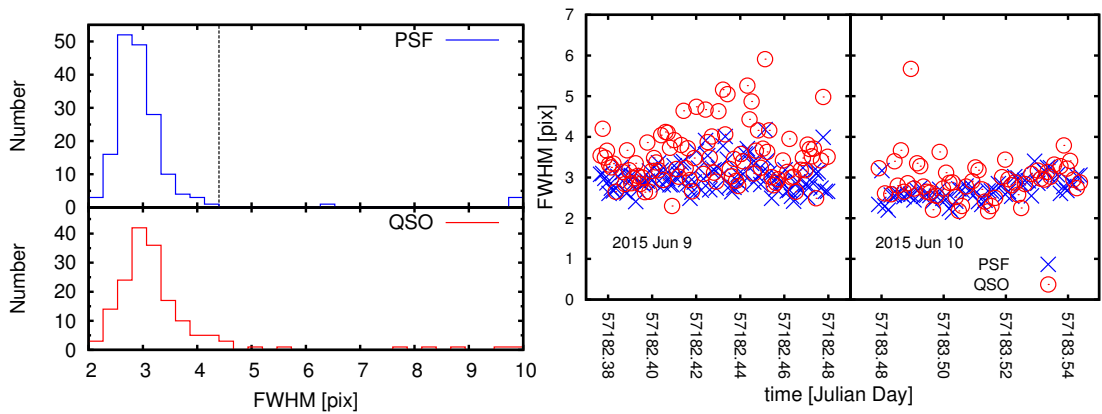


Figure 75 J1551J

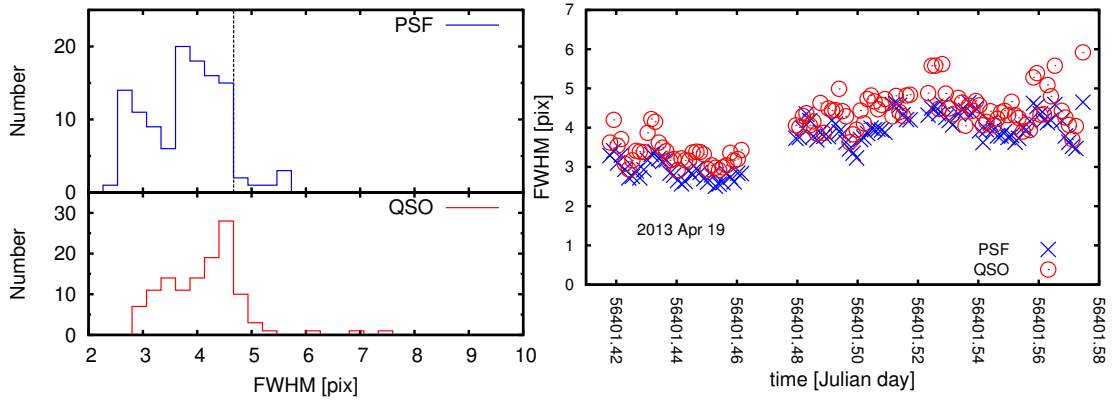


Figure 76 J1551K

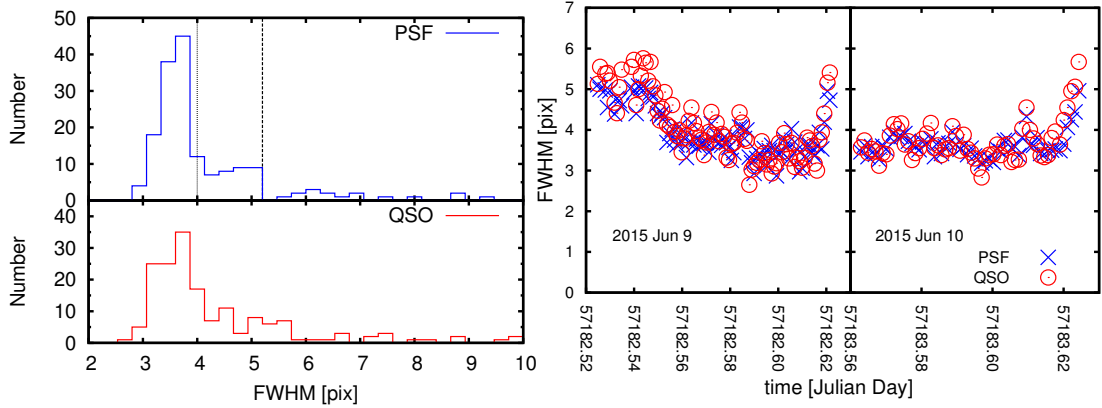


Figure 77 J2130J

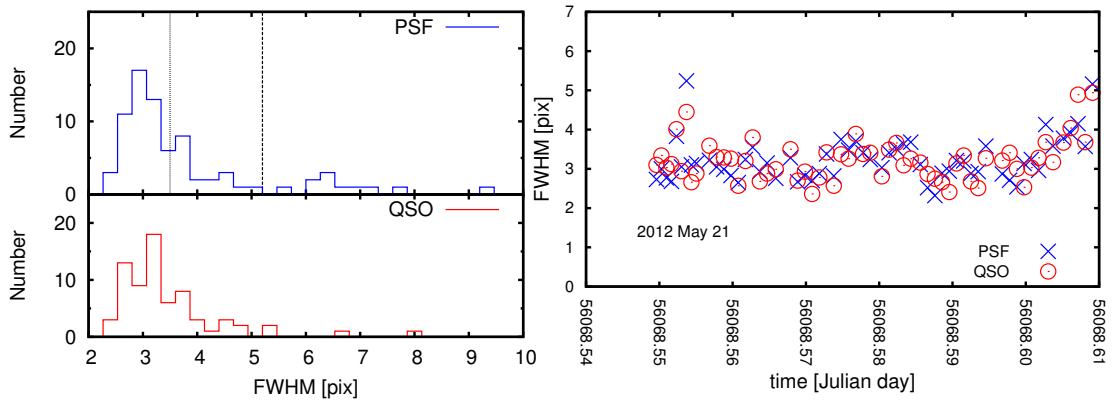


Figure 78 J2130K

AppendixB Fitting Test

B.1 Error caused by sky variation

Using the best fit model obtained as a result of PSF reference star fitting, we measured error caused by sky variation. We first clipped sky region from J1510 K' -band original image. After that we embedded PSF best fit model image into each clipped sky image, and then carried out fitting for all 12 images. If there is no noise in each image, best fit model parameters should be reproduced. However, fitting results are varied because of sky variation.

Randomly selected 12 sky areas with size of $50\text{pix}\times 50\text{pix}$ are clipped from J1510 K' -band original image (Figure 79, left). We also considered photon noise in addition to the best fit PSF model image.

Figure 79 (right) shows example images of in the embedding process.

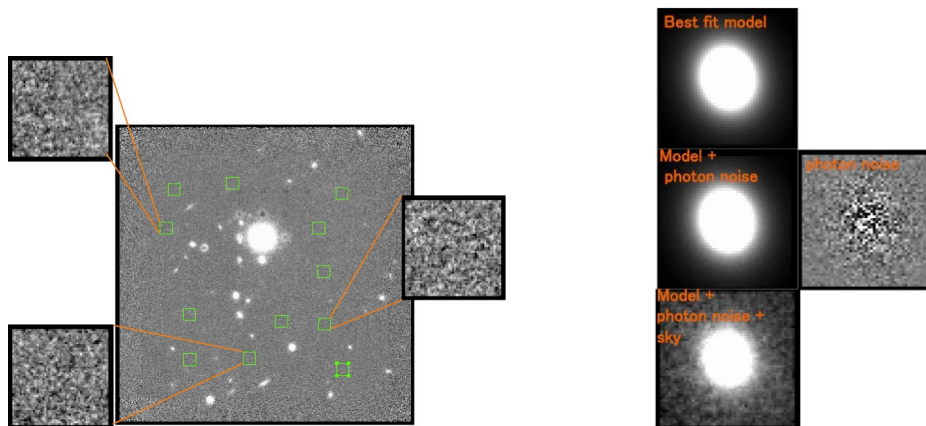


Figure 79 Left : 12 clipped sky regions for error estimate (green open squares), Right : process of embedding model PSF image (Top : Best fit PSF model image. Middle left : model + photon noise. Middle right : photon noise only. Bottom : model + photon noise + sky.).

We created the same image as the bottom panel of Figure 79, right, for the rest of 11 sky regions, and carried out fitting for all 12 images. Estimated error is summarized in Table 15.

According to Table 15, fitting results are systematically shifted from best fit parameters. It might be due to the size of the clipped area which is too small, and could not fit sky value well. We clipped $100\text{pix}\times 100\text{pix}$ sky regions and carried out the same fitting procedure. As a result, the systematic offset from best fit parameter was getting larger. Therefore, we considered the shift is caused by sky.

Table 15 Result of Error Estimate

Gaussian	best fit	fitting result
position x	26.0124	26.0075±0.0073
position y	25.9959	25.9993±0.0057
integral magnitude	18.5691	18.6580±0.0197
FWHM[pix]	4.2265	4.1470±0.0197
axis ratio(b/a)	0.7960	0.7910±0.0019
position angle (PA)	23.1689	23.0825±0.5801
Moffat	best fit	fitting result
position x	26.0466	26.0533±0.0211
position y	25.9669	25.9666±0.0208
integral magnitude	17.2162	16.8110±0.0628
FWHM[pix]	9.9883	8.7386±0.2290
Moffat powerlaw index	1.5427	1.2735±0.0261
axis ratio(b/a)	0.8619	0.8604±0.0033
position angle (PA)	16.0425	16.3340±1.2808

To further check the effect of sky background, we here checked how sky variation can affect fitting result. Firstly, we generate white noise within 50pix×50pix size of box, and embedded best fit PSF model into it. Then, fitted the image with 3 components, and confirmed that original parameters of best fit model was replicated. After that, we generated 2 patterns of artificial sky and carried our fitting. White noise was generated by normal random number with mean of 0, and $\sigma \sim 0.02$.

1. white noise (offset) + best fit model

This case corresponds to when there remains uniform sky residual in an image. Simply a constant offset + white noise with mean of 0 is given. The range of offset is from 0.005 to 0.05. The range was determined by actual sky images.

2. white noise(gradient) + best fit model

This case describes when there is sky gradient in an image. Offset is given by the formula, $z = ax + by$, where a=b and the range of a and b is from 0.000001 to 0.0001.

The range was determined by actual sky images.

result

1. Constant offset

Figure 80 shows fitting results with 2 components (Gaussian + Moffat), when sky offset is given within 0.005 to 0.05. We show results of magnitude and FWHM which are largely affected by sky variation in all fitting parameters and also critical for M_{spheroid} estimate. Red and Blue represent the results of Gaussian and Moffat, respectively. Solid lines correspond to the input value, points show fitting results. In Figure 80, fitting results for Moffat of both magnitude and FWHM are shifted from the input value with increasing sky or background offset value. The result shown in Figure 80 is when 50pix×50pix size images are used for the test. With 100pix×100pix size images, offset from the input model is larger and the fit does not converge when given offset is more than 0.025.

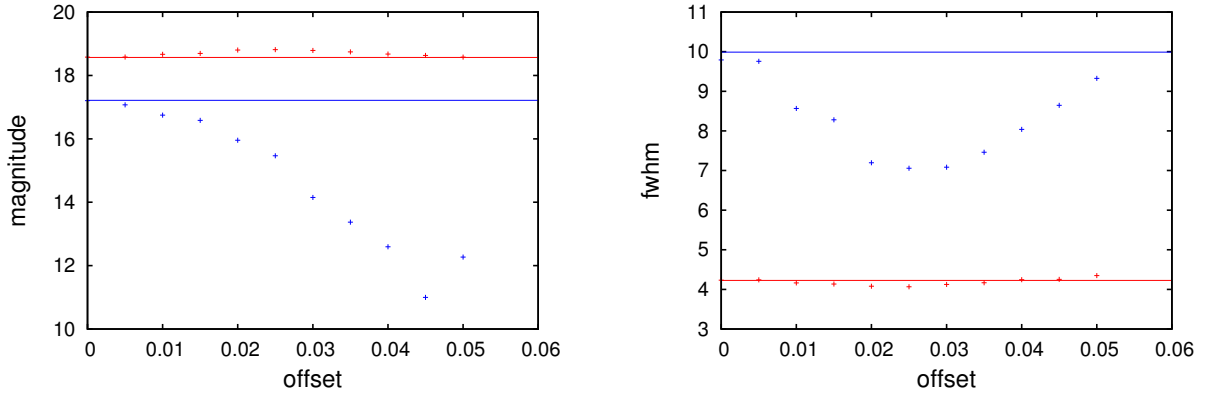


Figure 80 Left : magnitude vs sky offset, right : FWHM vs sky offset. PSF model was fitted by 2 components (Gaussian + Moffat). Red and blue denote the parameters for Gaussian and Moffat, respectively. Solid lines show the values of input model and points represent fitting result.

The fitting results with 3 components (Gaussian + Moffat + Sky) are shown in Figure 81 for mag and FWHM. Sky parameters are included in the fitting parameter for this case. In Figure 80, points and dotted lines represent the result of $50\text{pix} \times 50\text{pix}$ image, and $100\text{pix} \times 100\text{pix}$ image, respectively. It is clear from Figures 80 and 81 that best fit values are well replicated regardless given offset value, when sky component is considered.

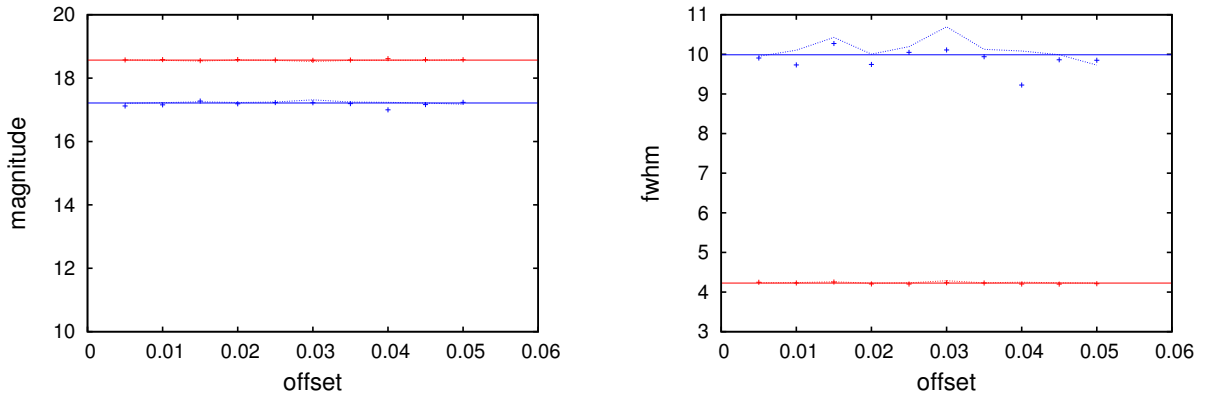


Figure 81 Left : magnitude vs sky offset, right : FWHM vs sky offset. PSF model was fitted by 3 components (Gaussian + Moffat + Sky). Red and blue denote the parameters for Gaussian and Moffat, respectively. Solid lines show the values of best fit model points represent $50 \times 50\text{pix}$ fitting result, and dashed lines show $100 \times 100\text{pix}$ fitting result.

Figures 82 and 83 show residual images obtained from fitting with and without sky parameter, respectively. Given offset value gets larger from top-left to bottom-right. Without sky parameter, residual is clearly seen with increasing given offset (Figure 82). On the other hand, with sky parameter, there is no clear residual seen in Figure 83, and we confirmed that the object was well fitted.

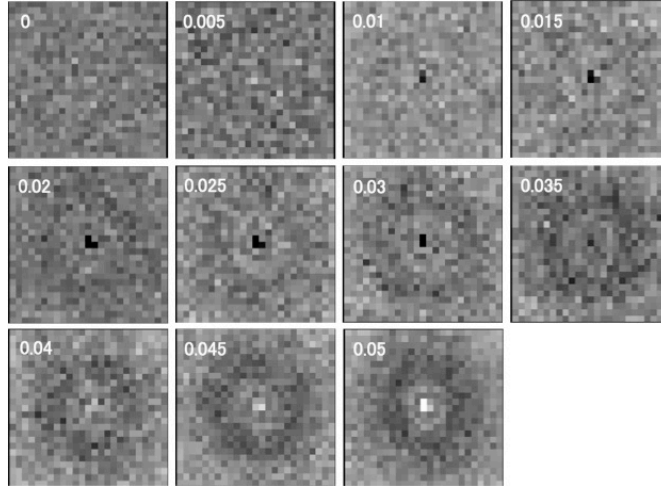


Figure 82 Model subtracted images obtained by fitting without sky parameter by changing sky offset value.

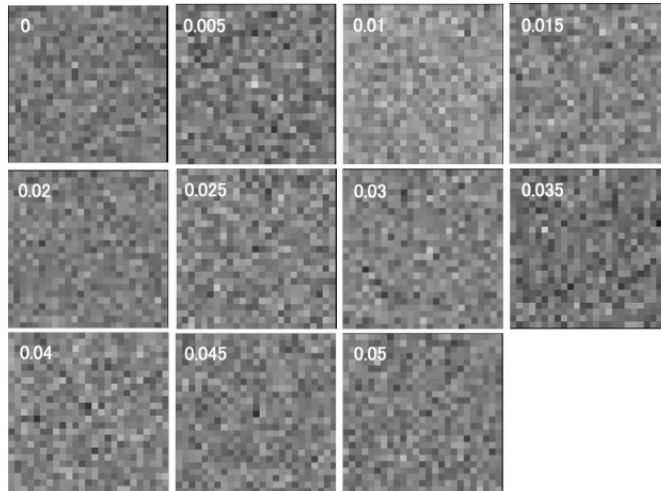


Figure 83 Model subtracted images obtained by fitting with sky parameter when sky offset varied.

2. Gradient

The fitting result with sky gradient given by the formula $z = ax + by$ is shown in Figure 84. The range of coefficients a and b is 0.000001–0.0001 ($a=b$), and fitting is carried out with 2 components (Gaussian + Moffat). Same as Figure 80, red and blue represent the result of Gaussian and Moffat respectively, and solid lines are best fit value. Points show the fitting result of 50pix×50pix image. Figure 84 indicates that gradient variation is not largely affect fitting results. It is because the gradient is very small (~ 2 dex) comparing to the offset value.

In the model subtracted images, also no variation can be seen with change of given gradient value (Figure 85).

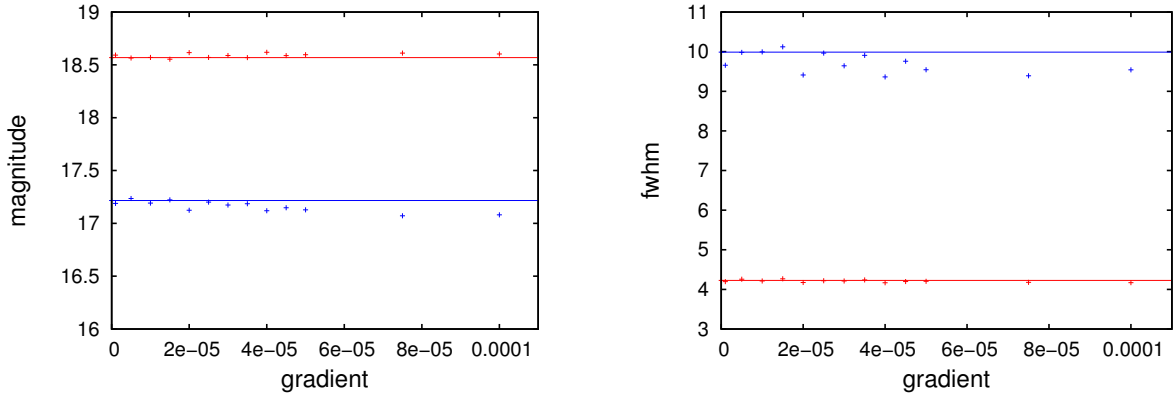


Figure 84 Left : magnitude vs sky gradient, right : FWHM vs sky gradient. PSF model was fitted by 2 components (Gaussian + Moffat). Red means Gaussian, blue means Moffat, solid lines show the values of best fit model and points represent 50×50 pix fitting result.

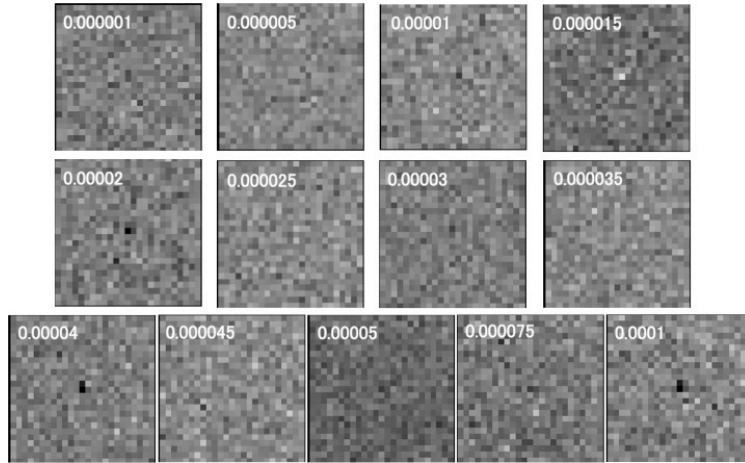


Figure 85 Residual images without sky fitting when sky gradient varied.

Final result of error estimate caused by sky variation

We re-fitted 12 images created in section 8.1.3 with 3 components (Gaussian + Moffat ; Sky) this time, and re-calculated fitting error from variation of parameters (Table 16). There was no systematic shift as seen in section A.1.3, and therefore we considered that fitting error was estimated more accurately.

Therefore, to obtain correct fitting result for PSF reference star fitting, it is important to measure sky offset around PSF reference star, and include sky as fitting components.

B.2 Test of our PSF fitting method

Here we test if our new fitting method described in Section 8, works in right way by using images of globular cluster M5.

Table 16 final result of error estimate

Gaussian	best fit	final result
position x	26.0124	26.0102±0.0053
position y	25.9959	25.9965±0.0057
integral magnitude	18.5691	18.5630±0.0150
FWHM[pix]	4.2265	4.2313±0.0222
axis ratio(b/a)	0.7960	0.7973±0.0022
position angle (PA)	23.1689	22.7586±0.5654
Moffat	best fit	final result
position x	26.0466	26.0551±0.0193
position y	25.9669	25.9677±0.0227
integral magnitude	17.2162	17.2382±0.0553
FWHM[pix]	9.9883	10.0922±0.2460
Moffat powerlaw index	1.5427	1.5714±0.0682
axis ratio(b/a)	0.8619	0.8606±0.0032
position angle (PA)	16.0425	16.1695±1.2941

13 stars which are not saturated are selected from the original M5 image for this test (Figure 86).

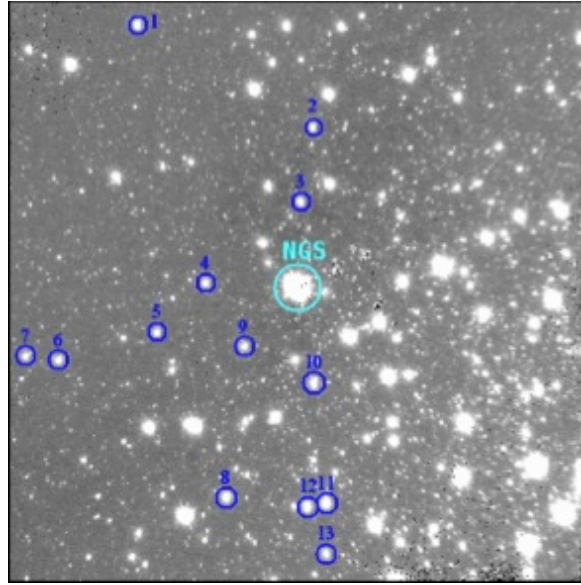


Figure 86 K'-band original image of M5.

First, we fit Star 10, and estimate strehl ratios for Star 1 to 13, by using Star 10 as a

PSF reference star. Fit each star with fixed Moffat shape (same parameters as Star 10), and constrained magnitude difference between Gaussian and Moffat. Then, see how χ^2 value changes with θ_0 .

Where χ^2 shows the minimum value is the best fit parameter. We compare parameters obtained by the fitting with Moffat parameter unfixed, and the best fit parameter obtained by our fitting method to see if those are consistent.

The relation between strehl ratio and distance from NGS is plotted in Figure 87. We confirmed that strehl ratio was getting worse with increasing distance from NGS, as expected.

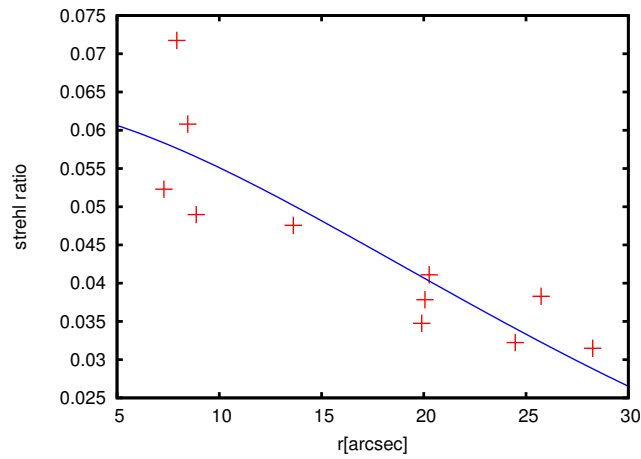


Figure 87 Relation between strehl ratio and distance from AO guide star for star 1 to 13. Blue line represents the expected relation following Eq.8.7.

The plot of χ^2 v.s. θ_0 for each star is shown in Figure 88.

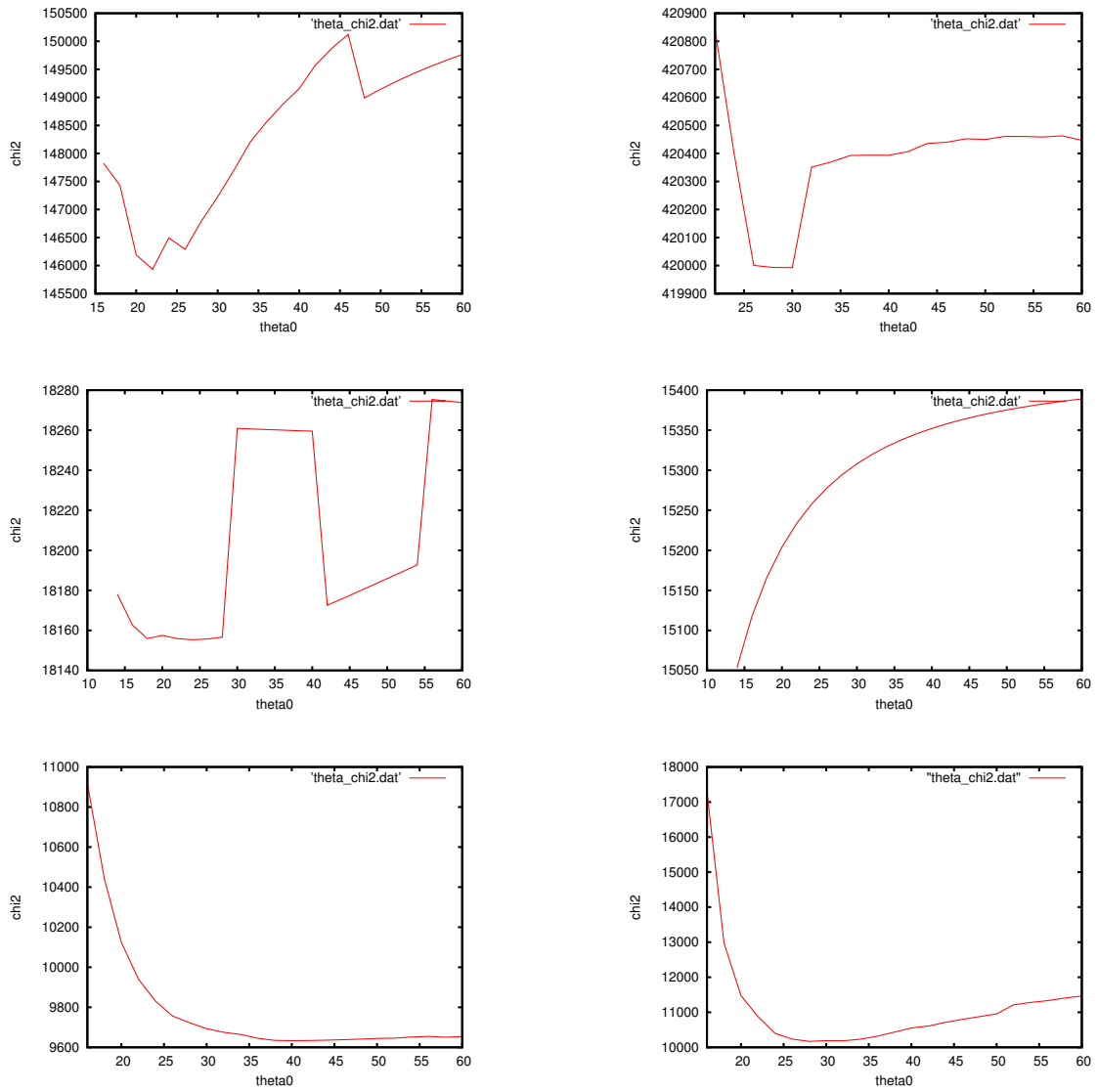


Figure 88 The plot of χ^2 v.s. θ_0 for each star. From top left to bottom right, star1, star2, ..., star6.

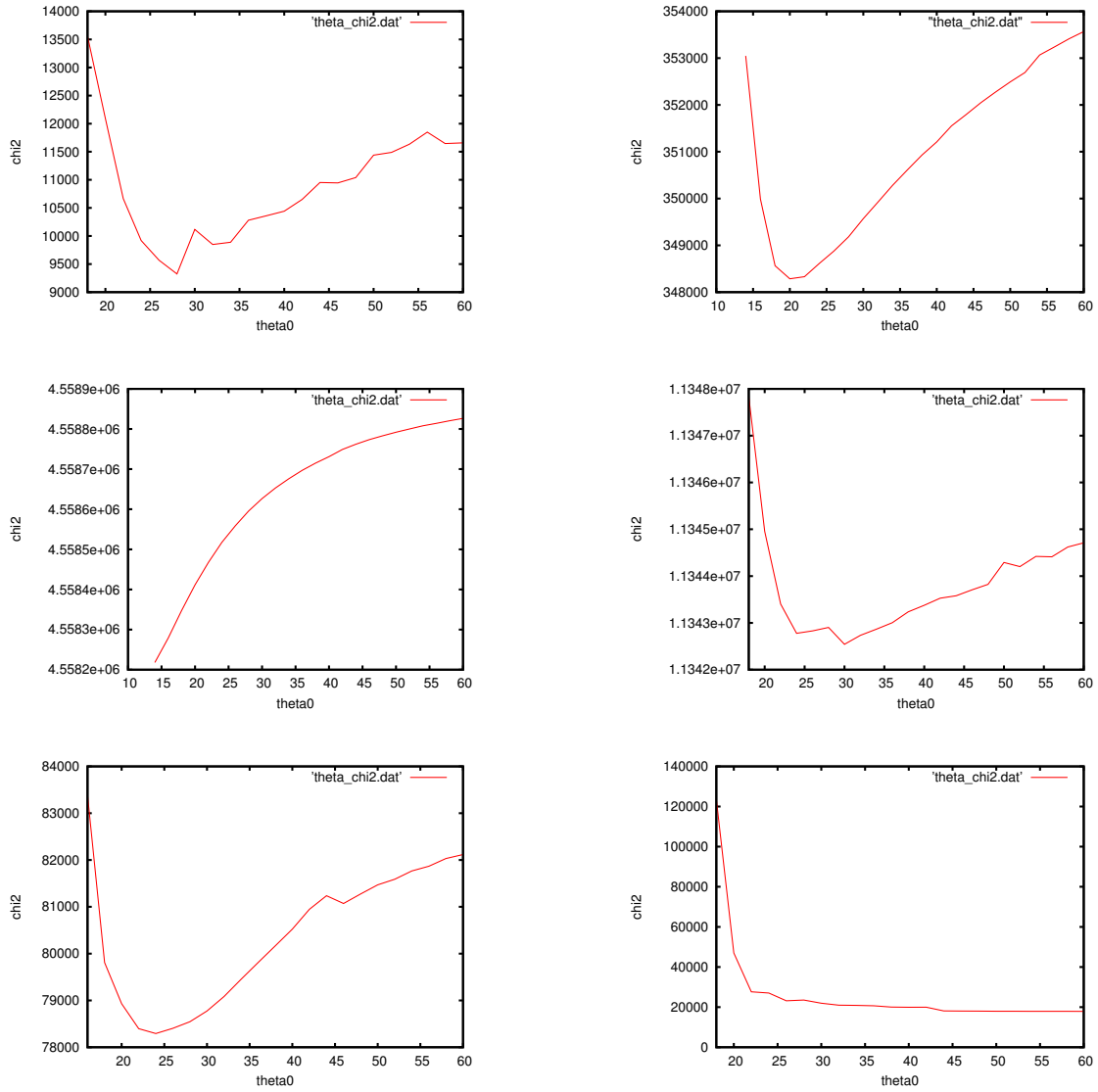


Figure 88 Continued. From top left to bottom right, star7, star8, ..., star13

We found that our method did not work correctly for the stars located almost same distance as star 10 (PSF reference star) from AO guide star. χ^2 v.s. θ_0 plot for those stars did not show χ^2 minimum value (in this case, Star 3, 4, and 9). For other stars, the minimum value was seen in their χ^2 v.s. θ_0 plot, and we confirmed that the best fit parameters obtained by direct fitting and our method was in good agreement.

AppendixC Fitting Result Images

C.1 J0146J

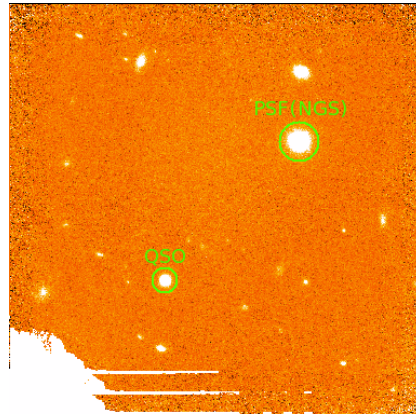


Figure 89 Final average combined image of J0146 *J*-band.

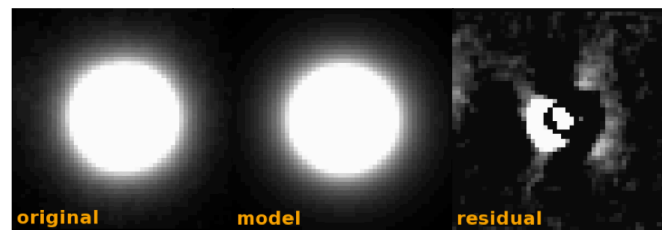


Figure 90 PSF reference star fitting result. Left : original PSF reference star image. Middle : best fit PSF model image. Right : residual image (original-model).

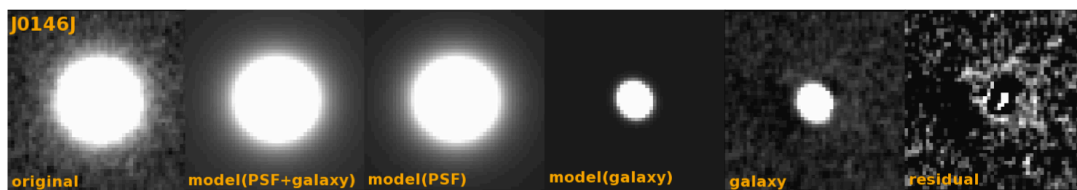


Figure 91 QSO fitting result. From left to right, original QSO image, best fit model(PSF+galaxy) image, best fit PSF model image, best fit galaxy model image, galaxy image (original – best fit PSF mode image), and residual image (original – model(PSF+galaxy) image).

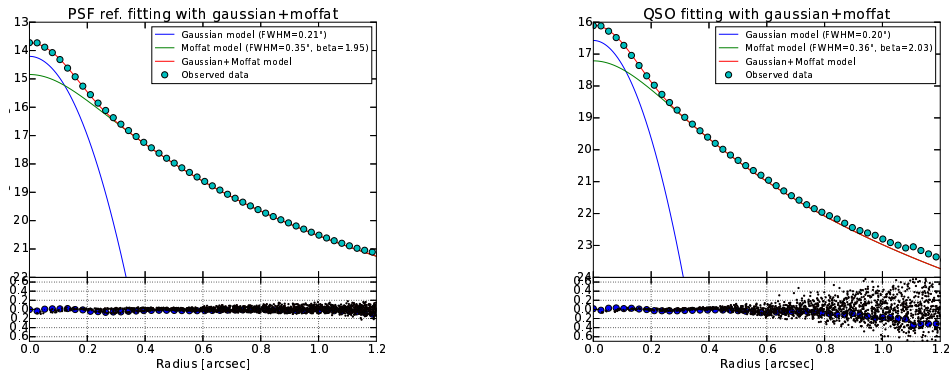


Figure 92 J0146 : Radial profile of PSF reference star (left) and QSO (right) when fitted with two components (Gaussian + Moffat).

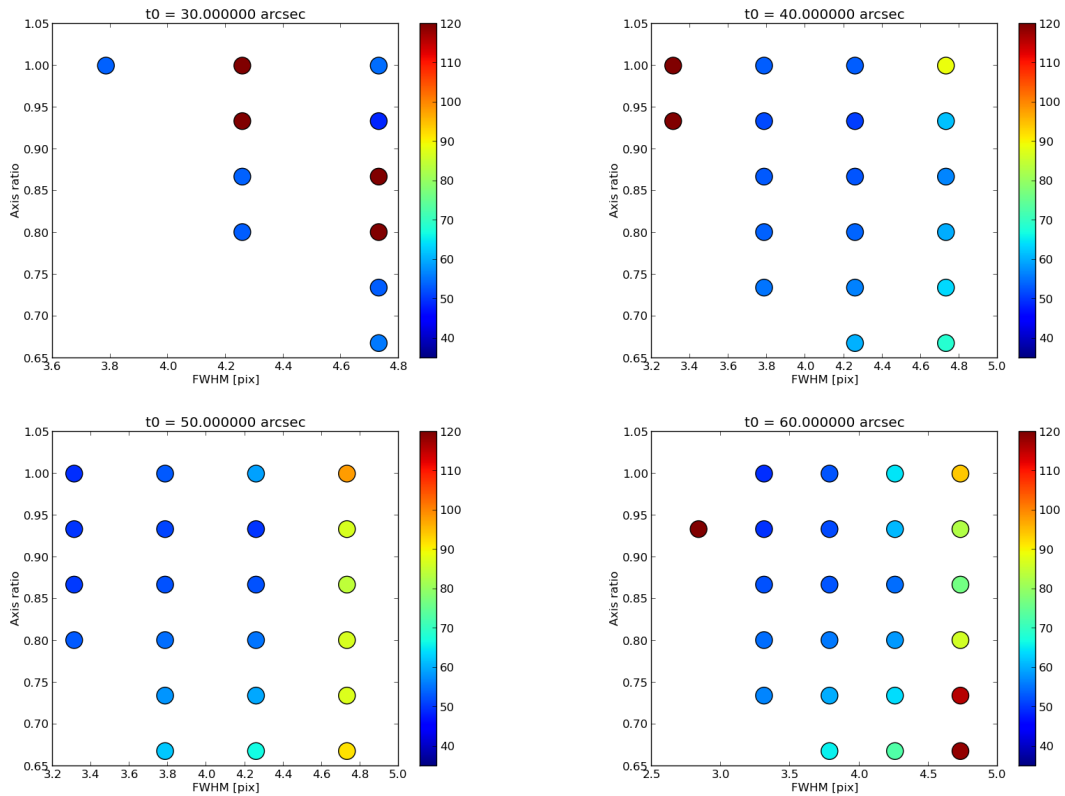


Figure 93 χ^2 map obtained by fitting of J0146 *J*-band data. X-axis is FWHM [pix], and Y-axis is axis ratio. The color bar represents χ^2 value (blue=small, red=large). From top left figure to bottom right figure, θ_0 ["] = 30, 40, 50, ..., 90. We adopted fitting result with the parameter set of q_g , fwhm_g and θ_0 where χ^2 shows the minimum value, as the best fit parameter. For this object, $\theta_0=80''$, $\text{fwhm}_g=3.31$ pix, and $q_g=0.93$.

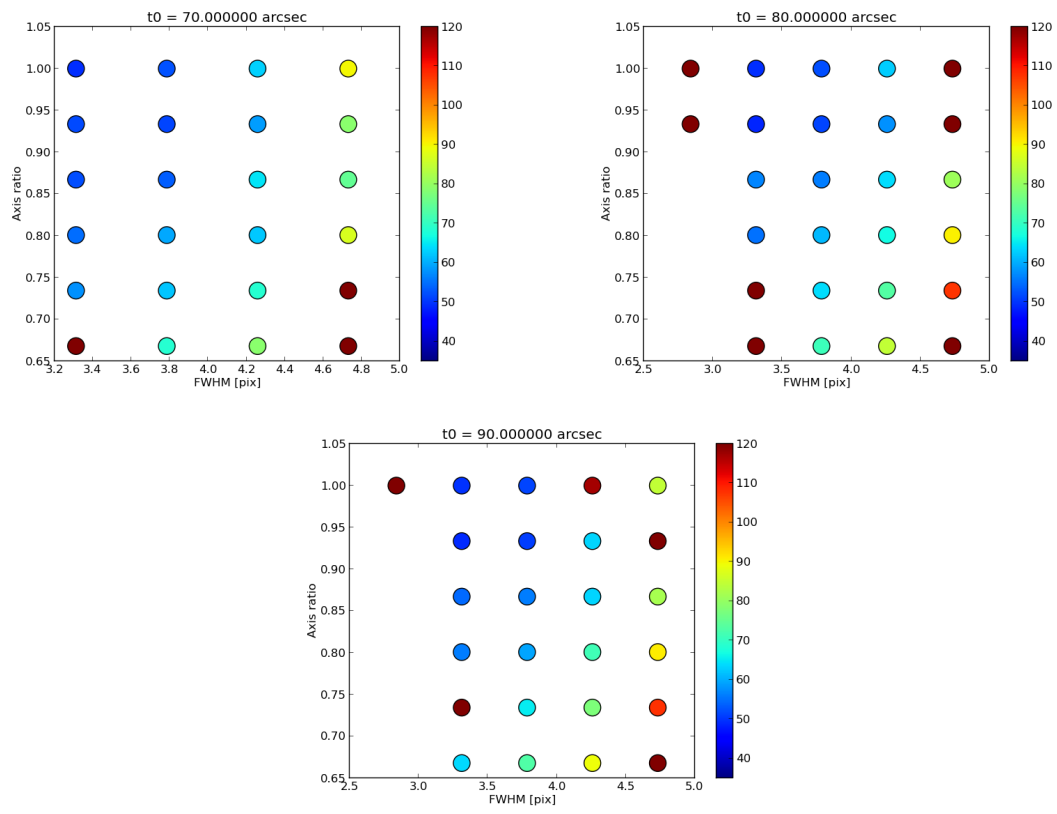


Figure 93 Continued.

C.2 J0146K

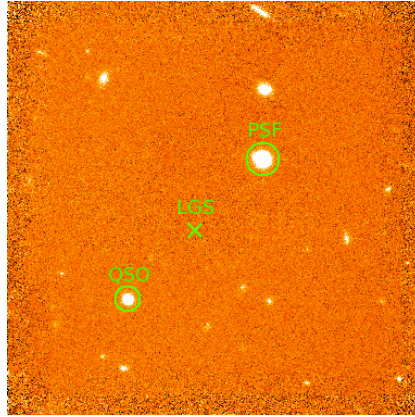


Figure 94 Final average combined image of J0146 K' -band.

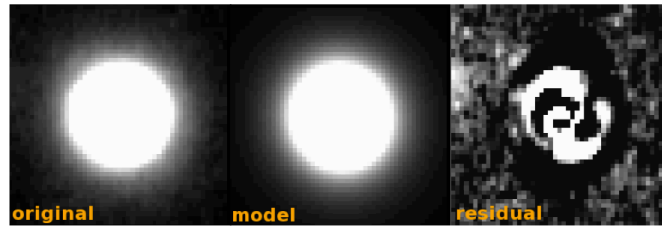


Figure 95 PSF reference star fitting result. Left : original PSF reference star image. Middle : best fit PSF model image. Right : residual image (original-model).

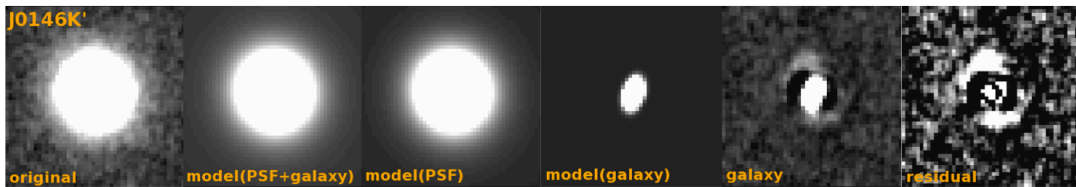


Figure 96 QSO fitting result. From left to right, original QSO image, best fit model(PSF+galaxy) image, best fit PSF model image, best fit galaxy model image, galaxy image (original - best fit PSF mode image), and residual image (original - model(PSF+galaxy) image).

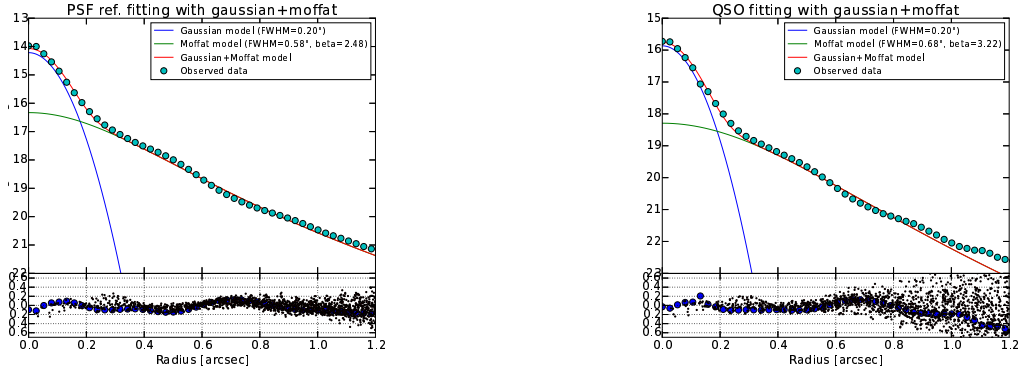


Figure 97 J0146K : Radial profile of PSF reference star (left) and QSO (right) when fitted with two components (Gaussian + Moffat).

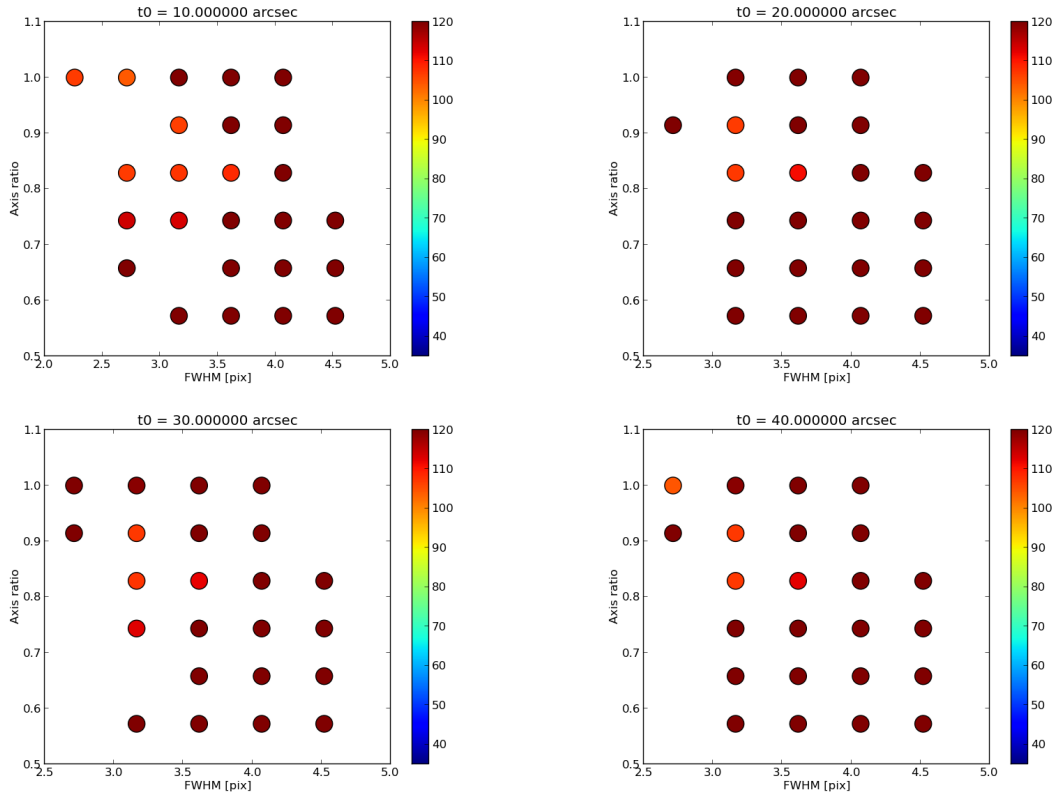


Figure 98 χ^2 map obtained by fitting of J0146 K' -band data. X-axis is FWHM [pix], and Y-axis is axis ratio. The color bar represents χ^2 value (blue=small, red=large). From top left figure to bottom right figure, θ_0 ["] = 10, 20, 30, ..., 90, 1000. $\theta_0=1000$ means that the same strehl ratio as PSF reference star is adopted to QSO. We adopted fitting result with the parameter set of q_g , $fwhm_g$ and θ_0 where χ^2 shows the minimum value, as the best fit parameter. For this object, $\theta_0=1000''$, $fwhm_g=2.69$ pix, and $q_g=0.91$.

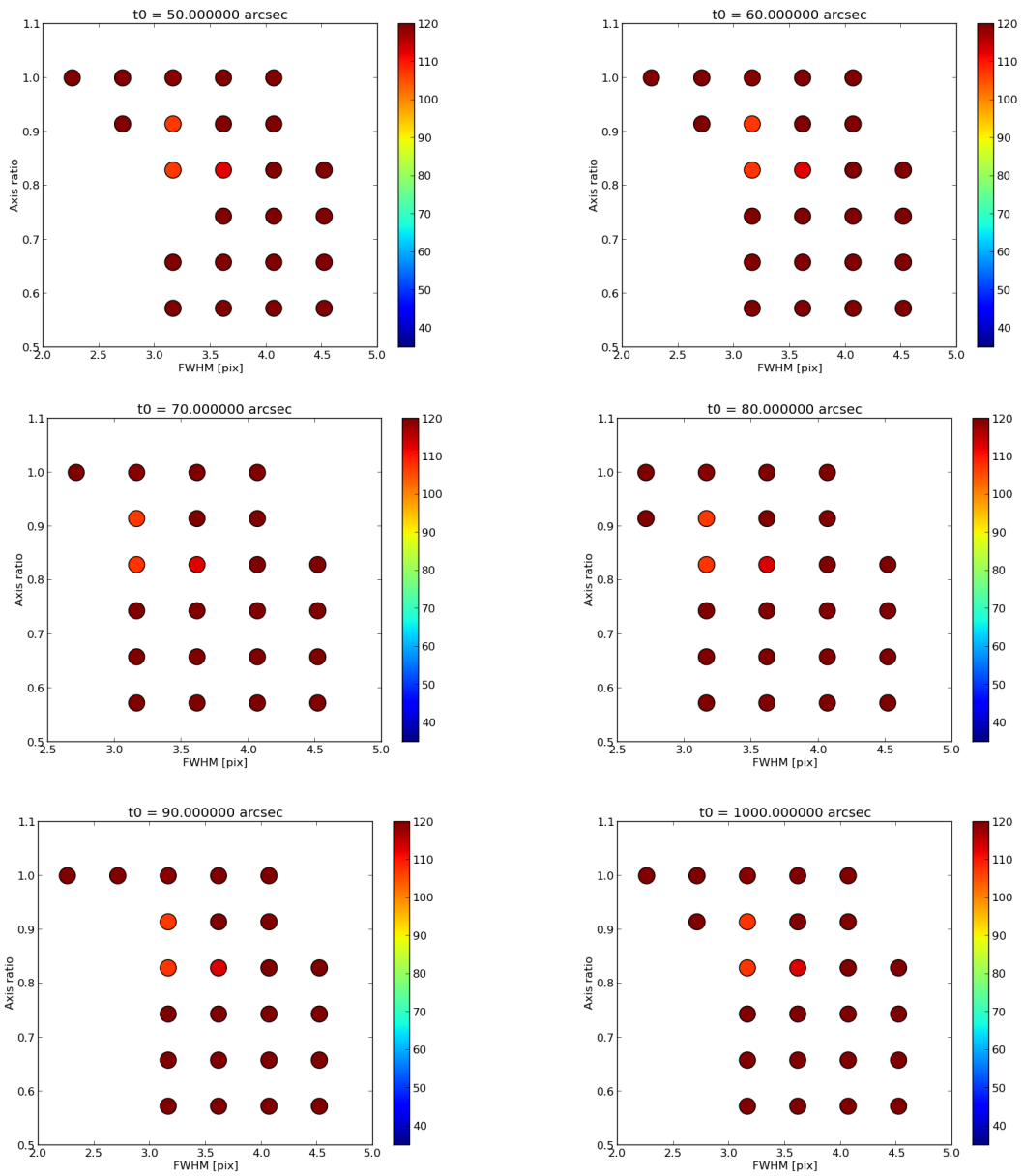


Figure 98 Continued.

C.3 J0725J

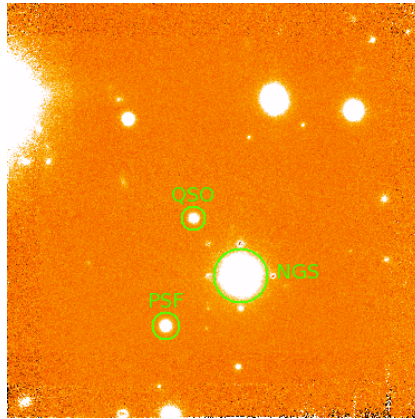


Figure 99 Final average combined image of J0725 *J*-band.

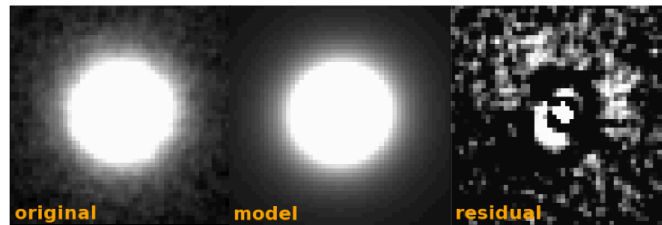


Figure 100 PSF reference star fitting result. Left : original PSF reference star image. Middle : best fit PSF model image. Right : residual image (original-model).

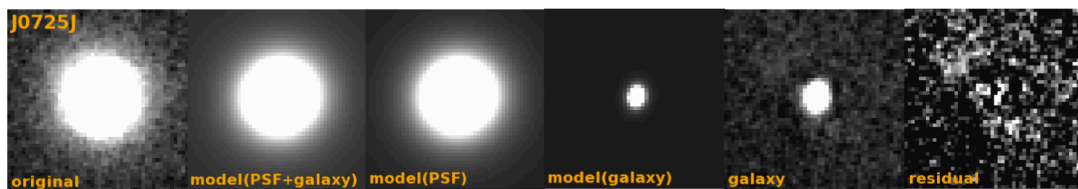


Figure 101 QSO fitting result. From left to right, original QSO image, best fit model(PSF+galaxy) image, best fit PSF model image, best fit galaxy model image, galaxy image (original – best fit PSF mode image), and residual image (original – model(PSF+galaxy) image).

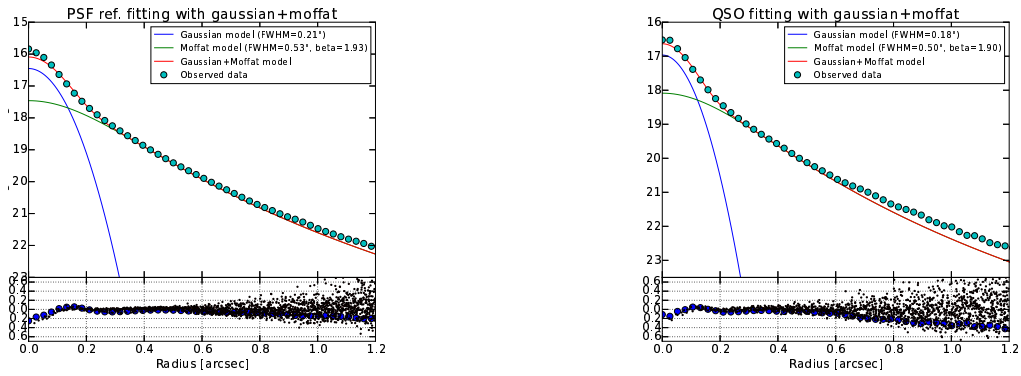


Figure 102 J0725J : Radial profile of PSF reference star (left) and QSO (right) when fitted with two components (Gaussian + Moffat).

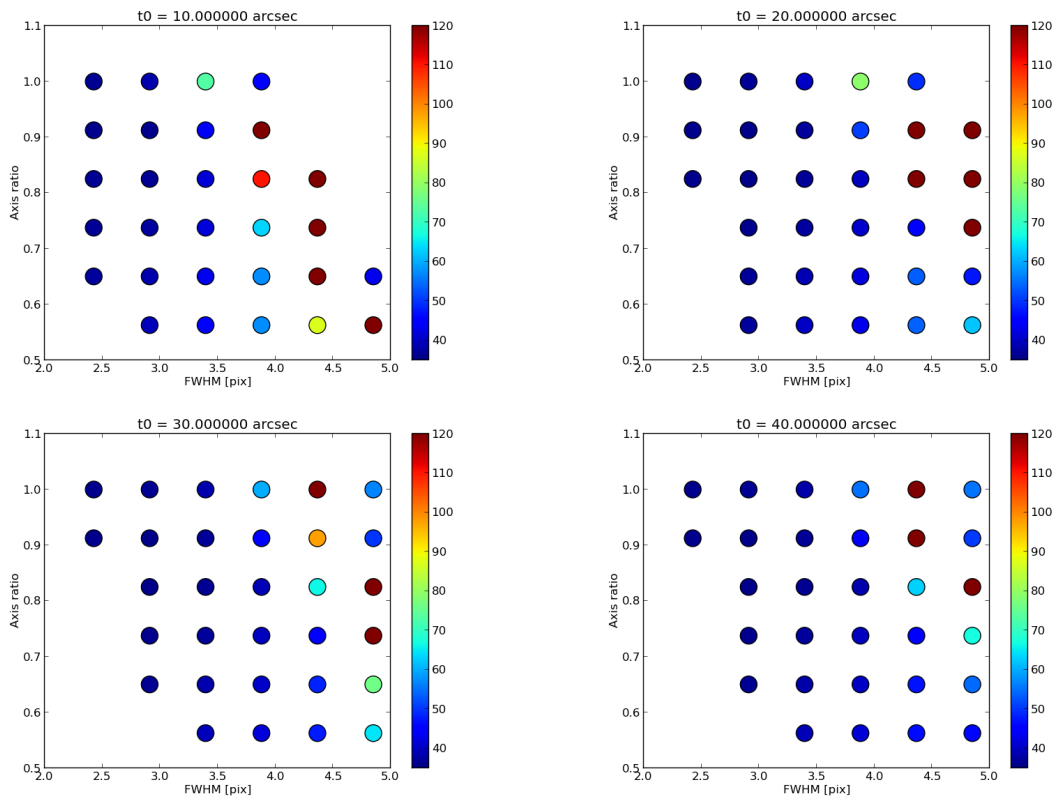


Figure 103 χ^2 map obtained by fitting of J0725 *J*-band data. X-axis is FWHM [pix], and Y-axis is axis ratio. The color bar represents χ^2 value (blue=small, red=large). From top left figure to bottom right figure, θ_0 ["] = 10, 20, 30, ..., 90, 1000. $\theta_0=1000$ means that the same strehl ratio as PSF reference star is adopted to QSO. We adopted fitting result with the parameter set of q_g , $fwhm_g$ and θ_0 where χ^2 shows the minimum value, as the best fit parameter. For this object, $\theta_0=1000''$, $fwhm_g=2.75$ pix, and $q_g=0.83$.

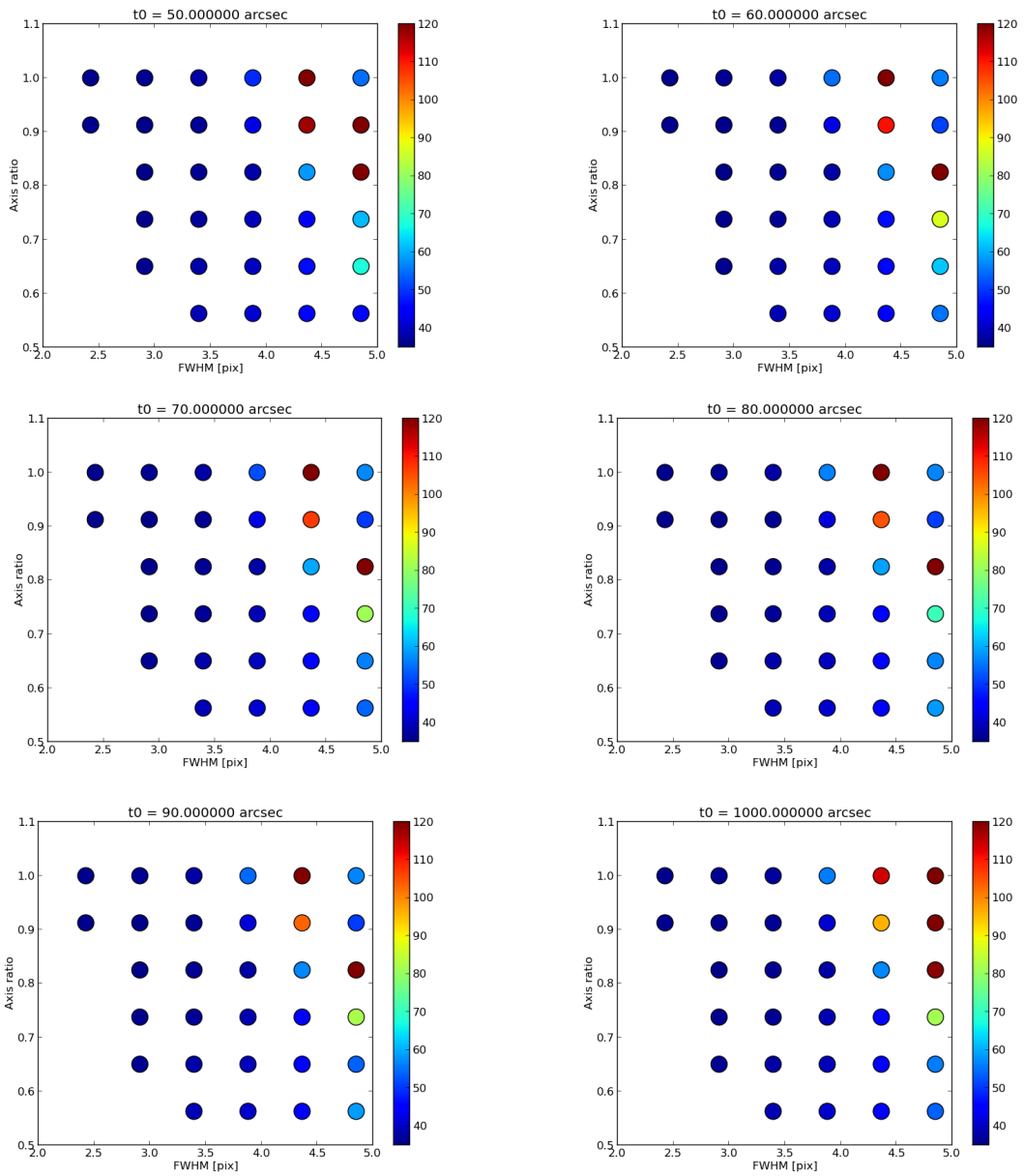


Figure 103 Continued.

C.4 J0725K

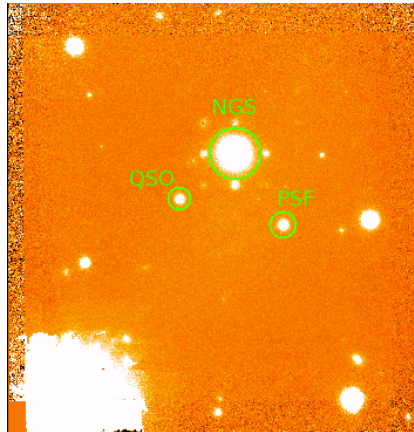


Figure 104 Final average combined image of J0725 K' -band.

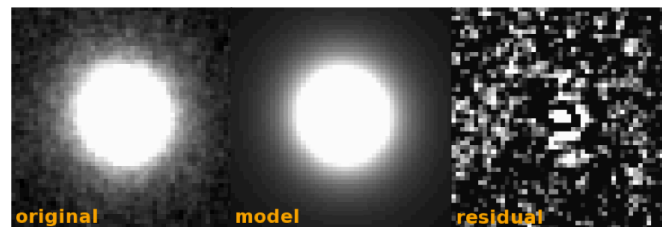


Figure 105 PSF reference star fitting result. Left : original PSF reference star image. Middle : best fit PSF model image. Right : residual image (original-model).

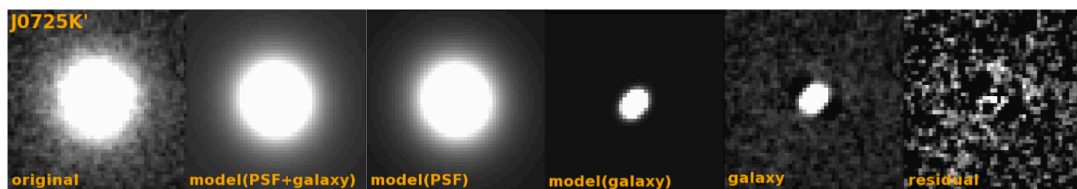


Figure 106 QSO fitting result. From left to right, original QSO image, best fit model(PSF+galaxy) image, best fit PSF model image, best fit galaxy model image, galaxy image (original - best fit PSF mode image), and residual image (original - model(PSF+galaxy) image).

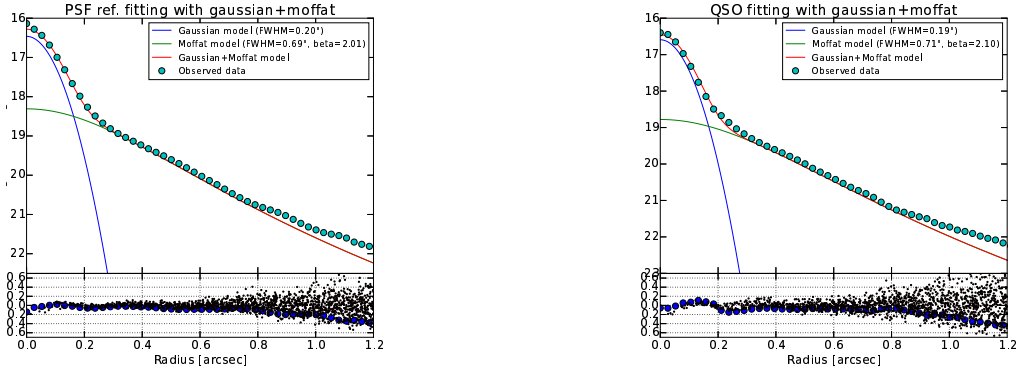


Figure 107 J0725K : Radial profile of PSF reference star (left) and QSO (right) when fitted with two components (Gaussian + Moffat).

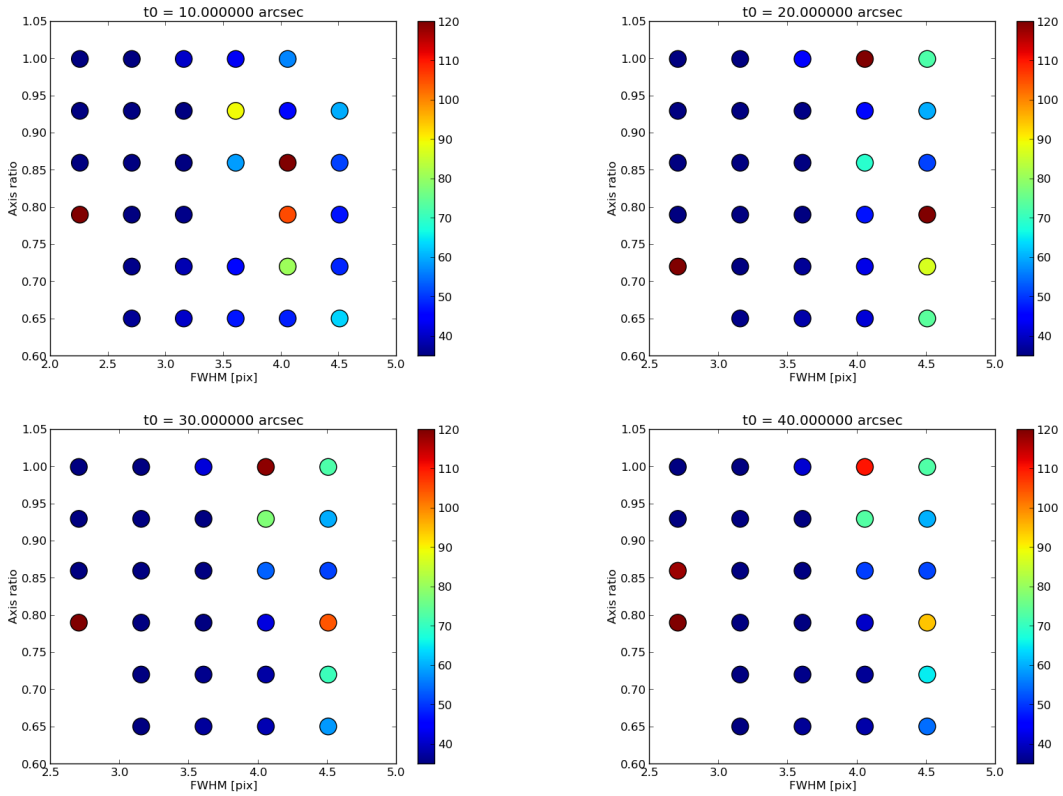


Figure 108 χ^2 map obtained by fitting of J0725 K' -band data. X-axis is FWHM [pix], and Y-axis is axis ratio. The color bar represents χ^2 value (blue=small, red=large). From top left figure to bottom right figure, θ_0 ["] = 10, 20, 30, ..., 90, 1000. $\theta_0=1000$ means that the same strehl ratio as PSF reference star is adopted to QSO. We adopted fitting result with the parameter set of q_g , $fwhm_g$ and θ_0 where χ^2 shows the minimum value, as the best fit parameter. For this object, $\theta_0=1000''$, $fwhm_g=2.70$ pix, and $q_g=0.93$.

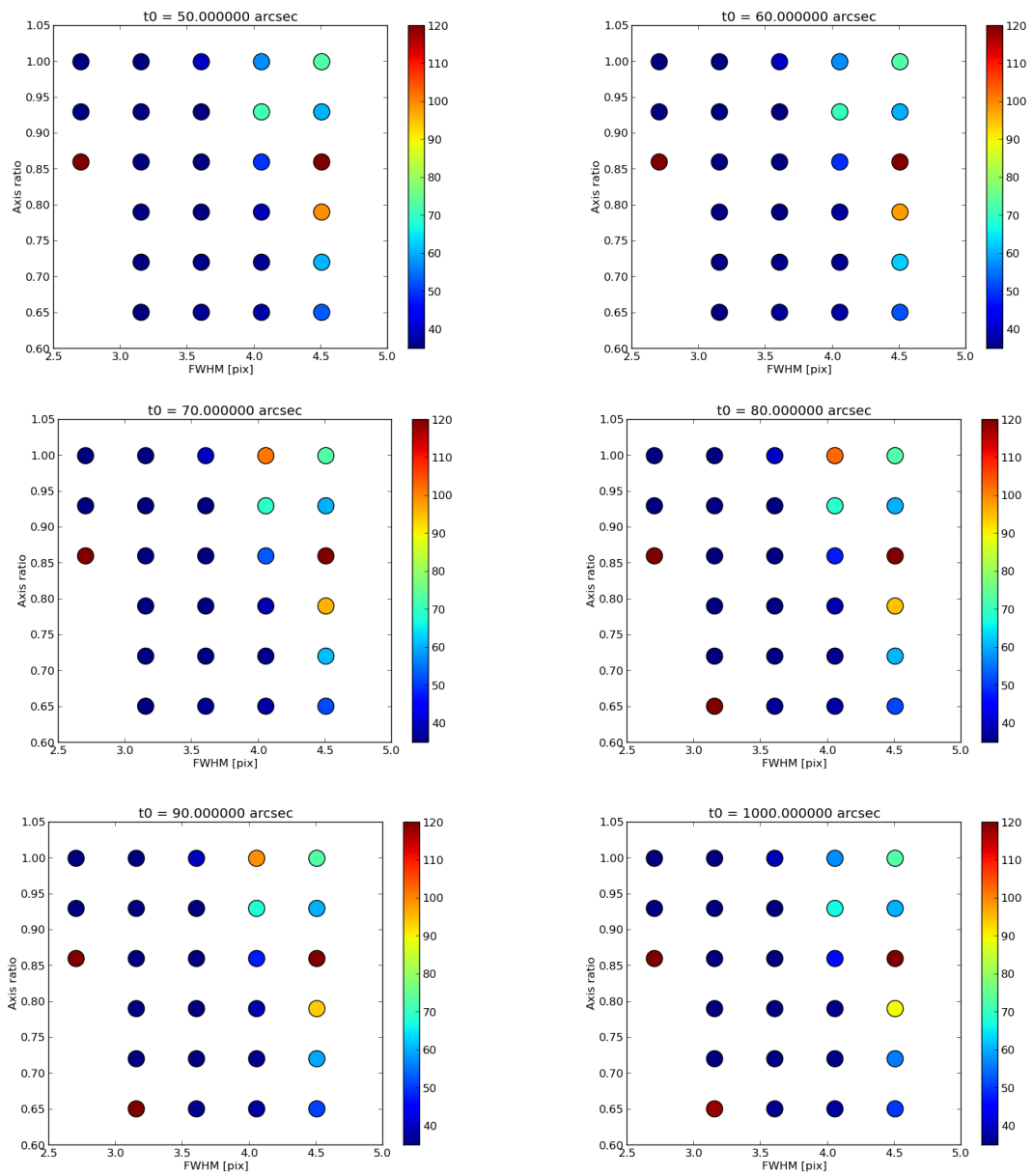


Figure 108 Continued.

C.5 J0847K

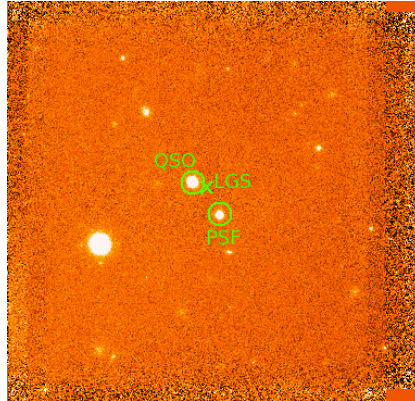


Figure 109 Final average combined image of J0847 K' -band.

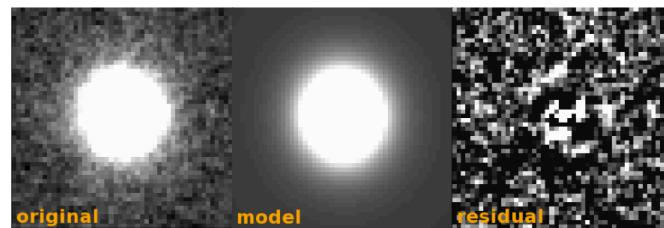


Figure 110 PSF reference star fitting result. Left : original PSF reference star image. Middle : best fit PSF model image. Right : residual image (original-model).

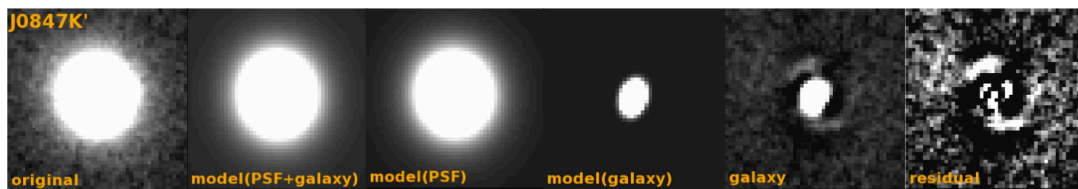


Figure 111 QSO fitting result. From left to right, original QSO image, best fit model(PSF+galaxy) image, best fit PSF model image, best fit galaxy model image, galaxy image (original - best fit PSF model image), and residual image (original - model(PSF+galaxy) image).

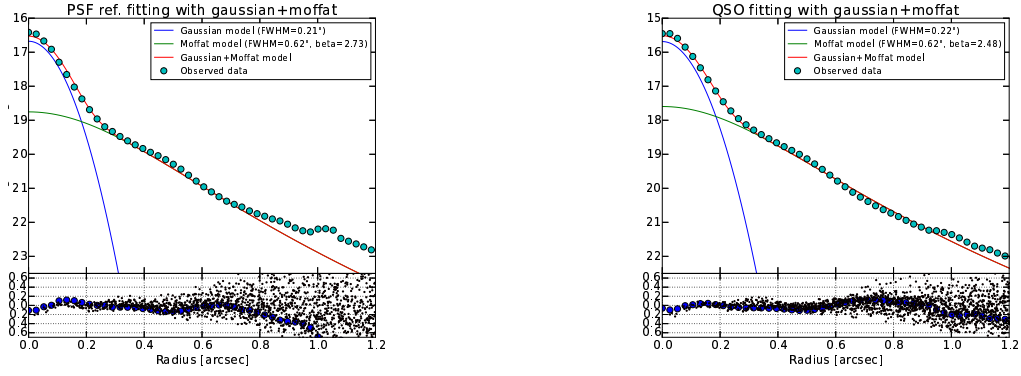


Figure 112 J0847K : Radial profile of PSF reference star (left) and QSO (right) when fitted with two components (Gaussian + Moffat).

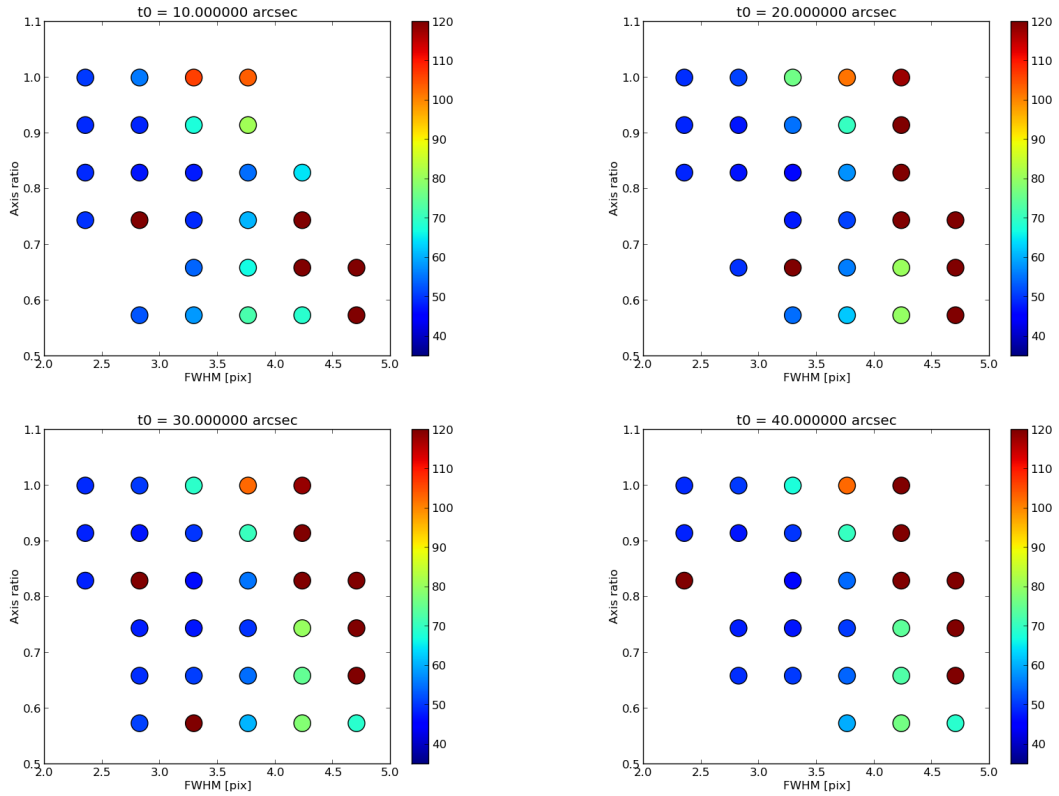


Figure 113 χ^2 map obtained by fitting of J0847 K' -band data. X-axis is FWHM [pix], and Y-axis is axis ratio. The color bar represents χ^2 value (blue=small, red=large). From top left figure to bottom right figure, θ_0 ["] = 10, 20, 30, ..., 90, 1000. $\theta_0=1000$ means that the same strehl ratio as PSF reference star is adopted to QSO. We adopted fitting result with the parameter set of q_g , $fwhm_g$ and θ_0 where χ^2 shows the minimum value, as the best fit parameter. For this object, $\theta_0=1000''$, $fwhm_g=3.07$ pix, and $q_g=0.83$.

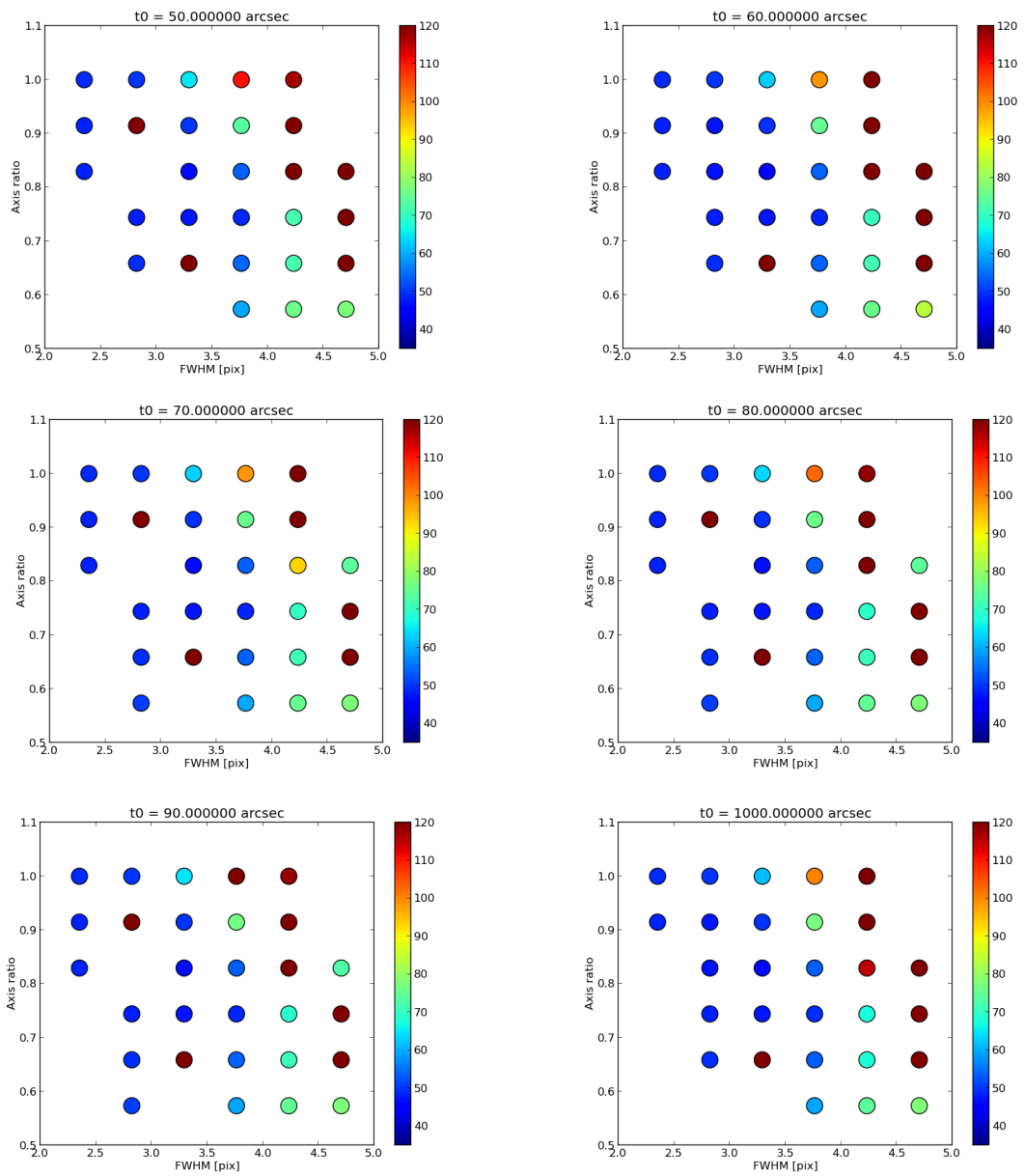


Figure 113 Continued.

C.6 J1116J

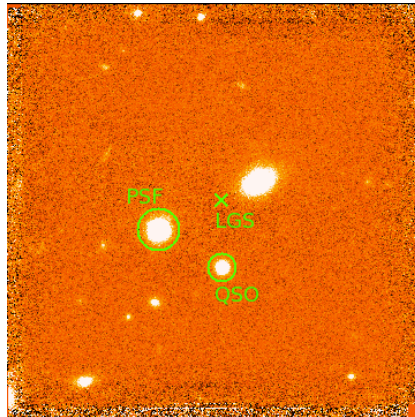


Figure 114 Final average combined image of J1116 *J*-band.

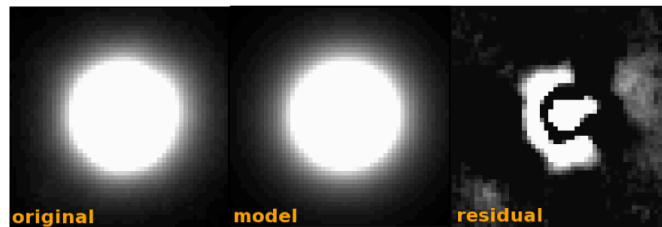


Figure 115 PSF reference star fitting result. Left : original PSF reference star image. Middle : best fit PSF model image. Right : residual image (original-model).

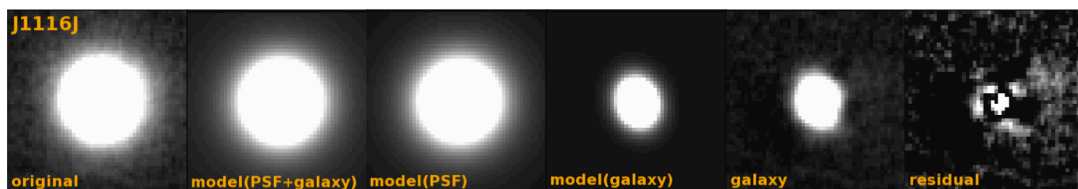


Figure 116 QSO fitting result. From left to right, original QSO image, best fit model(PSF+galaxy) image, best fit PSF model image, best fit galaxy model image, galaxy image (original – best fit PSF mode image), and residual image (original – model(PSF+galaxy) image).

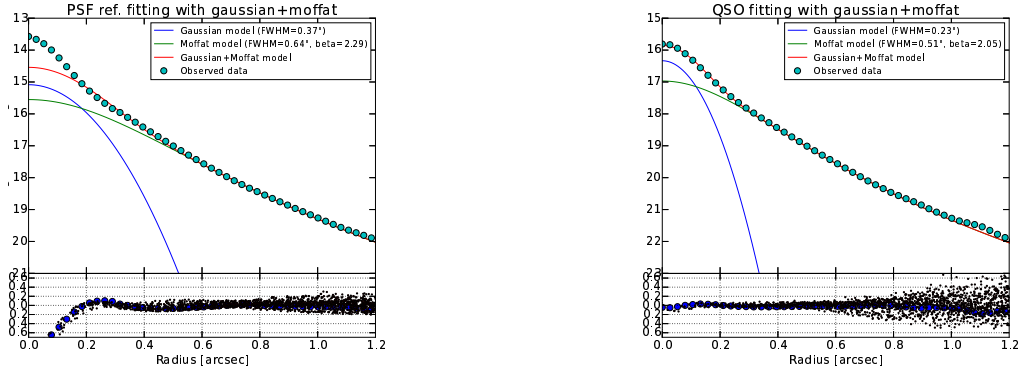


Figure 117 J1116J : Radial profile of PSF reference star (left) and QSO (right) when fitted with two components (Gaussian + Moffat).

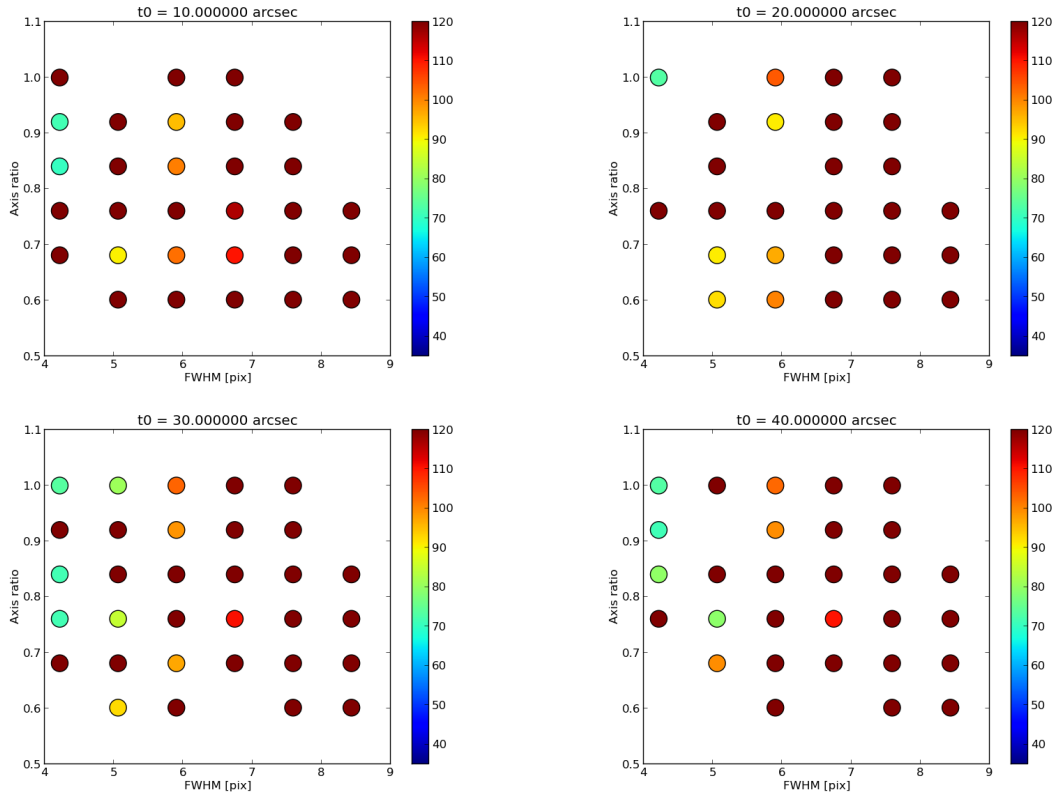


Figure 118 χ^2 map obtained by fitting of J1116 *J*-band data. X-axis is FWHM [pix], and Y-axis is axis ratio. The color bar represents χ^2 value (blue=small, red=large). From top left figure to bottom right figure, θ_0 ["] = 10, 20, 30, ..., 90, 1000. $\theta_0=1000$ means that the same strehl ratio as PSF reference star is adopted to QSO. We adopted fitting result with the parameter set of q_g , $fwhm_g$ and θ_0 where χ^2 shows the minimum value, as the best fit parameter. For this object, $\theta_0=1000''$, $fwhm_g=4.22$ pix, and $q_g=0.84$.

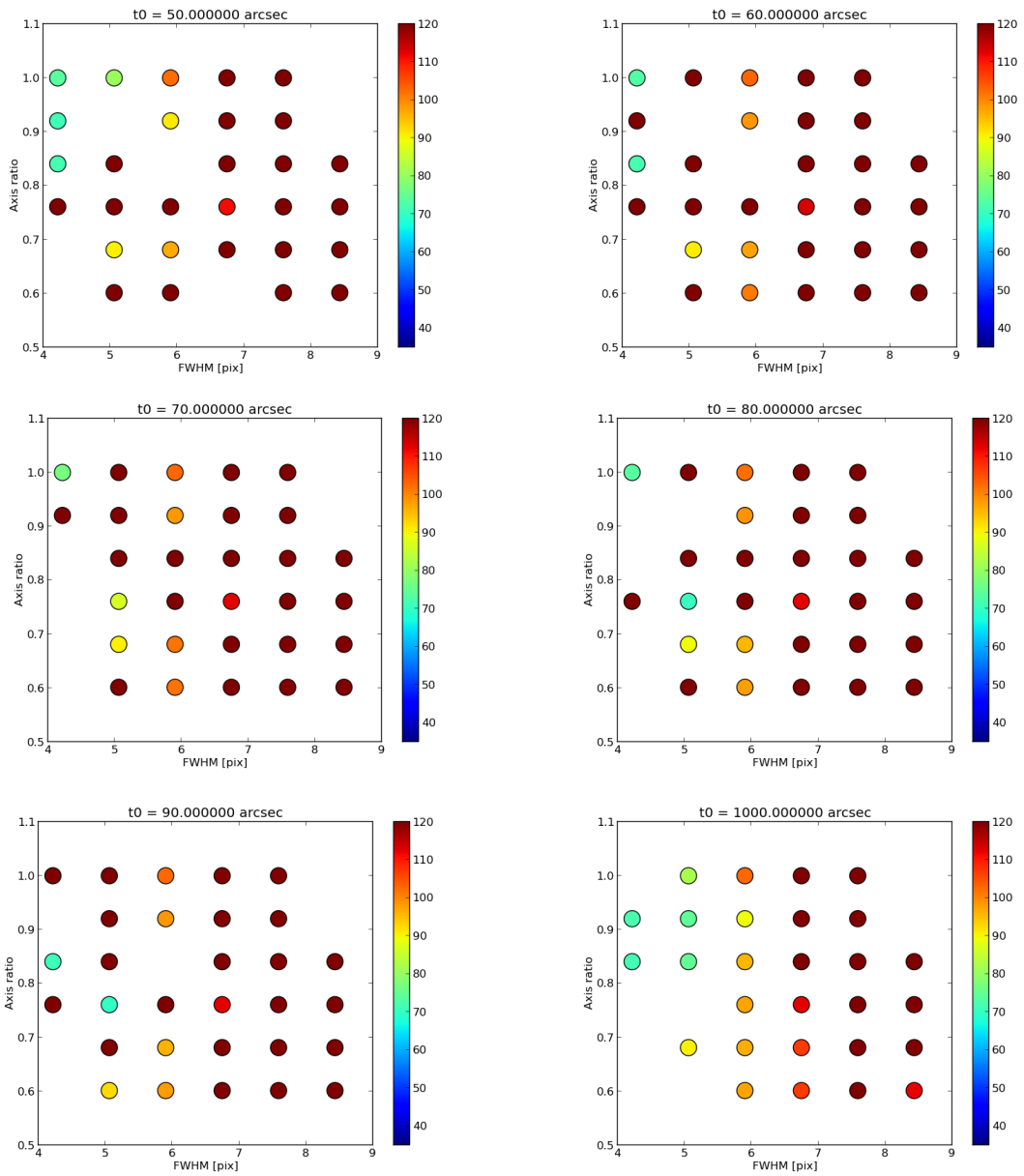


Figure 118 Continued.

C.7 J1116K

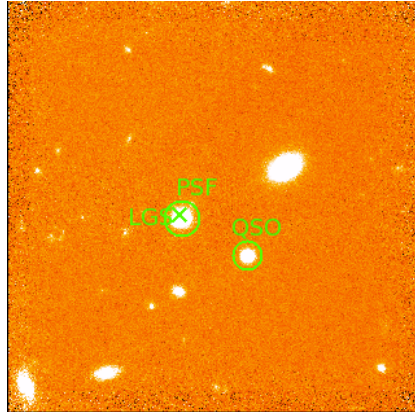


Figure 119 Final average combined image of J1116 K' -band.

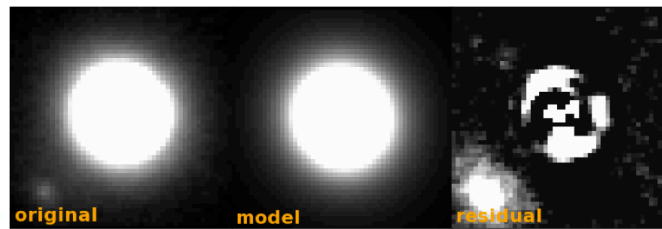


Figure 120 PSF reference star fitting result. Left : original PSF reference star image. Middle : best fit PSF model image. Right : residual image (original-model).

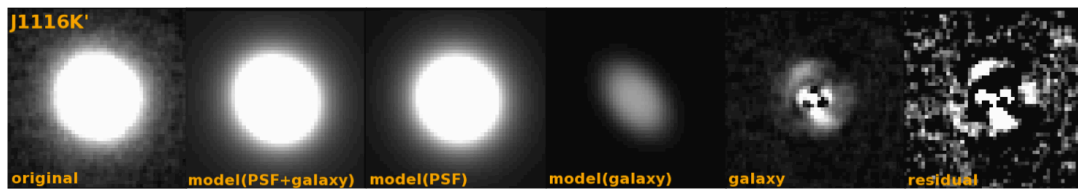


Figure 121 QSO fitting result. From left to right, original QSO image, best fit model(PSF+galaxy) image, best fit PSF model image, best fit galaxy model image, galaxy image (original – best fit PSF mode image), and residual image (original – model(PSF+galaxy) image).

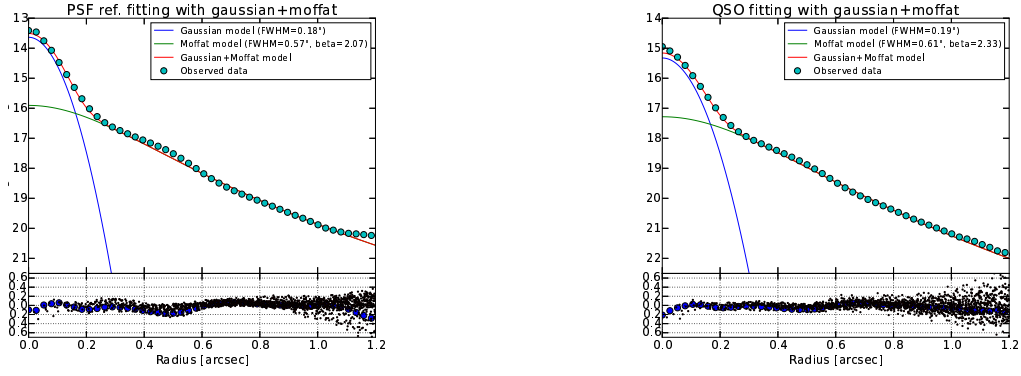


Figure 122 J1116K : Radial profile of PSF reference star (left) and QSO (right) when fitted with two components (Gaussian + Moffat).

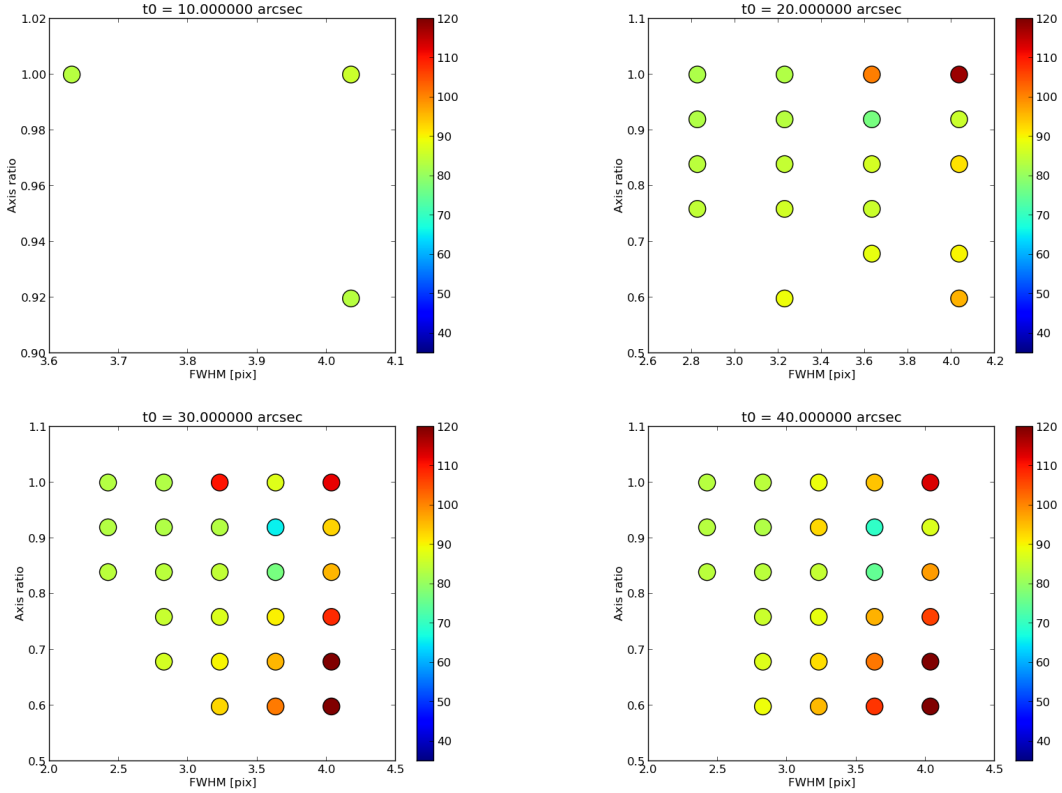


Figure 123 χ^2 map obtained by fitting of J1116 K' -band data. X-axis is FWHM [pix], and Y-axis is axis ratio. The color bar represents χ^2 value (blue=small, red=large). From top left figure to bottom right figure, θ_0 ["] = 10, 20, 30, ..., 90. We adopted fitting result with the parameter set of q_g , $fwhm_g$ and θ_0 where χ^2 shows the minimum value, as the best fit parameter. For this object, $\theta_0=30''$, $fwhm_g=3.63$ pix, and $q_g=0.92$.

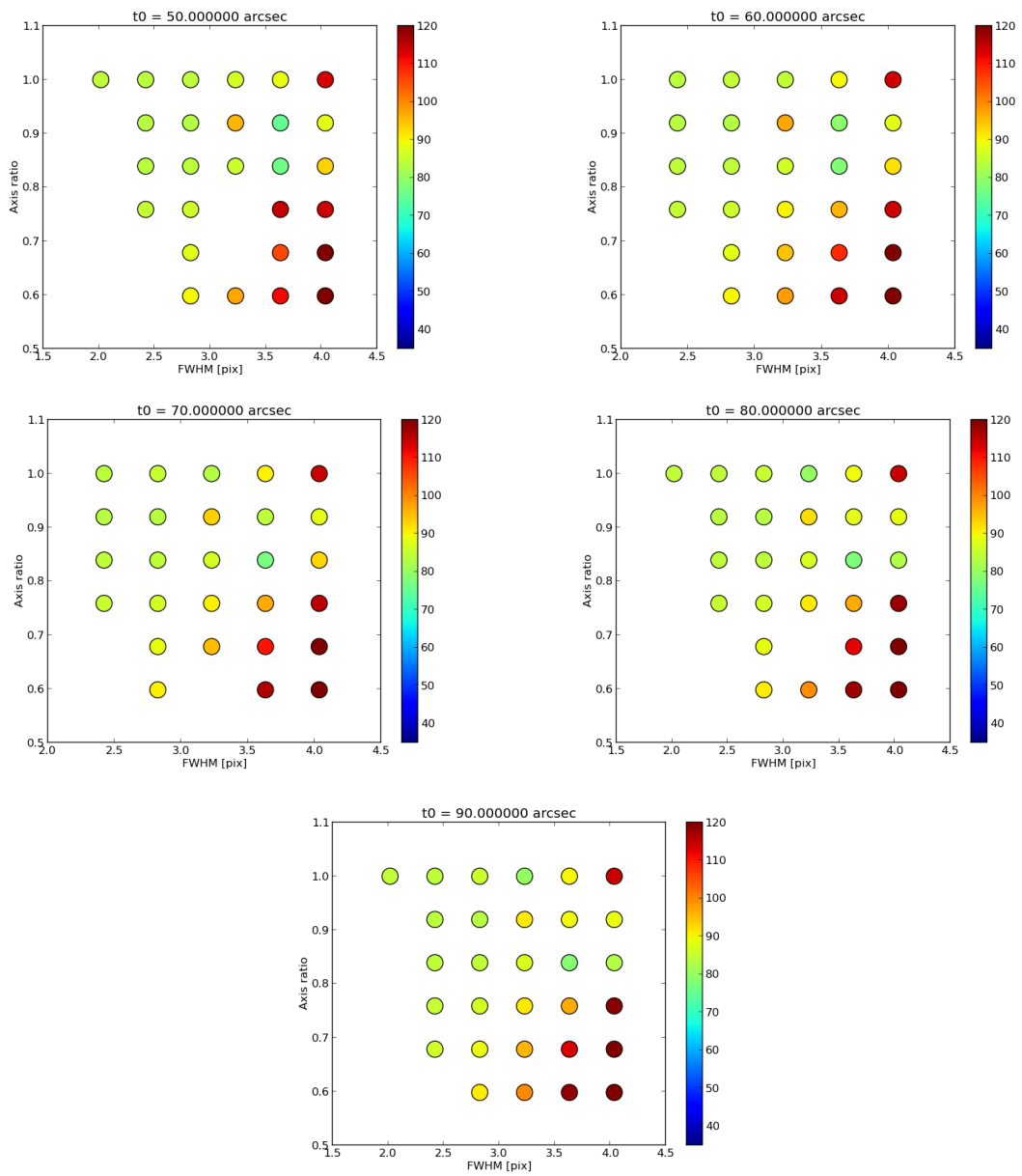


Figure 123 Continued.

C.8 J1337J

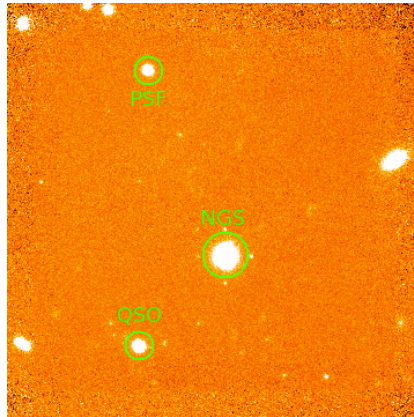


Figure 124 Final average combined image of J1337 *J*-band.

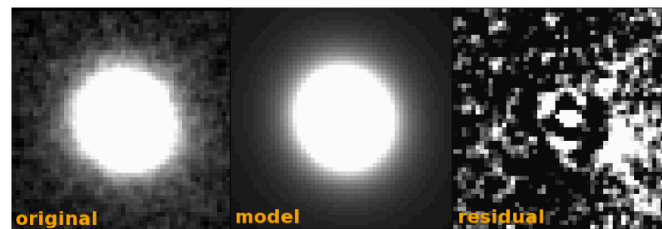


Figure 125 PSF reference star fitting result. Left : original PSF reference star image. Middle : best fit PSF model image. Right : residual image (original-model).

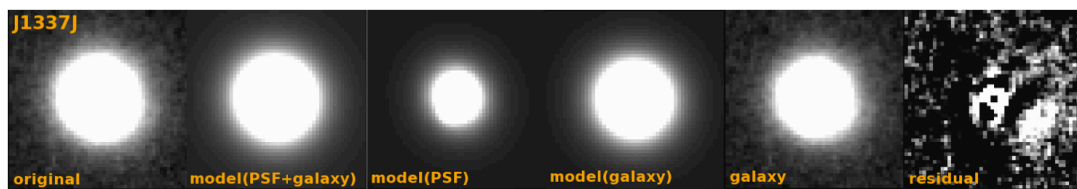


Figure 126 QSO fitting result. From left to right, original QSO image, best fit model(PSF+galaxy) image, best fit PSF model image, best fit galaxy model image, galaxy image (original – best fit PSF mode image), and residual image (original – model(PSF+galaxy) image).

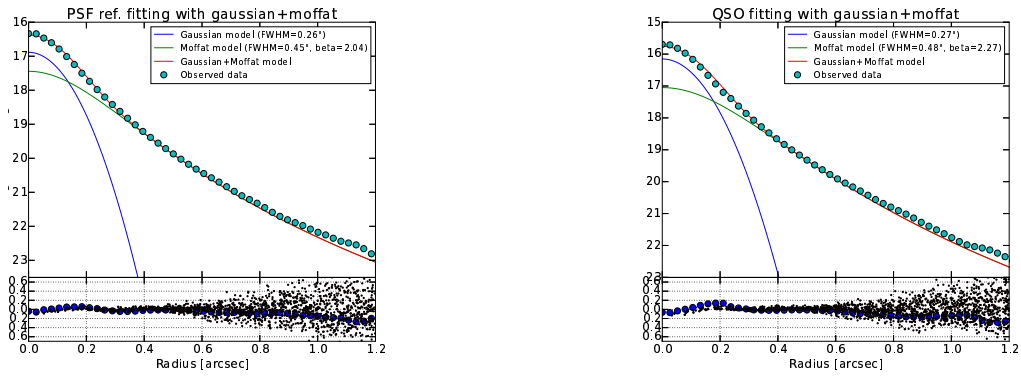


Figure 127 J1337J : Radial profile of PSF reference star (left) and QSO (right) when fitted with two components (Gaussian + Moffat).

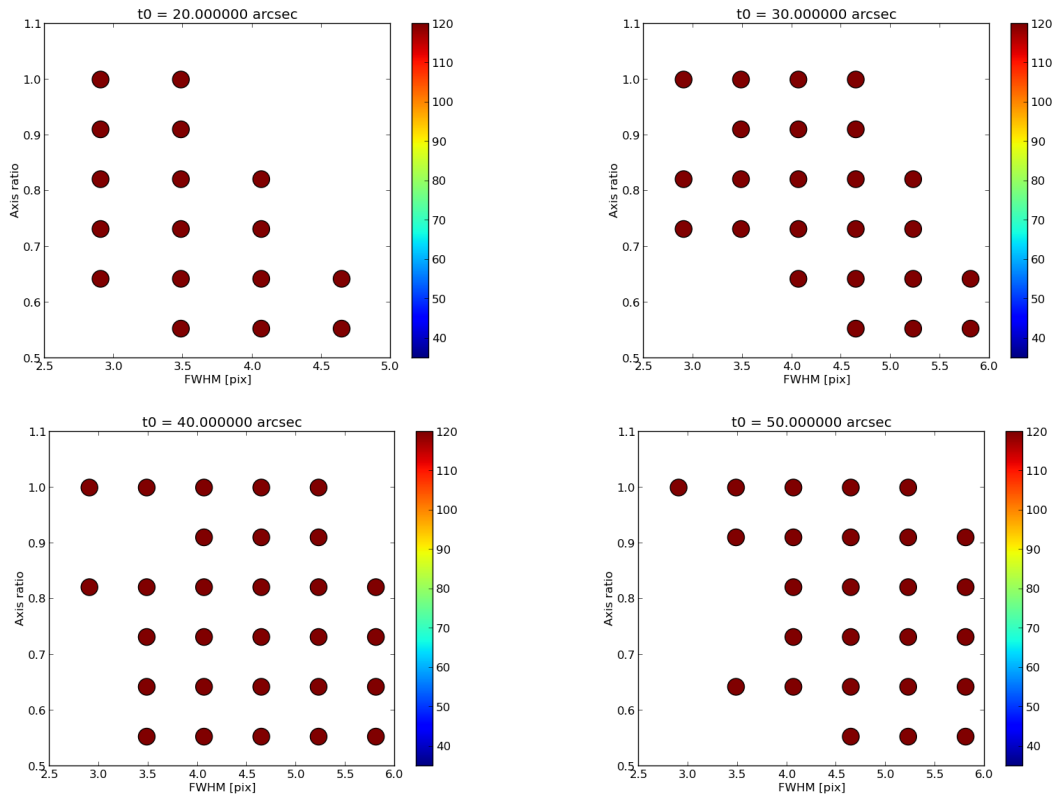


Figure 128 χ^2 map obtained by fitting of J1337 *J*-band data. X-axis is FWHM [pix], and Y-axis is axis ratio. The color bar represents χ^2 value (blue=small, red=large). From top left figure to bottom right figure, θ_0 ["] = 20, 30, 40, ..., 90. We adopted fitting result with the parameter set of q_g , $fwhm_g$ and θ_0 where χ^2 shows the minimum value, as the best fit parameter. For this object, $\theta_0=30''$, $fwhm_g=5.81$ pix, and $q_g=0.64$.

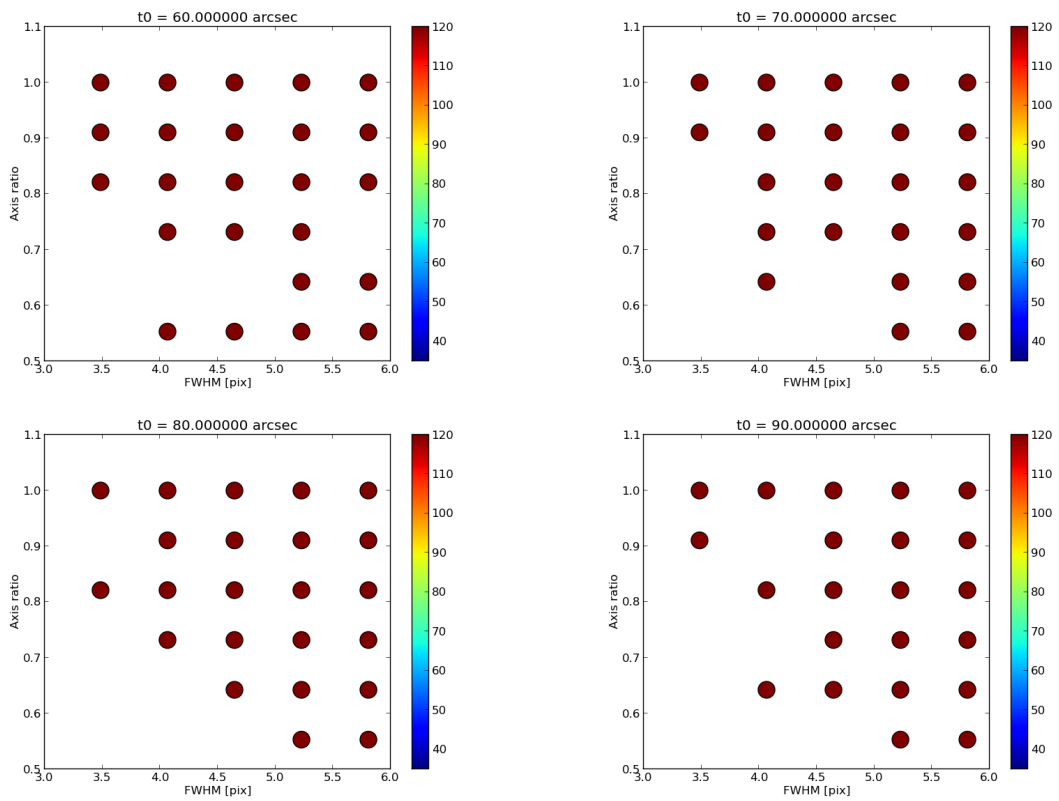


Figure 128 Continued.

C.9 J1337K

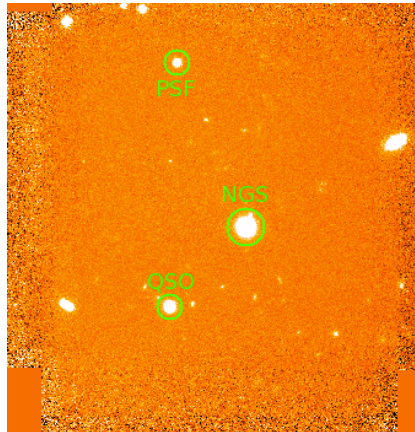


Figure 129 Final average combined image of J1337 K' -band.

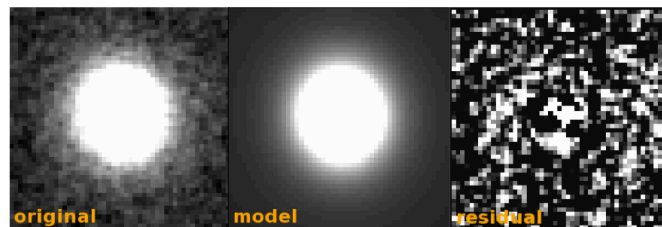


Figure 130 PSF reference star fitting result. Left : original PSF reference star image. Middle : best fit PSF model image. Right : residual image (original-model).

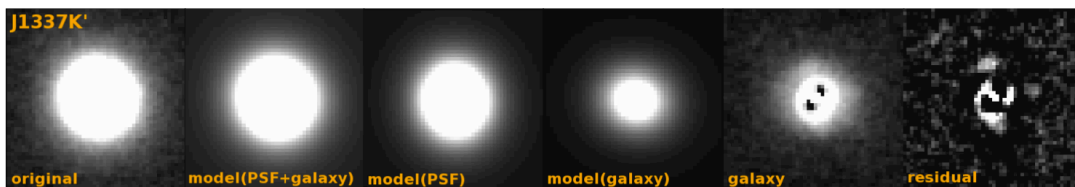


Figure 131 QSO fitting result. From left to right, original QSO image, best fit model(PSF+galaxy) image, best fit PSF model image, best fit galaxy model image, galaxy image (original - best fit PSF model image), and residual image (original - model(PSF+galaxy) image).

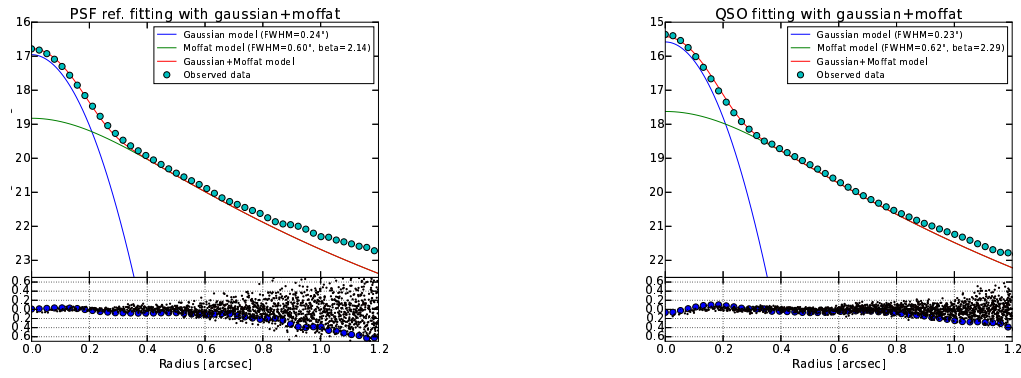


Figure 132 J1337K : Radial profile of PSF reference star (left) and QSO (right) when fitted with two components (Gaussian + Moffat).

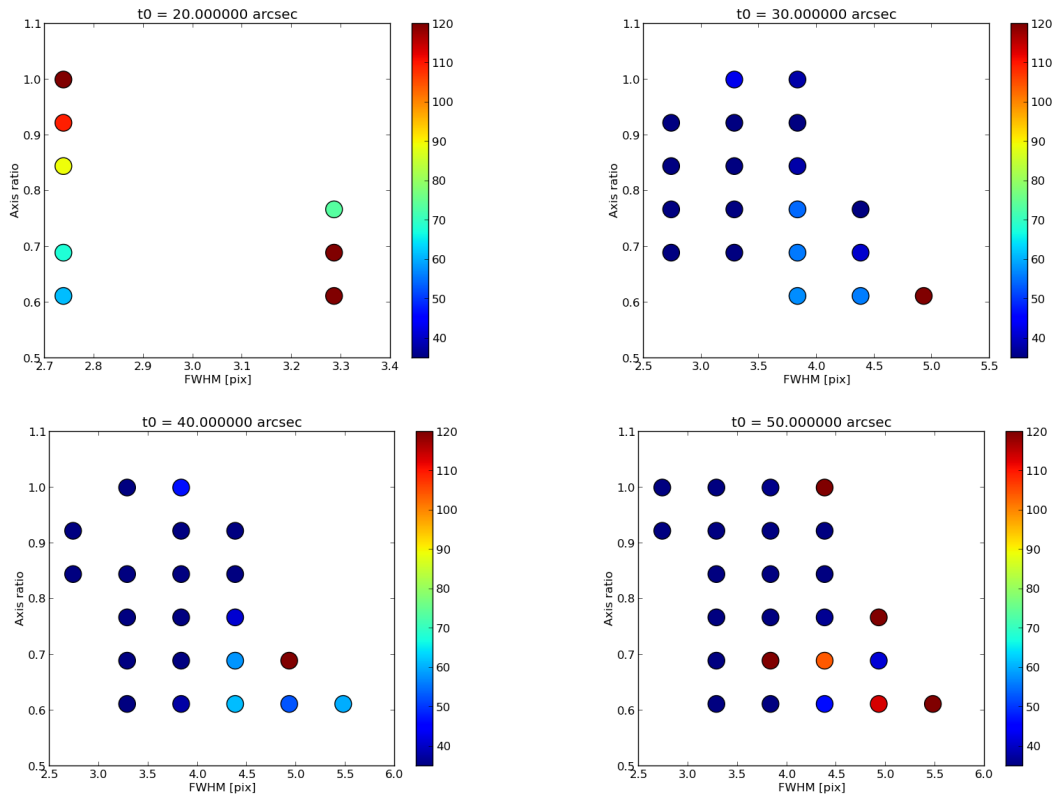


Figure 133 χ^2 map obtained by fitting of J1337 K' -band data. X-axis is FWHM [pix], and Y-axis is axis ratio. The color bar represents χ^2 value (blue=small, red=large). From top left figure to bottom right figure, θ_0 ["] = 20, 30, 40, ..., 90. We adopted fitting result with the parameter set of q_g , $fwhm_g$ and θ_0 where χ^2 shows the minimum value, as the best fit parameter. For this object, $\theta_0=40''$, $fwhm_g=4.06$ pix, and $q_g=0.84$.

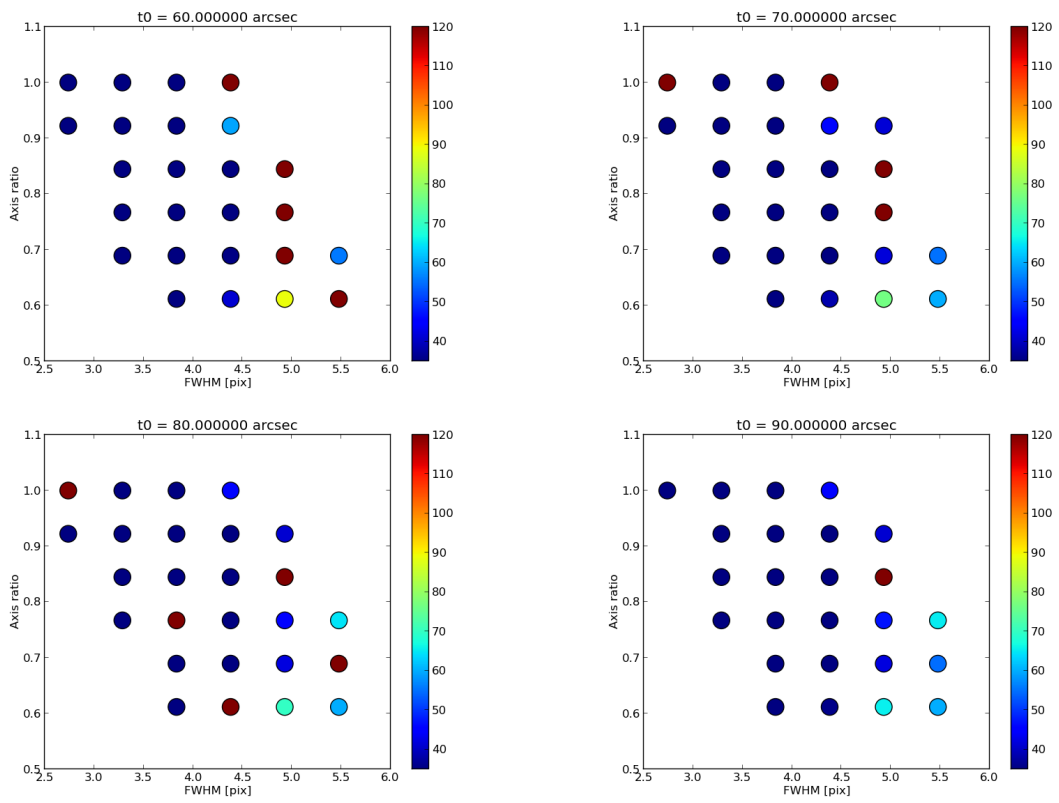


Figure 133 Continued.

C.10 J1407J

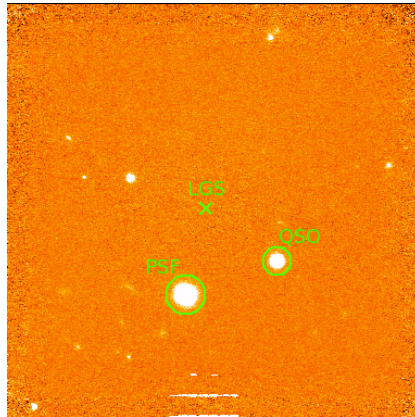


Figure 134 Final average combined image of J1407 *J*-band.

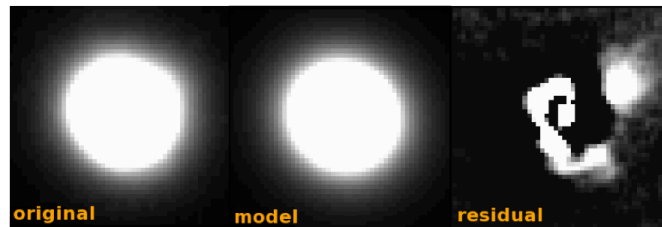


Figure 135 PSF reference star fitting result. Left : original PSF reference star image. Middle : best fit PSF model image. Right : residual image (original-model).

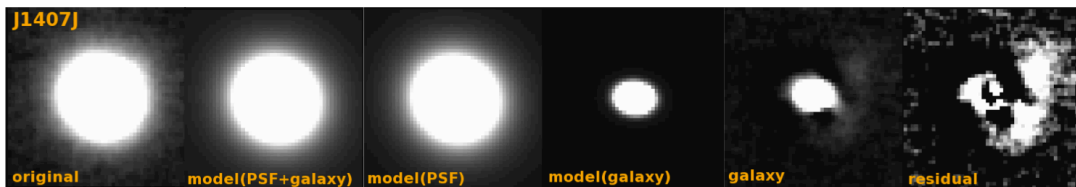


Figure 136 QSO fitting result. From left to right, original QSO image, best fit model(PSF+galaxy) image, best fit PSF model image, best fit galaxy model image, galaxy image (original – best fit PSF mode image), and residual image (original – model(PSF+galaxy) image).

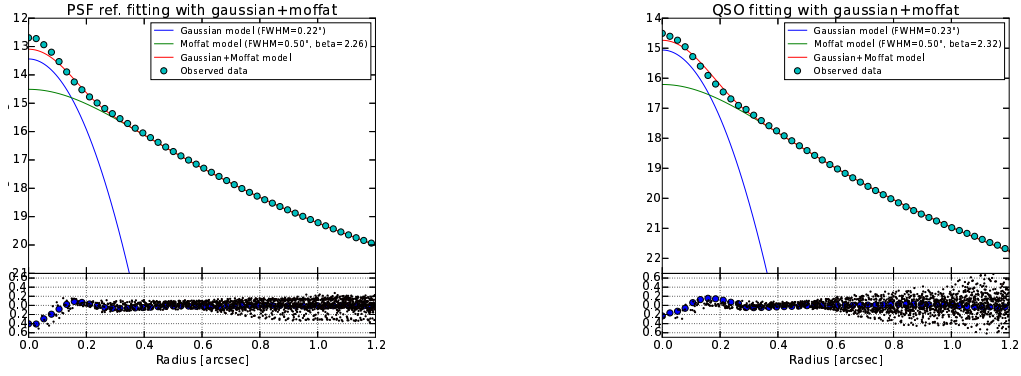


Figure 137 J1407J : Radial profile of PSF reference star (left) and QSO (right) when fitted with two components (Gaussian + Moffat).

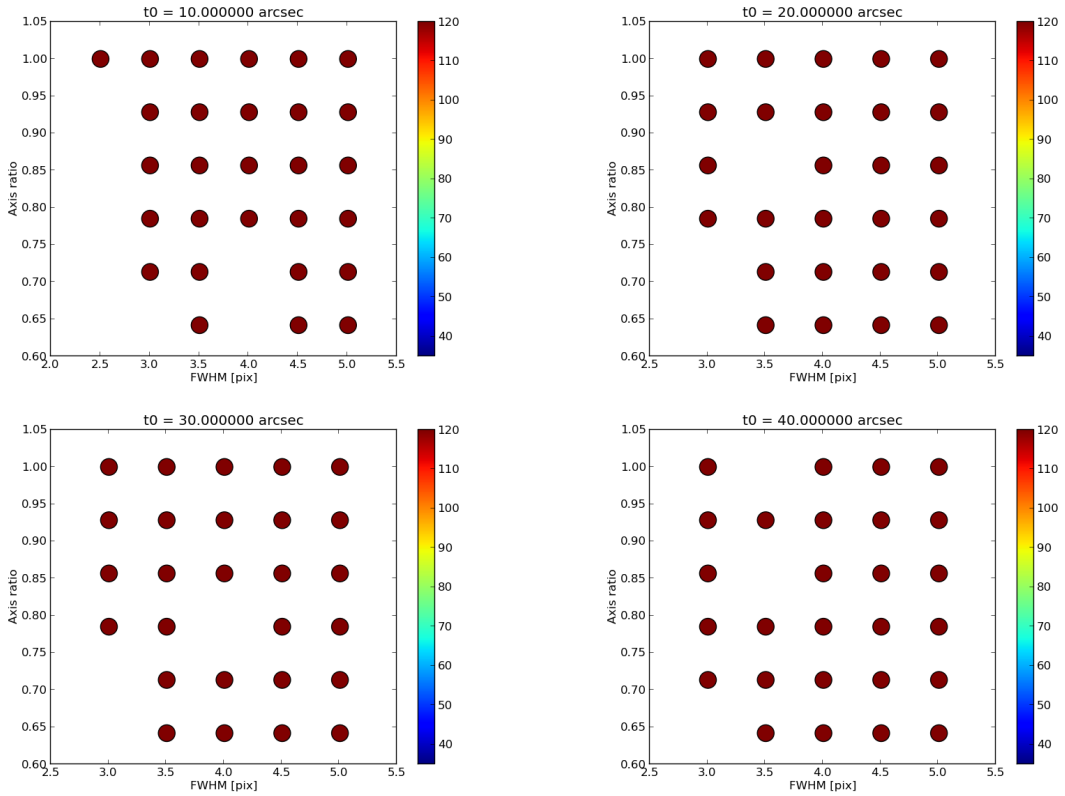


Figure 138 χ^2 map obtained by fitting of J1407 *J*-band data. X-axis is FWHM [pix], and Y-axis is axis ratio. The color bar represents χ^2 value (blue=small, red=large). From top left figure to bottom right figure, θ_0 ["] = 10, 20, 30, ..., 90, 1000. $\theta_0=1000$ means that the same strehl ratio as PSF reference star is adopted to QSO. We adopted fitting result with the parameter set of q_g , $fwhm_g$ and θ_0 where χ^2 shows the minimum value, as the best fit parameter. For this object, $\theta_0=1000''$, $fwhm_g=3.00$ pix, and $q_g=0.79$.

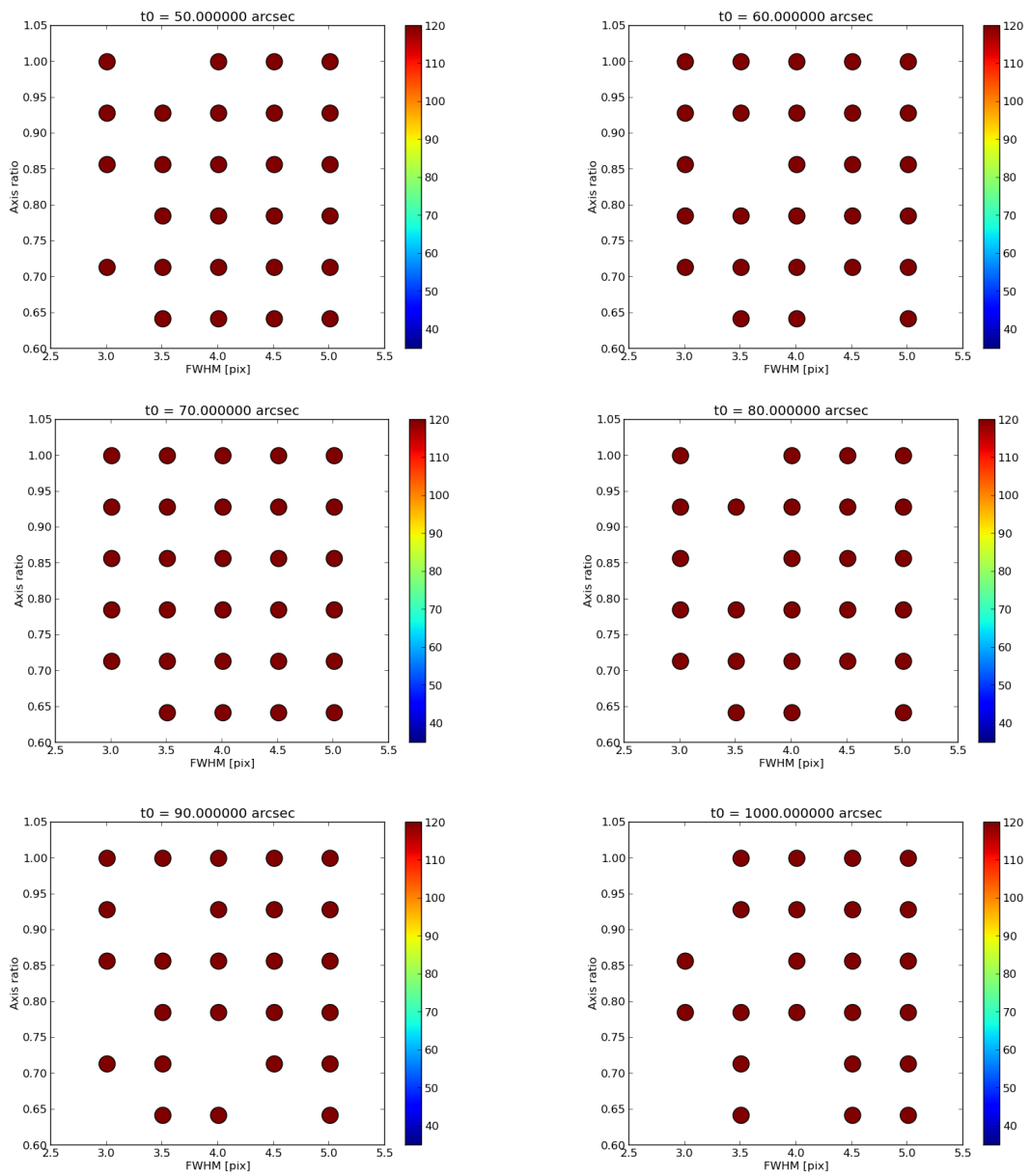


Figure 138 Continued.

C.11 J1407K

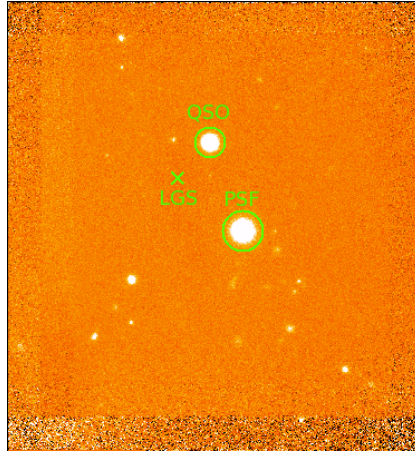


Figure 139 Final average combined image of J1407 K' -band.

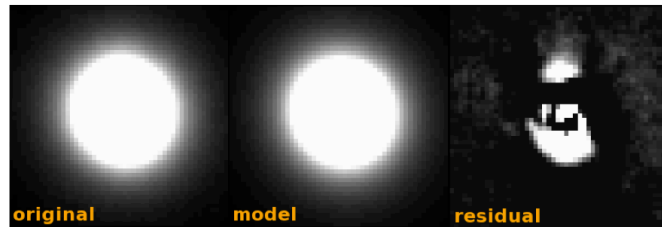


Figure 140 PSF reference star fitting result. Left : original PSF reference star image. Middle : best fit PSF model image. Right : residual image (original-model).

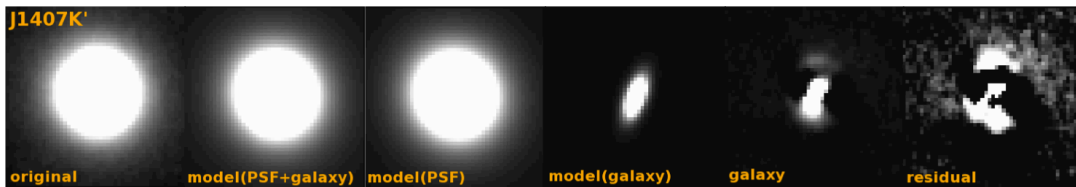


Figure 141 QSO fitting result. From left to right, original QSO image, best fit model(PSF+galaxy) image, best fit PSF model image, best fit galaxy model image, galaxy image (original – best fit PSF mode image), and residual image (original – model(PSF+galaxy) image).

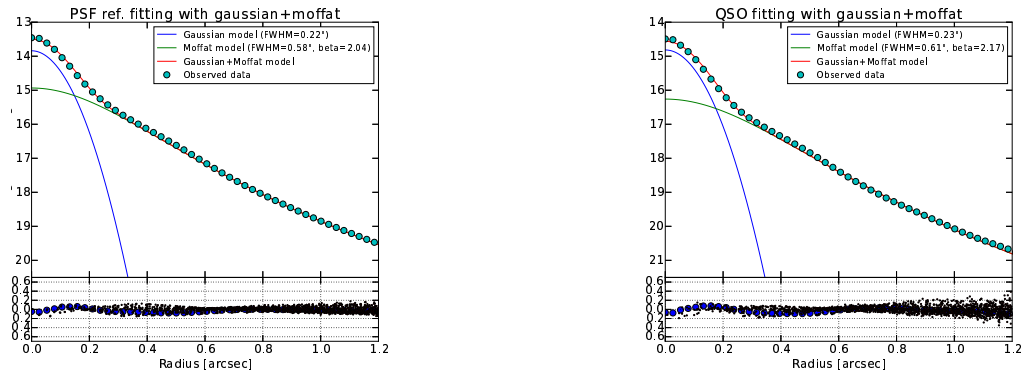


Figure 142 J1407K : Radial profile of PSF reference star (left) and QSO (right) when fitted with two components (Gaussian + Moffat).

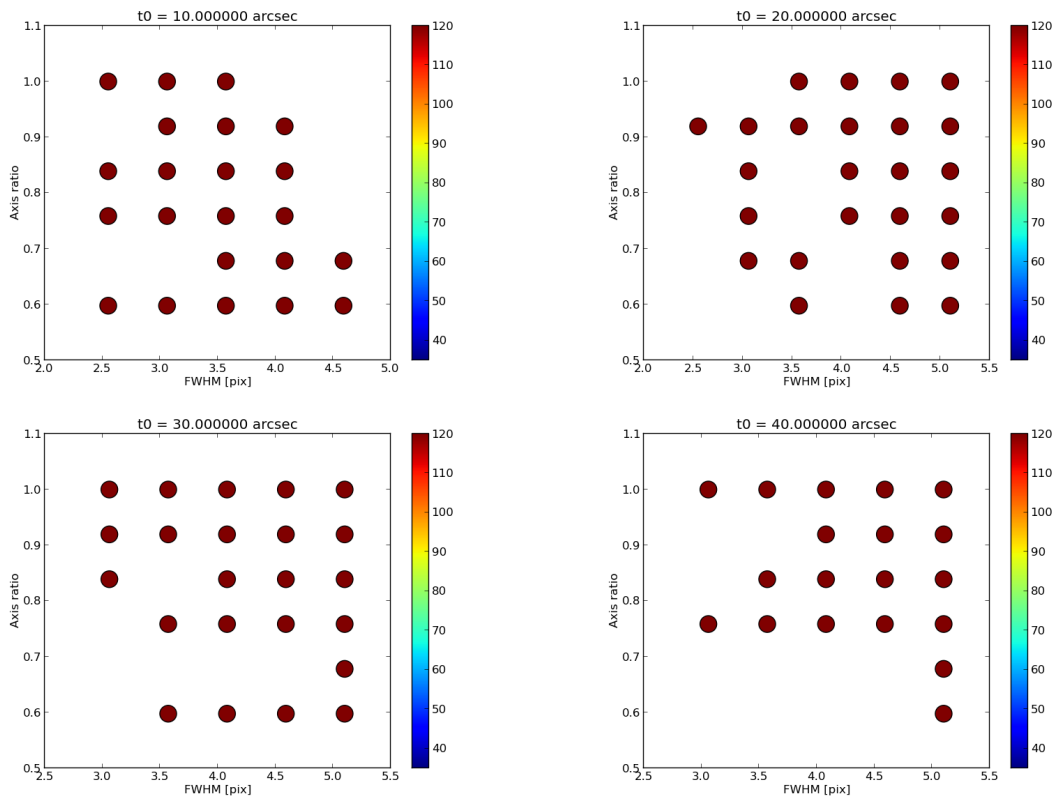


Figure 143 χ^2 map obtained by fitting of J1407 K' -band data. X-axis is FWHM [pix], and Y-axis is axis ratio. The color bar represents χ^2 value (blue=small, red=large). From top left figure to bottom right figure, θ_0 ["] = 10, 20, 30, ..., 90, 1000. $\theta_0=1000$ means that the same strehl ratio as PSF reference star is adopted to QSO. We adopted fitting result with the parameter set of q_g , $fwhm_g$ and θ_0 where χ^2 shows the minimum value, as the best fit parameter. For this object, $\theta_0=1000''$, $fwhm_g=3.57$ pix, and $q_g=1.00$.

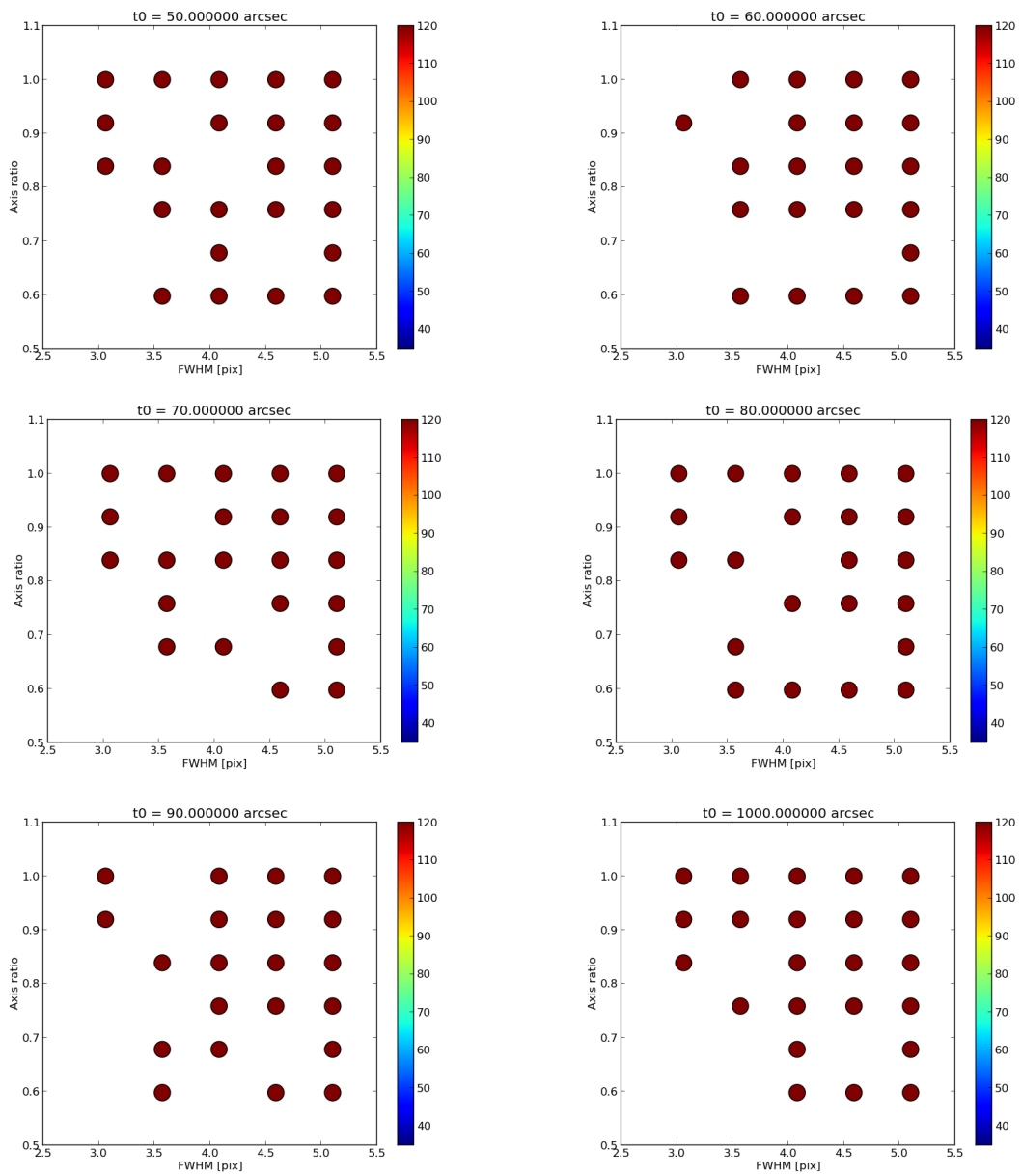


Figure 143 Continued.

C.12 J1510J

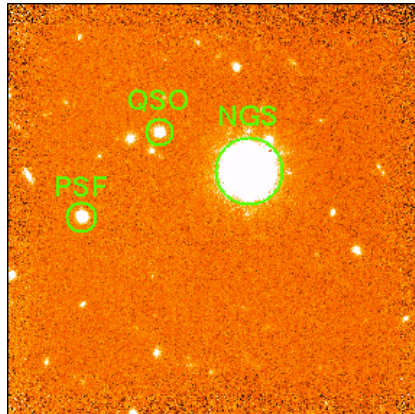


Figure 144 Final average combined image of J1510 *J*-band.

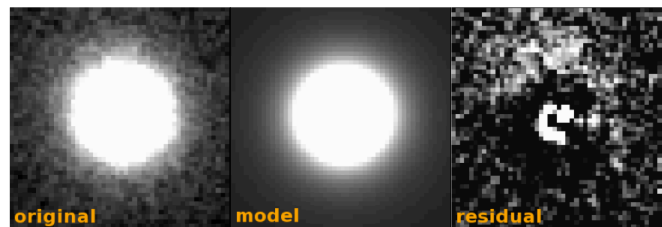


Figure 145 PSF reference star fitting result. Left : original PSF reference star image. Middle : best fit PSF model image. Right : residual image (original-model).

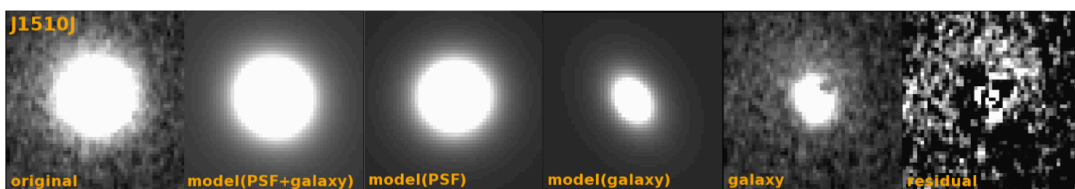


Figure 146 QSO fitting result. From left to right, original QSO image, best fit model(PSF+galaxy) image, best fit PSF model image, best fit galaxy model image, galaxy image (original – best fit PSF mode image), and residual image (original – model(PSF+galaxy) image).

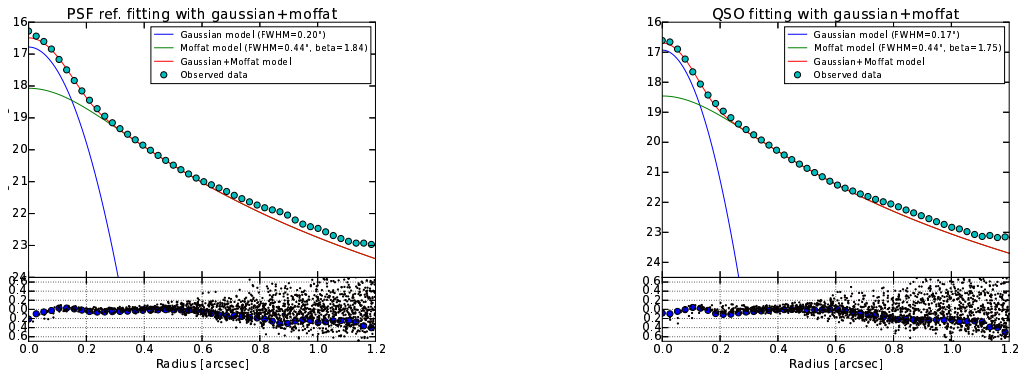


Figure 147 J1510J : Radial profile of PSF reference star (left) and QSO (right) when fitted with two components (Gaussian + Moffat).

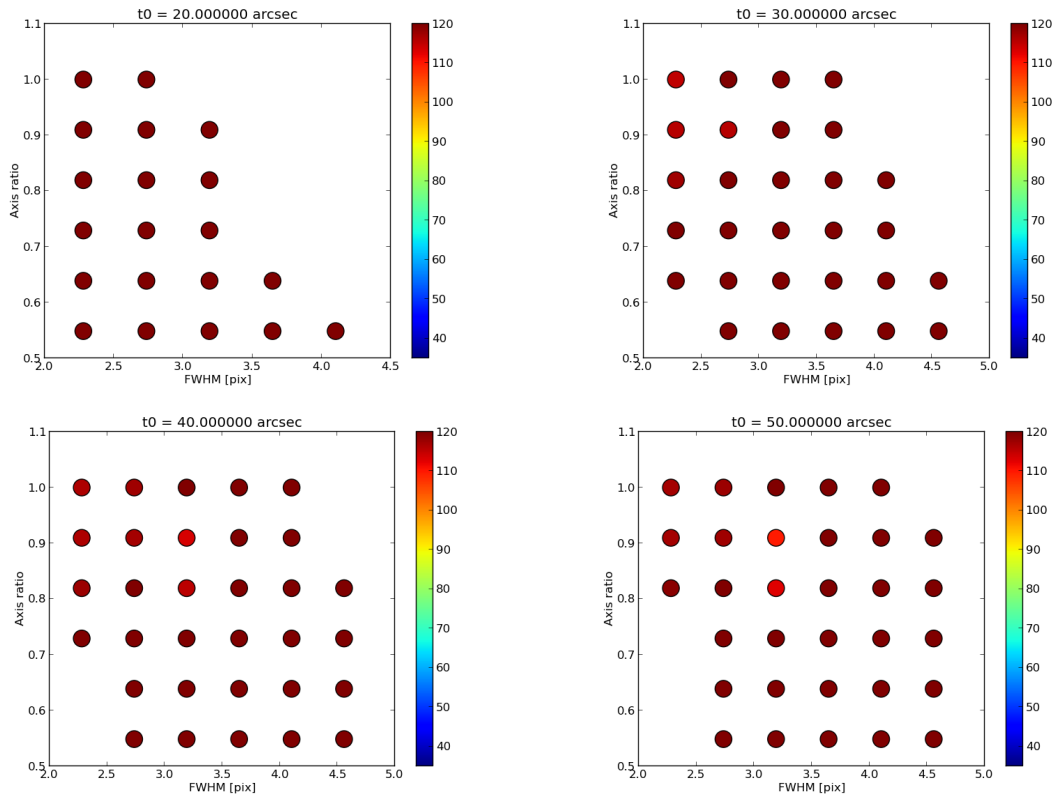


Figure 148 χ^2 map obtained by fitting of J1510 *J*-band data. X-axis is FWHM [pix], and Y-axis is axis ratio. The color bar represents χ^2 value (blue=small, red=large). From top left figure to bottom right figure, θ_0 ["] = 20, 30, 40, ..., 90. We adopted fitting result with the parameter set of q_g , fwhm_g and θ_0 where χ^2 shows the minimum value, as the best fit parameter. For this object, $\theta_0=60''$, $\text{fwhm}_g=3.19$ pix, and $q_g=0.91$.

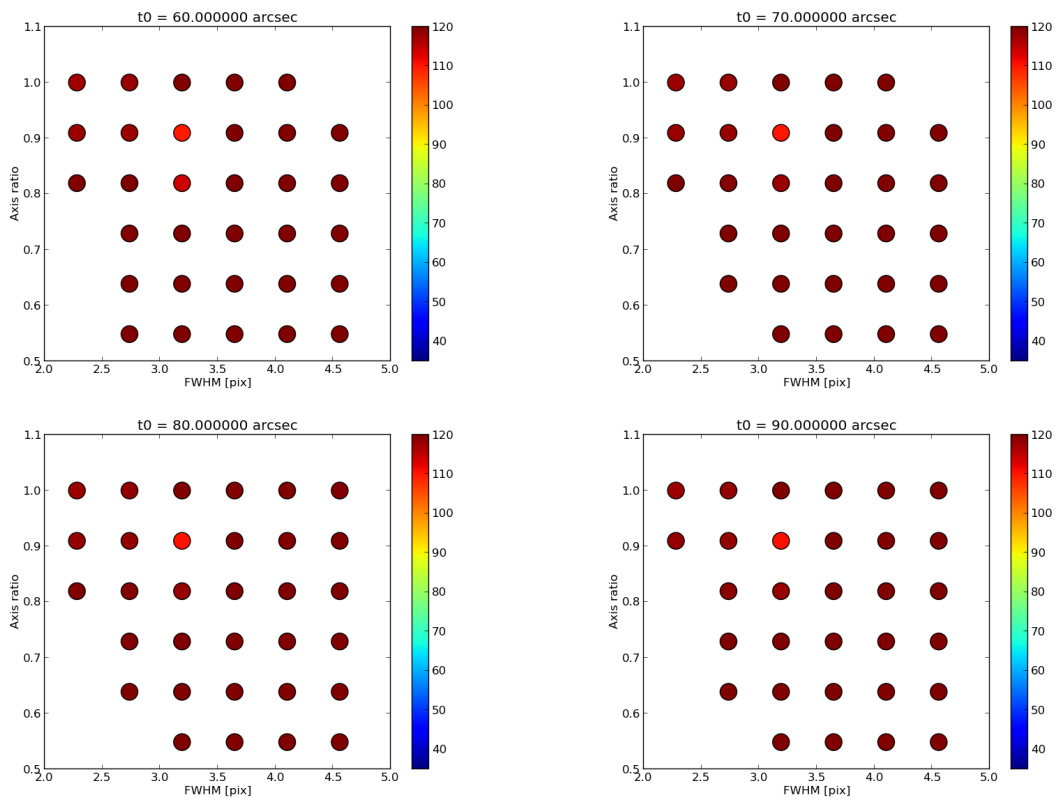


Figure 148 Continued.

C.13 J1510K

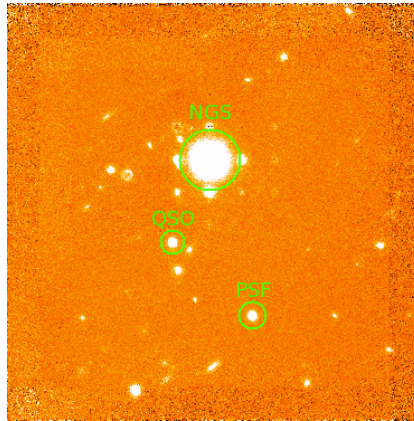


Figure 149 Final average combined image of J1510 K' -band.

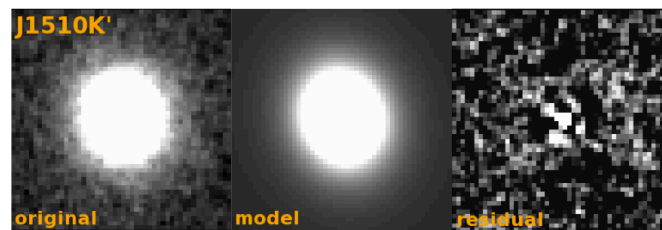


Figure 150 PSF reference star fitting result. Left : original PSF reference star image. Middle : best fit PSF model image. Right : residual image (original-model).

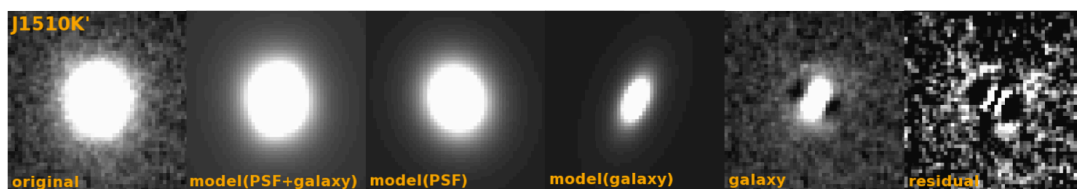


Figure 151 QSO fitting result. From left to right, original QSO image, best fit model(PSF+galaxy) image, best fit PSF model image, best fit galaxy model image, galaxy image (original – best fit PSF mode image), and residual image (original – model(PSF+galaxy) image).

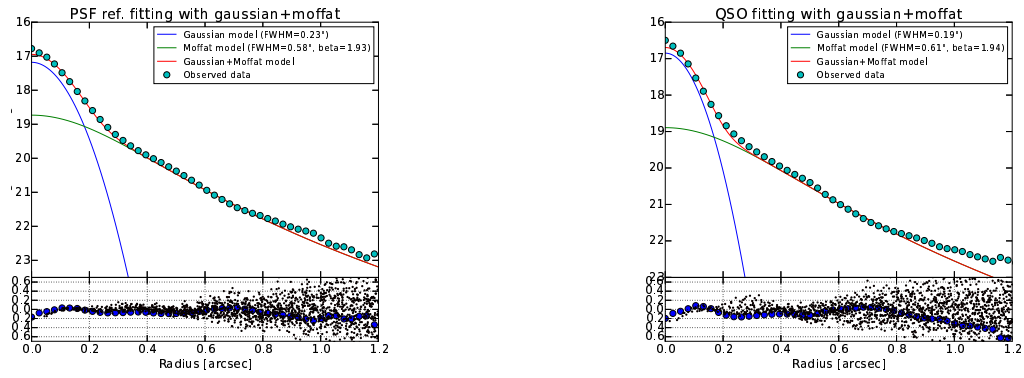


Figure 152 J1510K : Radial profile of PSF reference star (left) and QSO (right) when fitted with two components (Gaussian + Moffat).

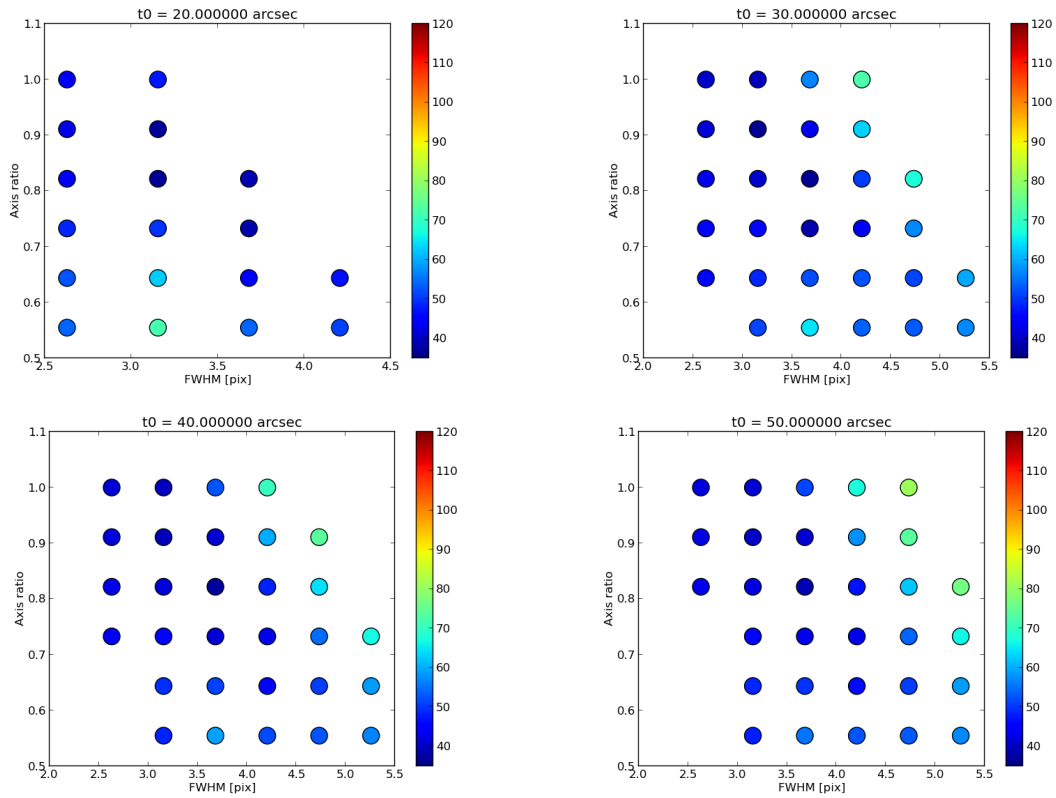


Figure 153 χ^2 map obtained by fitting of J1510 K' -band data. X-axis is FWHM [pix], and Y-axis is axis ratio. The color bar represents χ^2 value (blue=small, red=large). From top left figure to bottom right figure, θ_0 ["] = 20, 30, 40, ..., 90. We adopted fitting result with the parameter set of q_g , $fwhm_g$ and θ_0 where χ^2 shows the minimum value, as the best fit parameter. For this object, $\theta_0=30''$, $fwhm_g=3.47$ pix, and $q_g=0.83$.

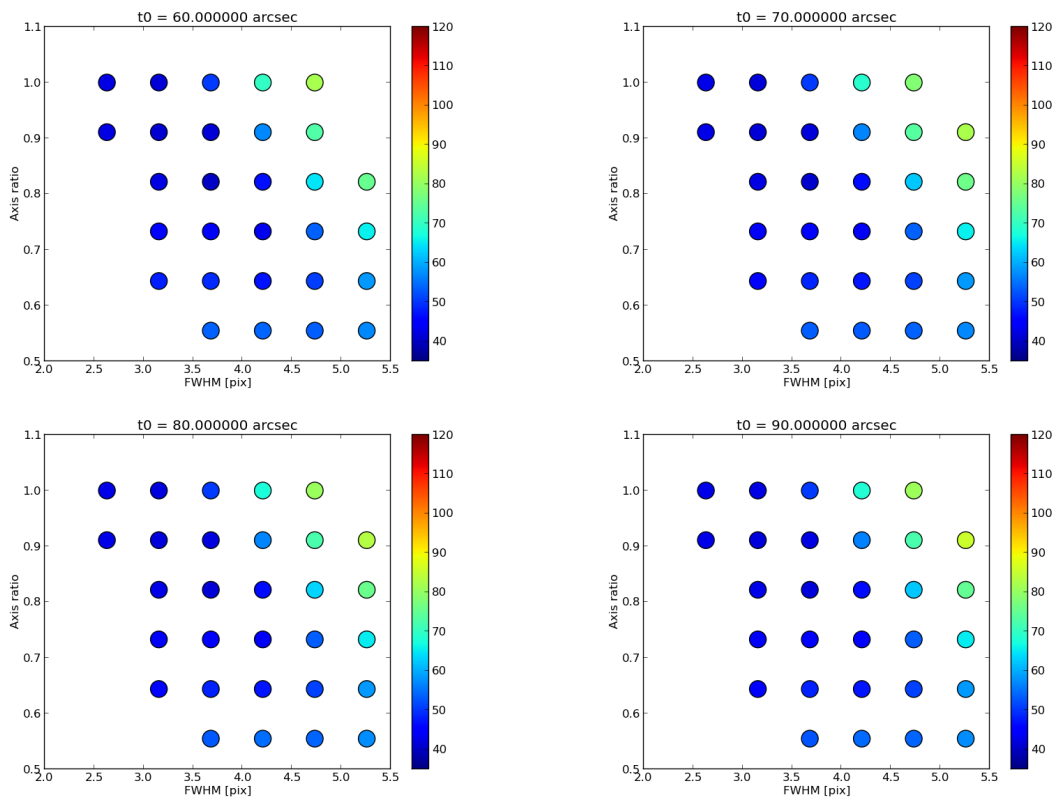


Figure 153 Continued.

C.14 J1551J

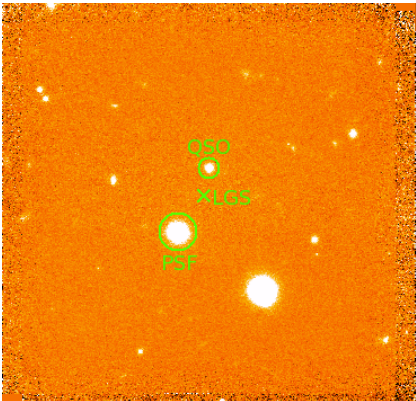


Figure 154 Final average combined image of J1551 *J*-band.

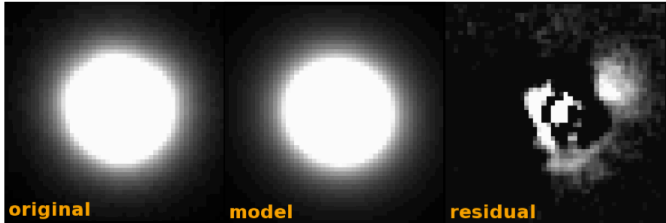


Figure 155 PSF reference star fitting result. Left : original PSF reference star image. Middle : best fit PSF model image. Right : residual image (original-model).

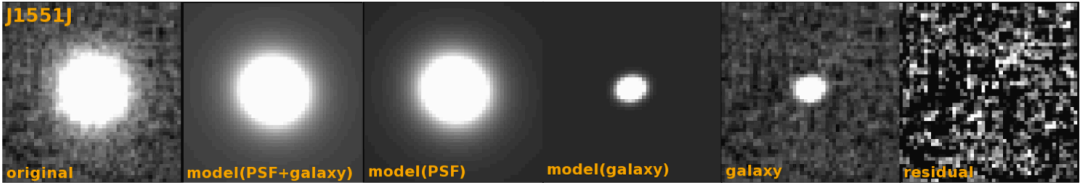


Figure 156 QSO fitting result. From left to right, original QSO image, best fit model(PSF+galaxy) image, best fit PSF model image, best fit galaxy model image, galaxy image (original – best fit PSF mode image), and residual image (original – model(PSF+galaxy) image).

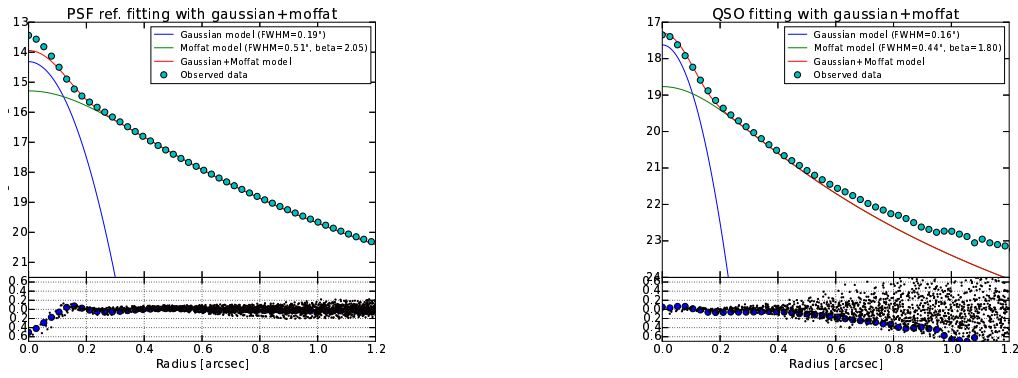


Figure 157 1551J : Radial profile of PSF reference star (left) and QSO (right) when fitted with two components (Gaussian + Moffat).

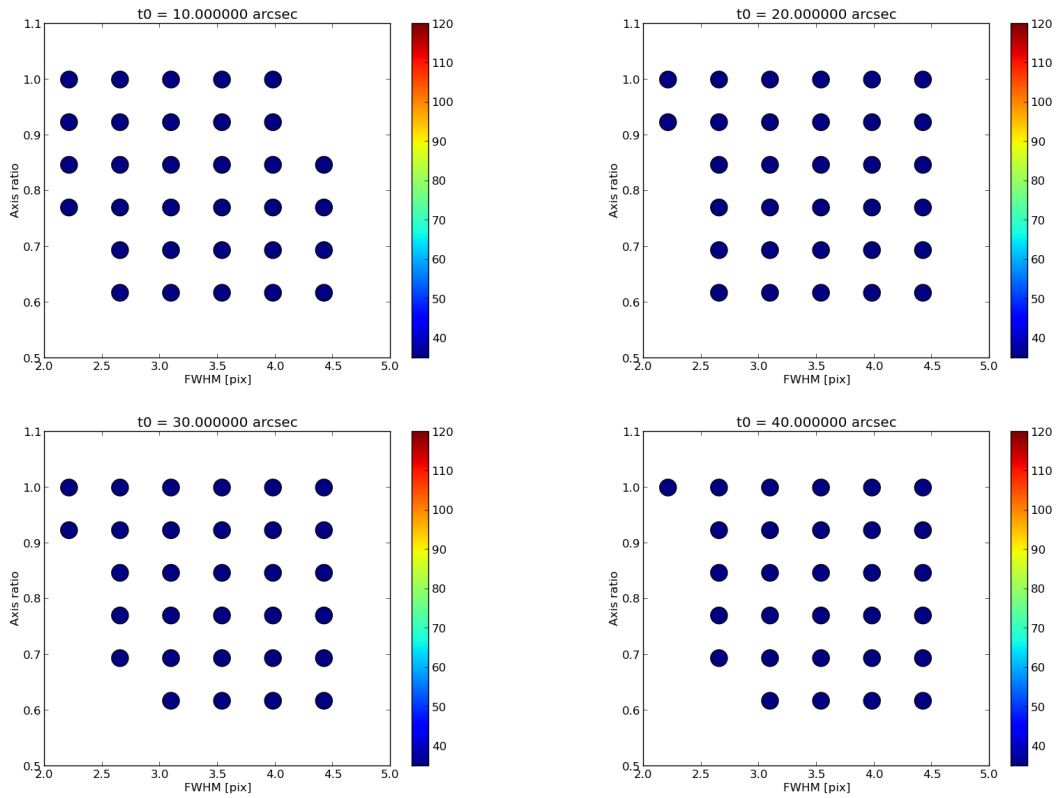


Figure 158 χ^2 map obtained by fitting of J1551 *J*-band data. X-axis is FWHM [pix], and Y-axis is axis ratio. The color bar represents χ^2 value (blue=small, red=large). From top left figure to bottom right figure, θ_0 ["] = 10, 20, 30, ..., 90, 1000. $\theta_0=1000$ means that the same strehl ratio as PSF reference star is adopted to QSO. We adopted fitting result with the parameter set of q_g , $fwhm_g$ and θ_0 where χ^2 shows the minimum value, as the best fit parameter. For this object, $\theta_0=1000''$, $fwhm_g=2.65$ pix, and $q_g=0.85$.

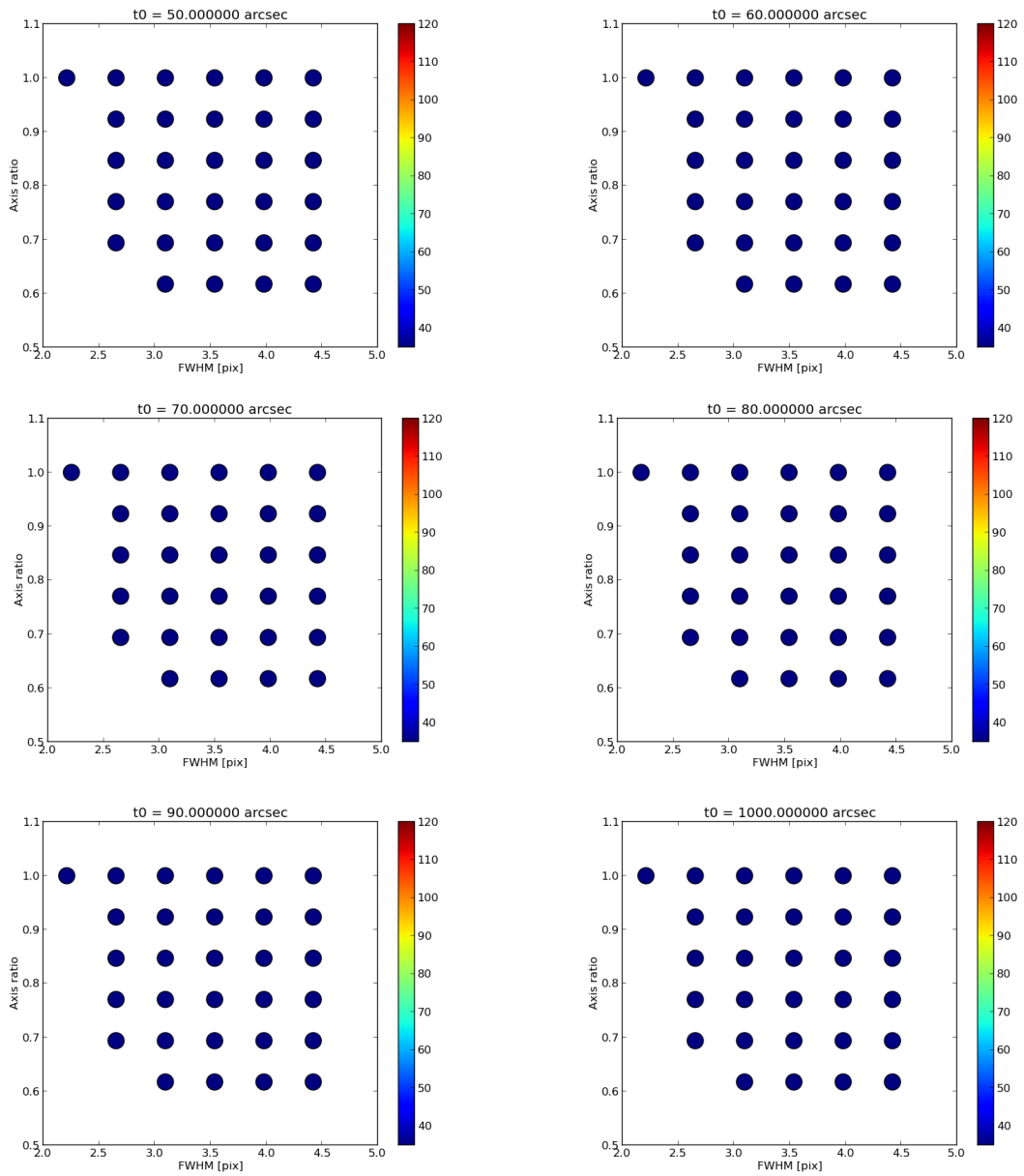


Figure 158 Continued.

C.15 J1551K

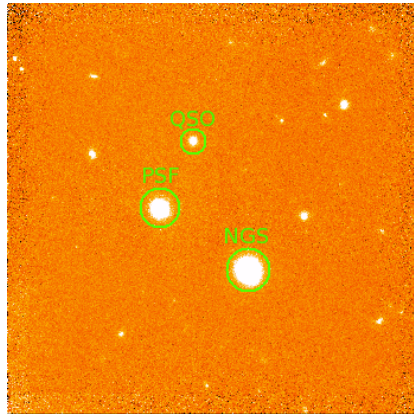


Figure 159 Final average combined image of J1551 K' -band.

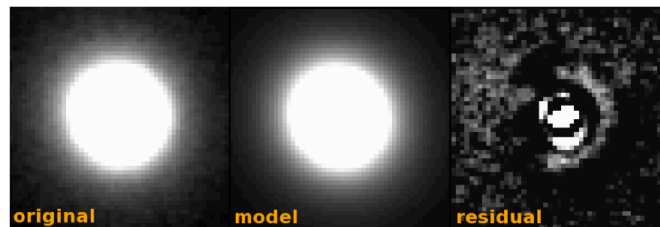


Figure 160 PSF reference star fitting result. Left : original PSF reference star image. Middle : best fit PSF model image. Right : residual image (original-model).

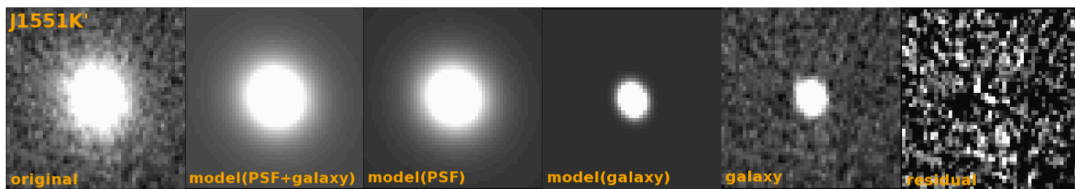


Figure 161 QSO fitting result. From left to right, original QSO image, best fit model(PSF+galaxy) image, best fit PSF model image, best fit galaxy model image, galaxy image (original - best fit PSF model image), and residual image (original - model(PSF+galaxy) image).

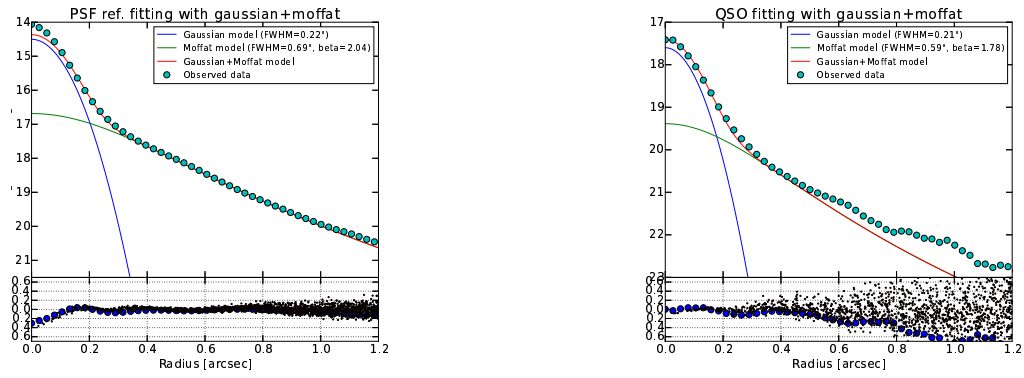


Figure 162 J1551K : Radial profile of PSF reference star (left) and QSO (right) when fitted with two components (Gaussian + Moffat).

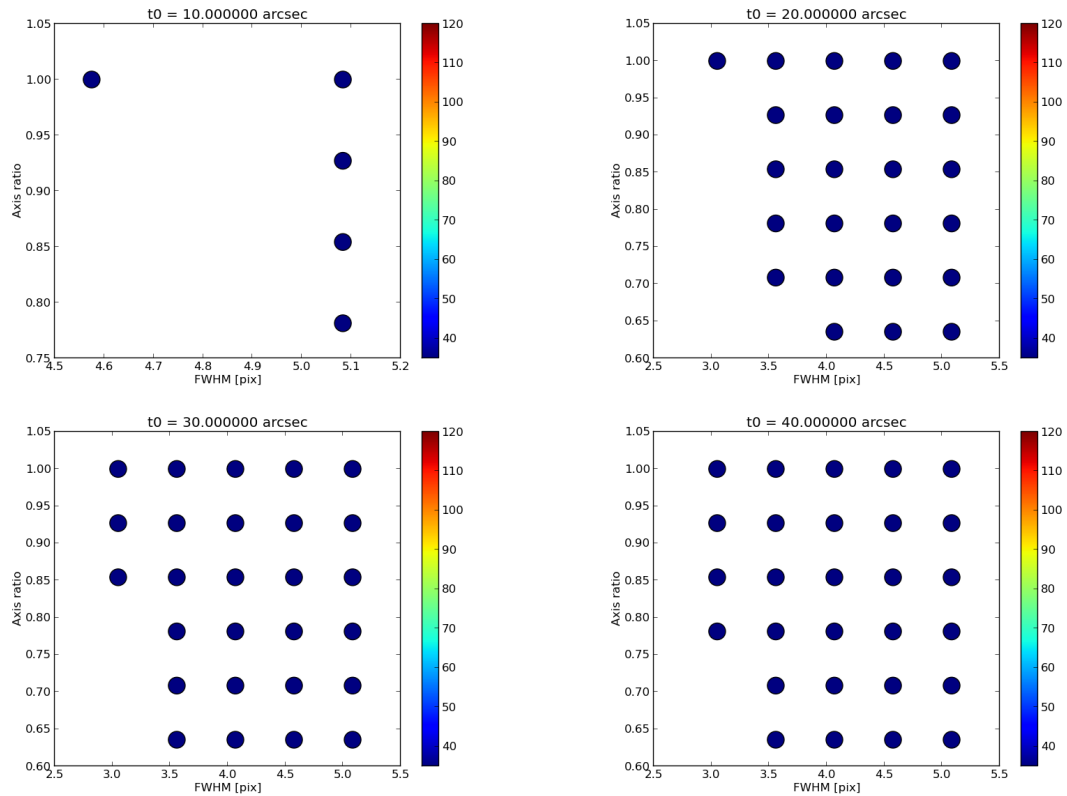


Figure 163 χ^2 map obtained by fitting of J1551 K' -band data. X-axis is FWHM [pix], and Y-axis is axis ratio. The color bar represents χ^2 value (blue=small, red=large). From top left figure to bottom right figure, θ_0 ["] = 10, 20, 30, ..., 90. We adopted fitting result with the parameter set of q_g , $fwhm_g$ and θ_0 where χ^2 shows the minimum value, as the best fit parameter. For this object, $\theta_0=90''$, $fwhm_g=3.56$ pix, and $q_g=0.93$.

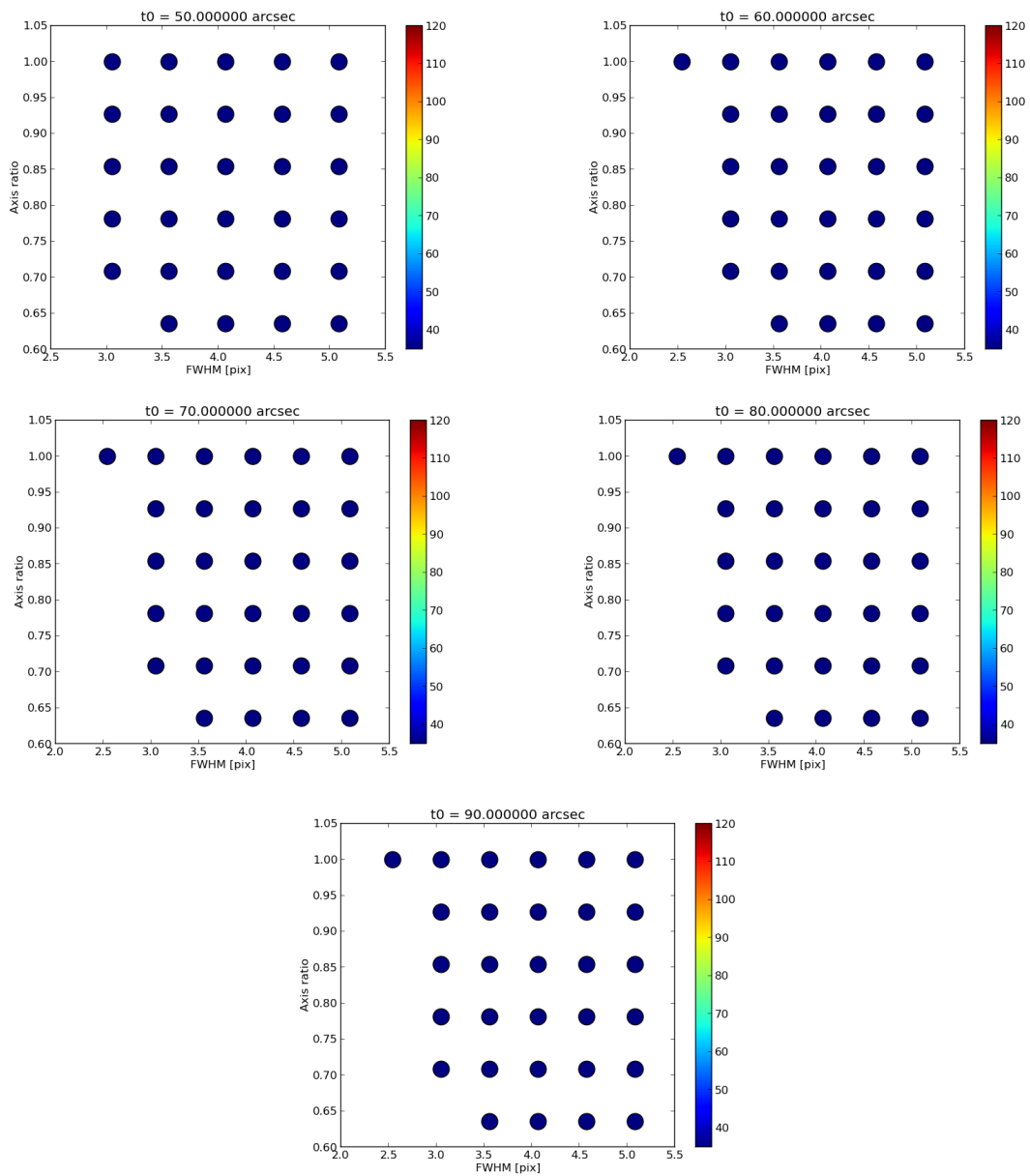


Figure 163 Continued.

C.16 J2130J

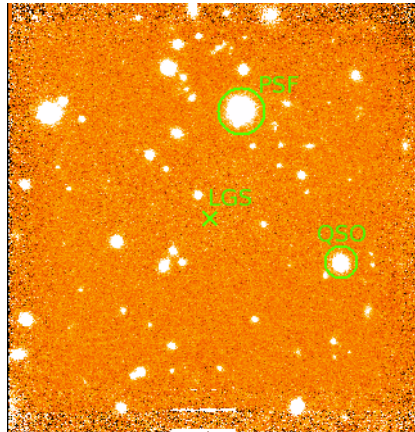


Figure 164 Final average combined image of J2130 *J*-band.

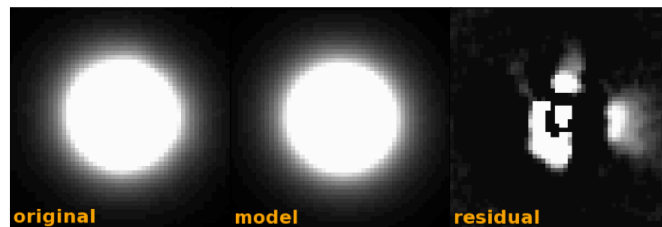


Figure 165 PSF reference star fitting result. Left : original PSF reference star image. Middle : best fit PSF model image. Right : residual image (original-model).

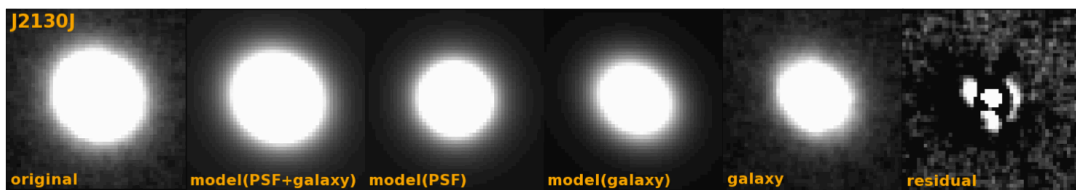


Figure 166 QSO fitting result. From left to right, original QSO image, best fit model(PSF+galaxy) image, best fit PSF model image, best fit galaxy model image, galaxy image (original - best fit PSF model image), and residual image (original - model(PSF+galaxy) image).

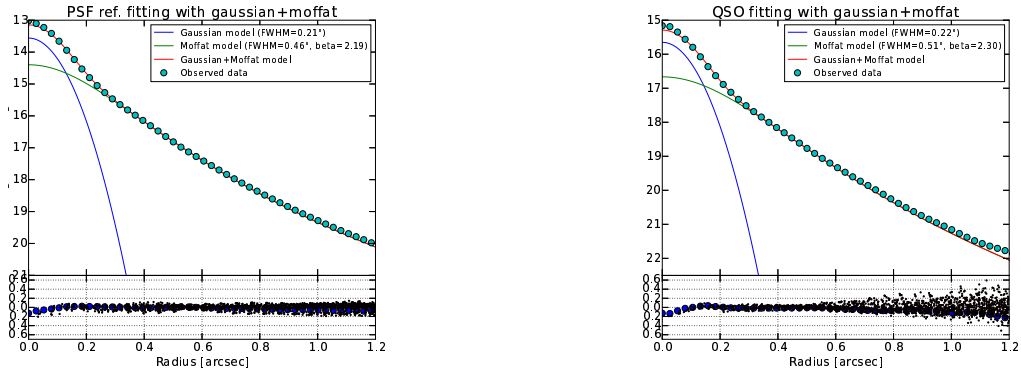


Figure 167 J2130J : Radial profile of PSF reference star (left) and QSO (right) when fitted with two components (Gaussian + Moffat).

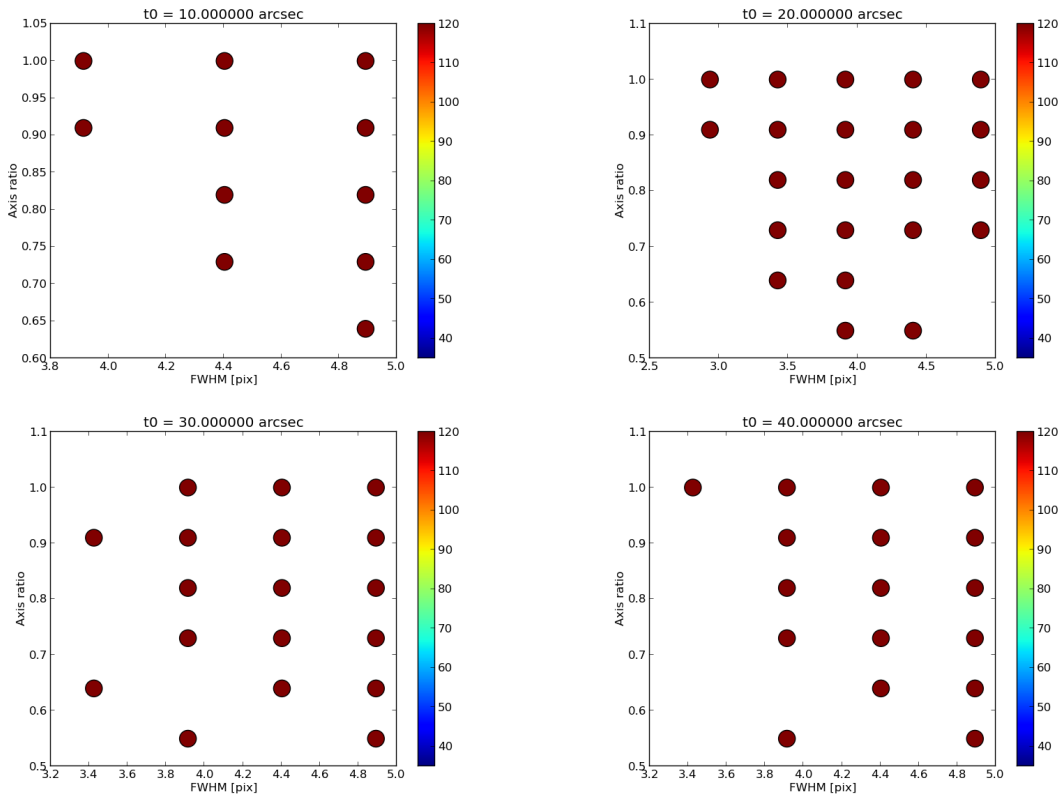


Figure 168 χ^2 map obtained by fitting of J2130 *J*-band data. X-axis is FWHM [pix], and Y-axis is axis ratio. The color bar represents χ^2 value (blue=small, red=large). From top left figure to bottom right figure, θ_0 ["] = 10, 20, 30, ..., 90, 1000. $\theta_0=1000$ means that the same strehl ratio as PSF reference star is adopted to QSO. We adopted fitting result with the parameter set of q_g , $fwhm_g$ and θ_0 where χ^2 shows the minimum value, as the best fit parameter. For this object, $\theta_0=1000''$, $fwhm_g=4.22$ pix, and $q_g=0.82$.

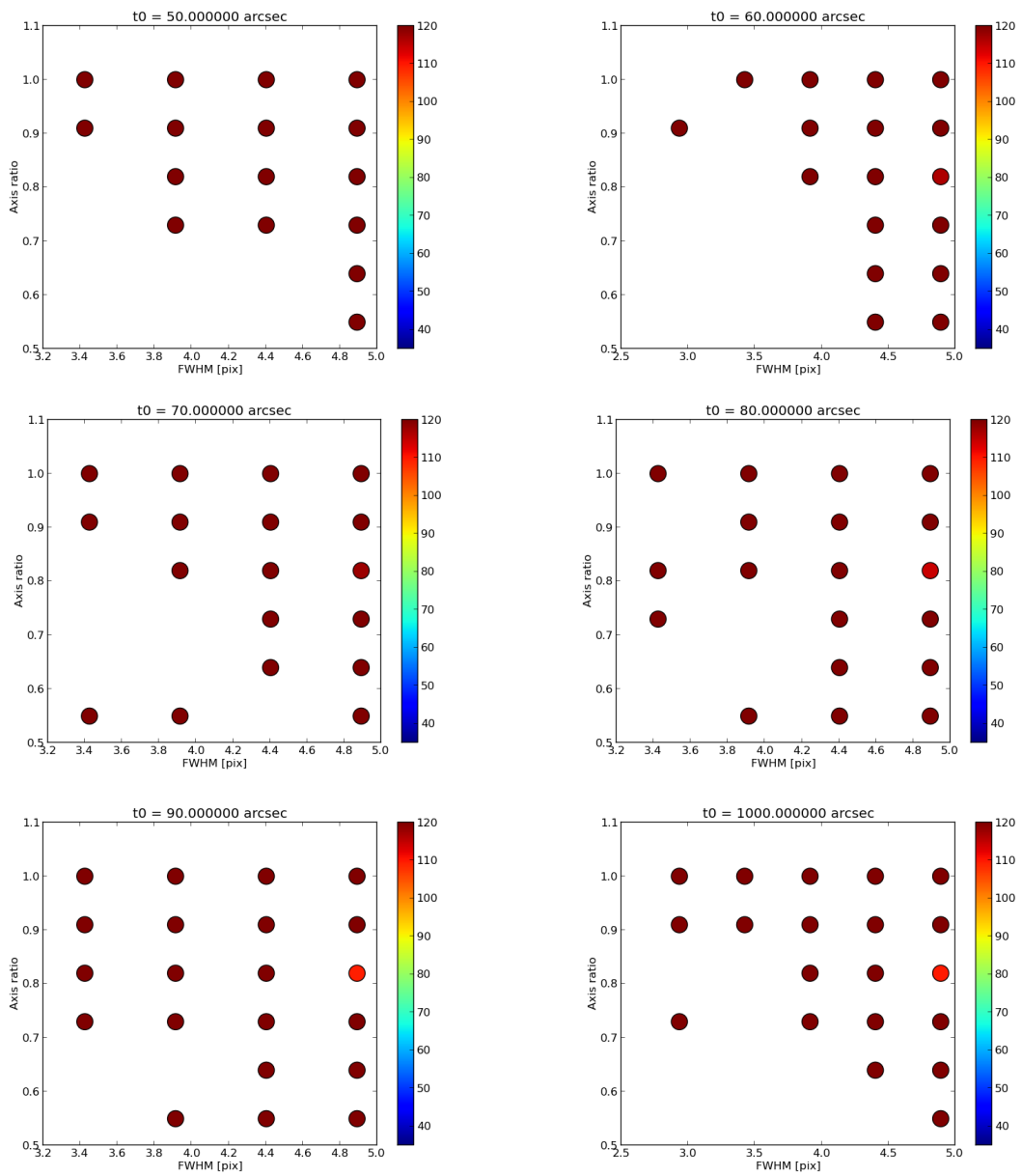


Figure 168 Continued.

C.17 J2130K

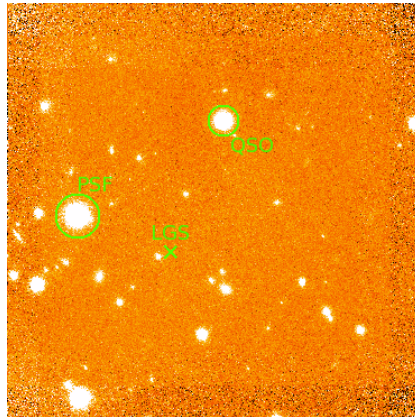


Figure 169 Final average combined image of J2130 K' -band.

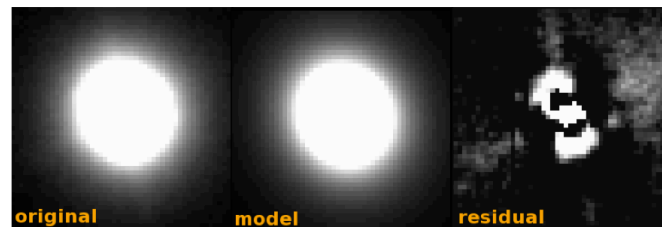


Figure 170 PSF reference star fitting result. Left : original PSF reference star image. Middle : best fit PSF model image. Right : residual image (original-model).

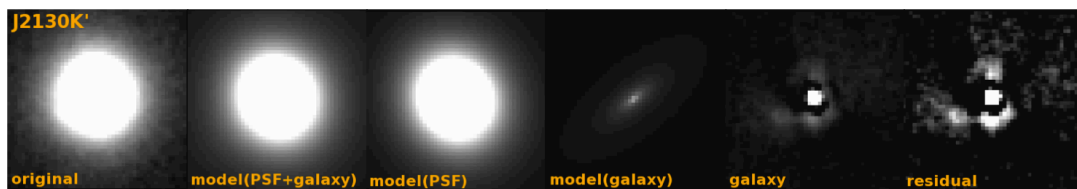


Figure 171 QSO fitting result. From left to right, original QSO image, best fit model(PSF+galaxy) image, best fit PSF model image, best fit galaxy model image, galaxy image (original – best fit PSF mode image), and residual image (original – model(PSF+galaxy) image).

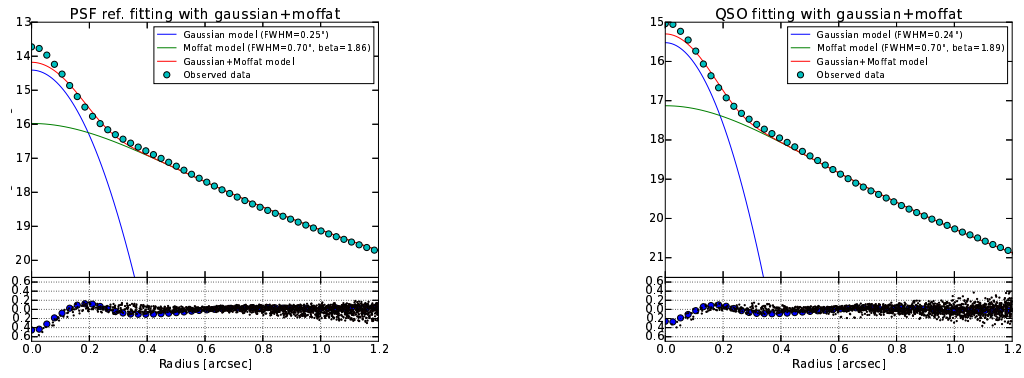


Figure 172 J2130K : Radial profile of PSF reference star (left) and QSO (right) when fitted with two components (Gaussian + Moffat).

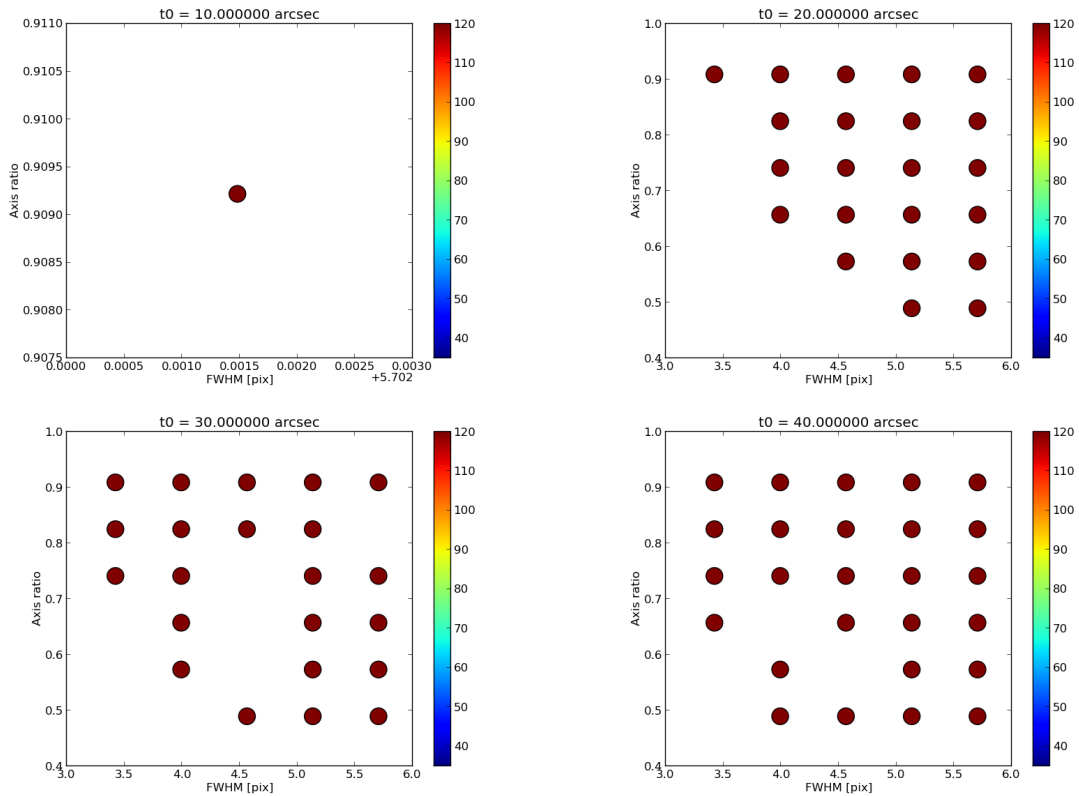


Figure 173 χ^2 map obtained by fitting of J2130 K' -band data. X-axis is FWHM [pix], and Y-axis is axis ratio. The color bar represents χ^2 value (blue=small, red=large). From top left figure to bottom right figure, θ_0 ["] = 10, 20, 30, ..., 90, 1000. $\theta_0=1000$ means that the same strehl ratio as PSF reference star is adopted to QSO. We adopted fitting result with the parameter set of q_g , $fwhm_g$ and θ_0 where χ^2 shows the minimum value, as the best fit parameter. For this object, $\theta_0=1000''$, $fwhm_g=4.22$ pix, and $q_g=0.82$.

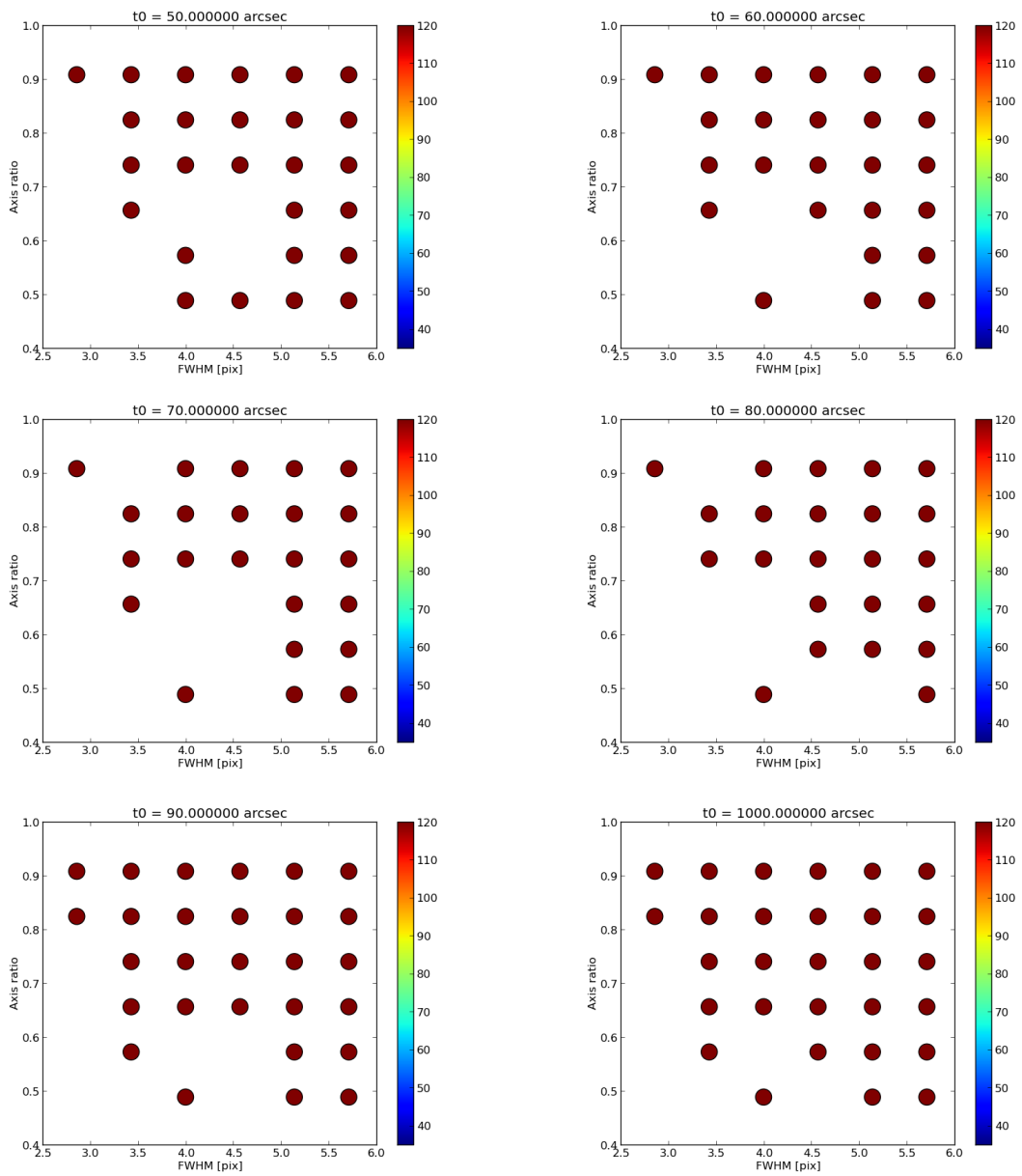


Figure 173 Continued.

AppendixD MCMC result

Table 17 Fitting result after MCMC simulation, Gaussian

Object name	band	position x [pix]	position y [pix]	magnitude [mag(AB)]	FWHM [pix] (["])	axis ratio	position angle
SDSSJ0146	J	25.81±0.11	25.53±0.12	20.22(-0.12, +0.14)	3.89±0.18 (0.20±0.01)	0.98±0.04	-4.63±26.056
SDSSJ0146	K'	25.41±0.11	26.52±0.08	19.77(-0.17, +0.20)	3.35±0.21(0.17±0.01)	0.87±0.04	-32.83±8.40
SDSSJ0725	J	26.47±0.18	26.21±0.24	20.98(-0.15, +0.18)	3.21±0.31 (0.17±0.02)	0.90±0.09	16.36±18.69
SDSSJ0725	K'	25.71±0.18	25.59±0.17	20.57(-0.16, +0.19)	3.12±0.21 (0.16±0.01)	1.11±0.09	52.86±13.37
SDSSJ0847	K'	25.68±0.07	26.43±0.07	19.14(-0.08, +0.08)	3.68±0.13 (0.19±0.01)	0.83±0.03	-42.29±5.46
SDSSJ1116	J	26.75±0.21	26.04±0.20	20.24(-0.19, +0.24)	3.96±0.29 (0.21±0.02)	1.01±0.08	-77.81±22.40
SDSSJ1337	J	25.58±0.09	25.60±0.08	19.38(-0.14, +0.16)	4.77±0.24 (0.25±0.01)	0.79±0.03	-18.69±4.30
SDSSJ1337	K'	25.57±0.05	26.01±0.07	18.65(-0.09, +0.10)	4.16±0.12 (0.22±0.01)	0.90±0.03	-21.35±4.70
SDSSJ1407	J	26.44±0.10	25.71±0.06	18.90(-0.12, +0.13)	3.76±0.17 (0.20±0.01)	0.79±0.03	-92.76±4.86
SDSSJ1407	K'	26.18±0.06	26.41±0.09	18.24(-0.06, +0.06)	3.83±0.17 (0.20±0.01)	0.88±0.04	-32.24±8.21
SDSSJ1510	J	25.56±0.12	26.33±0.15	21.39(-0.21, +0.26)	2.92±0.20 (0.15±0.01)	0.90±0.05	52.28±10.79
SDSSJ1510	K'	25.79±0.11	25.86±0.13	20.71(-0.13, +0.15)	3.38±0.21 (0.18±0.01)	0.86±0.05	-29.12±9.60
SDSSJ1551	J	25.63±0.48	26.16±0.42	22.52(-0.45, +0.78)	2.88±0.45 (0.15±0.02)	0.980±0.12	-44.42±42.53

Notes. 1pix = 0.052 arcsec

Table 18 Fitting result after MCMC simulation, Moffat

Object name	band	position x [pix]	position y [pix]	magnitude [mag(AB)]	FWHM [pix] (["])	powerlaw index	axis ratio	position angle
SDSSJ0146	J	26.28±0.13	25.67±0.14	19.11(-0.06, +0.06)	8.25±0.77 (0.43±0.04)	1.97±0.21	0.98±0.02	58.86±19.55
SDSSJ0146	K'	25.81±0.10	26.87±0.11	18.98(-0.04, +0.04)	14.21±0.41 (0.74±0.02)	6.51±1.33	0.90±0.02	18.34±5.09
SDSSJ0725	J	26.51±0.14	26.37±0.15	18.77(-0.10, +0.11)	9.03±0.70 (0.47±0.03)	1.61±0.14	0.99±0.03	-75.94±17.05
SDSSJ0725	K'	25.41±0.23	25.79±0.26	19.06(-0.11, +0.12)	15.35±1.14 (0.80±0.06)	2.44±0.42	0.95±0.04	7.76±11.08
SDSSJ0847	K'	25.48±0.13	26.97±0.19	18.51(-0.06, +0.07)	13.93±0.57 (0.72±0.03)	4.44±0.87	0.93±0.03	24.62±9.52
SDSSJ1116	J	27.51±0.35	26.01±0.21	18.34(-0.15, +0.18)	12.92±1.18 (0.67±0.06)	1.93±0.26	0.93±0.04	-64.21±9.19
SDSSJ1337	J	25.05±0.14	25.68±0.13	19.05(-0.14, +0.16)	8.42±0.74 (0.44±0.04)	5.40±1.42	0.88±0.02	-8.11±5.69
SDSSJ1337	K'	25.54±0.23	26.36±0.35	18.50(-0.12, +0.14)	11.43±1.13 (0.59±0.06)	2.08±0.33	1.04±0.06	-28.37±23.28
SDSSJ1407	J	27.01±0.13	25.28±0.08	17.64(-0.09, +0.09)	12.27±0.61 (0.64±0.03)	2.60±0.19	0.95±0.01	44.60±6.37
SDSSJ1407	K'	26.50±0.09	27.68±0.17	17.00(-0.06, +0.06)	11.30±0.37 (0.59±0.02)	1.95±0.14	0.96±0.01	25.58±6.48
SDSSJ1510	J	25.76±0.17	27.22±0.28	19.68(-0.12, +0.14)	10.80±0.94 (0.56±0.05)	1.57±0.16	1.00±0.04	-86.88±51.74
SDSSJ1510	K'	25.89±0.73	25.80±1.00	20.04(-0.19, +0.23)	14.24±1.92 (0.74±0.10)	1.84±0.32	0.85±0.08	28.05±16.02
SDSSJ1551	J	26.35±1.25	26.15±1.16	20.18(-0.34, +0.50)	10.37±1.74 (0.54±0.09)	1.54±0.34	1.02±0.09	32.65±43.94

Notes. 1pix = 0.052 arcsec

Table 19 Fitting result after MCMC simulation, Sersic

Object name	band	position x [pix]	position y [pix]	magnitude [mag(AB)]	Re [pix] ([kpc])	Sersic index	axis ratio	position angle
SDSSJ0146	J	25.55±0.19	25.40±0.23	19.91(−0.12, +0.14)	3.04±0.30 (1.20±0.05)	0.96±0.18	0.96±0.04	34.67±20.14
SDSSJ0146	K′	26.03±0.18	26.12±0.23	20.46(−0.29, +0.39)	2.82±0.32 (1.11±0.05)	0.64±0.16	0.62±0.06	−15.07±3.76
SDSSJ0725	J	26.26±0.42	26.11±0.53	20.88(−0.29, +0.40)	3.02±0.65 (1.18±0.10)	2.16±0.86	0.89±0.11	−12.26±13.94
SDSSJ0725	K′	25.61±0.42	25.59±0.43	20.65(−0.27, +0.35)	3.61±0.95 (1.41±0.18)	2.11±0.86	0.81±0.10	−36.28±10.70
SDSSJ0847	K′	25.08±0.24	25.28±0.44	19.87(−0.21, +0.27)	3.89±0.57 (1.53±0.11)	1.16±0.28	0.66±0.07	−4.78±7.00
SDSSJ1116	J	25.94±0.14	25.49±0.13	18.50(−0.17, +0.21)	4.91±0.38 (1.92±0.10)	1.12±0.13	0.84±0.03	18.11±3.47
SDSSJ1337	J	26.10±0.16	25.92±0.14	18.52(−0.08, +0.09)	7.82±0.50 (3.03±0.20)	1.20±0.16	0.93±0.02	49.04±6.55
SDSSJ1337	K′	25.31±0.38	25.27±0.77	19.44(−0.25, +0.33)	4.60±1.16 (1.78±0.28)	1.35±0.48	0.81±0.09	24.85±12.30
SDSSJ1407	J	25.73±0.11	25.94±0.06	18.15(−0.24, +0.16)	3.57±0.21 (1.40±0.04)	0.90±0.09	0.87±0.03	73.70±3.74
SDSSJ1407	K′	25.56±0.22	23.34±0.34	18.42(−0.16, +0.19)	5.07±0.25 (1.99±0.07)	1.08±0.11	1.13±0.06	−29.07±8.69
SDSSJ1510	J	25.46±0.12	25.93±0.16	20.38(−0.20, +0.24)	3.30±0.47 (1.26±0.08)	1.36±0.27	0.85±0.04	40.45±5.70
SDSSJ1510	K′	25.66±0.28	25.84±0.45	19.97(−0.22, +0.28)	7.26±1.82 (2.77±0.69)	2.51±0.90	0.70±0.08	−14.80±7.38
SDSSJ1551	J	25.51±0.30	26.25±0.24	20.32(−0.28, +0.38)	4.66±0.83 (1.83±0.20)	1.77±0.57	0.96±0.08	−85.74±16.74

Notes. 1pix = 0.052 arcsec

D.1 J0146J

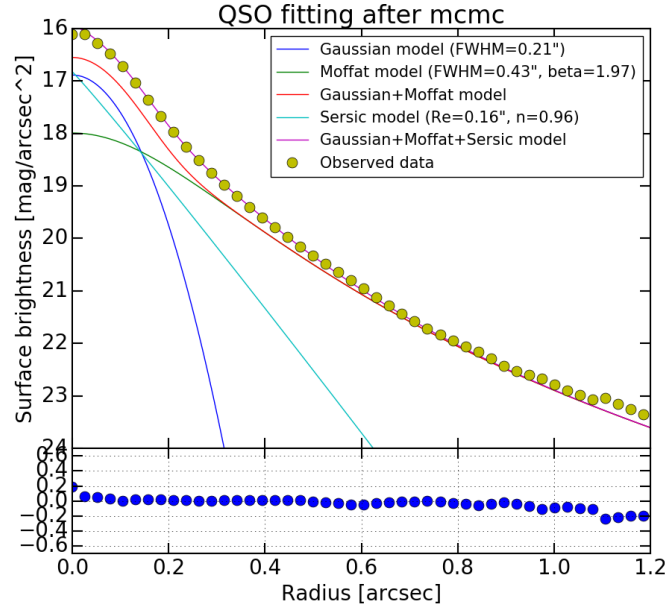


Figure 174 Final radial profile for J0146 *J*-band. Yellow dots correspond to observed data. Blue line shows Gaussian model, green line shows Moffat model, red line show Gaussian + Moffat model, light blue line shows Sersic model, and pink line shows the total (Gaussian + Moffat + Sersic) model. Lower panel is residual (observed data − total model) profile.

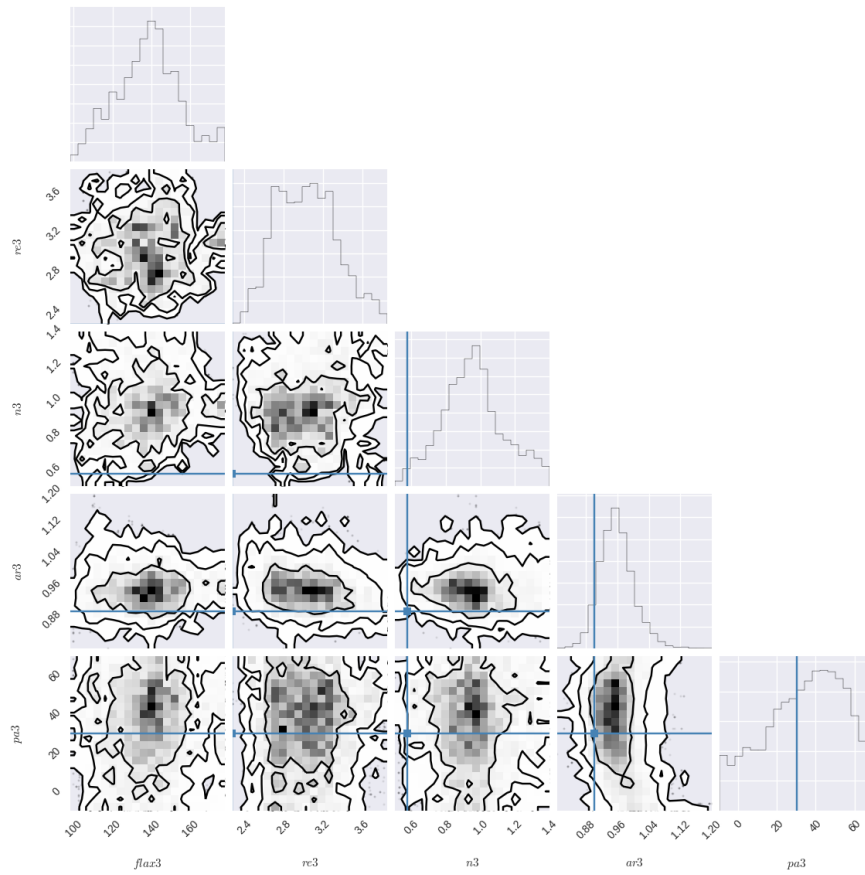


Figure 175 Probability map for Sersic component of J0146 *J*-band. Flux3 = flux, ar3 = axis ratio, n3 = Sersic index, re3 = effective radius, and pa3 = position angle of Sersic component. Each line of the contours shows 1σ , 2σ , and 3σ toward the outside. Blue lines correspond to the best fit values by GALFIT, and is also initial value for MCMC.

D.2 J0146K

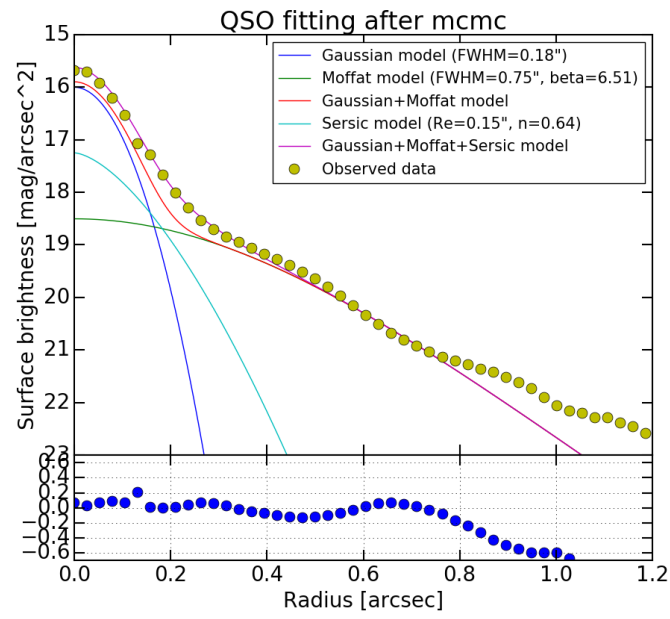


Figure 176 Final radial profile for J0146 K' -band.

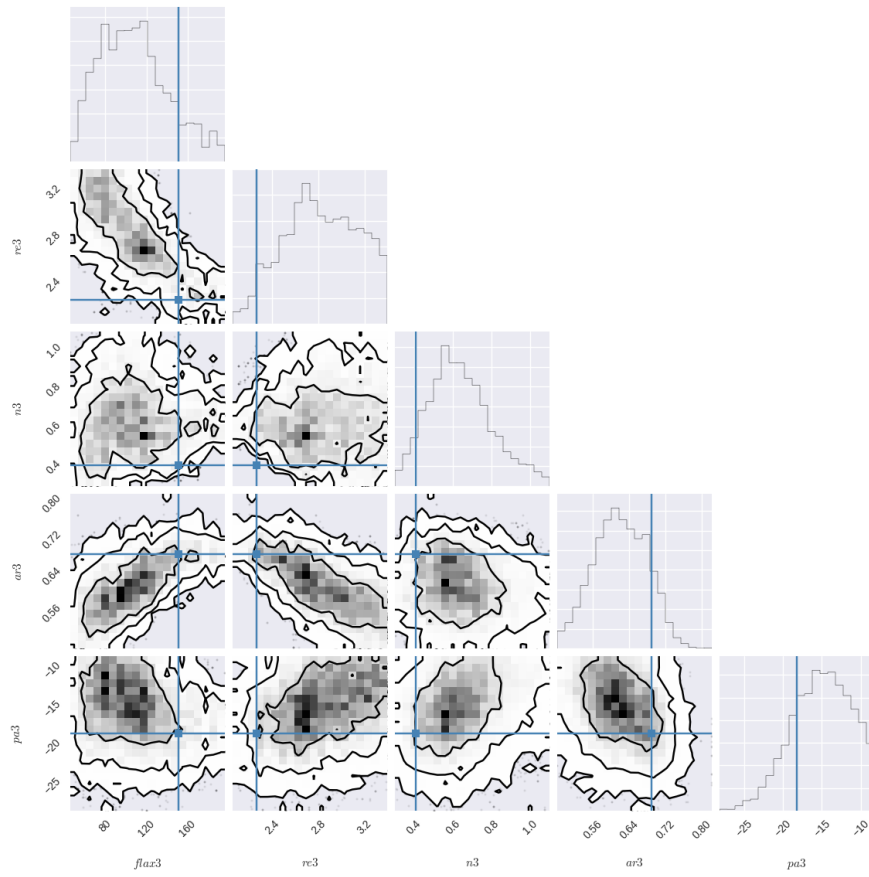


Figure 177 Probability map for Sersic component of J0146 K' -band.

D.3 J0725J

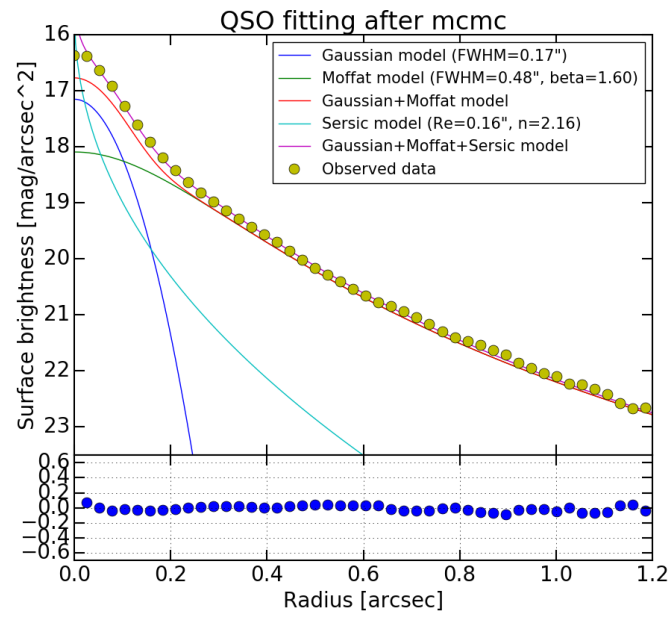


Figure 178 Final radial profile for J0725 *J*-band.

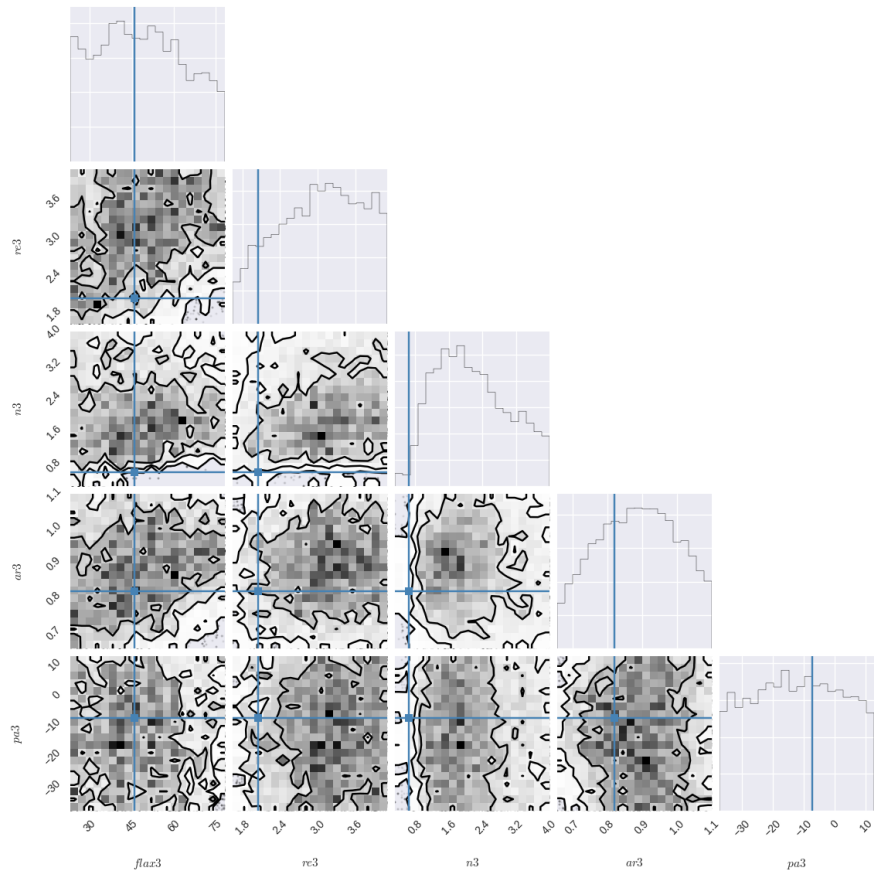


Figure 179 Probability map for Sersic component of J0725 *J*-band.

D.4 J0725K

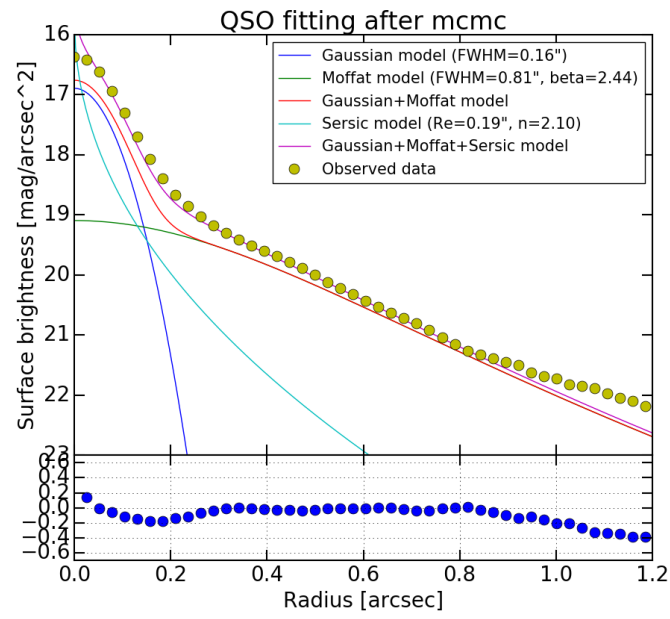


Figure 180 Final radial profile for J0725 K' -band.

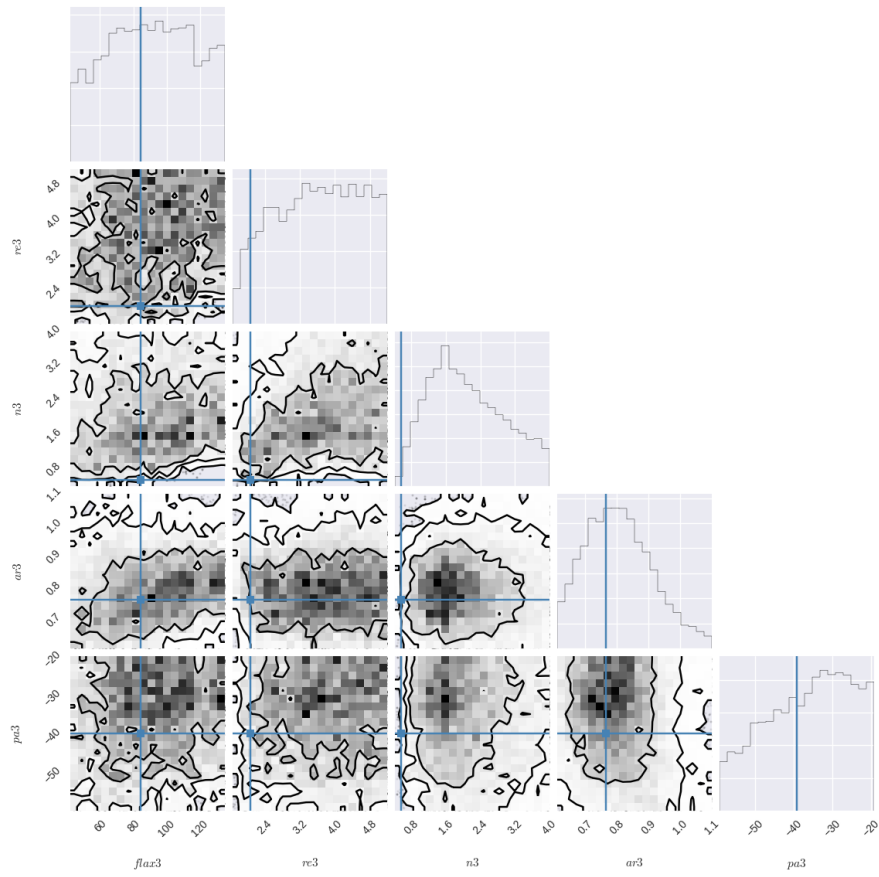


Figure 181 Probability map for Sersic component of J0725 K' -band.

D.5 J0847K

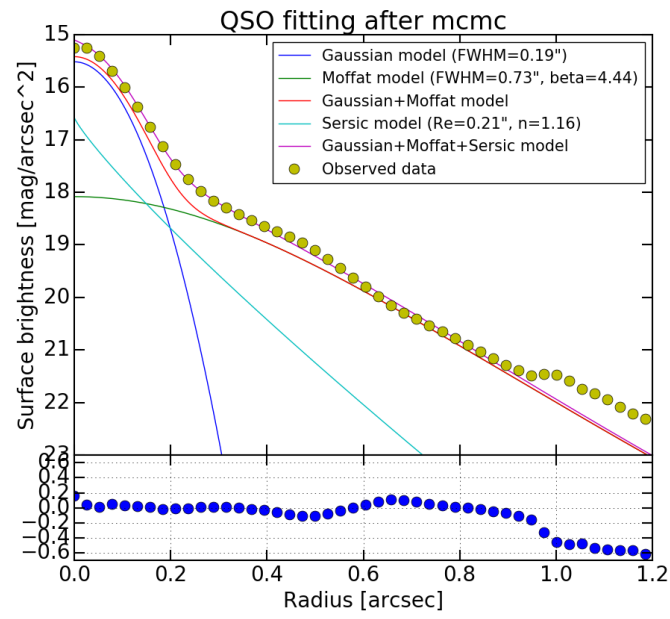


Figure 182 Final radial profile for J0847 K' -band.

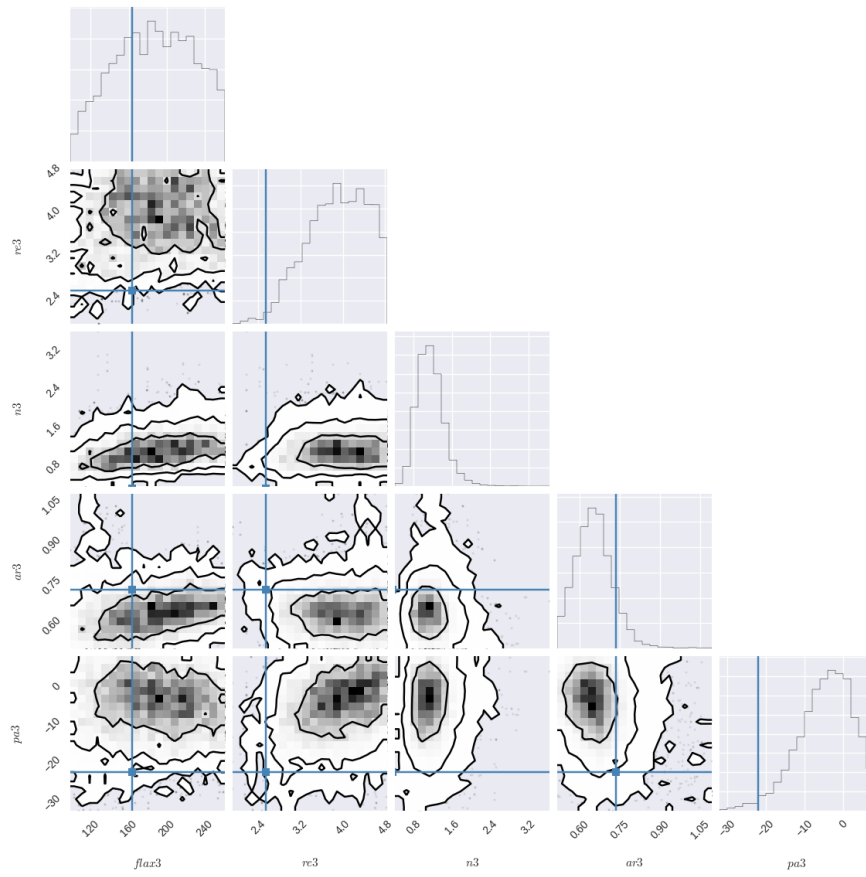


Figure 183 Probability map for Sersic component of J0847 K' -band.

D.6 J1116J

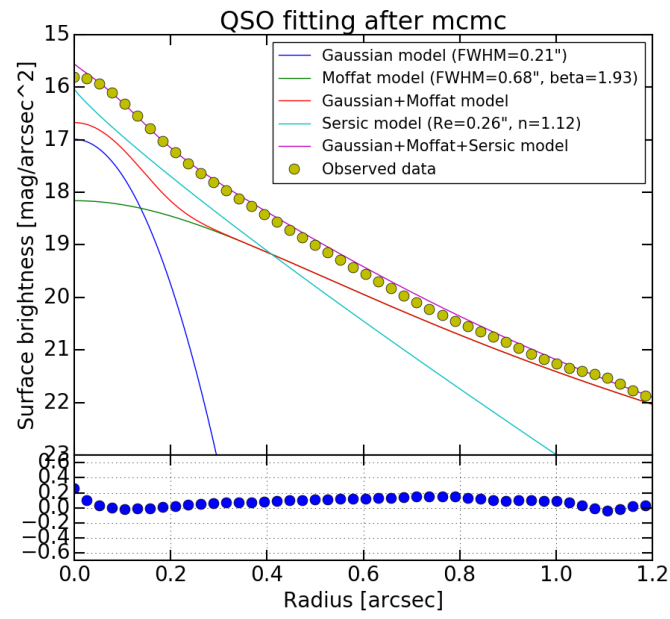


Figure 184 Final radial profile for J1116 *J*-band.

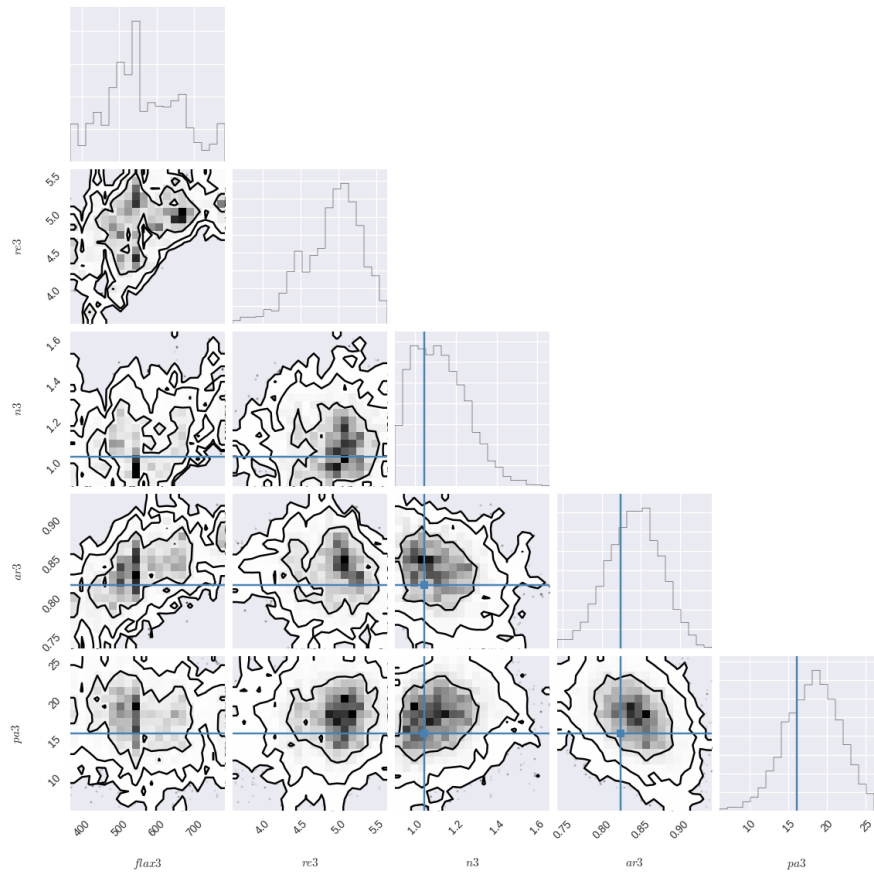


Figure 185 Probability map for Sersic component of J1116 *J*-band.

D.7 J1337J

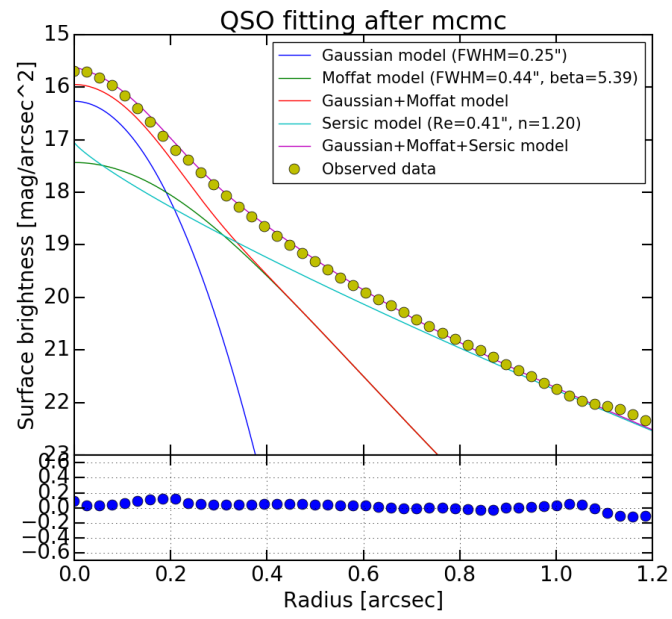


Figure 186 Final radial profile for J1337 *J*-band.

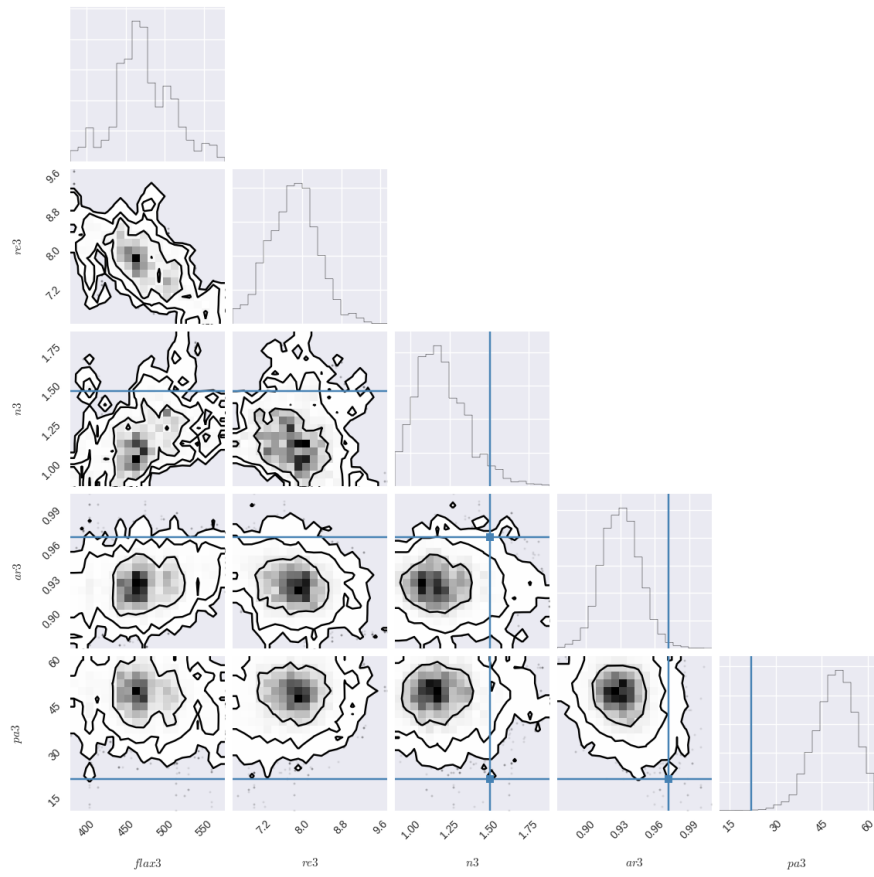


Figure 187 Probability map for Sersic component of J1337 J -band.

D.8 J1337K

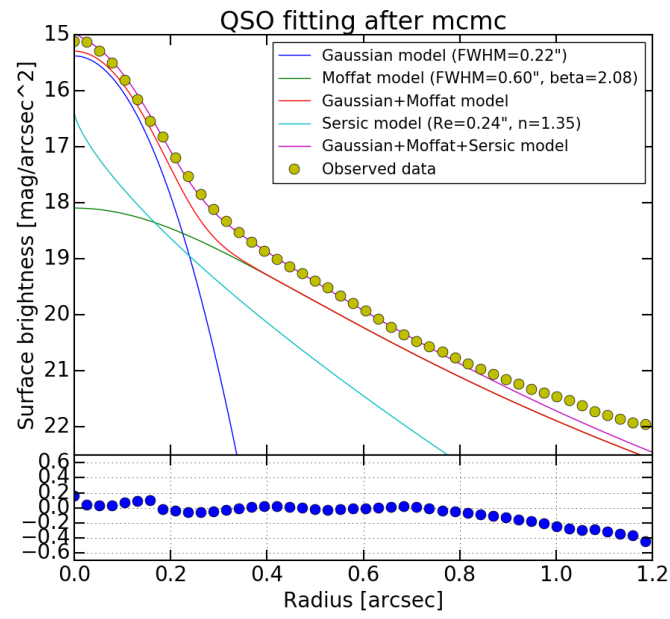


Figure 188 Final radial profile for J1337 K' -band.

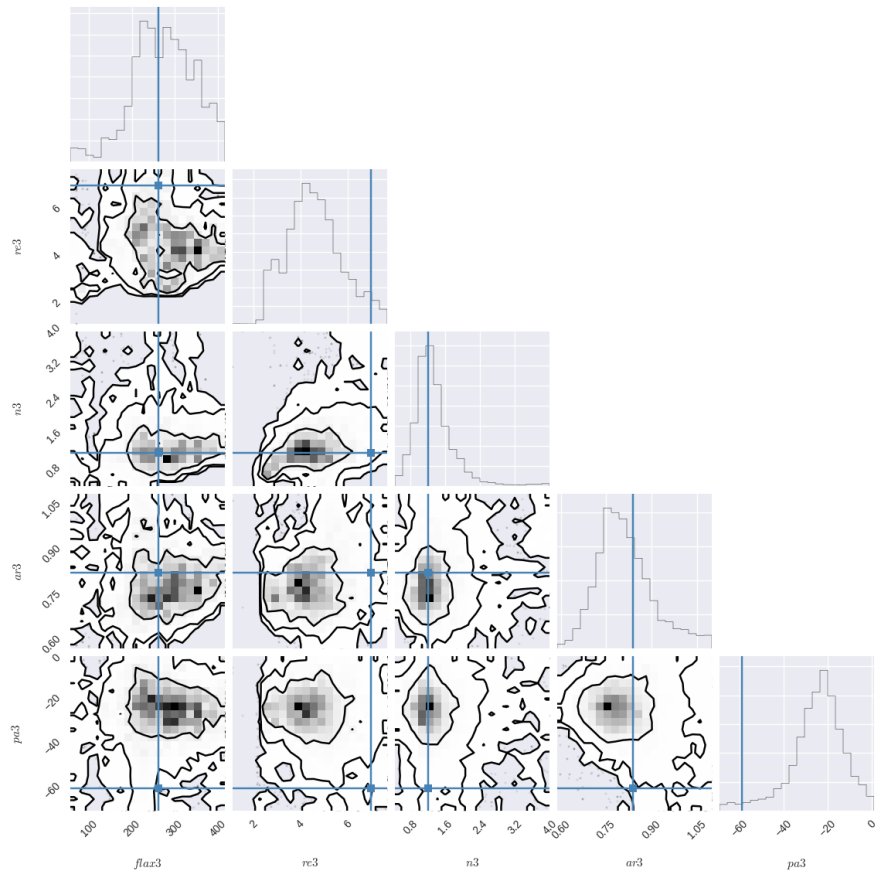


Figure 189 Probability map for Sersic component of J1337 K' -band.

D.9 J1407J

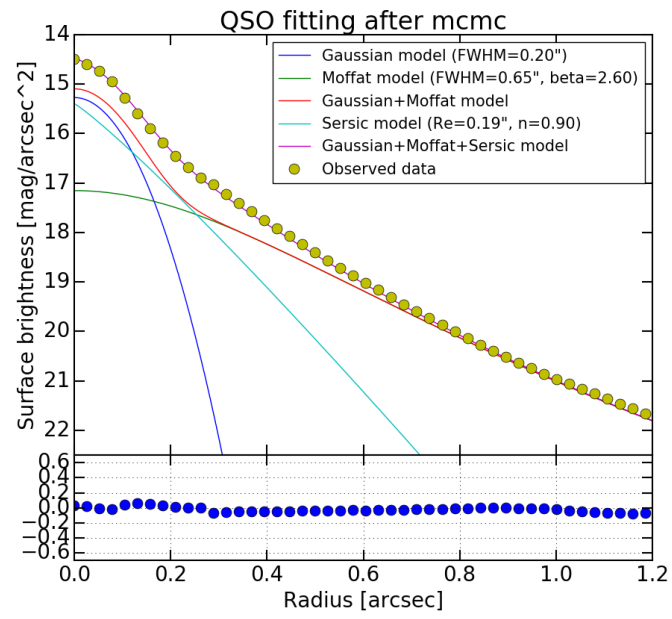


Figure 190 Final radial profile for J1407 *J*-band.

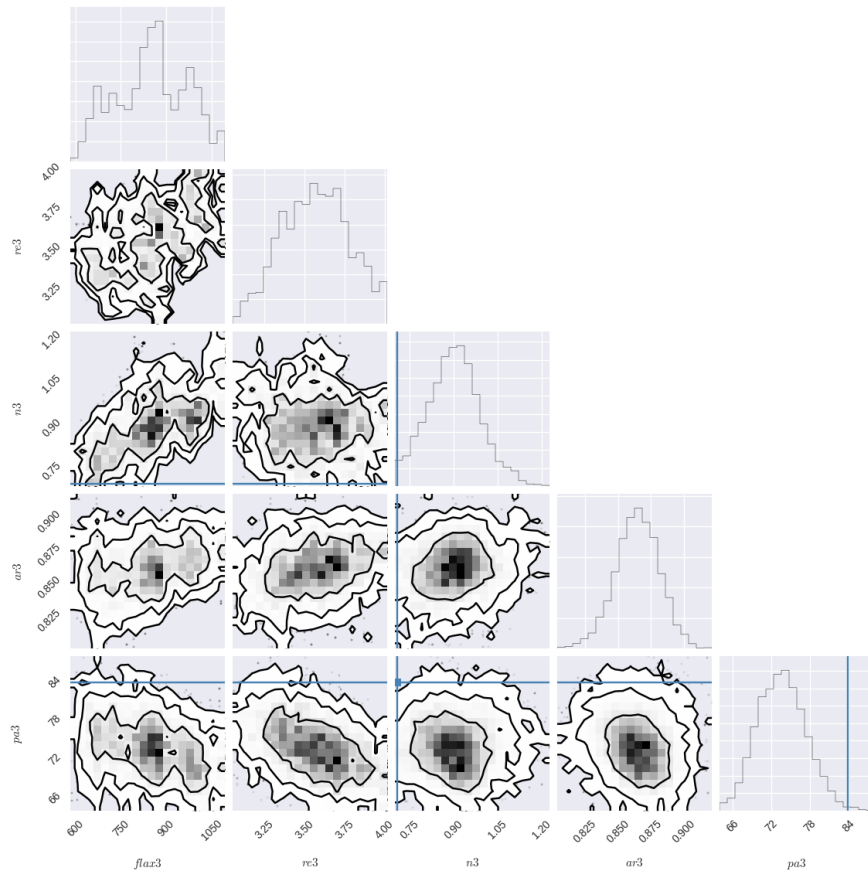


Figure 191 Probability map for Sersic component of J1407 *J*-band.

D.10 J1407K

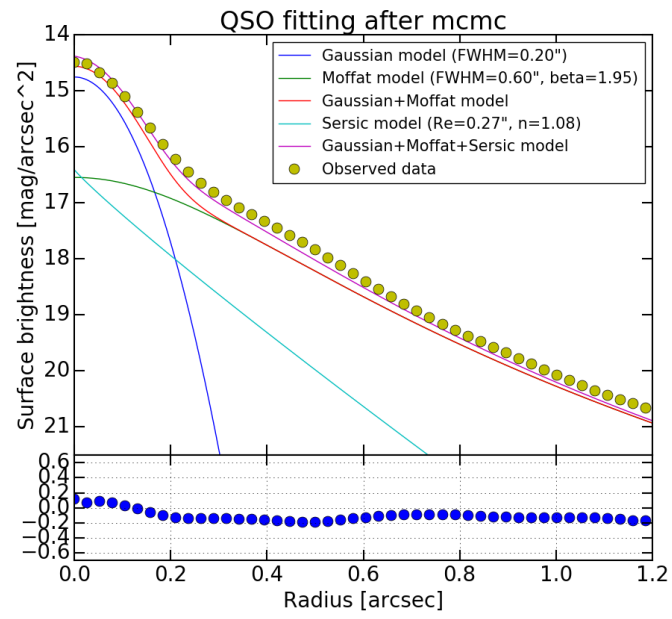


Figure 192 Final radial profile for J1407 K' -band.

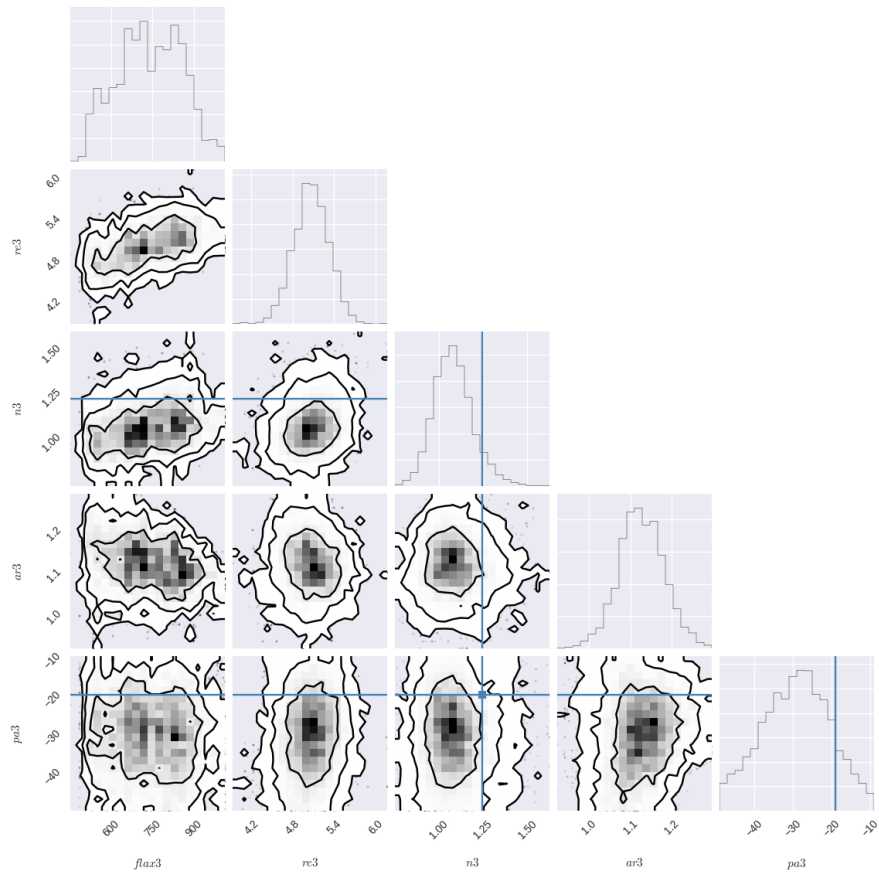


Figure 193 Probability map for Sersic component of J1407 K' -band.

D.11 J1510J

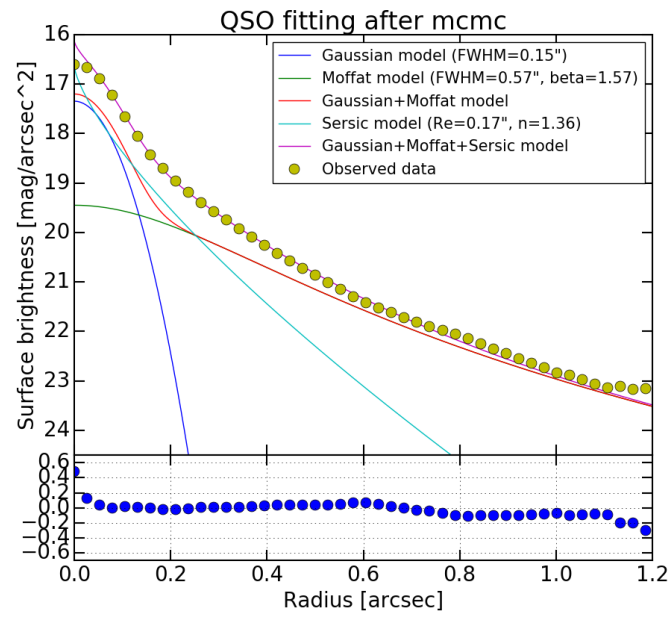


Figure 194 Final radial profile for J1510 *J*-band.

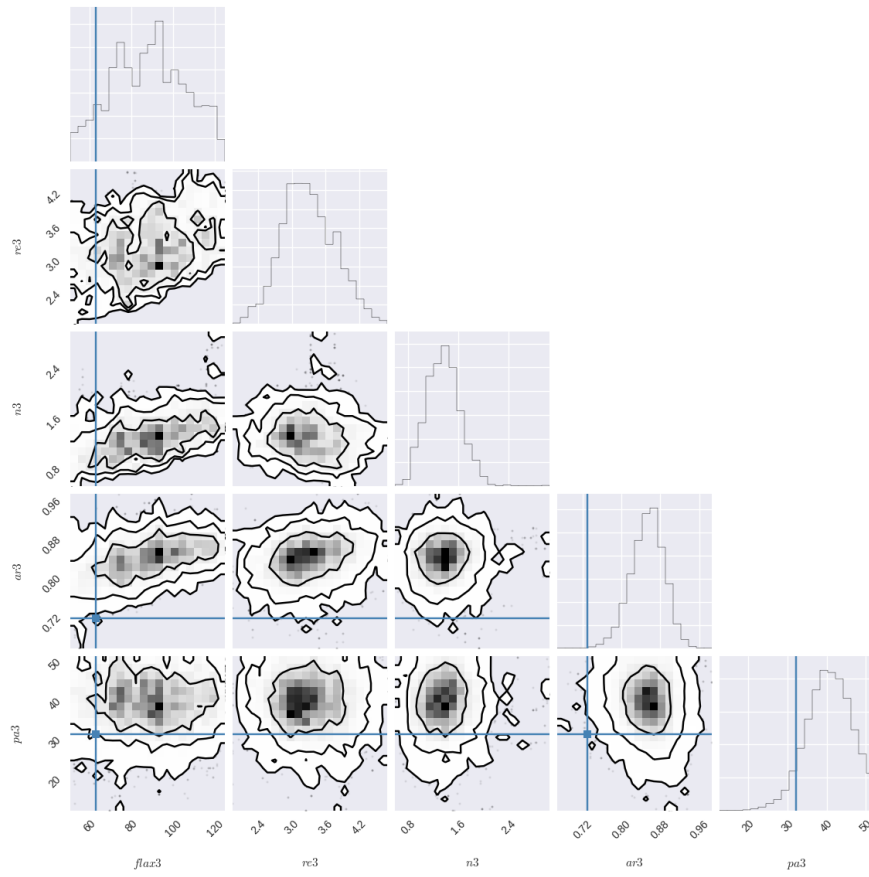


Figure 195 Probability map for Sersic component of J1510 *J*-band.

D.12 J1510K

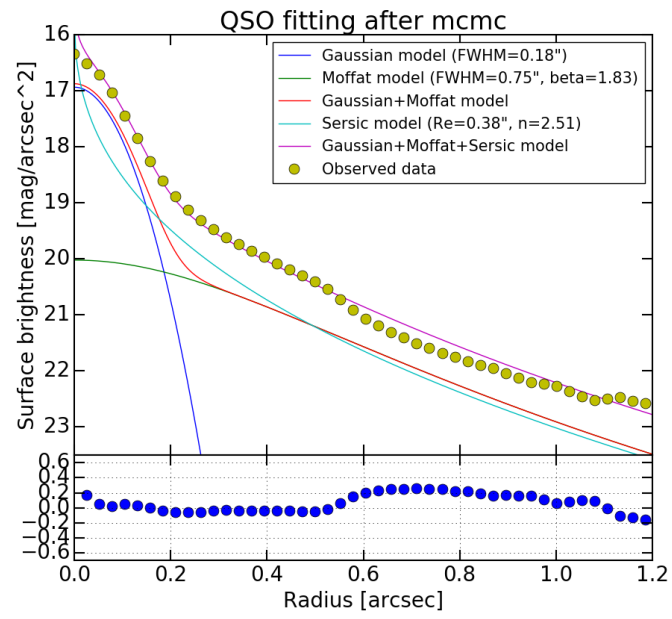


Figure 196 Final radial profile for J1510 K' -band.

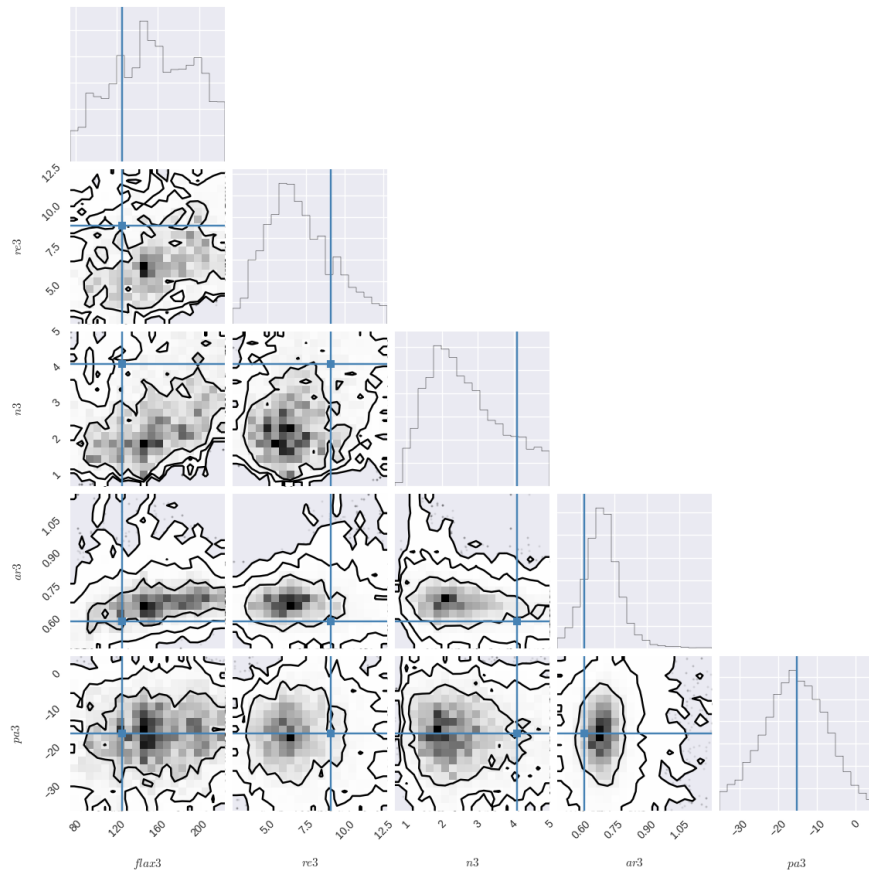


Figure 197 Probability map for Sersic component of J1510 K' -band.

D.13 J1551J

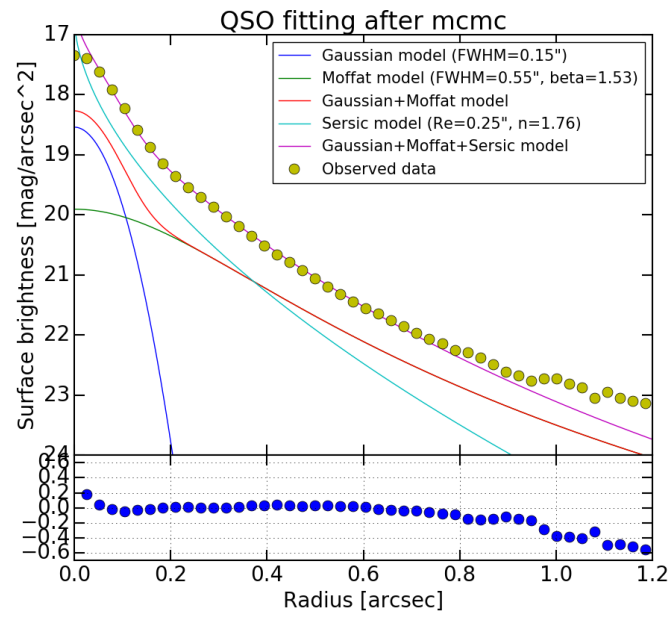


Figure 198 Final radial profile for J1551 *J*-band.

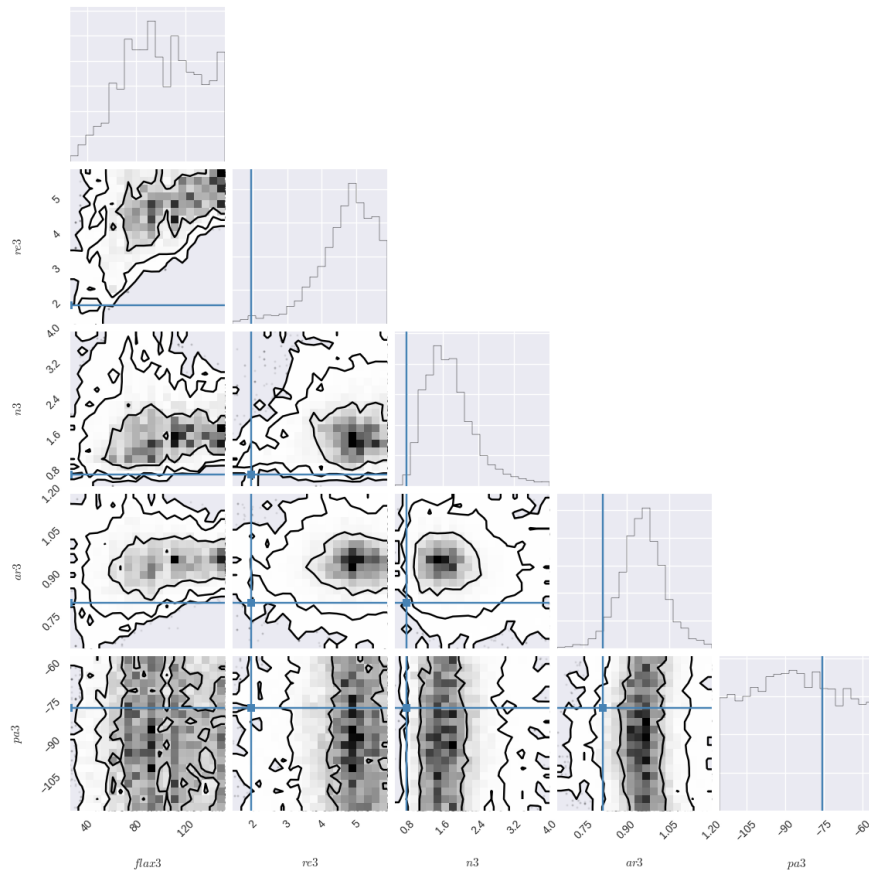


Figure 199 Probability map for Sersic component of J1551 J -band.